Study of the equilibrium and the transport of electrolytic solutions in confinement

Dandara Velasco Anez

THÈSE

Pour obtenir le grade de

DOCTEUR DE L'UNIVERSITÉ GRENOBLE ALPES

École doctorale : PHYS - Physique
Spécialité : Nanophysique
Unité de recherche : Laboratoire Interdisciplinaire de Physique

Étude de l'équilibre et du transport de solutions électrolytiques confinées

Study of the equilibrium and the transport of electrolytic solutions in confinement

Présentée par :

Dandara VELASCO ANEZ

Direction de thèse :

Benjamin CROSS Professeur des universités, UGA	Directeur de thèse
Enric SANTANACH-CARRERAS Ingénieur R&D, TotalEnergies	Co-encadrant de thèse
Elisabeth CHARLAIX Professeure des universités, UGA	Co-encadrante de thèse
Romain LHERMEROUT Chargé de recherche, CNRS	Co-encadrant de thèse

Rapporteurs :

Carlos DRUMMOND
Directeur de recherche, CNRS, CRPP Bordeaux

Christophe YBERT
Directeur de recherche, CNRS, ILM Lyon

Thèse soutenue publiquement le **10 juillet 2023**, devant le jury composé de :

Carlos DRUMMOND Directeur de recherche, CNRS, CRPP Bordeaux	Rapporteur
Christophe YBERT Directeur de recherche, CNRS, ILM Lyon	Rapporteur
Marie-Caroline JULLIEN Directrice de recherche, CNRS, IPR Rennes	Examinatrice
Hugues BODIGUEL Professeur des universités, Grenoble INP, LRP Grenoble	Président

Acknowledgements

These almost four years of thesis have truly been an adventure. Full of ups and downs where the only constants were the people surrounding me and supporting me. To these people I have such gratitude, that words cannot express enough.

I would like to start thanking Hugues Bodiguel, President of the jury, who has followed up my work closely over the years in the CSI (Comité de Suivi Individuel de thèse).

Thank you as well to Carlos Drummond and Christophe Ybert, for accepting to be my "Rapporteurs" and evaluating my work. Your insight on the SFA and nanofluidics, respectively, and your constructive feedback have been useful and greatly appreciated.

And Marie-Caroline Jullien, thank you for participating as my "Examinateur", and bringing your input and debate on soft matter.

I would like to continue thanking Elise Lorenceau, who accepted me as an intern in LIPhy and opened the way for me to apply later for the thesis. Know that you are one of a kind, as a professional but mostly importantly, as a person.

Thanks as well to Enric Santanach-Carreras from Total Energies, for trusting me to carry this project, and for always making sure that I work under the best conditions.

I suppose I do not need to explain why I feel grateful to have worked in the team of the brilliant Elisabeth Charlaix, your mind knows no boundaries and I am glad I experienced it first-hand.

I extend my gratefulness to my thesis director Benjamin Cross. I appreciate the patience and the guidance you offered during every step of my evolution and learning. Thank you for understanding when I decided to finish the thesis in parallel with a new job. It has not been easy but your support all the way through, made it possible.

To Romain Lhermerout, I want to thank you for having arrived to LIPhy in the right time (in the middle of the Covid crisis). Thanks to have dived and engaged in this project when it was the most needed. I am glad I got to "share" the struggles of the experimental development with you. Your positive attitude and good humor definitely made every day better. Don't ever lose that!

Thank you as well Jérôme Giraud, for all the support you gave me and your availability, especially in the first year while rebuilding the instrument, your help has been priceless.

I am deeply grateful to all the LIPhy personnel I got to work with. First, to Cyril Picard and Lionel Bureau from MODI team, whom I worked prior to the thesis but you set up the

bases for the future. Thanks to Bruno Travers for your important contribution on electronics, to Michaël Betton for the training in the use of the sputtering machine, and to the LAME team (Jean-Luc Martin, Guillaume Méjean, Samir Kassi and Léo Djevahirdjian), your help in laser-related subjects is immensely appreciated.

I want to thank all the PhD students that were in LIPhy when I was an intern and were one of the reasons for me staying in this lab, you have been greatly missed. Thanks as well to all the PhDs that started with me and those who kept arriving, I have learned so much from you all, I appreciate your support during hard times and I wish nothing but the best in life to each and every one of you. Hope our paths keep crossing and our friendship will last a lifetime!

And to my very favorite PhD student (now Doctor and husband) Edouardo Al Alam, thanks for deciding to go through this life by my side, only you and me know how much these past years have been challenging. Your strength, resilience and dedication in your own thesis were an inspiration for mine. I can only hope we keep achieving our goals together, supporting each other and overcoming the new obstacles life brings to us.

Thanks to the friends I have back in Bolivia and those I made in France, including the colleagues from Lancey that have become friends in a short time. You all make a difference in my life.

To my parents, siblings and all my family, you are the sunshine of my life and without your love, your support and your prayers, I would not be here. Know that all my achievements are dedicated to you.

Finally, but most importantly, thank God for opening the doors for me to come to France and to embark in this journey, for the people I got to meet and for the obstacles I had to face, both personally and professionally. I am mostly thankful for keeping me and my loved ones in good health, especially during Covid times. It has been definitely challenging being a "believer" while doing a PhD in Physics, but this experience has only made my faith stronger, in God, in people and in myself.

Abstract

Blue Energy is the term given to the energy generated by the salinity difference between two bodies of water. An osmotic process allows the conversion of this energy into electricity, from the ion flow through membranes like in PRO or RED energy harvesting processes. The estimated power to be produced from Blue Energy in the world is equivalent to 1000 nuclear plants. However, the power density of current technologies is too low to make the process cost-effective and technically viable.

From a physical point of view, this issue falls within the general theme of energy conversion in nanofluidics. These conversions are based on the coupling between hydrodynamics, electrokinetics and the transport of ionic species. These couplings obviously depend on the properties of the confined fluids but also on the equilibrium characteristics of the systems such as the surface charge. To our knowledge, there is no experiment allowing simultaneous measurements of the transport and equilibrium properties of a nanofluidic system.

In this manuscript, the instrumental development of a dynamic Force Surface Apparatus is presented. This machine and its surrounding have been adapted to study electrolyte solutions confined throughout five orders of magnitude (10 µm to 1 Å), with a strict environmental control. Experiments were performed on NaCl aqueous solutions, confined between Borosilicate glass or Boron Nitride coated glass surfaces. We have shown the existence of an over-dissipation induced by ions from electrolytes compared to a classical Newtonian behavior. Preliminary results on the influence of the ionic concentration and surface charge on electrolyte over-dissipation are presented.

Résumé

L'énergie bleue est le terme donné à l'énergie générée par la différence de salinité entre deux masses d'eau. Un processus osmotique permet de convertir cette énergie en électricité, à partir du flux d'ions à travers les membranes, comme dans les processus de collecte d'énergie PRO ou RED. On estime que l'énergie produite par l'Energie Bleue dans le monde équivaut à 1000 centrales nucléaires. Cependant, la densité de puissance des technologies actuelles est trop faible pour que le processus soit rentable et techniquement viable.

D'un point de vue physique, cette question s'inscrit dans le thème général de la conversion de l'énergie dans la nanofluidique. Ces conversions sont basées sur le couplage entre l'hydrodynamique, l'électrocinétique et le transport d'espèces ioniques. Ces couplages dépendent évidemment des propriétés des fluides confinés, mais aussi des caractéristiques d'équilibre des systèmes telles que la charge de surface. A notre connaissance, il n'existe pas d'expérience permettant de mesurer simultanément les propriétés de transport et des propriétés d'équilibre d'un système nanofluidique.

Dans ce manuscrit, le développement instrumental d'un Appareil à Force de Surface dynamique est présenté. Cette machine et son environnement ont été adaptés pour étudier des solutions d'électrolytes confinées sur cinq ordres de grandeur (10 µm à 1 Å), avec un contrôle environnemental strict. Les expériences ont été réalisées sur des solutions aqueuses de NaCl, confinées entre des surfaces de verre Borosilicaté ou revêtues de Nitrure de Bore. Nous avons montré l'existence d'une surdissipation induite par les ions des électrolytes par rapport à un comportement newtonien classique. Des résultats préliminaires sur l'influence de la concentration ionique et ceux de la charge de surface sur la surdissipation de l'électrolyte sont présentés.

Contents

Introduction

Electrolytes are a very special class of liquids. Like plasma with which they share certain characteristics, they are composed of charge carriers and remain electrically neutral. They play a role in many domains, from stratified flows in oceanography for example, to biology through the transmission of nerve impulses. From an application point of view, they are at the basis of batteries since Volta's discoveries at the beginning of the 19th century. Today, in the context of the energy transition, the interest in electrolytes is growing. The control of techniques at the nanometric scale allows a new field of applications. Electrolytes in confinement, at the nanoscale, are utilized in multiple domains, from the injection of charged polymer solutions into wells for Enhanced Oil Recovery (EOR) operations [1], to the application of electrical potential onto ionic liquids inside supercapacitors [2]. In this thesis, we are interested in the study of saline solutions such as those found in sea water, and in understanding the phenomena at the origin of osmotic processes to harvest the so-called Blue Energy [3].

Osmotic (or Blue) Energy is harvested by mixing two bodies of water with different saline concentrations. It has been estimated that the transfer of non-salty water found in the Amazonian river mouth that opens to the Atlantic ocean would generate 1 TW of power [4], equivalent to the production of 1000 nuclear plants. Although many efforts have been made to harvest osmotic energy with nanometric porous membranes, their performances are not good enough to make the technology viable [5]. However, nanotubes made of different materials, such as Carbon or Boron Nitride, have proved to exhibit giant power densities, attributed to a high density of electric charges on solid surfaces [6].

The electrokinetic processes at play in Blue Energy harvesting are by nature surface phenomena, due to the contact between the electrolyte solution and the solid surface [7]. They are enhanced in a situation of confinement down to the nanometric scale and the key parameters are the electrical (surface charges) and hydrodynamic (liquid slippage at the interface) boundary conditions. Theories have been developed for the equilibrium and out-of-equilibrium properties of diluted electrolytes, describing the electrostatic interactions and the coupled transport in confinement. Even if theories describing systems at equilibrium are well documented experimentally, in particular by the work of Israelachvili during the 1970s [8], those concerning transport are limited to assuming a state of equilibrium without

experimental validation of this strong hypothesis. So far, experimental studies focused on a particular transport coefficient, like electric conductivity or streaming current, providing inconsistent fitted values for the surface charge [9]. This is why an experimental technique allowing the simultaneous measurement of static and dynamic properties in nano-confined electrolytes is needed.

Although micro- and nano-fluidic techniques are commonly used to study liquids in confinement, they do not offer the possibility of probing the equilibrium properties and of varying the confinement during an experiment. The dynamic Surface Force Apparatus (dSFA) at LIPhy, device used in this thesis, does not have these limitations [10]. A liquid is confined in a sphere-plane geometry and the separation between the two surfaces can be continuously varied over five orders of magnitude (10 µm to 1 Å). A quasi-static approach allows to measure the force between the sphere and the plane as a function of their separation, including the electrostatic interaction and the electric boundary condition, i.e., the screening length and the surface charge. Simultaneously, the oscillation of one surface at a given frequency generates a drainage flow and gives access to the nanorheology of the liquid, including the viscosity and the hydrodynamic boundary condition, i.e. the slip length.

The dSFA at LIPhy was built during the thesis work of Garcia [11] and Barraud [12]. As the atmospheric conditions were not controlled, it was difficult to work with volatile liquids: evaporation changed the composition of the solution, produced large signal drifts and reduced the lifetime of an experiment. This is the case with aqueous solutions, the most common electrolytes on Earth and at the heart of Blue Energy recovery. Therefore, the first objective of my thesis was to improve the environmental conditions of the experiment, installing an atmospheric control and a thermal regulation system, and by working accordingly on the instrumentation of the dSFA to adapt it to the environmental changes. The main modification was the construction of new interferometers, with compact designs and optimized sensitivities. The second objective was to conduct experimental campaigns with different saline solutions and confining surfaces in order to vary the screening length and the surface charge.

The work done during the thesis has been summarized in this manuscript, divided into three sections:

I. State of the Art (Chapters 1 and 2), presents the electrostatic and electrokinetic processes in confined electrolytes, and central physical quantities such as the mechanical impedance and admittance that describe the nanorheology of a fluid confined between a sphere and a plane with the dSFA.

II. Materials and Methods (Chapters 3 and 4) describes the dSFA's operating principle, the improvements made to the instrument and the performances obtained, followed by the description of the experimental procedure from sample preparation to data treatment.

III. Results and Discussion (Chapters 5 and 6) presents and proposes first interpretations of experiments performed with NaCl aqueous solutions of different concentrations and pH, confined between Borosilicate glass and Boron Nitride coated glass surfaces.

The conclusion summarizes the main results and outlines the perspectives of this thesis work.

Part I

State of the Art

Chapter 1

Electrolytes in Confinement

Contents

Introduction

In this chapter I will present the physical phenomena involving electrolytes at- and out-of-equilibrium, and the theories to describe them. I will limit the study in this manuscript to dilute electrolytes as I have studied them experimentally. They represent the class of electrolytes used in applications related with osmotic energy harvesting. I will also try to present the open questions in the field, which motivated my research work presented in this thesis manuscript.

1.1 Equilibrium Properties

In the vicinity of a charged surface, the distribution of ions in the electrolyte is modified. This ionic distribution results from electrostatic forces that balance with entropic effects in solution. To describe this equilibrium state, one can introduce the electrochemical potential of the ions which, in addition to the traditional contribution of a dilute gas, includes the

electrostatic energy of the ions within the potential developed from the solid surface. At equilibrium, the electrochemical potential of the ions is uniform in the solution.

1.1.1 Characterization of the Interface

The contact between an electrolyte solution and a solid surface generally results in a charged solid-fluid interface, where long-range electrostatic interactions take place between the ions of the solution and between the ions and the charge supported by the surface. The surface charge is progressively screened by the counter-ions of the solution, in an interfacial region which structure and dynamics is governed by a range of physical and chemical processes. A broadly used model for charged interfaces is the Electric Double Layer (EDL) (Figure 1.1).

The Electric Double Layer

A solid surface can be charged electrostatically. The charging of conductive surfaces (electrodes) is commonly achieved by the application of an electrical voltage with an external source. In the case of dielectric surfaces, spontaneous charging occurs whether by the dissociation of surface groups, by the adsorption of ions from the solution, by the exchange of charges from one surface to the other when two different surfaces are very close to each other [13] etc. The resulting surface charge will be partially screened by an adsorbed layer of counter-ions (hydrated or partially-hydrated): this is the so-called Stern layer. The screening of the residual surface charge after the Stern layer is produced by counter-ions which keep a certain mobility. Their distribution is governed by the thermodynamic equilibrium of the solution in the vicinity of the charged surface: it is the so-called Diffuse layer. Both the Stern layer and the Diffuse layer form the EDL model, also called the Gouy-Chapman-Stern model.

Characteristic Lengths

The EDL develops from the solid-liquid interface to the bulk. Electrolytes at the vicinity of a solid surface or in confinement are first of all a matter of length scale. The Figure 1.2 represents the different length scales that can be found in equilibrium, confinement or flow situations. Before introducing these different lengths, we can already notice that they are all under the micrometer. Consequently, it is at the nanometric scale that we can expect surface or confinement effects for electrolytes.

Let's start with two lengths not shown on the Figure 1.2. The first length scale is the **Gouy-Chapman length** ℓ_{GC}. At this scale, of the order of a tenth of nanometer, the Coulombic energy between a single charge e and a surface of charge density σ is equal to the thermal energy, so that:

$$\ell_{\mathrm{GC}} = \frac{2\epsilon k_{\mathrm{B}} T}{e\,|\sigma|} \tag{1.1}$$

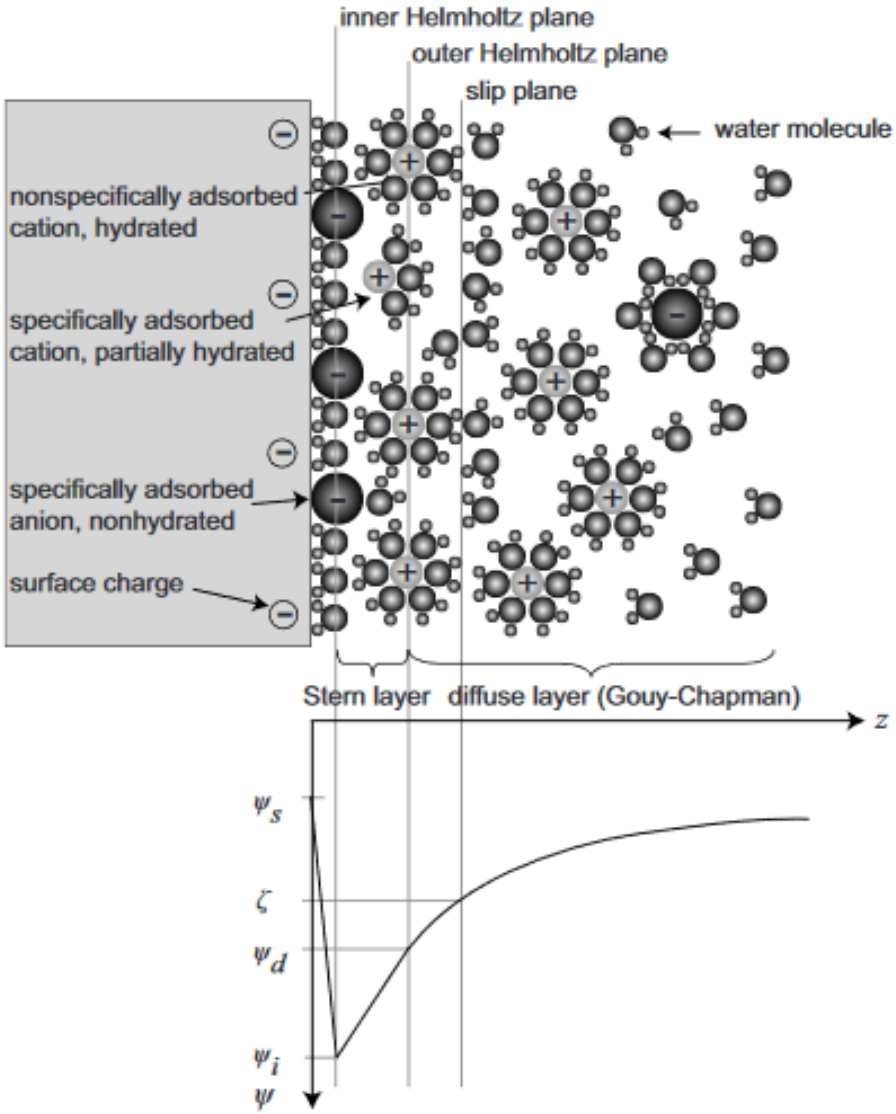

Figure 1.1 Schematic of the Gouy-Chapman-Stern model of the solid-electrolyte interface, with the corresponding potential distribution Ψ as a function of the distance z from the wall. Figure from [14].

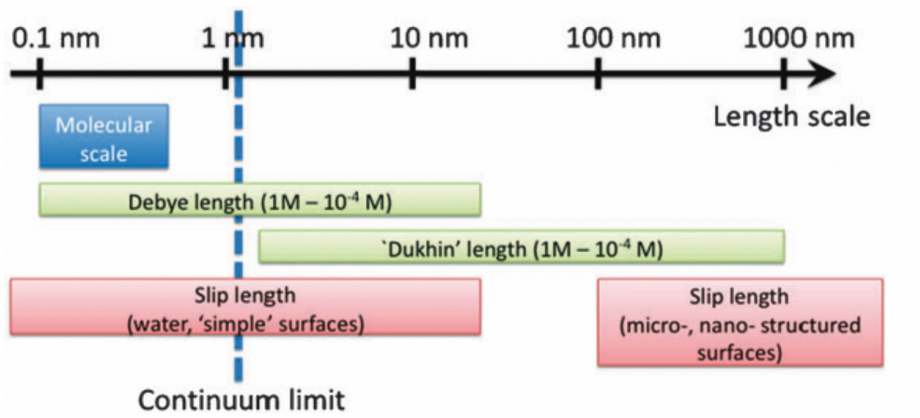

Figure 1.2 Characteristic Lengths. Figure from [7].

where $\epsilon = \epsilon_0 \epsilon_r$ is the absolute permittivity equal to ϵ_0 the vacuum permittivity times ϵ_r the relative dielectric constant of the medium, k_B is the Boltzmann constant, T is the temperature, e is the elementary charge, and σ is the surface charge density. The Gouy-Chapman length depends on the surface charge density, but not on the bulk ion concentration [7].

The second one is the **Bjerrum length** ℓ_B. Physically, the Bjerrum length is the distance between two charges at which their Coulombic interaction energy equals the thermal energy, written as:

$$\ell_B = \frac{e^2}{4\pi\epsilon k_B T} \tag{1.2}$$

For instance, the Bjerrum length for water at 298 K is equal 0.7 nm.

The **Debye length** λ_D is the characteristic thickness of the Diffuse layer [15]. Qualitatively, it corresponds to length necessary to screen any charge density fluctuation in the electrolyte:

$$\lambda_D = \sqrt{\frac{\epsilon k_B T}{2e^2 C}} = (8\pi \ell_B C)^{-1/2} \tag{1.3}$$

with C the concentration of ions in the bulk in number of ions per unit volume, in the simplest case of a single pair of monovalent ions. The Debye length depends solely on the bulk ion concentration and not of the surface charge. For instance, for an aqueous NaCl solution at 10^{-4} mol/L the Debye length is $\lambda_D = 30.4$ nm, and for pure water at pH 7, is $\lambda_D = 960$ nm.

The **Dukhin length** ℓ_{Du} compares the surface charge effects against volume charge effects, and it can also be rewritten in terms of Debye and Gouy-Chapman lenghts:

$$\ell_{Du} = \frac{|\sigma|}{eC} = \frac{4\lambda_D^2}{\ell_{GC}} \tag{1.4}$$

Since it is inversely proportional to the ions density, the Dukhin length can vary in many magnitude orders. For example in water, $\ell_{\mathrm{Du}} = 0.1$ nm for $C = 1$ mol/L and $\ell_{\mathrm{Du}} = 1000$ nm for $C = 10^{-4}$ mol/L.

Poisson-Boltzmann theory

We will describe quantitatively the behavior of an electrolyte near a surface. For this, we choose a monovalent electrolyte whose concentration far from the surface is noted C. The surface is flat and uniformly charged with a surface charge σ. We note z the coordinate perpendicular to the surface. The problem is then one-dimensional and the physical quantities only depend on z. We will start by writing the equality of the electrochemical potentials for the two ion species:

$$\mu_+ = \mu_- = k_{\mathrm{B}}T \ln(C)$$

where μ_+ is the electrochemical potential of cations and μ_- is the electrochemical potential of anions. The electrochemical potentials can be written as follows:

$$\mu_\pm = \pm eV(z) + k_{\mathrm{B}}T \ln C_\pm(z)$$

where V is the electric potential developed in the electrolyte at z and $C_\pm(z)$ is the ion concentration at z. We directly find that the concentrations follow a Boltzmann distribution:

$$C_\pm(z) = Ce^{\mp\frac{eV}{k_{\mathrm{B}}T}} \tag{1.5}$$

To access the concentrations and the potential in the electrolyte, we need an additional equation and for this we will use the Poisson equation from electrostatics:

$$\Delta V = -\frac{\rho}{\epsilon} \quad \text{with} \quad \rho = e(C_+ - C_-) \tag{1.6}$$

When combined, the normalized Poisson-Boltzmann (PB) equation allows to know the non-dimensional potential $\Psi = eV/k_{\mathrm{B}}T$ between the two surfaces:

$$\frac{\partial^2\Psi}{\partial z^2} = -\frac{1}{\lambda_{\mathrm{D}}^2}\sinh\Psi(z) \tag{1.7}$$

where λ_{D} is the Debye length.

In the case of electric potentials such that $e\,|V| \ll k_{\mathrm{B}}T$, i.e., $|V| \ll 25$ mV, the **Debye-Hückel approximation** is applied. The Poisson-Boltzmann equation is linearized (Eq. 1.8):

$$\frac{\partial^2\Psi}{\partial z^2} \approx -\frac{\Psi}{\lambda_{\mathrm{D}}^2} \tag{1.8}$$

Solving this equation requires electric boundary conditions. We consider here a simple configuration, where there is only one surface so that the electric potential reaches zero at infinite distances ($\Psi(z=\infty)=0$), and where a constant surface potential boundary condition applies ($\Psi(z=0)=\Psi_\mathrm{s}$). We obtain the solution of the Debye-Hückel approximation presented in Eq. 1.9:

$$\Psi(z) = \Psi_\mathrm{s} \exp^{-z/\lambda_\mathrm{D}} \tag{1.9}$$

which shows that the screening action of the ions in the EDL triggers an exponential decay of the electric potential. Note that this approximation can be applied for arbitrary large surface potentials Ψ_s, providing that the distance z considered is large enough, such that $\Psi(z) \ll 1$. In this case, Ψ_s is an apparent surface potential, obtained by extrapolating the large distance behavior to the surface.

In the Debye-Hückel approximation, it can be shown that the repulsive force between two planar and spherical surfaces, of same surface potential and separated by a distance D, is due to an excess of osmotic pressure. Its expression can be found in [13]:

$$F_\mathrm{repulsive} = RZ\lambda_\mathrm{D}^{-1} e^{-D/\lambda_\mathrm{D}} \tag{1.10}$$

with Z an interaction constant. For a monovalent 1:1 electrolyte such as NaCl, $Z = 64\pi\epsilon(k_\mathrm{B}T/e)^2 \tanh^2(eV_\mathrm{s}/4k_\mathrm{B}T)$.

Furthermore, thanks to **Grahame** equation (1.11), it is possible to relate the surface potential $V_\mathrm{s} = \frac{kT}{e}\Psi_s$ and the surface charge σ, supposing zero electric field in the solid:

$$|V_\mathrm{s}| = \frac{2k_\mathrm{B}T}{e}\mathrm{asinh}\Big(\frac{|\sigma|}{\sqrt{8\epsilon C k_\mathrm{B}T}}\Big) \approx \frac{2k_\mathrm{B}T}{e}\ln\Big(\frac{|\sigma|}{\sqrt{2\epsilon k_\mathrm{B}T}}\Big) + \frac{k_\mathrm{B}T\ln 10}{e}\mathrm{pC} \tag{1.11}$$

for $e\,|V_\mathrm{s}| \gg k_\mathrm{B}T$ and where $\mathrm{pC} = -\log(C)$.

1.1.2 The DLVO Theory and the Derjaguin approximation

From the contribution of Derjaguin, Landau, Verwey and Overbeek, the classical theory of DLVO was formulated, allowing to explain the stability of colloidal solutions. Here I give the basic ingredients of this theory, considering a sphere-plane geometry.

When two macroscopic solids are separated by an electrolyte, their interaction is the result of all the pair potentials acting between the molecules and ions involved. The DLVO theory describes the equilibrium of the attractive van der Waals forces at play between symmetric surfaces with the repulsive electrostatic interactions due to the surface charge screened by the counter-ions of the solution: $F(D) = F(D)_\mathrm{attractive} + F(D)_\mathrm{repulsive}$ (Figure 1.3).

We have already presented half of the DLVO theory thanks to the electrostatic contribution to the interaction force presented in the previous section. To finish, I present here the attractive contribution to the interaction based on van der Waals interactions.

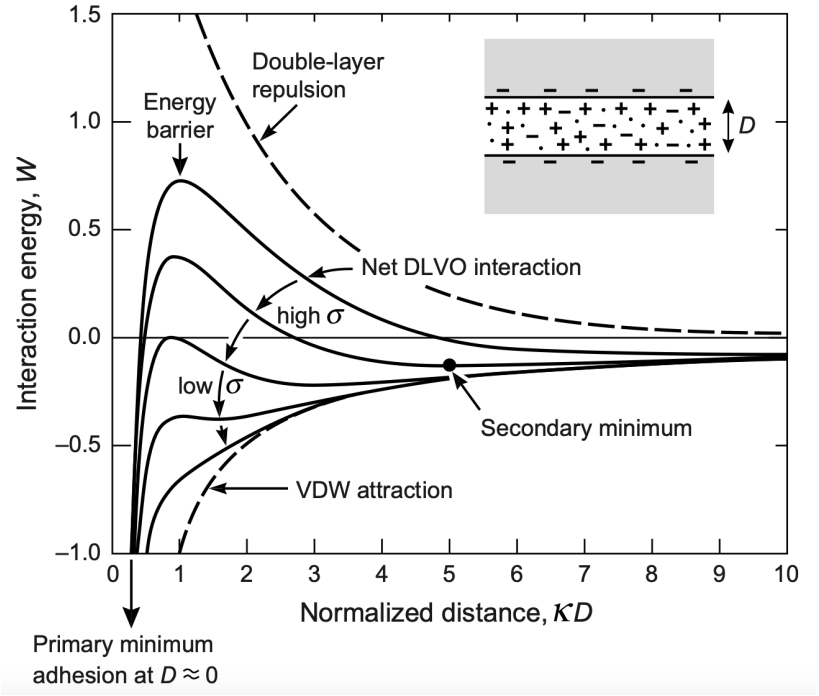

Figure 1.3 Schematic of the DLVO interaction energy profiles as a function of the distance between two flat surfaces. Figure from [13].

Derjaguin approximation

The disjoining pressure $\Pi(D)$ is the internal pressure needed to separate or approach two planar parallel surfaces, which depends on the distance D between them. The integration of the disjoining pressure gives direct access to the interaction energy by unit of surface W, as $\frac{dW(D)}{dD} = -\Pi(D)$. In realistic configurations with surfaces of finite curvatures, for example a sphere of radius R and a plane, one has to integrate the pair potential exerted between all the constituents in order to access the total force F acting between the surfaces.

However, in the limit $R \gg D$ Derjaguin showed that [16]:

$$F(D) = 2\pi R W(D) \tag{1.12}$$

Consequently, the equilibrium force $F(D)$, accessible experimentally between a sphere and a plane, can be rescaled by $2\pi R$ in order to get the interaction energy by unit of surface $W(D)$ or the disjoining pressure $\Pi(D)$ between equivalent planar parallel surfaces.

van der Waals interactions

Using the Derjaguin approximation, it can be shown that the attractive van der Waals force between a large-radius sphere R and a flat surface of same materials is equal to:

$$F_{\text{attractive}} = -\frac{AR}{6D^2} \tag{1.13}$$

where A is the so-called Hamaker constant.

1.2 Out-of-Equilibrium Phenomena

A range of electrokinetic phenomena are known in the colloid literature, from purely diffusive Brownian motion to more complex physical processes involving several couplings (hydrodynamics, diffusion, electric conduction, etc.).

A simple example is osmosis, the process that occurs when two reservoirs of different ion concentrations are separated by a semi-permeable membrane: a driving force will push solvent molecules through the membrane towards the more concentrated region, while retaining solute ions, and an (osmotic) pressure will be needed to counteract the flow. van 't Hoff formulated an equation analogous to the perfect gas law [17], where the solute particles exert an osmotic pressure in the solution that is equal to:

$$\Delta\Pi = k_{\text{B}}T\Delta C \tag{1.14}$$

with ΔC the solute gradient between reservoirs.

Figure 1.4 illustrates for example how diffusion and osmosis can provoke the displacement of ions or solvent molecules. Transport can be induced by purely electric, diffusive or hydrodynamic effects, and also by couplings of these effects. Identifying the multiple forces acting on the solvent and the solute is the key for understanding the subtle phenomena of osmosis and its derivatives, diffusio-osmosis and electric-osmosis processes from which breakthrough applications in different domains have been found in the last decades [18], [4], [19].

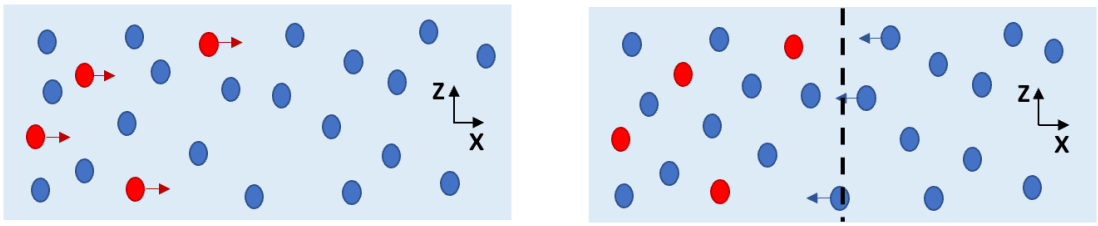

Figure 1.4 Schematics of diffusion versus osmosis, based on [20]. On the left, the displacement of solute ions is governed by diffusion, while on the right, the solvent is pushed through the membrane by osmosis towards the more concentrated region.

1.2.1 Hydrodynamic-Diffusive-Electric Coupling

Mazur and Overbeek [21] used a capillary containing an electrolyte solution to prove a series of relations between electrokinetic phenomena, such as electro-osmosis. These are Onsager relations, in the context of electrolytes near charged surfaces. More recently, Brunet and Adjari adapted them for any type of geometry, as a form of a symmetric transport matrix [22].

The transport matrix compiles the irreversible processes that relate the transport in electrolytes to three different origins (Figure 1.5). A hypothesis of linearity is made to proportionally reciprocate flows and fields for systems near thermodynamic equilibrium. The diagonal coefficients in the matrix relate respectively: a pressure gradient $-\nabla P$ to a hydrodynamic flow Q, an electric potential gradient $-\nabla V$ to an electrical current I and a concentration gradient $-\nabla C$ to a diffusive flux $J - CQ$. The anti-diagonal coefficients represent the diffusio-osmotic, electro-osmotic, and diffusio-electric couplings respectively.

$$\begin{pmatrix} Q \\ J - CQ \\ I \end{pmatrix} = \begin{pmatrix} \text{Permeability} & \text{Diffusio-osmotic flow} & \text{Electro-osmotic flow} \\ \text{Excess flux under pressure} & \text{Diffusion} & \text{Excess flux under electric field} \\ \text{Streaming ion current} & \text{Diffusio-osmotic ion current} & \text{Electric conductance} \end{pmatrix} \times \begin{pmatrix} -\nabla P \\ -\nabla C \\ -\nabla V \end{pmatrix}$$

Figure 1.5 Transport matrix, with colors indicating symmetric terms. Image adapted from [20].

Modeling these couplings is very important for application of osmotic energy harvesting. For instance, the matrix can be used to characterize microfluidic geometries and improve the efficiency of new devices for energy conversion, or to help understanding the influence of parameters such as surface charge and zeta potential in the aforementioned applications.

1.2.2 Example of Electro-Osmosis

When a solution is in contact with a charged solid surface and subjected to an electric field parallel to the surface, the motion of the non-electrically neutral Diffuse layer at the interface near the surface will create a flow of solvent parallel to the solid, by a so-called electro-osmotic process (Figure 1.6).

Starting from Stokes equation in the absence of a pressure gradient, we have the expression 1.15:

$$\eta \frac{\mathrm{d}^2 v}{\mathrm{d}z^2} + \rho_\mathrm{e} E = 0 \tag{1.15}$$

where E is the applied electric field parallel to the surface (direction x), ρ_e is the charge volume density, v is the fluid velocity in direction x, z is the distance to the surface and η is the fluid viscosity.

The charge volume density is given by the Poisson equation as:

$$\frac{d^2V}{dz^2} = -\frac{\rho_e}{\epsilon} \tag{1.16}$$

where V is the electrostatic potential. The Stokes equation can be integrated twice with two boundary conditions: a plug-like flow far from the surface ($\partial v/\partial z|_{z=\infty} = 0$), and a Navier slip boundary condition at the wall ($b\,\partial v/\partial z|_{z=0} = v(z=0)$) with a slip length b (more details in Chapter 2). The velocity profile is given in Equation 1.17:

$$v(z) = \frac{\epsilon}{\eta} E(V(z) - \zeta) \tag{1.17}$$

where ζ is the value of the potential at the point where the velocity vanishes. ζ is an important parameter associated with transport properties of the electrolyte. It can reasonably be assumed that its value is close to the surface potential, at least for a no-slip boundary condition. As illustrated in Figure 1.6, the velocity of the fluid flow is proportional to the electric field in the EDL, but far from the surface the electro-osmotic flow it reaches an asymptotic value. Far from the surface ($z = \infty$), the electric potential cancels out, and we get the electro-osmotic velocity v_{EO} first formulated by Smoluchowski [23]:

$$v_{EO} = -\frac{\epsilon\zeta}{\eta} E \tag{1.18}$$

This expression reflects the balance between the electric force driving the fluid and the viscous force opposing its motion.

In the Debye-Hückel approximation, it can be shown that the boundary parameters can be related by:

$$\zeta = V_s(1 + b/\lambda_D) \tag{1.19}$$

1.3 Open questions

Boundary Properties: Surface Charge and Zeta Potential

Based on the physical phenomena discussed in this chapter, I present here the main questions that will try to answer during my thesis.

We have seen that the **Surface Charge** σ intervenes in the characteristic lengths, which suggests that this parameter has a strong influence on the statics and dynamics of electrolyte solutions in confinement. In fact, it has been shown that surface charge can dominate electric

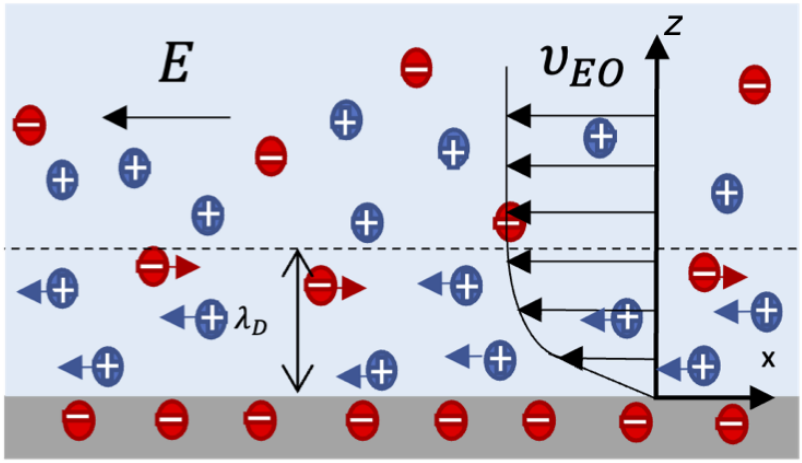

Figure 1.6 Schematic of electro-osmotic transport. A force $F_e = \rho_e E$ is applied to the diffuse layer, created from an electric field E and a density of ions ρ_e. By viscosity, the motion of ions drive the entire fluid.

transport in nanofluidic devices for solutions at low salt concentration [24]. Static surface charge can be measured by several different techniques, like potentiometric titration, UV spectometry or neutron reflectivity [25]. For instance, in Figure 1.7 we show measurements of the surface charge of silica for different concentrations of KCl solutions, obtained by acid-base titration [26]. However, it is often necessary to combine experimental and simulation results to understand all surface-charge-related properties of liquid-solid interfaces [9].

Indeed, one single parameter cannot explain all the interfacial properties. Another important parameter that can also be determined experimentally is the **Zeta Potential** ζ. It results from the distribution and flow of ions near the charged surface, and depends on the pH and ionic concentration of the solution [27]. It corresponds to the electric potential V at the shear (or no-slip) plane, and it is a priori different from the surface potential. The results compiled by Kirby [28] from electrokinetic measurements, represented in Figure 1.7, are consistent with those obtained by other techniques, such as Total Internal Reflection Fluorescence microscopy (TIRF) performed on microfluidic channels [29]. They provide a clear view of the dependence of the zeta potential as a function of ion concentration. A linear dependence of ζ is observed as a function of pC = -log(C) with C the ion concentration.

ζ is a quantity that depends on both static (distribution of charges) and dynamic (flow) properties. There are various technical constraints to measure static and dynamic properties onto the same sample. Thanks to Grahame equation (section 1.1.1) the electrostatic potential can be related to the electrokinetic surface charge, thus obtaining a dynamic measurement of σ. However, values of static surface charge (obtained by the measurement of electrostatic

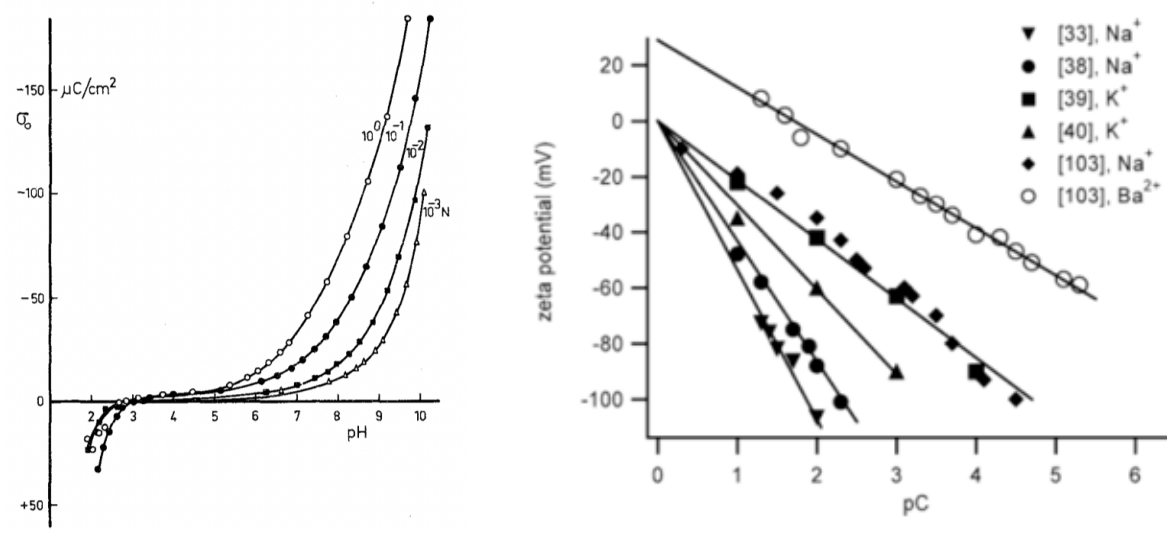

Figure 1.7 On the left, dependence of surface charge density on the pH of the solution, as a result of titration measurements for different concentrations of KCl on SiO_2 surfaces [26]. On the right, results of electrokinetic measurements show dependence of zeta potential on ion concentration [28].

surface potential) are not always consistent with those found in transport measurements (from electrokinetic couplings) [9]. This discrepancy can be related to contributions from the solid surface, the nature of the charge or the ion mobility. Once transport properties are added into the question, the complexity of the system is higher and requires support of modeling [30].

Electric and Hydrodynamic Boundary Conditions

The surface charge, equilibrium quantity, and the ζ potential, transport quantity, are two different physical parameters related as electrical boundary conditions. It is tempting to link them and, for lack of a better term, the Grahame equation is often used for this link. As a surprising example, we would like to give a comparison of two experiments. Current monitoring experiments [31] done on glass with a 0.1 mol/L KCl solution give a ζ potential equal to 90 mV which corresponds, using the Grahame equation, to a surface charge of 2 mC/m^2. Conductivity measurements on an identical system give a surface charge of 60 mC/m^2[24]. We are facing a major problem: either the surface charge strongly dependsy on the flow or the transport measurements lack a theoretical support to interpret the results correctly. And it is even more difficult if we include the hydrodynamic boundary condition on which the ζ potential depends.

The Grahame equation can relate these two parameters, but a choice must be made: whether to take the boundary condition at the non-slip plane (as seen in Figure 1.1 for the ζ

potential) or at the solid surface (as for the surface potential V_s). If we choose the latter, the surface charge must be considered, but how to define it?

In most cases, neither the surface charge nor the surface potential stay constant as the solution conditions change. Surface charge is not always fully dissociated, but it can also be partially neutralized by the binding of ions from the solution. Even for globally neutral surfaces, there could be patches of high local charge density. An independent measurement of the surface potential might be needed to validate the assumption of a constant potential, or if another EDL model needs to be considered, such as charge regulation [13].

Furthermore, ζ and σ play a major role in interfacial phenomena such as slippage. When there is no slippage, the ζ potential and the surface potential values might be very similar [29]. However, the larger the slippage, the larger the difference between these values. Most experiments on ion transport assume no slip, but do not measure it [31]. As well, there is no experimental evidence concerning the correct application of Grahame equation very close to the wall. Ideally, it would be necessary to measure simultaneously the slippage, in order to know where the non-slip plane is located.

Slippage has proven to amplify the values of zeta potential. Bouzigues measured by Total Internal Reflection Fluorescence (TIRF) the velocimetry profiles of nanoparticules in nanochannels [32]. The experimental data showed a good agreement with the theoretical expressions, both in the hydrophilic and hydrophobic cases (Figure 1.8). In the same way, Silkina showed by numerical simulations that electro-osmotic flows in carbon nanotubes and graphene nanoslits were enhanced in thin and thick channels by partial hydrodynamic slippage (and a possible combined effect of partial mobility of adsorbed surface charges) [33].

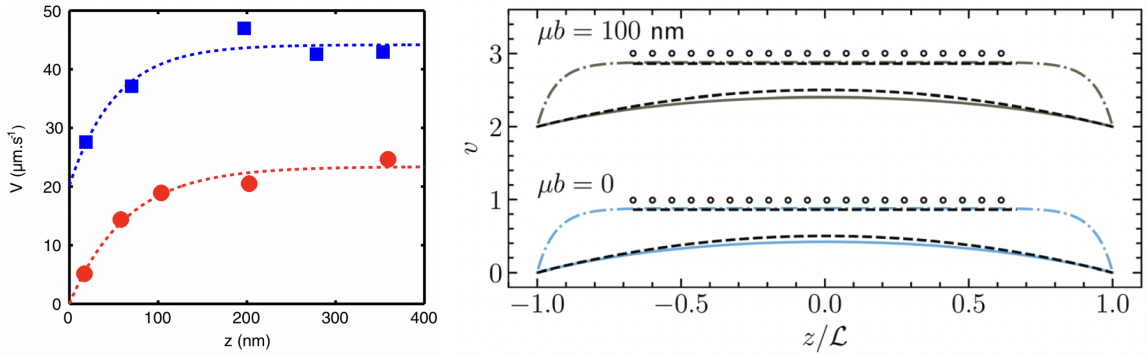

Figure 1.8 On the left, experimentally measured electro-osmotic velocity profiles for hydrophobic OTS (blue squares) and hydrophilic glass (red circles). Dashed lines are fits to the theoretical predictions, with slip lengths of $b = 38 \pm 6$ nm and $b = 0 \pm 10$ nm respectively [32]. On the right, results of simulations of electro-osmotic velocity profiles, for a thick (open circles with under dashed lines) and a thin (dashed lines) channel configuration. The theoretical curves were plotted with a constant surface charge boundary condition, for $\mu b = 100$ nm (green lines) and $\mu b = 0$ nm (blue lines), where μ is the lateral mobility of surface anions in response to the external electric field E [33].

For a better understanding of the situation, it seems essential to measure the electrical and hydrodynamic boundary conditions separately. For this reason, it is unavoidable to measure the equilibrium and hydrodynamic transport properties independently. We could then, without any ambiguity, have the values of the surface charge, the surface potential, and the hydrodynamic slip. These experiments could help to better understand the link between surface charge and ζ potential, beyond the use of Grahame equation.

1.4 Conclusion

In this chapter, I briefly described the existing models for the equilibrium and transport properties in confined electrolytes. These models have been exploited but never experimentally validated, because they require simultaneous measurement of equilibrium and transport properties, in particular the electrostatic (surface charge) and hydrodynamic (slip) boundary conditions.

To our knowledge, no experiment allows to carry out these equilibrium and transport measurements simultaneously. The work I present here is a first step in this direction, based on the instrumental development of the Surface Force Apparatus.

The Surface Force Apparatus (SFA) was originally designed for equilibrium measurements. Over time however, Chan [34], Israelachvili [35], Tonck [36], Restagno [37], and Garcia [10] built dynamic Surface Force Apparatus (dSFA), allowing simultaneous dynamic measurements and quantitative determination of the boundary conditions. Therefore I employed the dynamic Surface Force Apparatus during my thesis, in order to achieve a better understanding of the physics of confined electrolytes.

Chapter 2

Simple Fluids Confined Between a Sphere and a Plane

Contents

Introduction

This chapter proposes a theoretical description of the dynamic mechanical properties of simple fluids which are confined between a sphere and a plane down to the nanometric scale. The notions of viscosity, slip boundary condition and elastic response of the confining surfaces are recalled. We introduce the concept of mechanical impedance, a central physical quantity for the interpretation of the experiments performed during my thesis with the dynamic Surface Apparatus (dSFA).

2.1 Mechanical Impedance and Admittance

When two solid surfaces, a sphere and a plane, are approached one towards the other, a pressure field builds up in the surrounding fluid. This translates into a normal force F_{tot} that is exerted between the surfaces and depends on the distance D_{tot} that separates them (Figure 2.1). If the motion actually involves an harmonic oscillation $h_{\text{dyn}}\cos(\omega t + \varphi_H)$ at frequency $\omega/2\pi$ around a quasi-static position D with $h_{\text{dyn}} \ll D$, the oscillating pressure

field in the fluid creates an oscillatory flow. **In the framework of the linear response** of the system, distance and force can be described by a quasi-static component $\{D, F\}$ and a dynamic component $\{h_{\text{dyn}}\cos(\omega t + \varphi_H), f_{\text{dyn}}\cos(\omega t + \varphi_F)\}$, resulting in Equations 2.1 and 2.2 respectively.

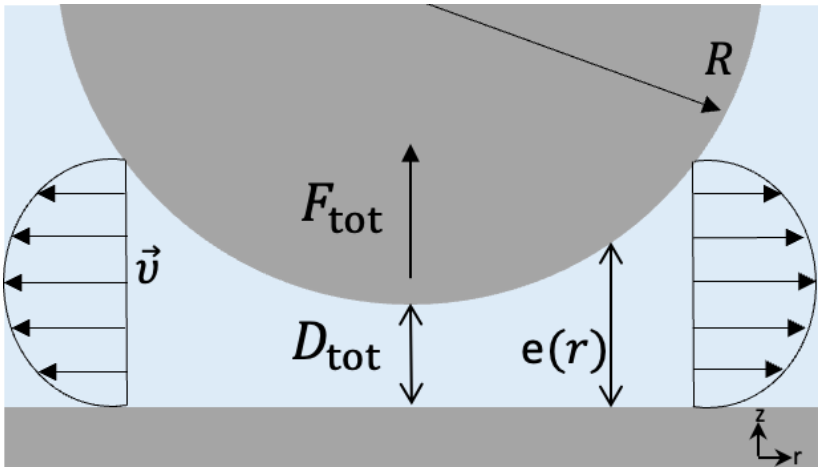

Figure 2.1 Schematic of the principle of the dynamic Surface Force Apparatus. An oscillation of the distance between a sphere and a plane around its quasi-static value induces a proportional force response between the surfaces. The drainage of the fluid is illustrated, with $\vec{v}$ the velocity profile of the flow and $e(r)$ the thickness of the fluid film at a radial distance r.

$$D_{\text{tot}} = D + h_{\text{dyn}}\cos(\omega t + \varphi_H) = D + \mathfrak{Re}[h_{\text{dyn}}e^{j(\omega t+\varphi_H)}] \tag{2.1}$$

$$F_{\text{tot}} = F + f_{\text{dyn}}\cos(\omega t + \varphi_F) = F + \mathfrak{Re}[f_{\text{dyn}}e^{j(\omega t+\varphi_F)}] \tag{2.2}$$

The dynamic component of the force has an amplitude proportional and a phase shifted compared to the dynamic component of the distance. Using complex formalism, we can define the complex **mechanical impedance** Z, first introduced by Israelachvili [35]:

$$Z(\omega, D) = Z' + jZ'' = \frac{f_{\text{dyn}}}{h_{\text{dyn}}}e^{j(\varphi_F-\varphi_H)} \tag{2.3}$$

This physical quantity describes the linear mechanical response of the system, in terms of in-phase, conservative contribution (real part Z') and out-of-phase, dissipative contribution (imaginary part Z''). We can also define the **mechanical admittance** as:

$$Y(\omega, D) = Y' + jY'' = \frac{1}{Z} \tag{2.4}$$

Qualitatively, the mechanical impedance is more convenient to manipulate when the different physical mechanisms at play involve additive forces, whereas the mechanical admit-

tance is preferable when these mechanisms involve additive displacements. Throughout this chapter, I will employ one or the other, and the reasons for each choice will be discussed accordingly.

2.2 Case of non-deformable and non-slippery surfaces

We position ourselves in the classical framework of continuum hydrodynamics, supported by the work of Bocquet and Charlaix [7] who showed how various experiments and simulations on simple fluids proved the validity of Navier-Stokes equations for confining distances down to ~ 1 nm. We assume the following hypotheses for the flow between the sphere and the plane:

- a Newtonian fluid, meaning that the shear stress $\tau(r, z)$ is proportional to the velocity gradient in the direction normal to the flow with a proportionality factor given by the dynamic viscosity η, i.e., $\tau(r, z) = \eta \frac{\partial v_r}{\partial z}$,
- an incompressible flow,
- lubrication conditions, with a distance much smaller than the sphere radius of the sphere $D \ll R$,
- negligible gravity effects,
- negligible non-stationary effects.

We add other hypotheses to start with the simplest case:

- non-deformable confining surfaces,
- a no-slip boundary condition, namely a tangential velocity of the flow is zero at the walls: $v_r(r, z = 0) = v_r(r, z = e(r)) = 0$.

From the previous hypotheses, we know that the flow between the sphere and the plane is described by the Stokes equation and is of Poiseuille type. By integrating the pressure gradient, we show that the pressure $P(r)$ is then written:

$$P(r) = P_0 - \frac{3\eta R \dot{D}_{\text{tot}}}{e(r)^2} \tag{2.5}$$

where P_0 is the pressure far from the confinement zone and $e(r)$ is the thickness of the fluid film at the distance r from the apex of the sphere. The pressure is maximum on the axis of symmetry where $e(r)$ is minimum. Since $D \ll R$, we can approximate the sphere profile by a parabola $e(r) \approx D + r^2/2R$. The pressure field decreases when the thickness $e(r)$

increases and it is reduced by a factor of 10 on a lateral extension $r = \sqrt{(\sqrt{10}-1)2RD}$. The associated velocity profile reads:

$$v_r(r,z) = -\frac{3\dot{D}_{\text{tot}} r}{e(r)^3} z(e(r)-z) \tag{2.6}$$

The radial velocity is zero at the walls, and reaches its maximum value $v_{r,\max} = -\frac{3\dot{D}_{\text{tot}}}{8}\sqrt{\frac{2R}{D}}$ when $z = e(r)/2$ and $r = \sqrt{2RD}$. The shear stress can be deduced as:

$$\tau(r,z) = -\frac{3\eta\dot{D}_{\text{tot}} r}{e(r)^3}(e(r)-2z) \tag{2.7}$$

The modulus of the shear stress is maximum at the walls and $r = \sqrt{2RD/3}$, where it is equal to $|\tau_{\max}(r,z)| = \frac{3^{5/2}}{2^{7/2}}\frac{\dot{D}_{\text{tot}}\sqrt{R}}{D^{3/2}}$.

In Figure 2.2 the characteristics of the drainage flow are illustrated: the velocity, pressure and shear stress profiles. These three quantities decay on the lateral direction on a typical lengthscale $\sim \sqrt{2RD}$, giving rise to the concept of **fluid probe**, introduced by Leroy and Charlaix [38, 39]. Measuring the viscous flow in such geometry of confinement allows to probe the mechanical properties of the system composed of the fluid and the confining solids, without direct contact between them, on a scale $\sim \sqrt{2RD}$.

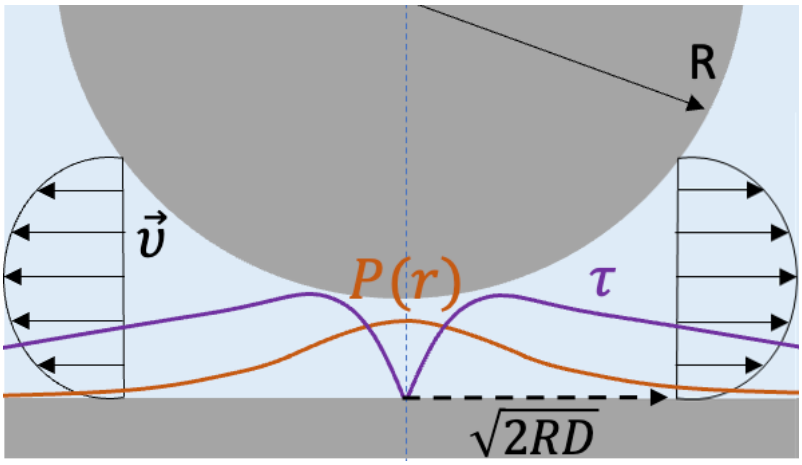

Figure 2.2 Schematic of the principle of the fluid probe, showing the velocity, pressure and shear stress profiles.

Integrating the pressure field over the surface of our probe, we obtain the total Reynolds force acting between the surfaces, of purely viscous origin :

$$F_{\text{tot,Rey}} = -\frac{6\pi\eta R^2\dot{D}_{\text{tot}}}{D} \tag{2.8}$$

Strictly speaking, the quasi-static component of the total force contains a viscous contribution because of the drainage flow at velocity $\dot{D}$, given by the Reynolds force:

$$F_{\text{Rey}} = -\frac{6\pi\eta R^2 \dot{D}}{D} \tag{2.9}$$

which is repulsive (taken positive) upon approach and attractive (taken negative) upon retraction.

The dynamic component of the total force contains a viscous contribution because of the oscillatory flow at velocity $-\omega h_{\text{dyn}} \sin(\omega t + \varphi_H) = \mathfrak{Re}[j\omega h_{\text{dyn}} e^{j(\omega t + \varphi_H)}]$, corresponding to a Reynolds impedance:

$$Z_{\text{Rey}}(\omega, D) = j\frac{6\pi\eta\omega R^2}{D} \tag{2.10}$$

The mechanical impedance is purely imaginary, and is inversely proportional to the distance between the surfaces. As proposed by Georges *et al.* [40] and Tonck *et al.* [36], looking at the inverse quantity is convenient when analyzing experimental data to define the position of the no-slip plane (the **hydrodynamic zero**). The Reynolds admittance reads:

$$Y_{\text{Rey}}(\omega, D) = -j\frac{D}{6\pi\eta\omega R^2} \tag{2.11}$$

which has only an imaginary component that varies linearly with the distance between the surfaces.

2.3 Case of partially slippery surfaces

As supposed since Bernoulli in 1738 [41], the velocity of a fluid is often considered to be zero at solid boundaries for macroscopic flows, namely a no-slip boundary condition is applied. However as the fluid is confined, it becomes evident that the velocity at solid boundaries is not necessarily zero. It was actually Navier in 1823 [42] who formulated this hypothesis: the tangential velocity of the fluid could be non-zero at the wall, based on the continuity of the tangential stress (Eq. 2.12). The viscous shear stress in the fluid is balanced by the friction stress exerted by the solid on the fluid, as:

$$\eta\frac{\partial v_r}{\partial z}\Big|_{z=0} = \lambda v_r(z=0) \tag{2.12}$$

where η is the fluid dynamic viscosity and λ is a solid friction coefficient.

A length-scale emerges from this (Navier) partial slip boundary condition: the **slip length** $b = \eta/\lambda$. This length characterizes the slippage and corresponds to the distance from the wall at which the linear extrapolation of the velocity profile cancels out:

- a zero slip length means a no-slip boundary condition,

- a positive slip length locates the no-slip plane in the solid,
- and a negative slip length locates the no-slip plane in the fluid, suggesting qualitatively a layer of fluid molecules that are blocked near the wall.

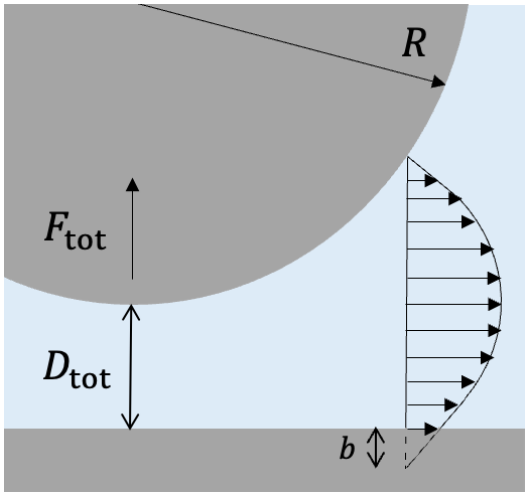

Figure 2.3 Illustration of a no-slip boundary condition (top surface) and of a positive slip boundary condition (bottom surface). The slip length is the distance from the fluid-solid interface where the linear extrapolation of the velocity profile is zero.

The effect of slippage on the viscous forces depends of its sign: a positive slippage decreases dissipation while a negative slippage increases it. Vinogradova [43] calculated the expression for the viscous force between a sphere and a plane in the case of positive slippage, resulting in:

$$F_{\text{slip}} = -\frac{6\pi\eta R^2 \dot{D}}{D} f^*(D/b) \tag{2.13}$$

where $f^*(D/b)$ is a corrective factor depending on the slip length, equal to:

$$f^*(D/b) = \frac{1}{4}\left[1 + \frac{6D}{4b}\left(\left(1 + \frac{D}{4b}\right)\ln\left(1 + \frac{4b}{D}\right) - 1\right)\right] \tag{2.14}$$

in the case of slippage on one surface, or equal to:

$$f^*(D/b) = \frac{D}{3b}\left[\left(1 + \frac{D}{6b}\right)\ln\left(1 + \frac{6b}{D}\right) - 1\right] \tag{2.15}$$

in the case of slippage on both surfaces. The mechanical impedance is given by the expression:

$$Z_{\text{slip}}(\omega, D) = j\frac{6\pi\eta\omega R^2}{D} f^*(D/b) \tag{2.16}$$

which shows that slippage induces a modification of the dissipative contribution Z'', while the conservative contribution Z' is still zero. The mechanical admittance reads:

$$Y_{\text{slip}}(\omega, D) = -j\frac{D}{6\pi\eta\omega R^2}\frac{1}{f^*(D/b)} \tag{2.17}$$

At large distances $D \gg b$ the corrective factor is equivalent to $f^*(D/b) \sim \frac{D}{D+b}$, so the admittance is of the form:

$$Y_{\text{slip}}(\omega, D) \sim -j\frac{D+b}{6\pi\eta\omega R^2} \quad \text{for} \quad D \gg b \tag{2.18}$$

which is equal to the Reynolds admittance shifted along the X axis by $-b < 0$ (so towards negative values of D). Therefore, fitting linearly the imaginary part Y'' of the admittance at large distances and extrapolating this fit to small distances allows to determine the positive slip length b.

In the case of negative slippage, the admittance is equal to the Reynolds admittance shifted along the X axis by $+b > 0$ (so towards positive values of D). Similarly, the negative slip length b can be characterized by fitting linearly the imaginary part Y'' of the admittance at large distances.

This phenomenon of partial slippage has been observed experimentally by various methods, but the dSFA has proved to a tool of choice to quantitatively measure slip lengths in the nanometric range. For instance, a change of the slip behavior with the wettability of the surfaces has been reported for water confined between glass surfaces [44], as represented in Figure 2.4.

2.4 Case of deformable surfaces: elasto-hydrodynamics

As seen previously, a pressure field builds up when two solid surfaces are approached one towards the other in a viscous fluid. Because this hydrodynamic pressure varies as D^{-2} on an area scaling like $\sqrt{2RD}$, it can be very large in a confinement situation, and can eventually deform the surfaces even if they are not in direct contact.

If these deformations are small, one can estimate the total indentation $U_{\text{tot}} = U + u_{\text{dyn}}\cos(\omega t + \varphi_U) = U + \mathfrak{Re}[u_{\text{dyn}}e^{j(\omega t+\varphi_U)}]$ of the surfaces by approximating the viscous force by the one calculated in the case of rigid surfaces. Considering a pressure exerted on a characteristic lateral distance of $\sqrt{2RD}$ and associated to a total Reynolds force $F_{\text{tot,Rey}}$, one can write down the Hooke's law:

$$\frac{U_{\text{tot}}}{\sqrt{2RD}} \sim \frac{F_{\text{tot,Rey}}/\pi 2RD}{E^*} \tag{2.19}$$

where $E^* = \frac{E}{2(1-\nu^2)}$ is the reduced Young modulus with E the Young modulus and ν the Poisson coefficient.

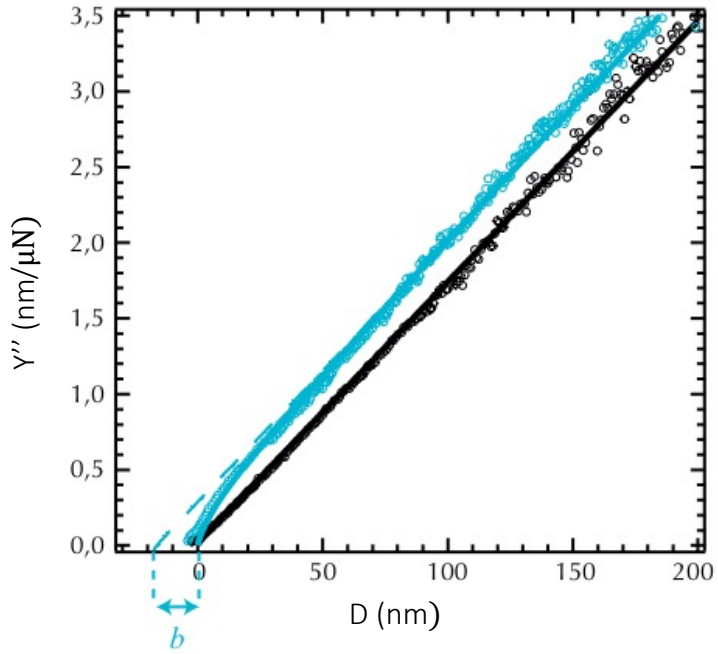

Figure 2.4 Imaginary part of the mechanical admittance as a function of distance, measured with a dSFA confining water confined between a sphere and a plane [44]. When the surfaces are hydrophilic (Pyrex, i.e., borosilicate glass), a zero slip is found (in black). However, for a hydrophobic plane (silanized Pyrex), a positive slip length of 17 ± 2 nm is obtained (in blue). The full lines correspond to the best adjustments using the expression 2.13, while the dashed line is the linear fit to large distances given by equation 2.18. Figure adapted from [44].

As illustrated in Fig. 2.5 in the case of an infinitely rigid sphere and a deformable plane, the system is equivalent to a damper and a spring that are associated in series [45]. The damping coefficient, related to the viscous flow in the fluid, is equal to:

$$\lambda(D) = \left| \frac{F_{\text{tot,Rey}}}{\dot{D}_{\text{tot}}} \right| \sim \frac{6\pi\eta \mathrm{R}^2}{D} \tag{2.20}$$

The spring stiffness, due to the elastic deformations of the solid surfaces, is given by:

$$k(D) = \frac{F_{\text{tot,Rey}}}{U_{\text{tot}}} \sim E^* \pi \sqrt{2RD} \tag{2.21}$$

The same force $F_{\text{tot,Rey}}$ applies to the two elements, while the displacements D_{tot} and U_{tot} should be added. Therefore it is convenient to use the mechanical admittance to describe the dynamic response, as:

$$Y_{\text{eh}}(\omega, D) \sim \frac{1}{k} + \frac{1}{j\omega\lambda} \sim \frac{1}{E^* \pi \sqrt{2RD}} - j \frac{D}{6\pi\eta\omega R^2} \tag{2.22}$$

The dynamic response presents a dissipative contribution due to the fluid viscosity, and a conservative contribution due to the solid elasticity. This expression is correct if the dynamic deformation is small, i.e., $h_{\text{dyn}} \gg u_{\text{dyn}}$, equivalent to:

$$\frac{1}{\omega\lambda} \gg \frac{1}{k} \quad \text{or} \quad D \gg D_{\text{c}} \propto R \left(\frac{\eta\omega}{E^*} \right)^{2/3} \tag{2.23}$$

and the admittance can be re-written as:

$$Y_{\text{eh}}(\omega, D) \sim \frac{D}{6\pi\eta\omega R^2} \left[\left(\frac{D_{\text{c}}}{D} \right)^{3/2} - j \right] \quad \text{for} \quad D \gg D_{\text{c}} \tag{2.24}$$

The mechanical impedance is deduced as:

$$Z_{\text{eh}}(\omega, D) \sim \frac{1}{\frac{1}{k} + \frac{1}{j\omega\lambda}} \sim \omega\lambda \left(\frac{\omega\lambda}{k} + j \right) \sim \frac{6\pi\eta\omega R^2}{D} \left[\left(\frac{D_{\text{c}}}{D} \right)^{3/2} + j \right] \quad \text{for} \quad D \gg D_{\text{c}} \tag{2.25}$$

Leroy *et al.* [39] developed a complete theory, which is valid for any deformations in the framework of linear elasticity. They showed that the dynamic response is of the form:

$$Y_{\text{eh}}(\omega, D) = \frac{D}{6\pi\eta\omega R^2} g_k^{-1} \left(\frac{D}{D_{\text{c}}} \right) \tag{2.26}$$

$$Z_{\text{eh}}(\omega, D) = \frac{6\pi\eta\omega R^2}{D} g_k \left(\frac{D}{D_{\text{c}}} \right) \tag{2.27}$$

where $D_{\text{c}} = 8R \left(\frac{\eta\omega}{E^*} \right)^{2/3}$ and g_k is a master function that can be calculated numerically.

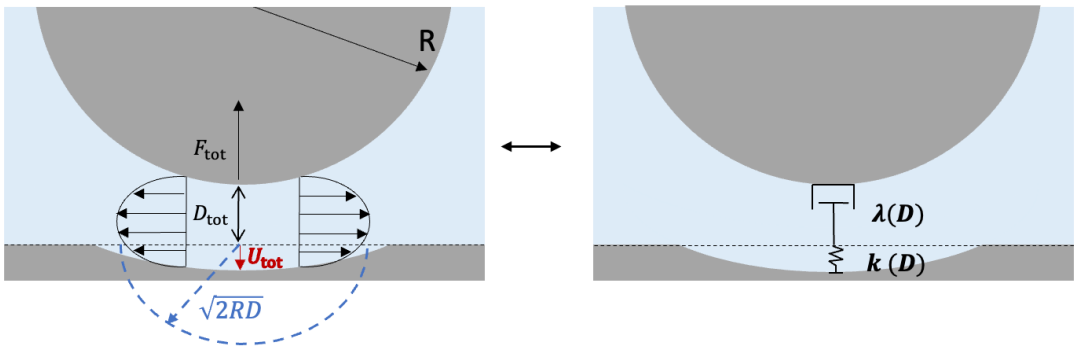

Figure 2.5 Schematic of the drainage flow (with a no-slip condition) for a Newtonian fluid confined between an infinitely rigid sphere and a deformable plane. The plane is deformed on a scale of $\sqrt{2RD}$, which is the characteristic size of the fluid probe. If the deformations are small (at large distances) the system is equivalent to a damper and a spring that are associated in series.

In Fig. 2.6 is shown a simulation of a model system, composed of a liquid of viscosity 2.4 mPa s confined between surfaces of Young modulus $E =$ 64 GPa and a Poisson ratio $\nu = 0.2$, corresponding to a reduced Young modulus 32 GPa (modeling propylene carbonate between Borosilicate glass surfaces), and an oscillation frequency of 130 Hz. At large distances $D \gg D_c \sim 1$ nm, the dynamic response is mainly viscous, with imaginary parts larger than real parts: it is the so-called viscous regime. The deformations are small so we recover the scaling laws obtained with the damper-spring model, with $Y' \propto D^{-1/2}$ and $Y'' \propto D^{1}$ (as in equation 2.24), $Z' \propto D^{-5/2}$ and $Z'' \propto D^{-1}$ (as in equation 2.25). At critical distance $D \sim D_c$, the elastic and viscous contributions are exactly equal. At small distances $D \ll D_c$, the dynamic response is mainly elastic, with real parts larger than imaginary parts, all signals exhibiting saturation: it is the so-called elastic regime.

2.5 Conclusion

From the measurement of the mechanical admittance or impedance, it is possible to explore the rheological behavior of a fluid confined between solid surfaces. The rheological properties involve the fluid flow, the fluid-solid slip boundary condition and the solid deformations. The dSFA is therefore a tool of choice to understand the transport phenomena in electrolytes near charged surfaces.
A few points are important to keep in mind from this chapter:

- The fluid viscosity can be measured thanks to the slope of the imaginary part of the mechanical admittance as a function of the distance between the surfaces.
- The slip boundary condition is obtained by fitting linearly the variation of the mechanical admittance with the distance at large distances, and by extrapolating this fit to small

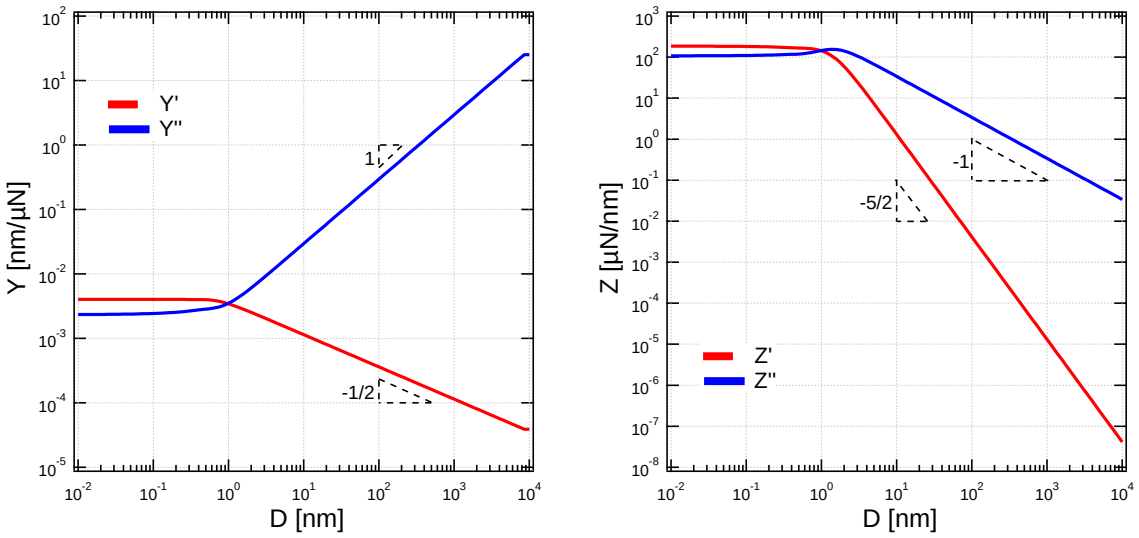

Figure 2.6 Mechanical admittance Y on the left and impedance Z on the right, numerically-solved for a system composed of a liquid of viscosity 2.4 mPa s confined between surfaces of reduced Young modulus 32 GPa (modeling propylene carbonate between Borosilicate glass surfaces), and an oscillation frequency of 130 Hz. The real parts are in red while the imaginary parts are in blue.

distances. The intersection with the X axis provides the hydrodynamic zero, which has to be compared to the mechanical zero (direct contact between the surfaces) to deduce the slip length.

- The elastic deformation of the surfaces induces a non-zero conservative contribution, and a saturation of the dynamic response below a critical distance. The elasto-hydrodynamic theory allows to describe these phenomena in a quantitative way.

Part II

Materials and Methods

Chapter 3

Instrumental Development

Contents

Introduction

During my thesis, the experimental characterization of the rheology of confined fluids has been possible thanks to the dynamic Surface Force Apparatus at LIPhy. While it has proven to be a unique tool to investigate interactions between two surfaces, with great resolution from the

bulk to the molecular scale, it is very sensitive to changes in the set-up or in its environment. In this chapter, the principle of the instrument will be described, the improvements made to the mechanical, optical, electronic and environmental aspects of the machine will be presented, and the consequences of these modifications as well as the challenges overcome during the instrumentation phase will be discussed.

3.1 Description of the dynamic Surface Force Apparatus at LIPhy

The dynamic Surface Force Apparatus (dSFA) at LIPhy has been conceived by E. Charlaix and B. Cross, and manufactured by J. Giraud [46], [10], [47]. The SFA was built during the theses of C. Barraud [12] and L. Garcia [11], who studied the rheological properties of polymer and electrolyte solutions, respectively. In this section, the machine and its environment is described, as well as the improvements implemented during my thesis work.

3.1.1 Brief Overview

The main elements of the dSFA are two surfaces. First, a sphere that is supported on the free extremity of a flexure hinge, acting as an elastic spring. Second, a plane that is supported by a plane-holder and fixed on a piezo-electric actuator, as observed in Figure 3.1. The sphere and the plane are positioned one on top of the other, normally separated by a few micrometers. In between the surfaces, a liquid is injected. The vertical arrangement of the surfaces allows to perform immersed measurements with volatile liquids.

First, a quasi-static displacement of the plane towards the sphere is applied, as in a classical SFA. However, the machine at LIPhy has a unique feature: it also allows to study the dynamic properties of the system by additionally applying a small harmonic oscillation to the plane. While the surfaces are brought into contact (and out of contact), the relative distance between the surfaces is measured, for both static and dynamic components $H_{\text{tot}} = h_{\text{stat}} + h_{\text{dyn}} \cos(\omega t + \varphi_H)$. At the same time, the flexure hinge senses the force exerted by the plane throughout the liquid and onto the sphere, translating it as a mechanical deflection. This deflection is measured and the force is deduced thanks to the flexure hinge transfer function obtained by calibration. In the framework of linear response, the force is also composed of static and dynamic components, resulting in $F_{\text{tot}} = f_{\text{stat}} + f_{\text{dyn}} \cos(\omega t + \varphi_F)$.

Two independent optical interferometers are used to measure the relative separation of the surfaces and the deflection of the elastic spring, based on polarization interferometry. In short, two pairs of mirrors are attached to the moving elements and are contained in what we call the heart of the machine (represented in Figure 3.2), together with the motors to control their position and the translation of the surfaces. The rest of the optical elements that compose the interferometers are accommodated on a optical board held above the dSFA's

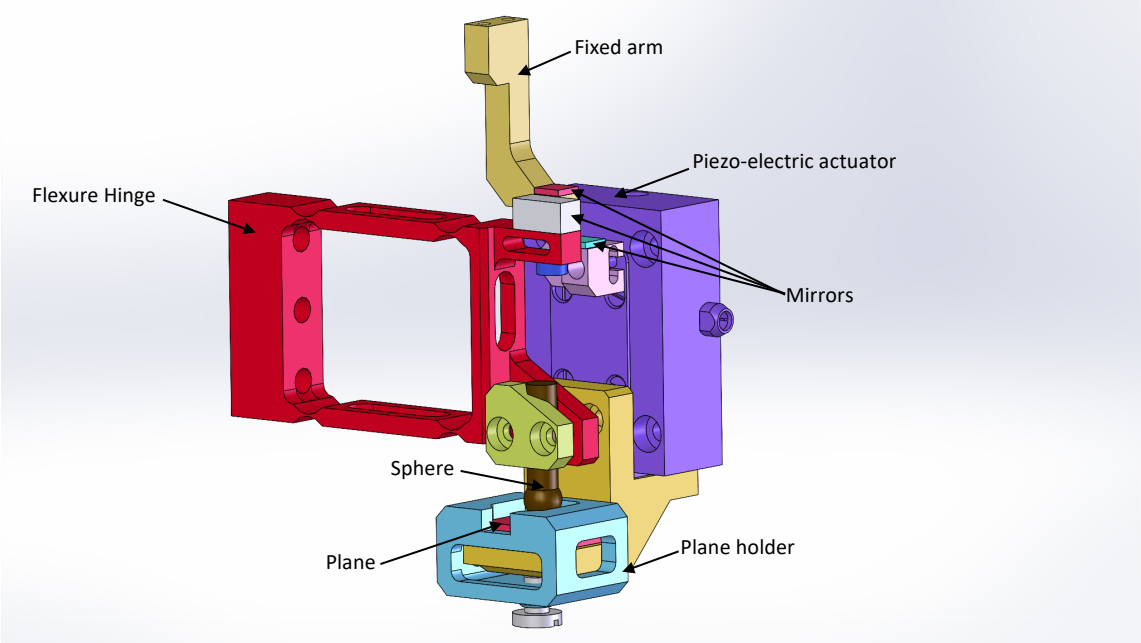

Figure 3.1 Schematic of the main elements of the dynamic Surface Force Apparatus, designed on Solidworks by J. Giraud. We can observe two facing surfaces (sphere and plane), the piezo-electric actuator, the mirrors: one on the fixed arm, one fixed to the piezo and a double one on top of the flexure hinge. Credit: J. Giraud.

heart, with a 45° mirror making the transition from the optical board to the heart. For each inteferometer, a linearly-polarized laser beam first reaches a birefringent calcite, leading to a separation of the beam into two orthogonally polarized beams. These beams are reflected by two different mirrors, and are reunited by the calcite on the way back. Interferometry is then used to determine the phase difference between these two beams, and so the distance between the mirrors. Further explanation of each component of the machine will be given later in the chapter.

3.1.2 Mechanical Elements

The dSFA's heart and all the mechanical components that it contains have not been modified from the previous version of this machine [12], [11]. We can identify as mechanical elements mainly the flexure hinge, as well as the translation/rotation elements for the mirrors and the surfaces, as shown in Figure 3.2.

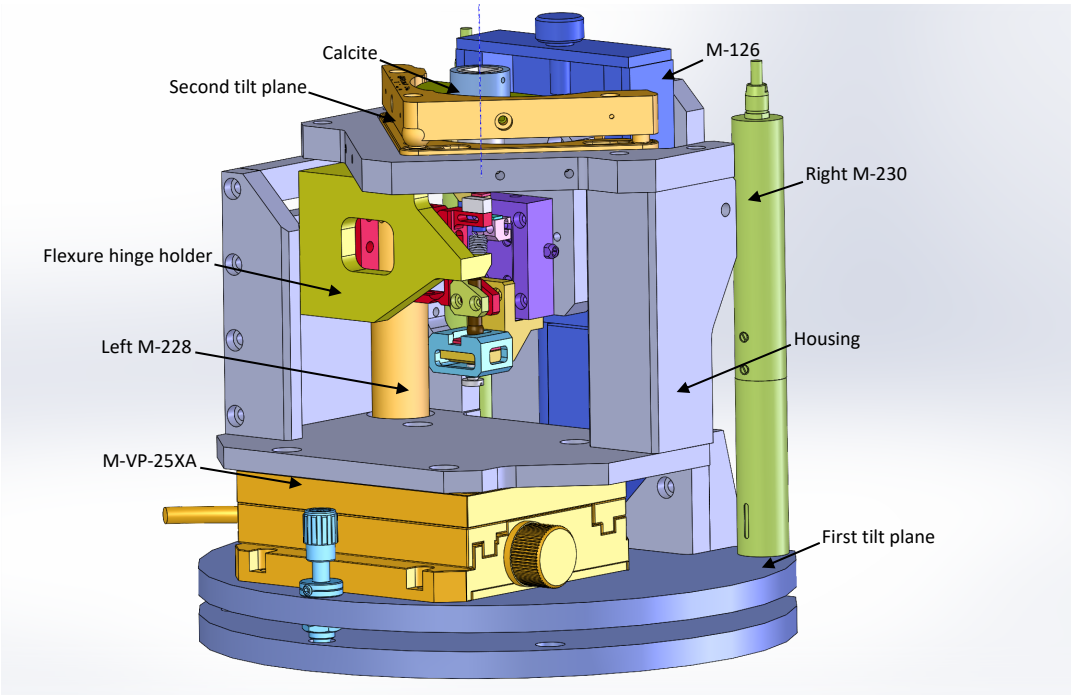

Figure 3.2 Schematic of the dSFA's heart and all the elements that it contains, designed on Solidworks by J. Giraud. The flexure hinge holder as well as the elements in charge of the translation of surfaces and the positioning of mirrors are identified. The birefringent calcite on the top and the mirrors in the dSFA can also be observed. Credits: J. Giraud.

Flexure hinge

The free end of the flexure hinge behaves like a double-beam whose static deflection is simply proportional to the force exerted on it. The chosen geometry, shown in Figure 3.3, ensures

a movement as close as possible to pure translation, with very little rotation. Since the deflection depends on the flexure hinge stiffness K, this parameter is essential for the design and fabrication of the flexure hinge. On one hand, the stiffness should be low in order to obtain a significant deflection from a small force. On the other hand, the flexure hinge should be light and stiff for it to be sensitive at high frequencies. As a compromise, a stiffness of 6000 N/m was desired.

The stiffness of an element can be predicted based on its material properties (here Al 7075-T6 Aluminum alloy) and its geometric characteristics. Supposing that the four hinges at the corners were identical, Smith's calculation [48] predicted that the stiffness K follows the relation $K = EI/\alpha RL^2$, with E the material's Young modulus (72 GPa), R the hinges radius of curvature (4 mm), L the length between the hinges (30 mm), I and α parameters depending on the geometry of the flexure hinge. I is the inertia moment given by $I = wt^3/12$ and α is a correction factor equal to $\alpha = 0.565t/R + 0.166$, with w the width of the flexure hinge (10 mm) and t its thickness (0.3 mm). Based on Smith's prediction and according to a simulation performed on SolidWorks by J. Giraud with these parameters, a deflection of 163 nm is observed when a force of 1 mN is applied, corresponding to a stiffness of 6135 N/m, which agrees well with the desired value for our experiments.

The actual stiffness and dynamic transfer function of the flexure hinge was obtained experimentally, thanks to a calibration procedure explained in section 3.2.4.

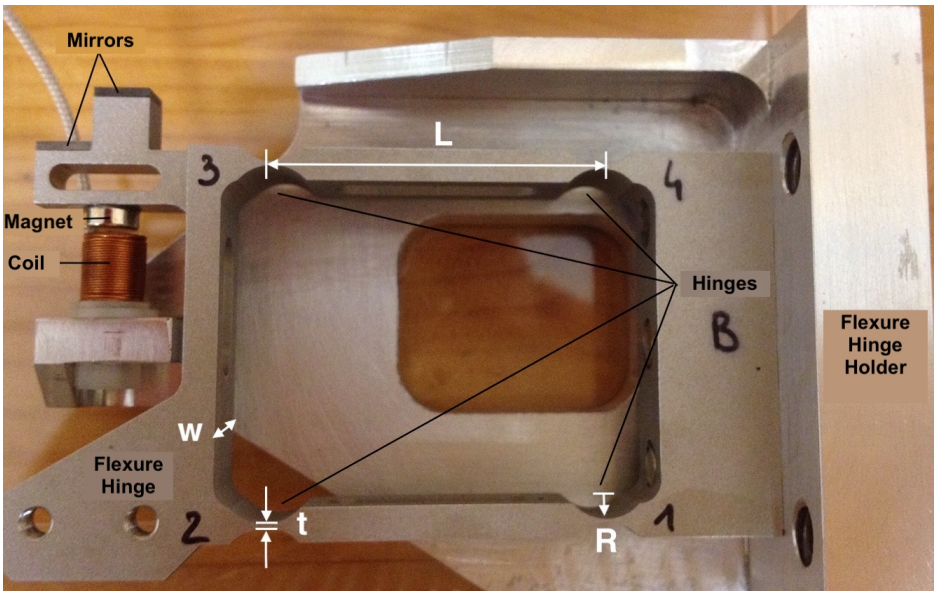

Figure 3.3 Photograph of the flexure hinge and identification of the elements that compose it and their sizes.

Coil-Magnet System

The coil-magnet system allows the calibrations of the flexure hinge and of the two interferometers. It is composed of a NdFeB magnet (diameter 4 mm, length 2 mm) glued onto the free extremity of the flexure hinge, and of a copper coil (diameter 5 mm, length 6 mm, 3000 turns per meter) attached to the fixed flexure hinge holder, with a distance between the coil and the magnet of typically 1 mm (see Figure 3.3). A current passing by the coil proportionality generates first a magnetic field, then a magnetic force acting on the magnet, there a deflection of the flexure hinge.

The current is controlled by applying voltages at the two ends of the solenoid. On one end, a quasi-DC voltage ramp (from -10 V to +10 V) is imposed to obtain a quasi-static displacement (of the order of 1 µm). On the other end, an AC voltage generated by a lock-in amplifier is applied to produce a dynamic excitation of desired amplitude (between 0.5 nm and 10 nm) and frequency (between 10 Hz and 1 kHz).

Piezo-electric actuator

The P-753.1CD ceramic piezo actuator[1] allows to carry out the fine displacement of the plane towards the sphere during measurements. The voltage applied to the actuator is first composed of a quasi-DC component (a slow ramp between 0 V and 120 V), resulting in a quasi-static approach-retraction of the surfaces on a range of 14 µm (the approximate linear sensitivity of the piezoelectric crystal being $\alpha = 110$ nm/V) at a constant speed chosen between 50 pm/s and 5 nm/s approximately. The speed limitations are due to thermal drifts at low velocities, and to the finite integration time for the acquisition of each measurement point at high velocities. Secondly, a harmonic voltage (AC component) generated by a lock-in amplifier is also applied to the actuator, resulting in a small oscillation of the plane at a desired amplitude (between 0.2 nm and 20 nm) and frequency (between 10 Hz and 1 kHz).

Vertical and Horizontal Translations

The surfaces have independent translation stages. A M-126 translation stage[2], with an overall stroke of 25 mm with a sub-micron resolution, is in charge of the coarse (micrometric) vertical displacement to bring the plane to approximately 10 µm from the sphere before injection of the liquid. A M-VP-25XA translation stage[3], located below the dSFA housing, admits displacements from 0.1 µm up to 25 mm in the horizontal direction for the ensemble of pieces attached to the frame. A translation with this stage shifts the position of the flexure hinge, and consequently of the sphere, while the plane stays immobile. This degree of freedom is

[1] P-753.1CD LISA Linear Actuator and Stage. Manufacturer: Physik Instrumente
[2] M-126: Precision Translation Stage. Manufacturer: Physik Instrumente
[3] M-VP-25XA Metric Precision Compact Linear Stage. Manufacturer: Newport Corporation

used to find a clean spot to perform the experiment, in case of presence of a dust particle on the plane. Note that this is not applicable if the dust particle is on the sphere.

Tilt Motors

Since the mirror related to the piezo-electric actuator is fixed and not controlled by any motorized stage, the alignment of the incident laser beam with respect to this mirror is performed by orienting the optical board, which is supported by three points of contact: one pinned support, one sliding support and one roller support.

In order to achieve the parallelism of the rest of mirrors, their orientation is defined by two planes, each plane controlled by two motors. The first tilt plane is the circular base of the dSFA's heart that controls the degree of inclination of elements attached to the housing (all elements except those related to the plane). The mirrors on top of the flexure hinge are then inclined to reach parallelism with the mirror related to the piezo, thanks to two M-230 motors[4] providing a linear motion for a travel range up to to 10 mm with steps as low as 1 µm. Given the design of the dSFA's heart, this corresponds to an orientation that can be tuned on a typical range of $\pm 4°$ with a precision of $4 \cdot 10^{-4°}$.

The second tilt plane is found in the structure that holds the calcite and the arm that supports the fixed mirror. The inclination of these two important elements is controlled by two M-228 motors[5], to reach parallelism with the mirrors of the flexure hinge. These motors can travel linearly up to 10 mm with a minimal incremental motion of 1 µm, corresponding to an orientation that can be tuned on a typical range of $\pm 7°$ with a precision of $7 \cdot 10^{-4°}$.

3.1.3 Optical Elements

New interferometers were built to adapt to the new environment of the dSFA (see section 3.1.5), in order to measure independently the distance between the surfaces and the deflection of the flexure hinge. The two interferometers are identical and based on a quadrature-phase Nomarsky interferometer.

In short, for each interferometer a linearly-polarized laser beam is sent on a birefringent element separating the incident beam into two orthogonally polarized beams. These beams are reflected by a pair of mirrors on the dSFA, they are reunited by the calcite thereafter and then they reach a beam-splitter cube. On one side, the beam hits another birefringent element, producing interference and giving an intensity that varies with the cosine of the phase difference between the two polarization states. On the other side, the beam hits a quarter-wave plate and another birefringent element, similarly producing interference and giving an intensity that varies with the sine of the phase difference between the two polarization states.

[4] M-230 High-Resolution Linear Actuator with DC and Stepper Motor. Manufacturer: Physik Instrumente
[5] M-228 High-Resolution Linear Actuator with Stepper Motor. Manufacturer: Physik Instrumente

Such a choice of interferometer allows to measure the phase difference with a sensitivity which is both high and constant with the phase difference, as well as for the distance between the surfaces or the deflection of the flexure hinge which can be deduced from the phase difference.

Laser Coupling System

A linearly-polarized, frequency and amplitude stabilized He-Ne laser[6] ($\lambda = 632.8$ nm in air) generates the beam that is coupled into a polarization-maintaining optical fiber. As illustrated in Figure 3.4, the laser head is aligned so that the beam has the same horizontal polarization as the optical table plane. A Faraday isolator turns the polarization of the beam on 45°, stopping any parasite reflection from returning and destabilizing the laser source. The beam is then reflected by a mirror, goes through a lens mounted on the optical fiber and finally enters the fiber. The beam and the lens-fiber ensemble are aligned in position and angle with four adjustment screws (two for the orientation of the mirror and two for the orientation of the lens-fiber ensemble), so that the maximal light intensity is obtained. The light source as well as the coupling system are placed in the airlock compartment (see section 3.1.5).

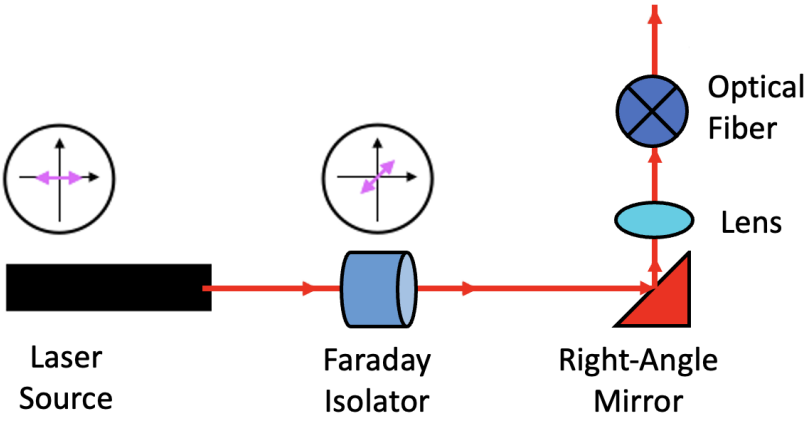

Figure 3.4 Schematic of the laser coupling system installed in the airlock compartment, allowing to inject the laser beam into a polarization-maintaining optical fiber that travels to the dSFA in the experimental room.

Interferometers

When the optical fiber travels to the experimental room, it is introduced inside the isolating box (see section 3.1.5), up the optical board, where its output is held by a beam collimator.

[6] Manufacturer: Sios Precision. Model: SL-04A. Output power ~ 1.5 mW. Stabilization in frequency of ± 1 MHz or in amplitude $< 2\%$ over 1 hour.

That is the point where the actual interferometric set-up starts. Figure 3.5 shows a schematic diagram of the new interferometers.

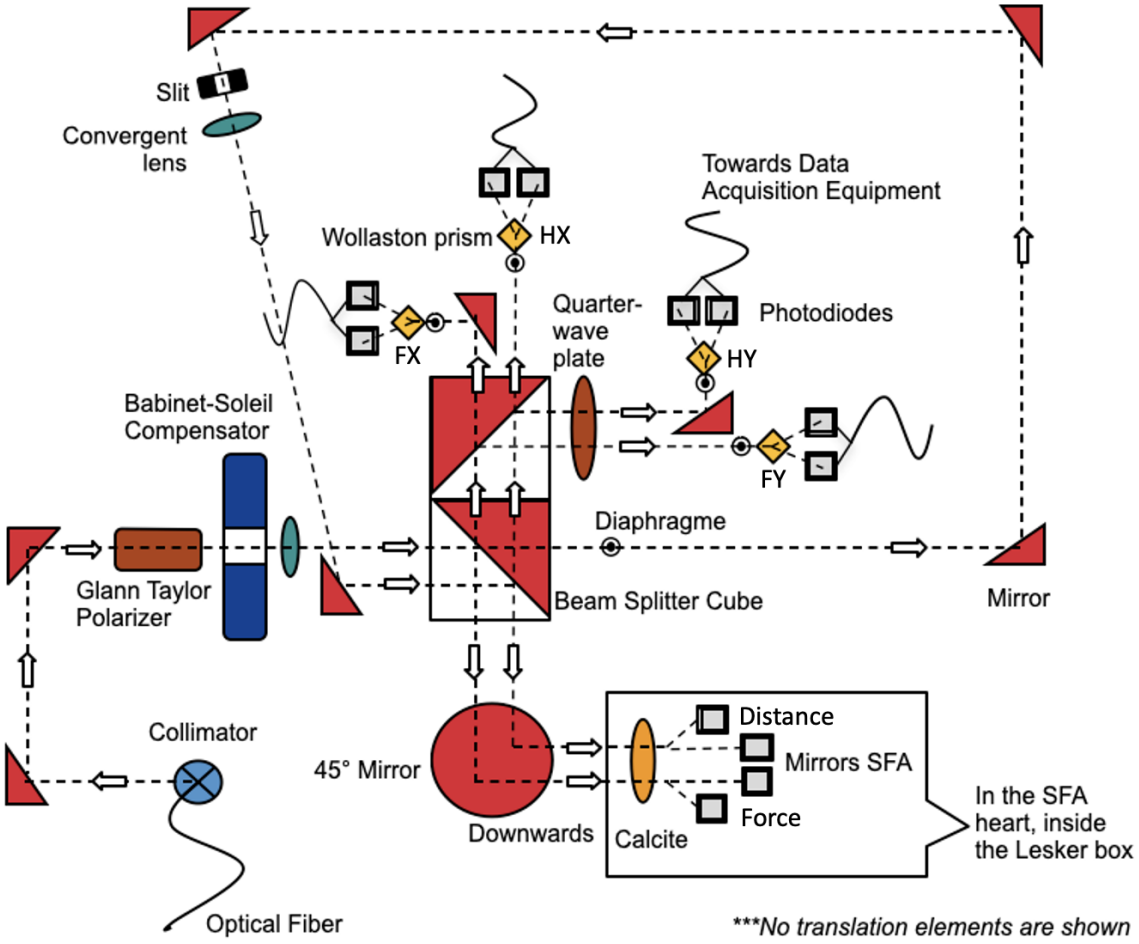

Figure 3.5 Schematic of the new interferometers showing the trajectory (following the arrows) of the laser beam from the collimator at the output of the optical fiber. Various optical elements create a second optical path (one for the force and one for the distance), and both beams go downwards through the calcite and to the mirrors of the dSFA, and then back upwards to the analysis units and the photodiodes.

Following the arrows leading the optical path, it can be observed that after leaving the guiding optical fiber, the beam is reflected by two mirrors, whose orientations allow to finely tune the position and direction of the beam. The beam then passes though a Glann-Taylor polarizer oriented at 45°, ensuring two states of polarization e_s and e_p of same intensity. We use it in case the polarization-maintaining fiber does not play its role perfectly, because of thermal or mechanical drifts, etc. It is important to mention that possible variations of polarization are translated into variations of intensity, which will be taken into account in the analysis.

When desired, the translation of the prism inside the Babinet-Soleil compensator is used to add a phase shift between the two states of polarization. This can be useful to change the operating point or for troubleshooting. Afterwards, the beam hits a 50% : 50% non-polarizing beam-splitter cube, where one part of the beam is redirected towards the dSFA (the force interferometer), and the other part passes through a series of mirrors, in order to be reintroduced into the beam-splitter cube, creating a second optical path next to the first one. Again, a part of this second beam is redirected towards the dSFA (the distance interferometer), and the other part is blocked by a diaphragm to stop the cycle.

Both beams going to the dSFA are reflected by a 45° mirror and sent downwards, passing through the optical board and entering the vacuum chamber, where the dSFA's heart is placed. A calcite crystal separates spatially each beam into two beams of polarizations e_s and e_p, which hit the two pairs of mirrors below. One pair of mirrors allows to collect information for the distance (one mirror attached to the piezo actuator, the other to the flexure hinge), and the other pair for the force (one mirror attached to the flexure hinge, one mirror attached to a fixed frame). After reflection by the mirrors, the beams are spatially recombined by the calcite, and a phase shift is accumulated between the states of polarization e_s and e_p, because of the different positions of the mirrors.

The beams then travel towards their own interferometer. On each case, the beam hits a second 50% : 50% non-polarizing beam-splitter cube. One part is sent directly to an analysis unit called X, producing interference and giving an intensity that varies with the cosine of the phase difference between e_s and e_p. The other part is sent through a quarter-wave plate adding a shift of $\pi/2$ between the two polarization states, and then to an analysis unit called Y, producing interference and giving an intensity that varies with the sine of the phase difference between e_s and e_p. This quadrature measurement ensures maximal sensitivity at all times: when the sensitivity of the optical path X is zero, the sensitivity of the optical path Y is maximum, and vice versa.

Each unit contains a Wollaston prism oriented at 45°, which projects the polarization states and splits the beam into two beams separated by an angle of 2°, giving rise to interferences in opposition to the two beams that are collected by photodiodes. A good alignment of the mirrors in the dSFA's heart, and a good orientation of all birefringent elements is needed to obtain interferences with maximum contrast.

3.1.4 Electronic Elements

Very few electronic elements are involved in the new version of the dSFA developed during this thesis: a circuit controlling the quasi-static displacement of the piezo-electric actuator, the photodiodes converting the optical signals into electrical signals, and the multimeters and lock-in amplifiers collecting the quasi-static and dynamic signals.

Controller of the piezo-electric actuator

For quasi-static displacements, the piezo-actuator is powered by a quasi-DC voltage, which is supplied by an electronic unit composed of an integrator amplifier and a subtractor amplifier[7], as seen in Figure 3.6. These operational amplifiers are supplied by a stabilized DC source[8] providing $V_{\max} = 120$ V. The first amplifier integrates a constant input voltage V_{in} ranging from -5 V to +5 V given by a signal generator[9], creating for V_{int} a voltage ramp from 0 V to 120 V with a slope of $-V_{\text{in}}/RC$, where $R = 1$ MΩ is the resistance and $C = 10$ μF is the capacity[10]. The second amplifier subtracts $V_{\max}$ and V_{int}, so that the "discharged state" of the capacitor corresponds to the maximum distance between the plane and the sphere, i.e., to a piezo crystal that is fully expanded under 120 V. Finally, the output voltage V_{out} presents a voltage ramp from 120 V to 0 V with a slope of $+V_{\text{in}}/RC$.

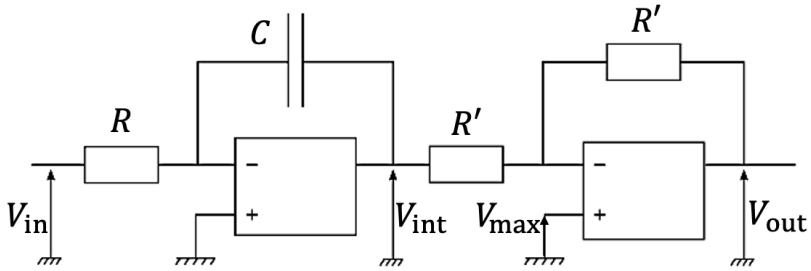

Figure 3.6 Schematic of the electronic assembly of integrator and subtractor amplifiers used to supply the piezoelectric actuator with a voltage ramp and so to control the approach-retraction of the plane towards the sphere at constant speed.

As described in section 3.1.2, the linear sensitivity of the piezoelectric crystal is $\alpha = 110$ nm/V, so we expect the velocity of the plane to be equal to $\alpha V_{\text{in}}/RC$. However, in practice we have observed that the response of the piezoelectric actuator with this controller is not perfectly linear, and that the speed does not cancel at zero voltage (Figure 3.7). Empirically, the relation between the applied voltage V_{in} and the velocity U follows the quadratic expression:

$$U = a(V_{\text{in}} - V_0) + b(V_{\text{in}} - V_0)^2$$

where V_0 is an offset of order typically around 45 ± 10 mV, which slightly depends on the thermal drift. Accurately knowing this relationship is important to choose the right pace for the approach and retraction of the plane, that is why it has been calibrated.

[7]Manufacturer: Linear Technology. Model: LTC6090.
[8]Manufacturer: Aim-TTi. Model: PLH120
[9]Manufacturer: Agilent. Model: 33220A
[10]Manufacturer: Cornell Dubilier. Model: 935C2W10K

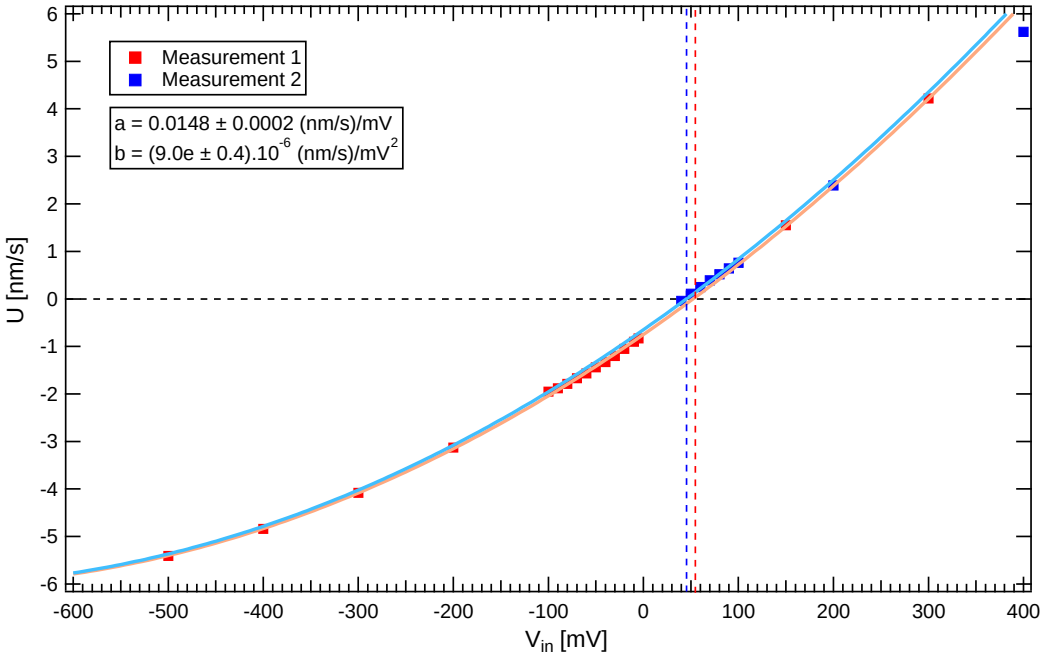

Figure 3.7 Non-linear relation between the voltage applied to the piezo-electric actuator and its velocity. The two groups of measurements were taken at different times and therefore with different drifts. The approach-retraction threshold is found at 45 ± 3 mV and 52 ± 2 mV for these two measurements.

Photodiodes

The role of the photodiodes is to convert the optical intensities into electrical currents. In our set-up, these currents are typically of the order of 1 µA. The photodiodes were chosen for their high shunt resistance, minimizing the measurement noise for low light intensity[11]. Used in photovoltaic mode, dark current is avoided and low noise and best linearity are ensured, at a modest price in terms of dynamics given the frequencies used (<1 kHz).

Multimeters and Lock-in Amplifiers

The DC current coming from each of the eight photodiodes is measured with a multimeter[12]. These high precision multimeters present a 1-day precision of ~ 1 nA when working on DC current mode with an adapted range of 10 µA.

The AC current coming from each of four photodiodes (one per analysis unit, labeled as 1) is measured with a lock-in amplifier[13], plugged in series with a multimeter (Figure 3.8). A master lock-in amplifier generates a harmonic signal of desired amplitude (typically between 0.004 V_{RMS} and 0.3 V_{RMS}) and frequency (typically between 10 Hz and 1 kHz)

[11] Manufacturer: Osram Opto Semiconductors. Model: SFH206K.
[12] Manufacturer: Keysight. Model: 34465A
[13] Manufacturer: Stanford Research Systems. Model: SR830

which is applied to the piezo-electric actuator, while the other lock-in amplifiers are locked in frequency and phase with the master one. The lock-in amplifiers are configured in current mode, and are able to measure an oscillation typically between 1 nA and 100 nA with an amplitude resolution of 100 pA and a phase resolution of 0.01°.

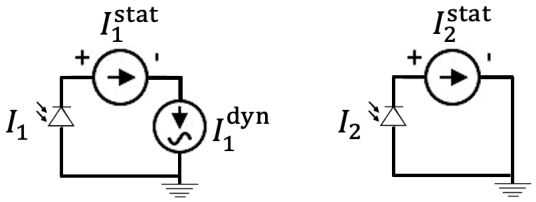

Figure 3.8 Schematic of the electric circuit between the photodiodes and the precision multimeters and lock-in amplifiers for both static and dynamic measurements, for one analysis unit (for example, HX).

These devices are connected by ethernet or GPIB to the computer. The signals are acquired simultaneously by TTL triggering every 500 ms, with an integration time of 300 ms. Several LabVIEW programs are used to pilot all the stages and function generators, and to record the data in text format. These data are visualized and processed in real time using dedicated procedures with the Igor (WaveMetrics) software.

3.1.5 Environmental Control

White Room Conditions

The protection of the dSFA machine from contamination is crucial for reliable results. Any particle of dust deposited on the surfaces close enough to the apex of the sphere would falsify the results, as the measured forces would reflect the mechanical properties of the dust particle and not the surface forces between the surfaces across the surrounding liquid. The ideal work space must be critically unpolluted, so the cleanliness of the environment and the surfaces is a priority. A protocol similar to that of a clean room is employed to work in the dSFA's surrounding rooms. Certain protective equipment such as gloves, lab coat, mask and cap are needed in order to enter the room. The experimental room is isolated from any public transit area in the laboratory, and it is over-pressurized for air removal and renewal between experiments only.

All the surfaces, syringes, beakers and tools are carefully cleaned following a strict protocol, detailed in section 4.1.1. As a last resort, the sphere can be moved in the horizontal direction in a way to get further from the dust particle and find a clean spot to work with.

Mechanical Stability

Another source of *pollution* for the experiments are vibrations, because they could displace the mirrors and eventually be sensed by the flexure hinge. Since air damping would be detrimental for the measurement, the set-up is mounted on a passive anti-vibration table[14], which attenuates any vibration above 0.5 Hz (Figure 3.9). Its working mechanism is composed of a weight load, a set of springs and a damping element. The weight range needed for the optimal functioning of our table is $286 - 408$ kg. In our case, besides the weight of the interferometer and dSFA's heart, several weights made of stainless steel, corresponding to an added mass of 350 kg, were installed since the previous version of the dSFA to increase the inertia of the table. This works also as a thermal mass, since it helps slowing down the thermal drift. The table as well as the added weights are visible on Figure 3.12.

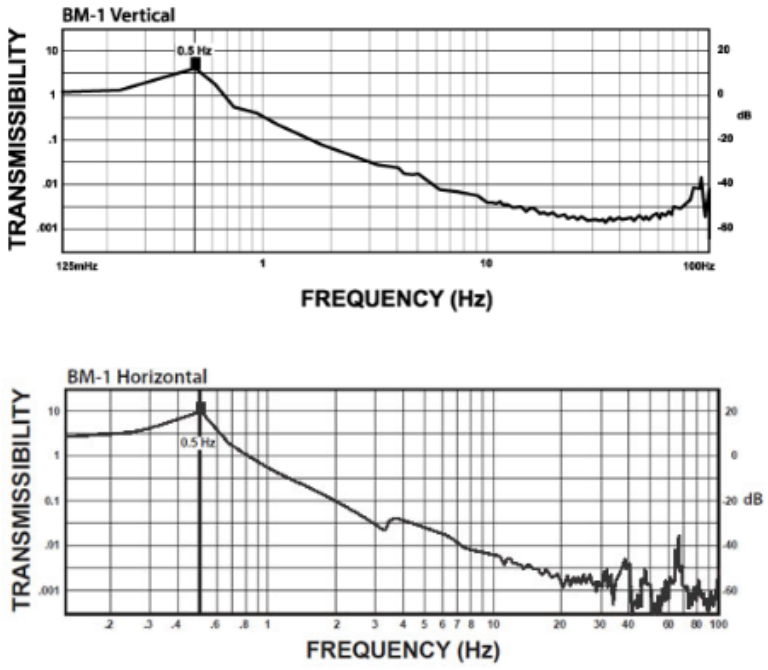

Figure 3.9 Manufacturer's data of the vertical and the horizontal transmissibility of the anti-vibration table for a frequency range between 125 mHz and 100 Hz.

The isolating box used for thermal stability (see section 3.1.5) is also used as an additional protection layer against acoustic vibrations in the air, complementing the protection for mechanical stability of the set-up.

[14]Manufacturer: Minus-K. Model: BM-1 Bench Top Vibration Isolation Platform

Thermal Stability

To achieve the best control of temperature, we encapsulate the set-up with four thermalized levels of increasing quality controls: the experimental room, the airlock compartment, the thermal insulating box and the vacuum chamber. Each of this isolation elements constitutes a thermal barrier for temperature changes.

The firsts thermal barriers are the two rooms that accommodate the experimental set-up (Figure 3.10), separated by a common wall. The airlock compartment contains the laser injection system, the data acquisition equipment, the thermal regulation circuit, and allows the connection of hydraulic and electric circuits to the room above, where the command equipment is placed, to remotely control the circulation of thermalized fluid and the mechanic movement of the dSFA, respectively, as well as the visualization of the collected data. These equipment have been placed in the airlock compartment to avoid any sources of heat and air convection inside the experimental room.

A thermal regulation system was installed in the airlock compartment, as shown in Figure 3.11. This thermal circuit was built from a series of radiators working in cooling mode, fixed near the ceiling, and fed by the cold water lines from the laboratory. Since we aim to have the slowest possible temperature change in the room and to attenuate the thermal drift in the experiment, the circulation system has to regulate the flow of water in the circuit depending on the external heat transfer during the day. Such a regulation is performed by a PID temperature controller (PID), which adjusts the mixing of cold water with a three-way valve (M) if the temperature of control (TC), measured with a PT-100 resistance, deviates from the target point of 24°C. Unlike air conditioning, the regulation of this system presents little oscillation and little convection. In conditions of an experiment, i.e., when nobody is present in the room and the room has stabilized over typically one day, the temperature in the airlock compartment fluctuates only by 0.3°C around 24°C.

The experimental room contains the dSFA's heart, the interferometer, and other equipment used for atmospheric and thermal control. Cables, optical fiber, as well as hydraulic connections built for the circulation in the hydraulic circuit and the vacuum chamber go from the airlock compartment to the experimental room through properly isolated wall passages, as seen in Figure 3.10.

The third thermal barrier is the thermal isolating box, conceived to weaken temperature drifts around the dSFA. This box is homemade from polyurethane foam of 10 cm thickness and wrapped with isolating adhesive tape. This passive enclosure reduces the acoustic vibrations from the environment and helps controlling the thermal drift around the set-up. Additional layers of foam were added below and around the set-up (Figure 3.12) to ensure the damping of vibrations from the floor and to block the passage of air, in order to avoid convection air rolls playing against the mechanical stability of the set-up.

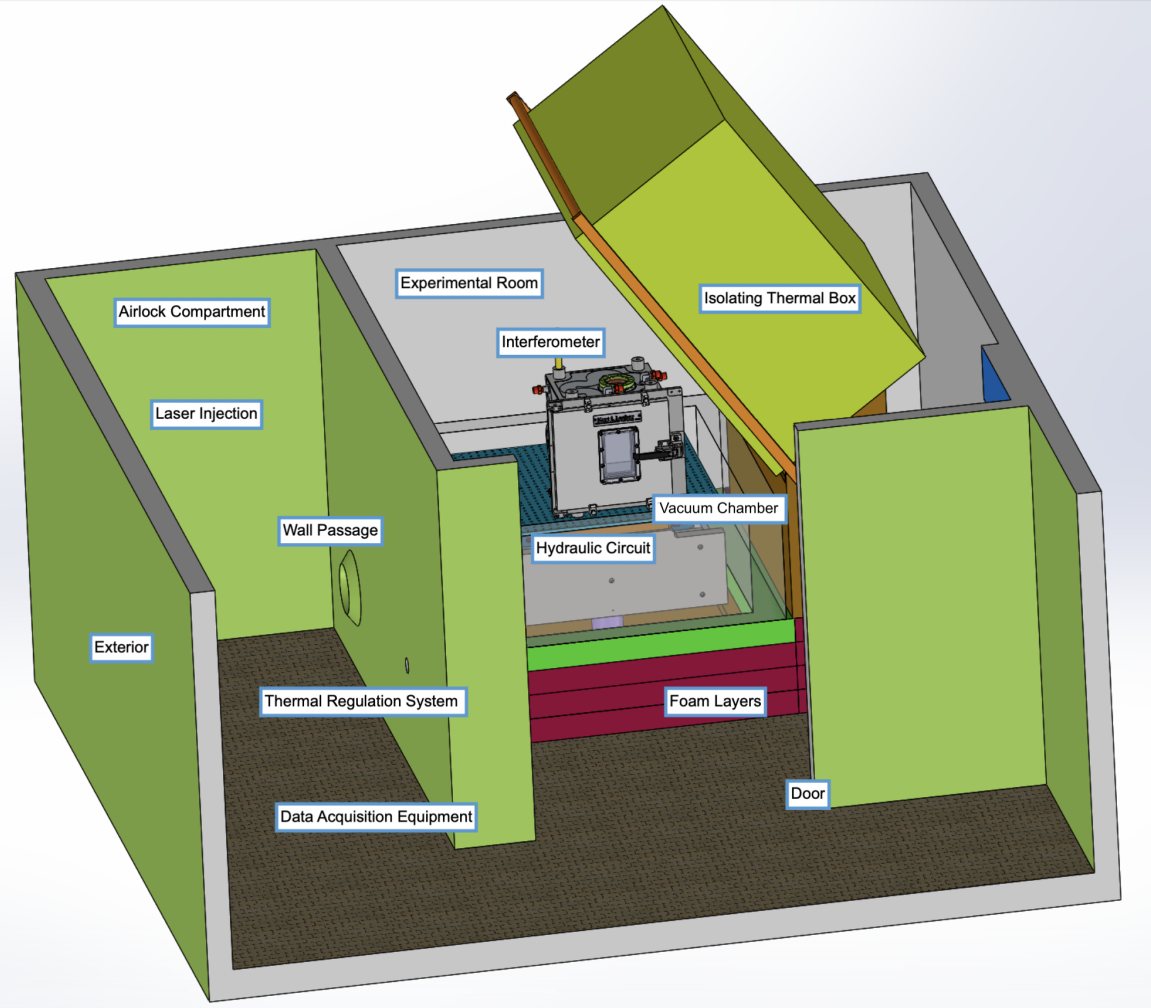

Figure 3.10 Schematic of the accommodation of the dSFA, with the corresponding data acquisition equipment, optical set-up and environmental control elements, distributed in the experimental room and the airlock compartment.

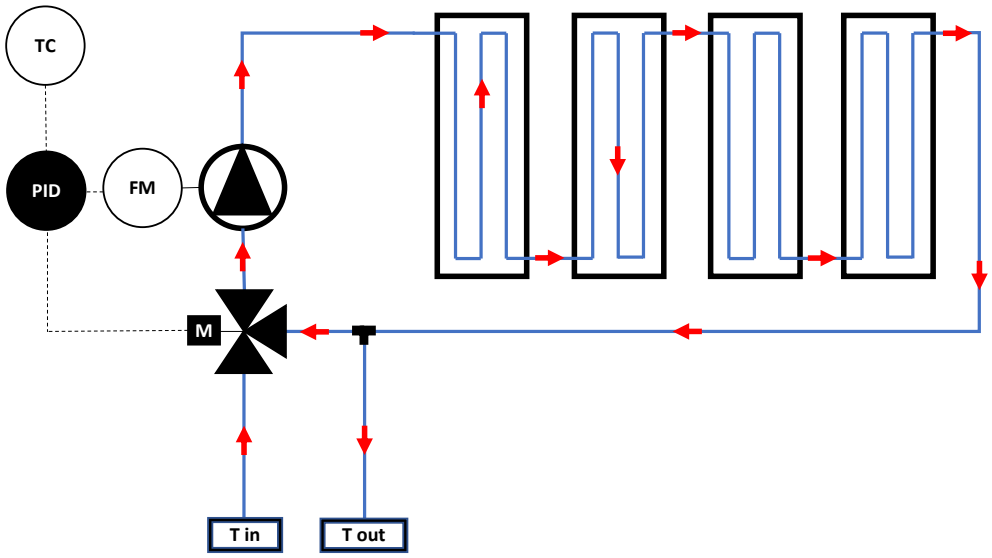

Figure 3.11 Schematic of the thermal regulation system, based on a series of radiators working in cooling mode and operated by a PID temperature controller (PID), a three-way valve (M), a the temperature of control (TC) measured with a PT-100 resistance and a flow meter (FM). The red arrows show the water flow direction.

During my thesis, a vacuum chamber has been added to contain the dSFA's heart, acting as a fourth thermal barrier (further information in section 3.1.5).

In order to control the stability and the homogeneity of the temperature, nine PT-100 Platinum resistances have been placed at different locations (in both the airlock compartment and the experimental room, inside and outside the isolating box), the reading been performed with a data acquisition unit[15] equipped with a multiplexer module[16]. Finally, all these efforts allow to obtain thermal drifts inside the vacuum chamber that are as low as $\sim 0.04°C$ in 4 hours (the typical time needed for recording one approach-retraction curve). Figure 3.13 shows the temperature measured from the sensor installed inside the vacuum chamber during an experiment.

Atmospheric Stability

The vacuum chamber mentioned above[17] allows to have a stable and controlled temperature, and to control the atmosphere around the liquid used. Additionally, it could potentially let us work under vacuum, under inert atmosphere (Ar, N_2, etc.), or under controlled vapor

[15]Manufacturer: Agilent, model: 34972A.
[16]Manufacturer: Agilent, model: 34901A.
[17]Manufacturer: Lesker, product specifications met by our requirements.

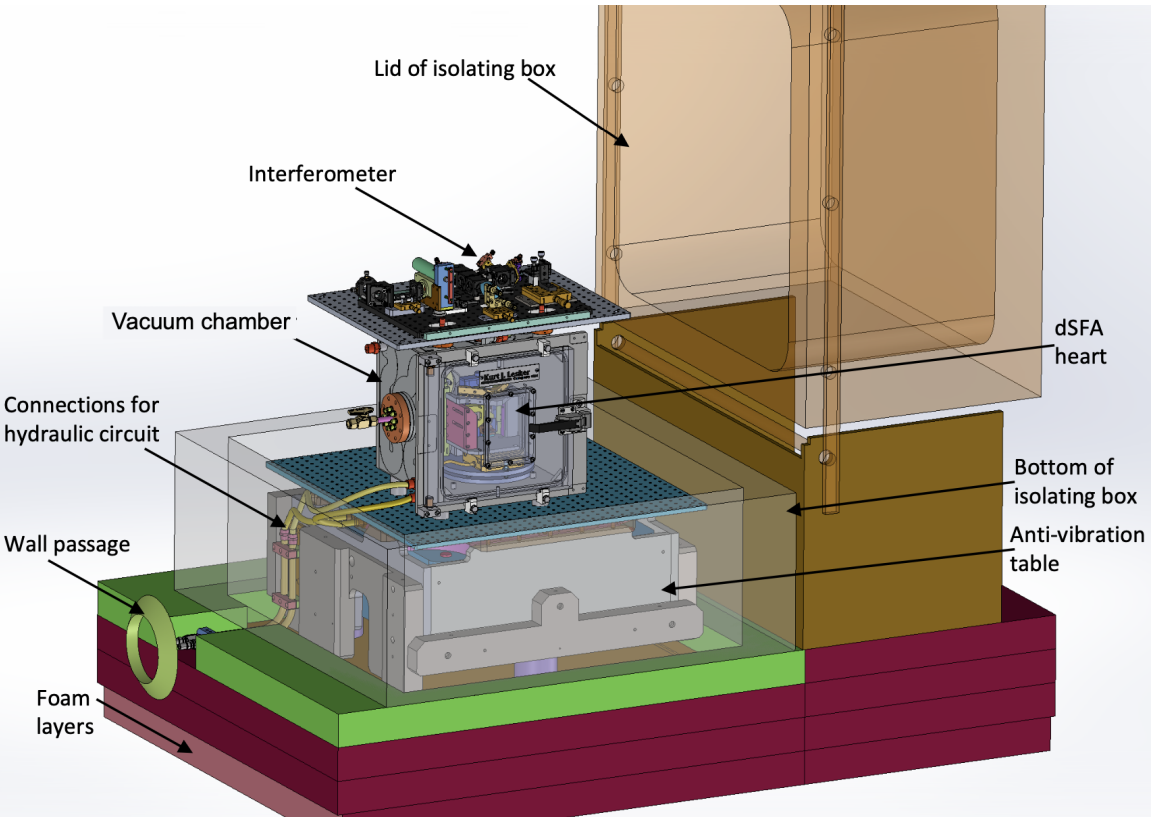

Figure 3.12 Schematic of the set-up of the dSFA inside the vacuum chamber, below the interferometer. Both are placed on top of an anti-vibration table, surrounded by a thermal isolating box. Other elements are also illustrated and labeled.

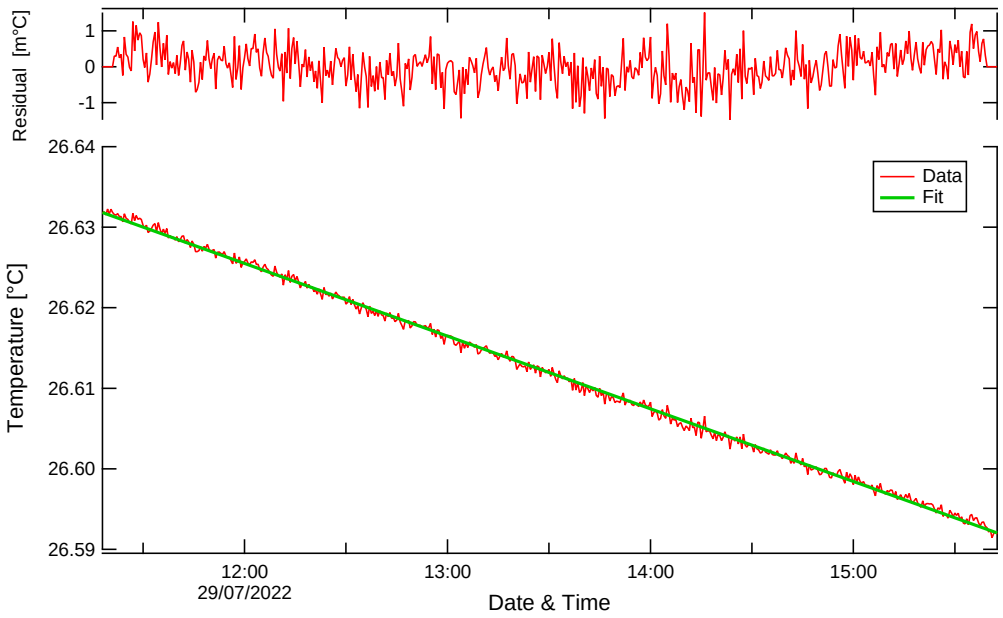

Figure 3.13 Temperature measured inside the vacuum chamber by a thermo-resistance sensor. The thermal drift measured inside the chamber is $(9.00 \pm 0.02) \cdot 10^{-3}$°C/h.

pressure and humidity, which is useful for hygroscopic and volatile liquids, among other advantages.

The vacuum chamber as seen in Figure 3.14 is fabricated out of stainless steel, and a hydraulic circuit its carved on its walls, allowing a circulating flow of regulated temperature. The hydraulic circuit of the vacuum chamber is connected to a spiral-shaped hydraulic circuit below the optical table holding the set-up. This hydraulic circuit contains the water coming in from the thermostatic bath, placed at the floor above the experimental room.

3.2 Analysis of the Interferometric Measurement

With the new double interferometer and the new electronic configuration, the pre-treatment procedure to obtain the static and dynamic distance and force has changed. Below we describe the new procedure for ideal then real signals, and we present an extension of the analysis when the detectors operate in non-linear regime.

3.2.1 Ideal Signals

For illustration purposes, a general expression is shown in Eq.3.1 for all eight signals coming from the photodiodes (two interferometers with two analysis units each, and two photodiodes in each unit). Here $I_{\substack{\mathrm{H}\\\mathrm{L}}\substack{\mathrm{X1}\\\mathrm{Y2}}}$ and $\phi_{\substack{\mathrm{H}\\\mathrm{L}}}$ respectively represent the electrical current flowing from the photodiode and the optical phase shift between the two polarization states, considered as

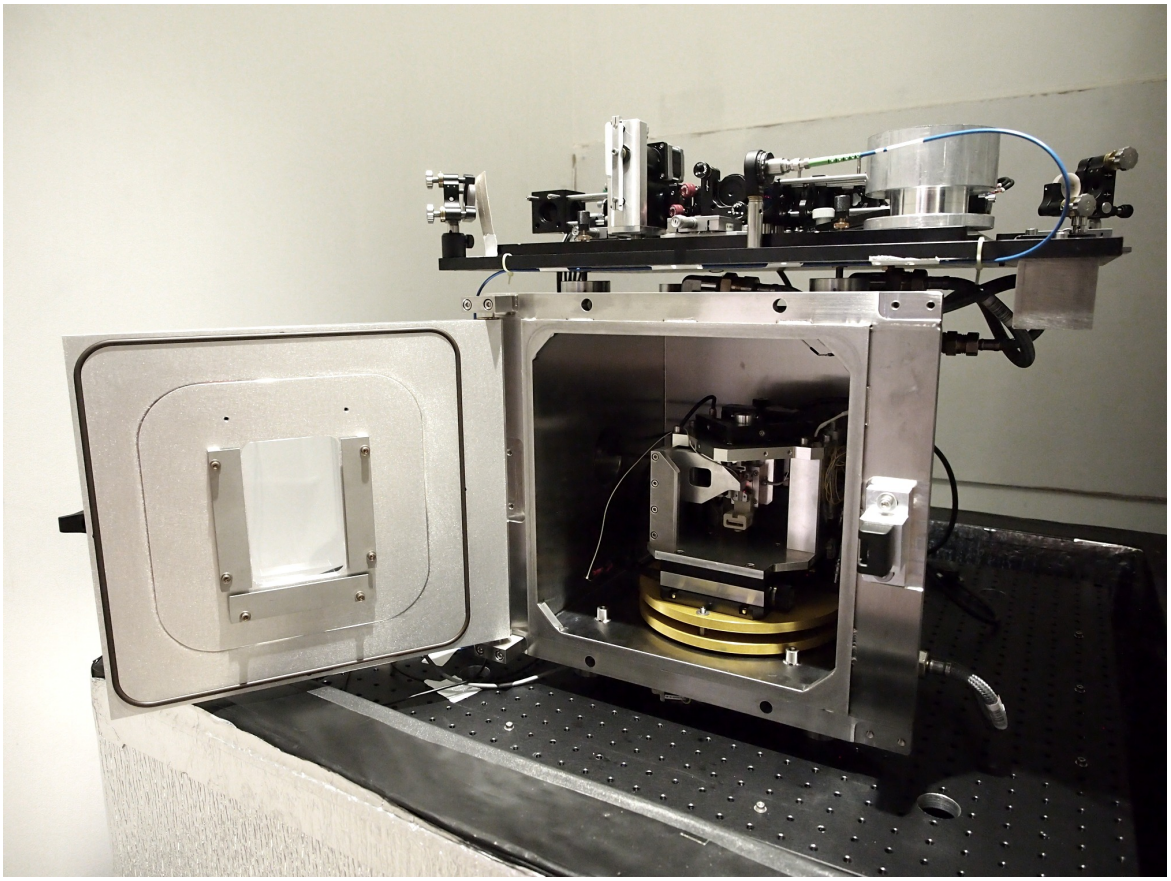

Figure 3.14 Photograph of the new version of the dSFA, showing the addition of a vacuum chamber containing the dSFA's heart, with the interferometers built on the optical board above.

instantaneous (i.e., without integration at this stage) and total (i.e., containing both static and dynamic information). There is no difference between both interferometers, with index H for distance and index L for force. However, for quadrature purposes, there is a 90° phase-shift between the channel X and Y (blue index) of each analysis unit, which explains the choice of cosine or sine, highlighted in blue. Additionally, a change of sign between photodiodes 1 and 2 (red index) of each channel for the subtraction of signals is represented in the red symbol. The prefactor I_0 corresponds to the total intensity arriving on each analysis unit.

$$I_{\substack{\mathrm{H}\,\mathrm{X}\,1\\ \mathrm{L}\,\mathrm{Y}\,2}} = I_0\left[1 \pm \begin{matrix}\cos\\ \sin\end{matrix}\left(\phi_{\substack{\mathrm{H}\\ \mathrm{L}}}\right)\right] \tag{3.1}$$

In the following, to avoid redundant mathematical development for all signals, only the development for one pair of signals $I_{\mathrm{HX}_2^1}$ is presented in equation 3.2, showing the sign variations corresponding to one pair of photodiodes. This same applies to the other 3 pairs of signals: $I_{\mathrm{HY}_2^1}$, $I_{\mathrm{LX}_2^1}$ and $I_{\mathrm{LY}_2^1}$.

$$I_{\mathrm{HX}_2^1} = I_0\Big[1 \pm \cos(\phi_{\mathrm{H}})\Big] \tag{3.2}$$

The expression of the phase shift is given by equation 3.3. We note that the factor 2 is due to the back and forth of the interfering laser beams in the dSFA's heart.

$$\phi_{\mathrm{H}} = \frac{4\pi}{\lambda}[h_{\mathrm{stat}} + \mathrm{h_{dyn}}\cos(\omega \mathrm{t} + \varphi_{\mathrm{H}})] \tag{3.3}$$

In all experiments, the amplitude of the dynamic oscillation is small: $h_{\mathrm{dyn}} \ll \lambda/4\pi \simeq 50$ nm. Therefore, we can develop the expression of $I_{\mathrm{HX}_2^1}$ with the ratio $4\pi h_{\mathrm{dyn}}/\lambda$. In this section, we will first consider the simplest case where the detector operates in the linear-regime, i.e., we will limit the development to the first order in $4\pi h_{\mathrm{dyn}}/\lambda$:

$$I_{\mathrm{HX}_2^1} \simeq I_0\Big[1 \pm \cos\Big(\frac{4\pi}{\lambda}h_{\mathrm{stat}}\Big) \mp \sin\Big(\frac{4\pi}{\lambda}h_{\mathrm{stat}}\Big)\frac{4\pi}{\lambda}h_{\mathrm{dyn}}\cos(\omega t + \varphi_{\mathrm{H}})\Big] \tag{3.4}$$

We begin by writing the expressions of the quasi-static and dynamic signals measured experimentally. The multimeters collect the quasi-static component by integrating the signals over $\mathrm{T} = 300$ ms at a time t:

$$I^{\mathrm{stat}}_{\mathrm{HX}_2^1}(t) \equiv \int_t^{t+T} I_{\mathrm{HX}_2^1}(t')\frac{dt'}{T} \tag{3.5}$$

In the following, we suppose that h_{stat} varies quasi-statically, i.e., that the temporal variations of h_{stat} are slow at the scale of T:

$$\frac{4\pi}{\lambda}|U|\mathrm{T} \ll 1 \quad \text{so a speed} \quad |\mathrm{U}| \ll \frac{\lambda}{4\pi\mathrm{T}} \simeq 170 \text{ nm/s}$$

One can then easily calculate:

$$I^{\text{stat}}_{\text{HX}^1_2}(t) \simeq I_0\Big[1 \pm \cos\Big(\frac{4\pi}{\lambda}h_{\text{stat}}\Big) \mp \sin\Big(\frac{4\pi}{\lambda}h_{\text{stat}}\Big)\frac{4\pi}{\lambda}h_{\text{dyn}}\cos\Big(\omega\Big(t+\frac{T}{2}\Big)+\varphi_{\text{H}}\Big)\text{sinc}\Big(\frac{\omega T}{2}\Big)\Big] \quad (3.6)$$

The third term is due to the fact that in general T is not a multiple of $2\pi/\omega$. But its amplitude is damped by the sinc function if the oscillation frequency and integration time are large enough:

$$\frac{\omega T}{2} \gg 1$$

In our case, T = 300 ms and $\omega/2\pi \geq 10$ Hz, giving $\omega T/2 \geq 9.4$, so this condition is reasonably verified. We finally get the quasi-static component, i.e., only the zero order:

$$I^{\text{stat}}_{\text{HX}^1_2}(t) \simeq I_0\Big[1 \pm \cos\Big(\frac{4\pi}{\lambda}h_{\text{stat}}\Big)\Big] \quad (3.7)$$

The lock-in amplifier, plugged in series on photodiode 1, collects the two quadratures of the dynamic component (real and imaginary parts). It can formally be written as:

$$I^{\mathfrak{Re}}_{\text{HX1}}(t) \equiv \int_t^{t+T} I_{\text{HX}^1_2}(t')2\cos(\omega t)\frac{dt'}{T} \quad (3.8)$$

$$I^{\mathfrak{Im}}_{\text{HX1}}(t) \equiv \int_t^{t+T} I_{\text{HX}^1_2}(t')2\cos\Big(\omega t+\frac{\pi}{2}\Big)\frac{dt'}{T} \quad (3.9)$$

Similarly than for the static-component, one can show that if $\omega T \gg 1$ we get the dynamic component oscillating at ω, i.e., only the first order:

$$I^{\mathfrak{Re}}_{\text{HX1}}(t) \simeq -I_0\sin\Big(\frac{4\pi}{\lambda}h_{\text{stat}}\Big)\frac{4\pi}{\lambda}h_{\text{dyn}}\cos(\varphi_{\text{H}}) \quad (3.10)$$

$$I^{\mathfrak{Im}}_{\text{HX1}}(t) \simeq -I_0\sin\Big(\frac{4\pi}{\lambda}h_{\text{stat}}\Big)\frac{4\pi}{\lambda}h_{\text{dyn}}\sin(\varphi_{\text{H}}) \quad (3.11)$$

Equivalently, we obtain the modulus and argument of the dynamic component:

$$I^{\text{mod}}_{\text{HX1}}(t) = I_0\Big|\sin\Big(\frac{4\pi}{\lambda}h_{\text{stat}}\Big)\Big|\frac{4\pi}{\lambda}h_{\text{dyn}} \quad (3.12)$$

$$I^{\text{arg}}_{\text{HX1}}(t) = \varphi_{\text{H}} \quad \text{if} \quad \sin\Big(\frac{4\pi}{\lambda}h_{\text{stat}}\Big) < 0, \quad \varphi_{\text{H}} - \pi \quad \text{otherwise} \quad (3.13)$$

The mathematical expressions for HY, FX and FY are similar. In the case of ideal signals in linear regime, the pre-treatment of the data is straightforward. We numerically compute

normalized "contrast" quantities, to be insensitive to any intensity fluctuations of the light source. For example for HX:

$$V_{\mathrm{HX}}^{\mathrm{stat}} \equiv 10\frac{I_{\mathrm{HX1}}^{\mathrm{stat}} - I_{\mathrm{HX2}}^{\mathrm{stat}}}{I_{\mathrm{HX1}}^{\mathrm{stat}} + I_{\mathrm{HX2}}^{\mathrm{stat}}} = 10\cos\Big(\frac{4\pi}{\lambda}h_{\mathrm{stat}}\Big) \tag{3.14}$$

$$V_{\mathrm{HX}}^{\mathrm{mod}} \equiv 20\frac{I_{\mathrm{HX1}}^{\mathrm{mod}}}{I_{\mathrm{HX1}}^{\mathrm{stat}} + I_{\mathrm{HX2}}^{\mathrm{stat}}} = 10\,\Big|\sin\Big(\frac{4\pi}{\lambda}h_{\mathrm{stat}}\Big)\Big|\frac{4\pi}{\lambda}h_{\mathrm{dyn}} \tag{3.15}$$

$$V_{\mathrm{HX}}^{\mathrm{arg}} \equiv I_{\mathrm{HX}}^{\mathrm{arg}} \tag{3.16}$$

Then, in principle we can obtain the quasi-static displacements h_{stat}, l_{stat}, and the dynamic moduli h_{dyn}, l_{dyn} and phases φ_{H}, φ_{L} corresponding to the oscillatory displacements.

3.2.2 Real Signals in Linear Regime

Real signals are affected by various optical and electronic subtleties. For simplicity, we will express them only for the channel HX. Experimentally, we observed that the quasi-static signal has the form:

$$I_{\mathrm{HX}_2^1}^{\mathrm{stat}} = a_{\substack{1\\2}}\; I_0\Big[1 \pm b_{\substack{1\\2}}\cos\Big(\frac{4\pi}{\lambda}h_{\mathrm{stat}} + \Delta\varphi_{\substack{1\\2}}^{\mathrm{stat}}\Big)\Big] \tag{3.17}$$

The parameter $a_{\substack{1\\2}}$ is due to several effects, which we list in a non-exhaustive way:

- different adsorptions for lasers beams traveling along different optical path,
- beams clipped on the edges of the photodiodes,
- different photodiodes sensitivities.

The parameter $b_{\substack{1\\2}}$ includes effects caused by:

- an imperfect superposition of interfering beams (due to imperfect alignment of the pairs of mirrors, or to beams of slightly different diameters on the detector),
- Wollaston prism's angles not perfectly adjusted.

The parameter $\Delta\varphi_{\substack{1\\2}}^{\mathrm{stat}}$ is possibly caused by:

- a time delay in triggering the acquisitions of the multimeters,
- an optical phase shift originating from reflection and transmission coefficients on the optical pathways which vary slightly with polarization.

Also experimentally, we observed that the modulus and argument of the dynamic signal have the form:

$$I_{\mathrm{HX1}}^{\mathrm{mod}} = a_1\ b_1\ I_0 \left| \sin\left(\frac{4\pi}{\lambda} h_{\mathrm{stat}} + \Delta\varphi_1^{\mathrm{stat/dyn}}\right)\right| \frac{4\pi}{\lambda} h_{\mathrm{dyn}} \tag{3.18}$$

$$I_{\mathrm{H}}^{\mathrm{arg}} = \varphi_{\mathrm{H}} \quad \text{if} \quad \sin\left(\frac{4\pi}{\lambda} h_{\mathrm{stat}} + \Delta\varphi_1^{\mathrm{stat/dyn}}\right) < 0, \quad \varphi_{\mathrm{H}} - \pi \quad \text{otherwise} \tag{3.19}$$

The parameters a_1 and b_1 are the same than for the static measurement, whereas $\varphi_1^{\mathrm{stat/dyn}}$ is a shift between the measurements coming from the multimeter and the lock-in amplifier plugged in series on the same photodiode. It clearly originates from a time delay in triggering the acquisitions of these equipment.

Calibration

In order to quantify the values of the different parameters in the real signals and to be able to correct them, we perform a calibration. With the help of the coil-magnet system, we set the flexure hinge into motion, which can be detected on the two inteferometers thanks to the double mirror fixed on it (see Figure 3.3). First, a quasi-static displacement is obtained by imposing a quasi-DC voltage ramp of 20 V, equivalent to a ~ 1 µm travel, to one end of the coil. Simultaneously, an AC voltage is applied on the other end of the coil to produce a dynamic excitation. A typical amplitude of oscillation is 2 nm, with a voltage depending on the chosen work frequency.

The first step of the analysis of the calibration is to fit a sine onto the temporal evolution of each quasi-static current. For instance, on channel HX: $I_{\mathrm{HX}_2^1}^{\mathrm{stat}}$ are fitted while imposing an average frequency f_{ramp}, obtaining each signal's offset, amplitude and phase (Figure 3.15). The amplitude ratio is calculated as $r = \frac{a_1\ b_1}{a_2\ b_2}$, and the phase shift is deduced as $\Delta\varphi_{2-1}^{\mathrm{stat}} = \Delta\varphi_2^{\mathrm{stat}} - \Delta\varphi_1^{\mathrm{stat}}$. The signal coming from photodiode 2 is thereafter shifted temporally and multiplied by the amplitude ratio to obtain a corrected sum:

$$I_{\mathrm{HXsum}}^{\mathrm{stat}}(t) = I_{\mathrm{HX1}}^{\mathrm{stat}}(t) + r\ I_{\mathrm{HX2}}^{\mathrm{stat}}(t - \Delta\varphi_{2-1}^{\mathrm{stat}}/2\pi f_{\mathrm{ramp}}) \tag{3.20}$$

Checking that this corrected sum is constant with time is a way to validate the calibration (Figure 3.15).

The second step of the analysis of the calibration is to fit a sine onto the temporal evolution of each dynamic current together with the corresponding quasi-static component. For instance, on channel HX: $I_{\mathrm{HX1}}^{\mathrm{stat}}$ and $I_{\mathrm{HX1}}^{\mathfrak{Re}}$ are fitted while imposing an average frequency f_{ramp} (Figure 3.16). The phase shift between the dynamic and static signals is deduced as $\Delta\varphi_1^{\mathrm{dyn-stat}} = \Delta\varphi_1^{\mathrm{dyn}} - \Delta\varphi_1^{\mathrm{stat}}$. The dynamic signals in quadrature coming from the lock-in amplifier are thereafter shifted temporally to recover synchronization with the quasi-static

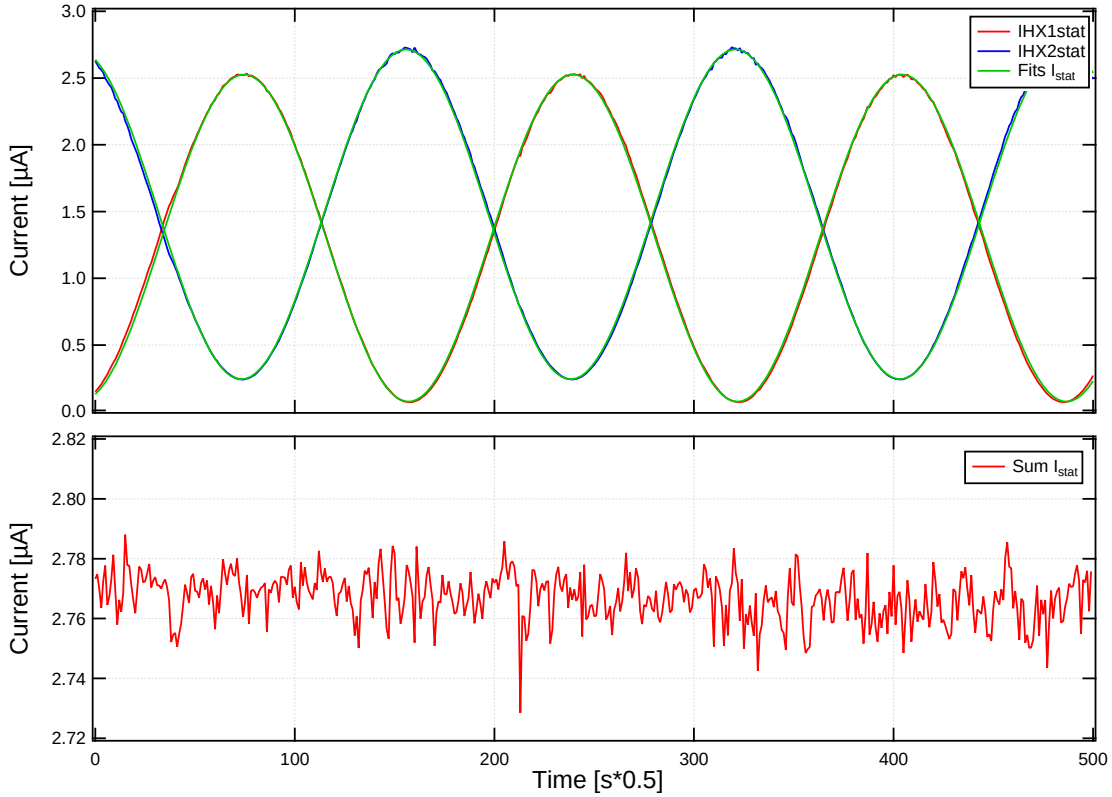

Figure 3.15 Sinus fitting of current signals from photodiodes 1 and 2 of channel HX and correction of their time lag and amplitude difference to calculate a constant corrected sum.

signal coming from the multimeter. In the same ways as in the first step, a corrected sum can be calculated to validate the calibration (Figure 3.16).

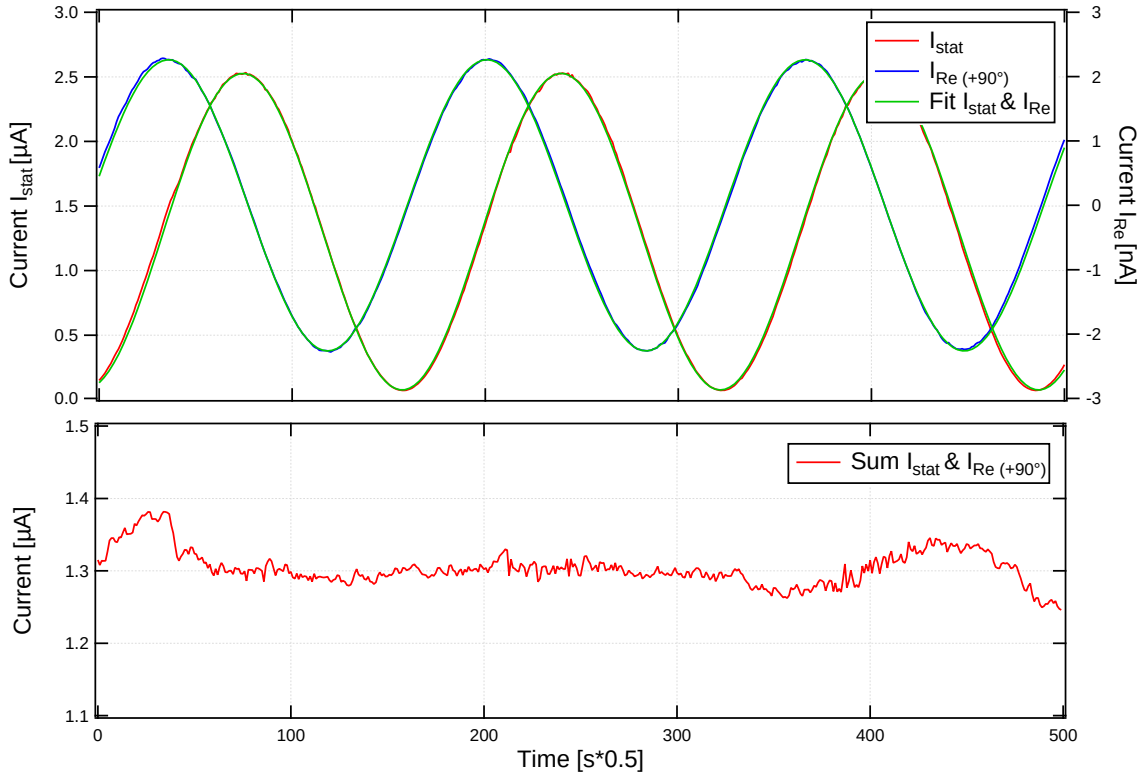

Figure 3.16 Sinus fitting of current signals from static and dynamic measurements and correction of their time lag that results in a constant sum of current intensities. For their addition, the real part of the dynamic signal was shifted by $\pi/2$.

After these two steps, we can numerically calculate contrasts, corrected by the amplitude ratio and the phase shift:

$$V_{\mathrm{HX}}^{\mathrm{stat}}(t) \equiv 10\frac{I_{\mathrm{HX1}}^{\mathrm{stat}}(t) - r\ I_{\mathrm{HX2}}^{\mathrm{stat}}(t - \Delta\varphi_{2-1}^{\mathrm{stat}}/2\pi f_{\mathrm{ramp}})}{I_{\mathrm{HX1}}^{\mathrm{stat}}(t) + r\ I_{\mathrm{HX2}}^{\mathrm{stat}}(t - \Delta\varphi_{2-1}^{\mathrm{stat}}/2\pi f_{\mathrm{ramp}})} \tag{3.21}$$

$$V_{\mathrm{HX}}^{\mathrm{mod}}(t) \equiv 20\frac{I_{\mathrm{HX1}}^{\mathrm{mod}}(t - \Delta\varphi_{1}^{\mathrm{dyn-stat}})}{I_{\mathrm{HX1}}^{\mathrm{stat}}(t) + r\ I_{\mathrm{HX2}}^{\mathrm{stat}}(t - \Delta\varphi_{2-1}^{\mathrm{stat}}/2\pi f_{\mathrm{ramp}})} \tag{3.22}$$

$$V_{\mathrm{HX}}^{\mathrm{arg}}(t) \equiv I_{\mathrm{HX1}}^{\mathrm{arg}}(t - \Delta\varphi_{1}^{\mathrm{dyn-stat}}) \tag{3.23}$$

One can deduce:

$$V_{\mathrm{HX}}^{\mathrm{stat}}(t) = 10\frac{b_2 - b_1}{b_2 + b_1} + 20\frac{b_2\ b_1}{b_2 + b_1}\cos\left(\frac{4\pi}{\lambda}h_{\mathrm{stat}}\right) \tag{3.24}$$

$$V_{\mathrm{HX}}^{\mathrm{mod}}(t) = 20\frac{b_2\ b_1}{b_2 + b_1}\left|\sin\left(\frac{4\pi}{\lambda}h_{\mathrm{stat}}\right)\right|\frac{4\pi}{\lambda}h_{\mathrm{dyn}} \tag{3.25}$$

$$V_{\mathrm{HX}}^{\mathrm{arg}}(t) = \varphi_{\mathrm{H}} \quad \text{if} \quad \sin\left(\frac{4\pi}{\lambda}h_{\mathrm{stat}}\right) < 0, \quad \varphi_{\mathrm{H}} - \pi \quad \text{otherwise} \tag{3.26}$$

From these equations we define the offset $V_{\mathrm{HX}}^{\mathrm{off}} = 10\frac{b_2 - b_1}{b_2 + b_1}$ and amplitude $V_{\mathrm{HX}}^{\mathrm{amp}} = 20\frac{b_2\ b_1}{b_2 + b_1}$.

We follow the same steps for the channel HY and get similar expressions, except that the phases are shifted by $-\pi/2 + \psi_{\mathrm{H}}$, because of the (imperfect) setting of the quarter-wave plate. We end up with the following expressions for the quasi-static components:

$$V_{\mathrm{HX}}^{\mathrm{stat}} = V_{\mathrm{HX}}^{\mathrm{off}} + V_{\mathrm{HX}}^{\mathrm{amp}}\cos\left(\frac{4\pi}{\lambda}h_{\mathrm{stat}}\right) \tag{3.27}$$

$$V_{\mathrm{HY}}^{\mathrm{stat}} = V_{\mathrm{HY}}^{\mathrm{off}} + V_{\mathrm{HY}}^{\mathrm{amp}}\sin\left(\frac{4\pi}{\lambda}h_{\mathrm{stat}} + \psi_{\mathrm{H}}\right) \tag{3.28}$$

The expressions for the dynamic components read:

$$V_{\mathrm{HX}}^{\mathrm{mod}} = V_{\mathrm{HX}}^{\mathrm{amp}}\left|\sin\left(\frac{4\pi}{\lambda}h_{\mathrm{stat}}\right)\right|\frac{4\pi}{\lambda}h_{\mathrm{dyn}} \tag{3.29}$$

$$V_{\mathrm{HY}}^{\mathrm{mod}} = V_{\mathrm{HY}}^{\mathrm{amp}}\left|\cos\left(\frac{4\pi}{\lambda}h_{\mathrm{stat}} + \psi_{\mathrm{H}}\right)\right|\frac{4\pi}{\lambda}h_{\mathrm{dyn}} \tag{3.30}$$

$$V_{\mathrm{HX}}^{\mathrm{arg}} = \varphi_{\mathrm{H}} \quad \text{if} \quad \sin\left(\frac{4\pi}{\lambda}h_{\mathrm{stat}}\right) < 0, \quad \varphi_{\mathrm{H}} - \pi \quad \text{otherwise} \tag{3.31}$$

$$V_{\mathrm{HY}}^{\mathrm{arg}} = \varphi_{\mathrm{H}} \quad \text{if} \quad \cos\left(\frac{4\pi}{\lambda}h_{\mathrm{stat}} + \psi_{\mathrm{H}}\right) > 0, \quad \varphi_{\mathrm{H}} - \pi \quad \text{otherwise} \tag{3.32}$$

The third step of the analysis of the calibration consists in plotting the quasi-static $V_{\mathrm{HY}}^{\mathrm{stat}}$ versus $V_{\mathrm{HX}}^{\mathrm{stat}}$, and in adjusting an elliptic function to obtain the values of $V_{\mathrm{HX}}^{\mathrm{off}}$, $V_{\mathrm{HY}}^{\mathrm{off}}$, $V_{\mathrm{HX}}^{\mathrm{amp}}$, $V_{\mathrm{HY}}^{\mathrm{amp}}$ and ψ_{H} (Figure 3.17). The residuals between the fit and the data show random noise of maximum amplitude $\sim 5 \cdot 10^{-3}$ for ellipse amplitudes of ~ 9.

The same three-step analysis is performed to calibrate the force interferometer.

Calculation of quasi-static displacements

Once the calibration is done, all the measured signals are pre-treated as follows. The raw electric currents, static and dynamic, are numerically converted for each analysis unit into corrected contrasts (for example $V_{\mathrm{HX}}^{\mathrm{stat}}$ and $V_{\mathrm{HX}}^{\mathrm{dyn}}$ for HX), knowing the amplitude ratio r and the phase shifts $\Delta\varphi_{2-1}^{\mathrm{stat}}$ and $\Delta\varphi_{1}^{\mathrm{dyn-stat}}$ (following equations 3.21 and 3.22). These contrasts can then be used to determine the quasi-static displacement for each interferometer, knowing the ellipse parameters. For example for the distance interferometer, the offsets $V_{\mathrm{HX}}^{\mathrm{off}}$ and

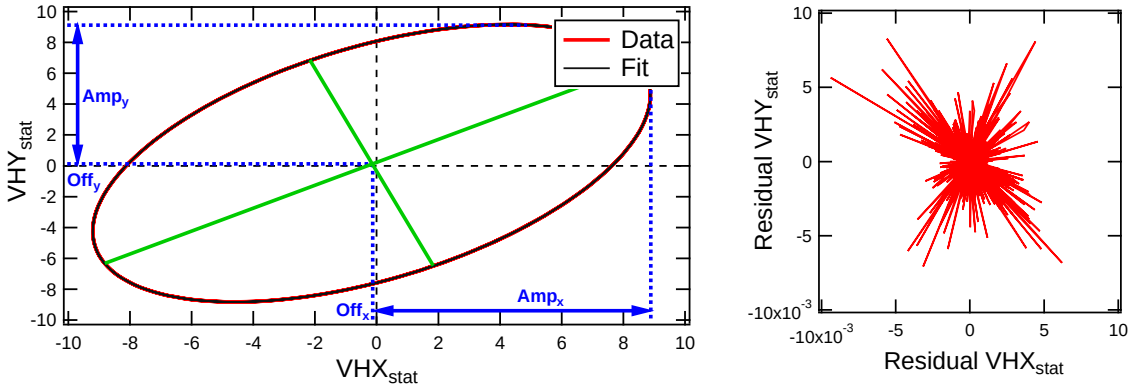

Figure 3.17 On the left, fitting of $V_{\mathrm{HY}}^{\mathrm{stat}}$ as a function of $V_{\mathrm{HX}}^{\mathrm{stat}}$ with an ellipse to calibrate the parameters of offset, amplitude and the phase shift. On the right, residuals associated to the fit.

$V_{\mathrm{HY}}^{\mathrm{off}}$, amplitudes $V_{\mathrm{HX}}^{\mathrm{amp}}$ and $V_{\mathrm{HY}}^{\mathrm{amp}}$, and phase shift ψ_{H} are known, and one can numerically calculate:

$$\cos\left(\frac{4\pi}{\lambda}h_{\mathrm{stat}}\right) = \frac{V_{\mathrm{HX}}^{\mathrm{stat}} - V_{\mathrm{HX}}^{\mathrm{off}}}{V_{\mathrm{HX}}^{\mathrm{amp}}} \tag{3.33}$$

$$\sin\left(\frac{4\pi}{\lambda}h_{\mathrm{stat}}\right) = \left[\frac{V_{\mathrm{HY}}^{\mathrm{stat}} - V_{\mathrm{HY}}^{\mathrm{off}}}{V_{\mathrm{HY}}^{\mathrm{amp}}} - \frac{V_{\mathrm{HX}}^{\mathrm{stat}} - V_{\mathrm{HX}}^{\mathrm{off}}}{V_{\mathrm{HX}}^{\mathrm{amp}}}\sin(\psi_H)\right]\frac{1}{\cos(\psi_H)} \tag{3.34}$$

Knowing the cosine and the sine of the static phase $\frac{4\pi}{\lambda}h_{\mathrm{stat}}$ allows to determine the static phase with a constant sensitivity whatever its value. The phase at initial time $t = 0$ is computed modulo 2π, because one does not know the position of the optical contact (corresponding by definition to $h_{\mathrm{stat}} = 0$). However for subsequent times, it is possible to "count" the passing interference fringes, and so to determine variations of the phase by more than 2π by simply unwrapping the signal. The quasi-static displacement h_{stat} can therefore be deduced to within one constant (Figure 3.18).

Calculation of dynamic displacements

For example, on the distance interferometer, the static and dynamic contrasts are combined by numerically computing the quantities $c_{\mathrm{H}}^{\mathfrak{Re}}$ and $c_{\mathrm{H}}^{\mathfrak{Im}}$, defined as:

$$c_{\mathrm{H}}^{\mathfrak{Re}} \equiv -V_{\mathrm{HX}}^{\mathrm{mod}}\cos(V_{\mathrm{HX}}^{\mathrm{arg}})(V_{\mathrm{HY}}^{\mathrm{stat}} - V_{\mathrm{HY}}^{\mathrm{off}}) + V_{\mathrm{HY}}^{\mathrm{mod}}\cos(V_{\mathrm{HY}}^{\mathrm{arg}})(V_{\mathrm{HX}}^{\mathrm{stat}} - V_{\mathrm{HX}}^{\mathrm{off}}) \tag{3.35}$$

$$c_{\mathrm{H}}^{\mathfrak{Im}} \equiv -V_{\mathrm{HX}}^{\mathrm{mod}}\sin(V_{\mathrm{HX}}^{\mathrm{arg}})(V_{\mathrm{HY}}^{\mathrm{stat}} - V_{\mathrm{HY}}^{\mathrm{off}}) + V_{\mathrm{HY}}^{\mathrm{mod}}\sin(V_{\mathrm{HY}}^{\mathrm{arg}})(V_{\mathrm{HX}}^{\mathrm{stat}} - V_{\mathrm{HX}}^{\mathrm{off}}) \tag{3.36}$$

One can show that:

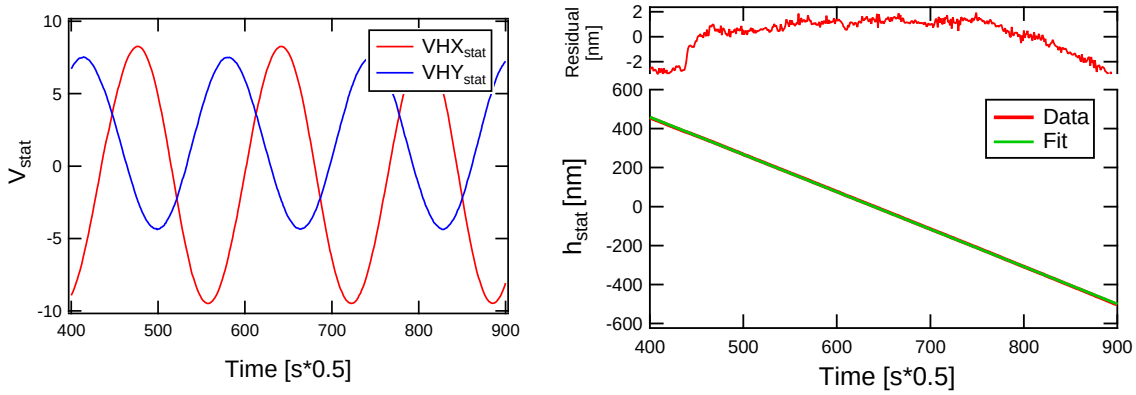

Figure 3.18 On the left, the contrast signals $V_{\mathrm{HX}}^{\mathrm{stat}}$ and $V_{\mathrm{HY}}^{\mathrm{stat}}$ from the distance interferometer during the calibration with the coil-magnet system. On the right, the resulting quasi-static distance h_{stat}. The small deviation from linearity is due to the non-linear voltage/displacement conversion of the piezo-electric actuator.

$$h_{\mathrm{dyn}} = \frac{\lambda}{4\pi} \frac{\sqrt{{c_{\mathrm{H}}^{\mathfrak{Re}}}^2 + {c_{\mathrm{H}}^{\mathfrak{Im}}}^2}}{V_{\mathrm{HX}}^{\mathrm{amp}} V_{\mathrm{HY}}^{\mathrm{amp}} \cos(\psi_{\mathrm{H}})} \tag{3.37}$$

We can therefore determine the amplitude h_{dyn} of the dynamic displacement, with a constant sensitivity whatever the operating point (Figure 3.19).

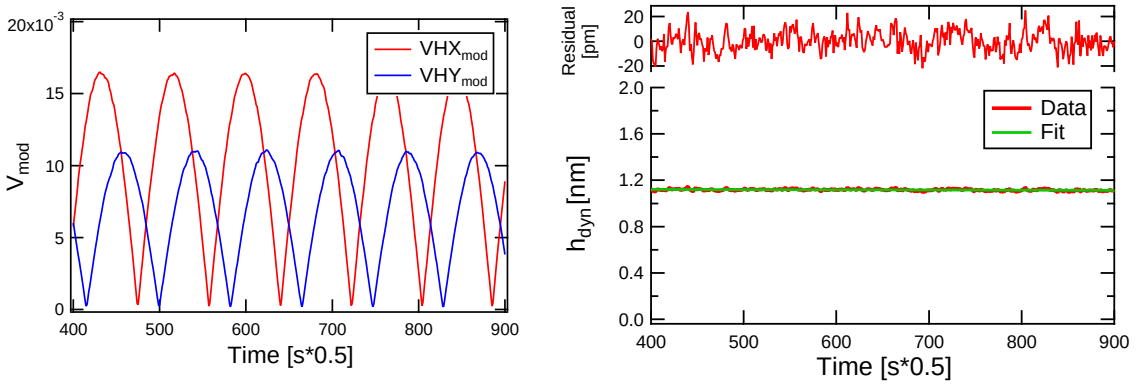

Figure 3.19 On the left, the dynamic modulus $V_{\mathrm{HX}}^{\mathrm{mod}}$ and $V_{\mathrm{HX}}^{\mathrm{mod}}$ from the distance interferometer during the calibration with the coil-magnet system. On the right, the resulting dynamic displacement h_{dyn} for the distance interferometer. Errors in measurements and analysis result in fluctuations of the order of 1 %.

The arguments $V_{\mathrm{HX}}^{\mathrm{arg}}$ and $V_{\mathrm{HY}}^{\mathrm{arg}}$ of the dynamic components are equal to the phase φ_{H} of the dynamic displacement, except that they present jumps of amplitude $\pm\pi$. These jumps can be removed by unwrapping the signals. However, measurements are significantly noisier around the jumps, because it corresponds to the operation point where the sensitivity of a given channel is zero: $\sin\left(\frac{4\pi}{\lambda} h_{\mathrm{stat}}\right) = 0$ for HX and $\cos\left(\frac{4\pi}{\lambda} h_{\mathrm{stat}} + \psi_{\mathrm{H}}\right) = 0$ for HY. We build

a combined phase signal which does not present this imperfection, by periodically switching from one channel to the other. The phase φ_H is then known modulo π (Figure 3.19).

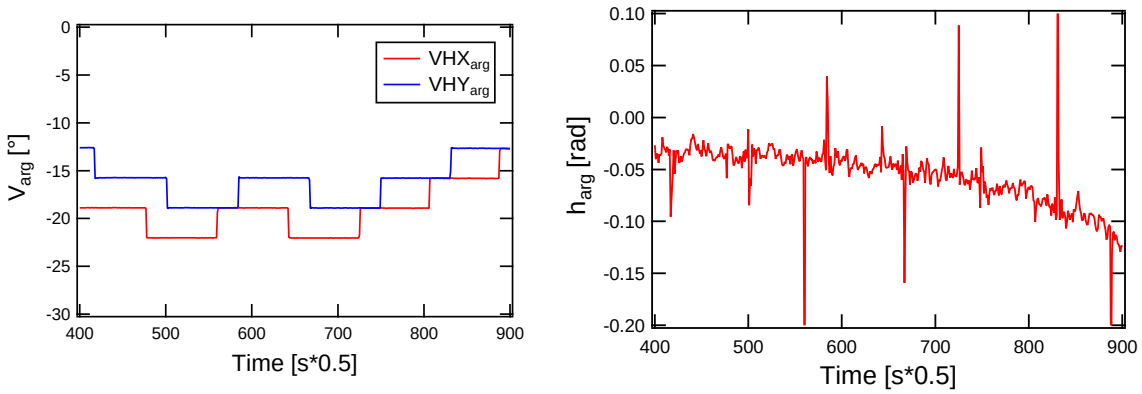

Figure 3.20 On the left, the dynamic arguments V_{HX}^{arg} and V_{HX}^{arg} from the distance interferometer during the calibration with the coil-magnet system. On the right, the resulting phase of the dynamic phase h_{arg} for the distance interferometer.

3.2.3 Extension to the non-linear regime

The linear analysis presented in the previous section allows to work with small oscillation amplitudes, typically $h_{dyn} < 10$ nm. It can be useful to be able to quantitatively measure larger oscillation amplitudes. This is typically the case at large distances between the surfaces where the force is small: increasing the amplitude of the dynamic distance will proportionally increase the amplitude of the dynamic force, making it larger than the noise level. Thus an extension to the non-linear regime was needed for the distance interferometer, typically when $h_{dyn} \sim 30$ nm.

This required to install a current divider before each lock-in amplifier associated to the distance interferometer, in order to avoid its saturation. The current divider was built with two resistors in parallel, 1 kΩ and 10 kΩ, dividing the voltage by 11.

In the same vein of the calculation done in section 3.2.1, we have developed the expression of the instantaneous total current $I_{HX_2^1}$ to the third order in $4\pi h_{dyn}/\lambda$. Here we will not write these calculations, but simply summarize the results.

The first effect of non-linearity of the detector is to reduce the moduli of the dynamic contrast V_{HX}^{mod} and V_{HY}^{mod} by a factor $(1 - \alpha h_{dyn}^2)$ with $\alpha = 2\pi^2/\lambda = 4.9.10^{-5}$ nm^{-2}. As a result, the apparent dynamic amplitude $h_{dyn,\ app}$ that is obtained with the linear analysis is smaller than the true dynamic amplitude h_{dyn}:

$$h_{dyn,\ app} = h_{dyn} - \alpha h_{dyn}^3 \tag{3.38}$$

The second effect of non-linearity of the detector is to reduce the amplitudes of the quasi-static contrast $V_{\mathrm{HX}}^{\mathrm{stat}}$ and $V_{\mathrm{HY}}^{\mathrm{stat}}$ by a factor $(1-\beta h_{\mathrm{dyn}}^2)$ with $\beta = 2\alpha = 4\pi^2/\lambda = 9.8.10^{-5}$ nm^2. The apparent quasi-static amplitudes $V_{\mathrm{HX,\ app}}^{\mathrm{amp}}$ and $V_{\mathrm{HY,\ app}}^{\mathrm{amp}}$ are smaller than the amplitudes $V_{\mathrm{HX}}^{\mathrm{amp}}$ and $V_{\mathrm{HY}}^{\mathrm{amp}}$ calibrated in the linear regime:

$$V_{\mathrm{HX,\ app}}^{\mathrm{amp}} = V_{\mathrm{HX}}^{\mathrm{amp}}(1-\beta h_{\mathrm{dyn}}^2) \tag{3.39}$$

$$V_{\mathrm{HY,\ app}}^{\mathrm{amp}} = V_{\mathrm{HY}}^{\mathrm{amp}}(1-\beta h_{\mathrm{dyn}}^2) \tag{3.40}$$

As a result, the quasi-static signals follow an ellipse of smaller semi axes, and the apparent quasi-static amplitude $h_{\mathrm{stat,\ app}}$ that is obtained with the linear analysis is not equal to the true quasi-static amplitude h_{stat}.

Taking these corrections into account in the analysis is not straightforward, because the quasi-static and dynamic signals are mixed. Indeed, first we need to know the true dynamic amplitude h_{dyn} to correct for the reduction of the quasi-static amplitudes $V_{\mathrm{HX,\ app}}^{\mathrm{amp}}$ and $V_{\mathrm{HY,\ app}}^{\mathrm{amp}}$, then to deduce the true quasi-static amplitude h_{stat} and the apparent dynamic amplitude $h_{\mathrm{dyn,\ app}}$, then to get the true dynamic amplitude h_{dyn}. Therefore we proceed perturbatively:

- first we perform the linear analysis (i.e., we suppose $\alpha = \beta = 0$) to get estimates $h_{\mathrm{stat,0}}$ and $h_{\mathrm{dyn,0}}$,
- secondly we give back their standard values to α and β, use $h_{\mathrm{dyn,0}}$ in the right-hand sides of equations 3.38, 3.39 and 3.40, and follow the whole analysis to obtain better estimates $h_{\mathrm{stat,1}}$ and $h_{\mathrm{dyn,1}}$,
- then we iterate the previous step as many times as necessary.

Empirically, we estimated that $N \sim 2$ iterations are enough for the values of $h_{\mathrm{stat,N}}$ and $h_{\mathrm{dyn,N}}$ to converge within 1%.

In practice, we find that the theoretical values of α and β do not provide a quantitative correction for the non-linearities. Instead, their values are manually adjusted for each experiment. β is determined by plotting the corrected quasi-static $V_{\mathrm{HY,\ co}}^{\mathrm{stat}} = V_{\mathrm{HY,\ app}}^{\mathrm{amp}}/(1-\beta h_{\mathrm{dyn}}^2)$ versus $V_{\mathrm{HX,\ co}}^{\mathrm{stat}} = V_{\mathrm{HX,\ app}}^{\mathrm{amp}}/(1-\beta h_{\mathrm{dyn}}^2)$, and making that all the data from the experiment collapse on the same ellipse (Figure 3.21). α is fixed by ensuring that the true dynamic amplitude h_{dyn} varies proportionally with the dynamic voltage applied to the piezo actuator. A wrong value for α also reflects in a ratio $l_{\mathrm{dyn}}/h_{\mathrm{dyn}}$ which presents a jump when changing h_{dyn} in the non-linear range (Figure 3.22). The typical values of α and β coefficients at 32 Hz are 1.10^{-4} nm^{-2} and 2.10^{-4} nm^{-2} respectively, and can vary from 50% to 200% with the chosen frequency.

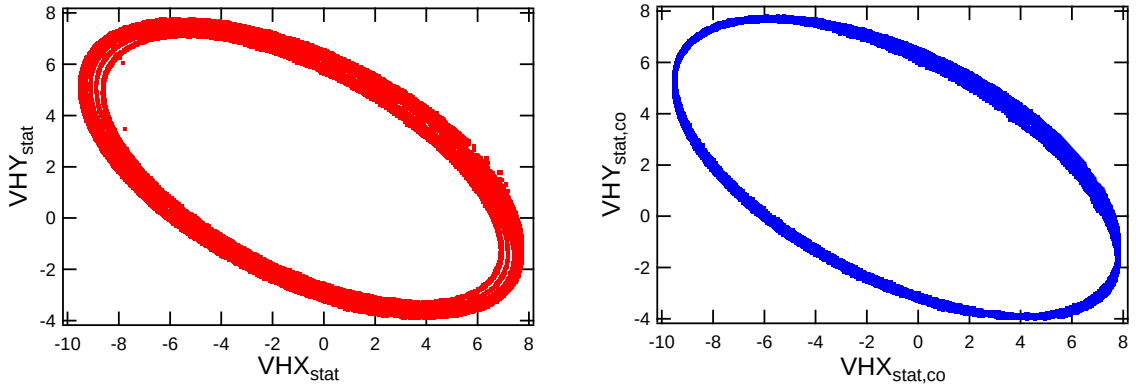

Figure 3.21 On the left, the ellipse formed by the apparent amplitudes of $V^{\mathrm{stat}}_{\mathrm{HY,\ app}}$ as a function of $V^{\mathrm{stat}}_{\mathrm{HX,\ app}}$ for the distance interferometer during an experiment. On the right, the resulting ellipse after correction of the quasi-static amplitudes by the $(1 - \beta h^2_{\mathrm{dyn}})$ factor.

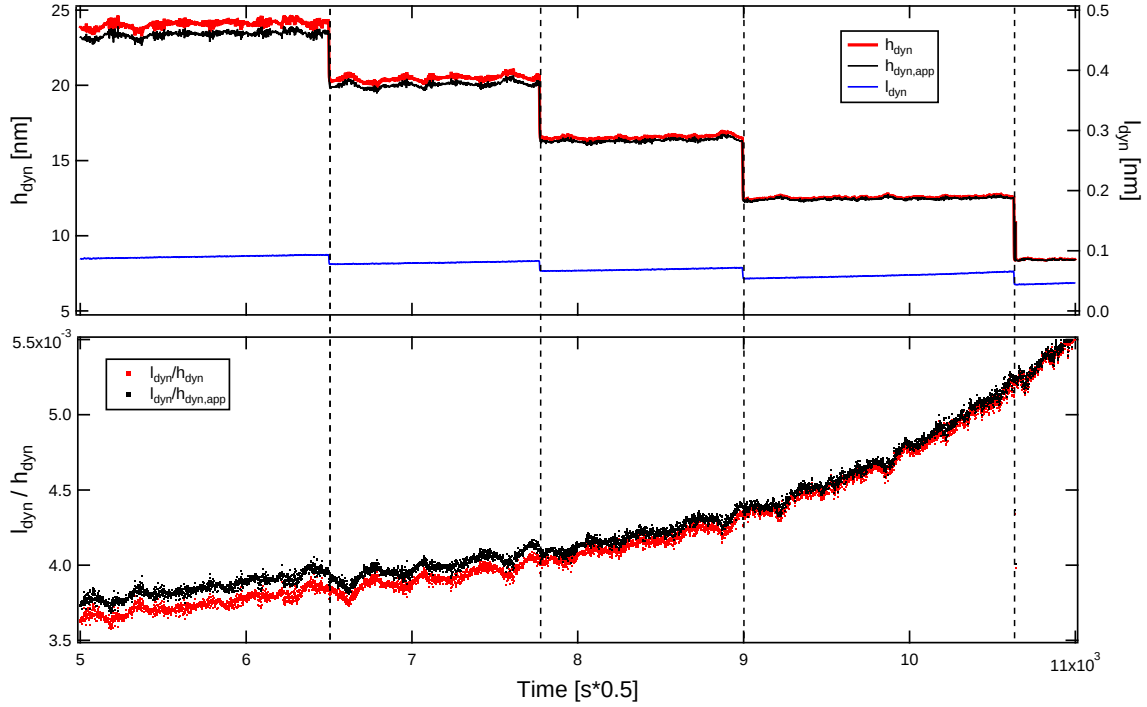

Figure 3.22 On the top graph, the measured h_{dyn} (and the apparent $h_{\mathrm{dyn,\ app}}$) dynamic amplitude of the distance interferometer according to the voltage applied to the piezo-electric actuator during an experiment (surface separation decreased from ~ 10 µm to ~ 1 µm). The measured dynamic force amplitude l_{dyn} is added on the right axis. On the bottom graph, the ratio of force and distance dynamic amplitudes (h_{dyn} and $h_{\mathrm{dyn,\ app}}$) is plotted for the same time interval.

3.2.4 Deduction of Mechanical Quantities

Relation between Force and Deflection

The force interferometer allows to measure the total deflection of the flexure hinge. In the framework of linear response, it is composed of a quasi-static component plus a dynamic component:

$$L_{\text{tot}} = l_{\text{stat}} + l_{\text{dyn}} \cos(\omega t + \varphi_{\text{L}}) \tag{3.41}$$

The force exerted on the flexure hinge is deduced from the deflection:

$$\begin{aligned} F_{\text{tot}} &= f_{\text{stat}} + f_{\text{dyn}} \cos(\omega t + \varphi_{\text{F}}) && (3.42)\\ &= K l_{\text{stat}} + |G(\omega)|\, l_{\text{dyn}} \cos\left(\omega t + \arg(G(\omega)) + \varphi_{\text{L}}\right) && (3.43) \end{aligned}$$

where K is the static stiffness and $G^{-1}(\omega)$ is the complex transfer function of the flexure hinge.

The flexure hinge's free extremity is modeled as an harmonic oscillator, presenting an effective mass M, a stiffness K and viscous damping coefficient C. The flexure hinge is driven by a force F, and its deflection L obeys Newton second law: $M\ddot{L} = -C\dot{L} - KL + F$, where $\dot{L}$ and $\ddot{L}$ correspond to the velocity and acceleration respectively. Using complex formalism $F^\star = f_{\text{dyn}} \exp(j(\omega t + \varphi_{\text{F}}))$, $L^\star = l_{\text{dyn}} \exp(j(\omega t + \varphi_{\text{L}}))$, one can show that:

$$[K - M\omega^2 + j\omega C]L^\star = F^\star \tag{3.44}$$

The complex transfer function is deduced as:

$$\begin{aligned} G^{-1}(\omega) &\equiv \frac{L^\star}{F^\star} = \frac{1/K}{1 - (\omega/\omega_0)^2 + j(\omega/\omega_0)/Q} && (3.45)\\ \left|G^{-1}(\omega)\right| &\equiv \frac{l_{\text{dyn}}}{f_{\text{dyn}}} = \frac{1/K}{\sqrt{(1 - (\omega/\omega_0)^2)^2 + ((\omega/\omega_0)/Q)^2}} && (3.46)\\ \arg(\mathrm{G}^{-1}(\omega)) &\equiv \varphi_{\text{L}} - \varphi_{\text{F}} && (3.47)\\ &= -\arctan\left(\frac{(\omega/\omega_0)/Q}{1 - (\omega/\omega_0)^2}\right) \text{ for } \omega < \omega_0, && (3.48)\\ &= -\arctan\left(\frac{(\omega/\omega_0)/Q}{1 - (\omega/\omega_0)^2}\right) - \pi \text{ for } \omega > \omega_0 && (3.49) \end{aligned}$$

where $\omega_0/2\pi = \sqrt{K/M}/2\pi$ is the resonance frequency and $Q = \sqrt{KM}/C$ is the quality factor.

Flexure Hinge Calibration

To characterize the mechanical response of the flexure hinge $G^{-1}(\omega)$, we perform a calibration while there is no liquid in between the planar and spherical surfaces. We set the flexure hinge into motion at a given frequency $f = \omega/2\pi$, by powering the coil-magnet system with an AC voltage u_{dyn} supplied by a lock-in amplifier. We include a resistance R in series with the coil in the circuit and we measure the dynamic voltage across the resistor with a lock-in amplifier (Figure 3.23). This voltage has the advantage to be proportional to the current flowing through the coil, which is proportional to the magnetic force exerted by the coil on the magnet, i.e., the force F acting on the flexure hinge.

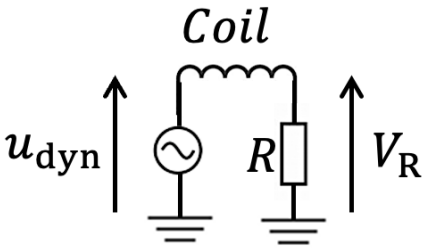

Figure 3.23 Schematic of the electronic assembly to perform the flexure hinge's calibration. The voltage u_{dyn} is applied by a lock-in amplifier and we measure the dynamic voltage V_{R} across the resistor, with another lock-in amplifier.

We simultaneously measure the dynamic deflection L of the flexure hinge thanks to two other lock-in amplifiers associated to the force interferometer. We then scan the frequency of the excitation from 10 Hz to 1 kHz, to get the complex transfer function $G^{-1}(\omega)$ to a multiplicative constant (see Figure 3.25). Because the modulus of the transfer function spans other about four orders of magnitude, several scans are actually performed:

- In the first scan, the frequency is swept from 10 Hz to 1 kHz with a large amplitude $u_{\text{dyn}} = 100$ mV_{RMS} and a small resistance $R = 100$ Ω, to induce a large excitation and so to reduce noise at high frequencies far from the resonance.
- In the second scan, the frequency is swept from $\sim$ 110 Hz to $\sim$ 120 Hz with a small amplitude $u_{\text{dyn}} = 20$ mV_{RMS} and a large resistance $R = 10$ kΩ, to induce a small excitation and so to avoid saturation of the deflection measurement very close to the resonance.
- In the third scan, the frequency is swept from $\sim$ 60 Hz to $\sim$ 160 Hz with a large amplitude $u_{\text{dyn}} = 100$ mV_{RMS} and a large resistance $R = 10$ kΩ, for frequencies moderately far away from the resonance.

The complex transfer function is fitted as follow: first the phase in Figure 3.24 is fitted with equation 3.49, because it depends only on two fitting parameters (versus three for

the modulus) and it is very sensitive to the quality factor around the resonance. This sets the resonance frequency and the quality factor, to respectively $f_0 = 116.25 \pm 0.05$ Hz and $Q = 450 \pm 50$. Secondly, the modulus shown in Figure 3.25, is fitted with equation 3.46, to check if a good agreement is achieved. But this does not allow to access the stiffness, because the transfer function is only known at a multiplicative constant.

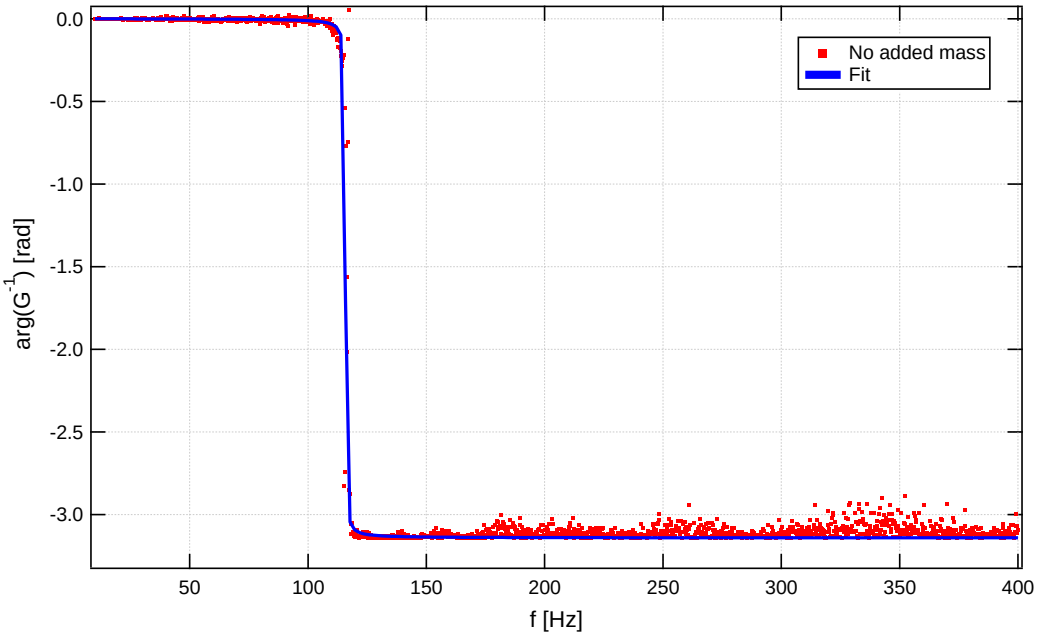

Figure 3.24 Flexure hinge's transfer function argument for no added mass and its corresponding fit.

The stiffness is calibrated thanks to the added mass method. It consists in measuring the resonance frequency while adding masses at the end of the flexure hinge. Indeed, the resonance frequency is equal to $f_0 = \sqrt{K/M}/2\pi$, and is expected to decrease with the total effective mass $M = m + \Delta m$, with m the initial mass (flexure hinge plus the sphere) and Δm the added mass. As shown in Figure 3.26, we observe such a shift of the resonance, that we can fit to extract the resonance frequency for different added masses. Because ${f_0}^{-2} = 4\pi^2(m + \Delta m)/K$, it is convenient to plot the inverse of the squared of the resonance frequency ${f_0}^{-2}$ as a function of the added mass Δm (Figure 3.27), and to perform a linear fit to obtain the stiffness of $K = 5567 \pm 85$ N/m (and the initial mass $m = 10.44 \pm 0.16$ g).

Calculation of the mechanical impedance and admittance

The complex mechanical impedance is given by:

$$Z = Z' + jZ'' = \frac{|G(\omega)|\, l_{\text{dyn}}}{h_{\text{dyn}}} \times \exp\left[j\left(\arg\left(G(\omega)\right) + \varphi_{\text{L}} - \varphi_{\text{H}}\ (+\pi)\right)\right] \tag{3.50}$$

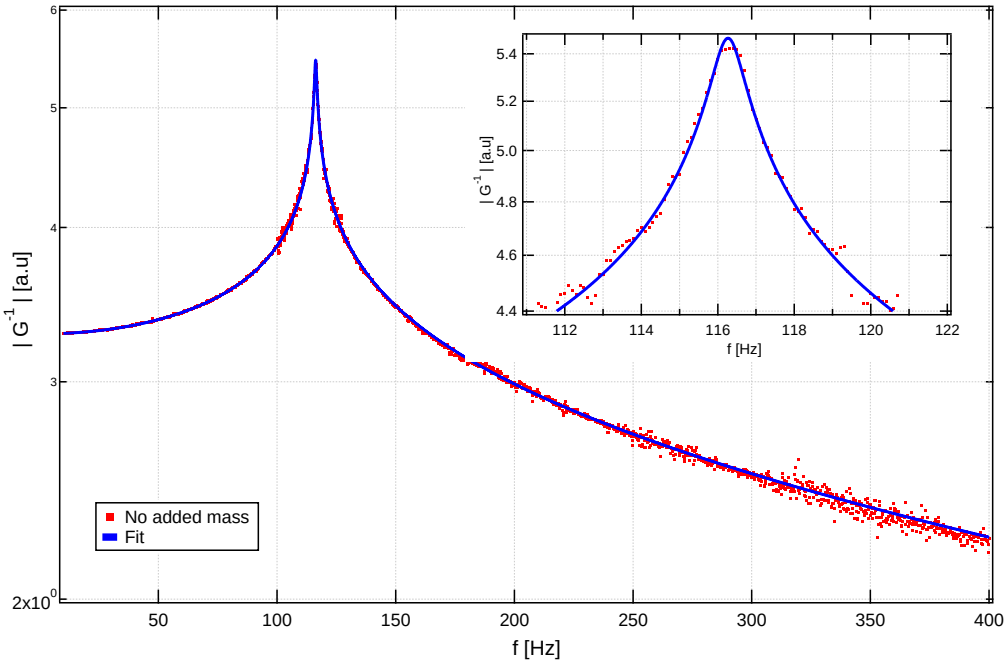

Figure 3.25 Flexure hinge's transfer function modulus for no added mass and its corresponding fit. Inset zooms on the peak of the resonance around 116.25 ±0.05 Hz.

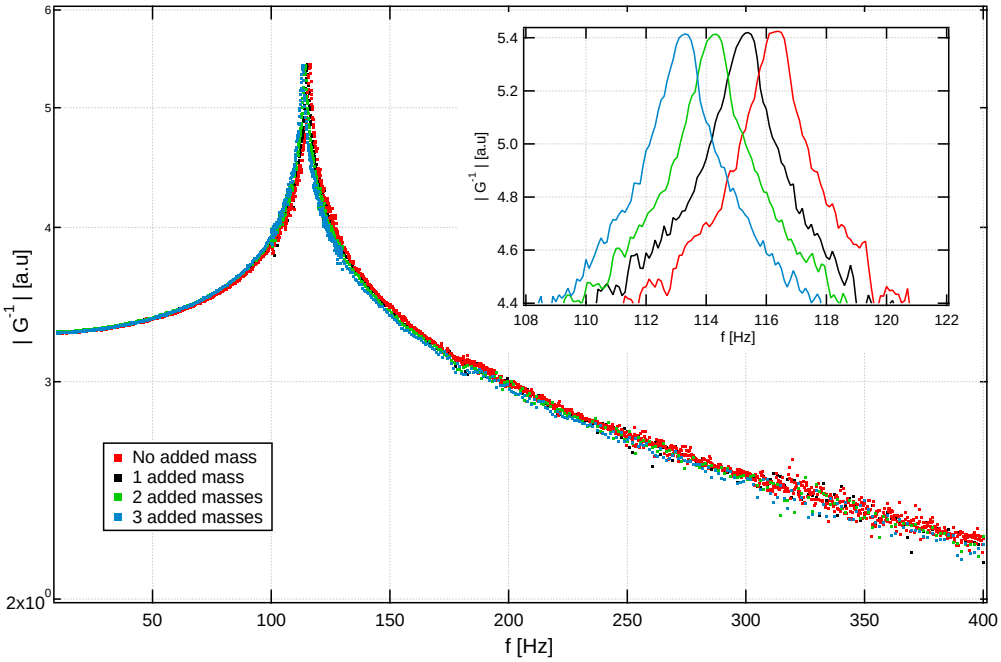

Figure 3.26 Flexure hinge's transfer function for no added mass and for one, two and three added masses, as a function of frequency. Inset zooms on the peaks of the resonance for each curve.

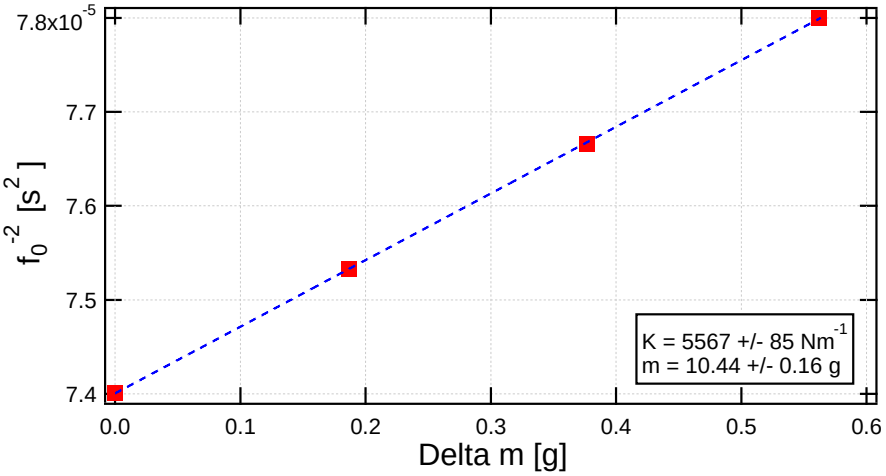

Figure 3.27 Inverse of the squared of the flexure hinge's resonance frequency, as a function of the added mass. The slope gives access to the stiffness of the flexure hinge and its initial mass.

where the term π is added or not to get $Z'' > 0$, because φ_{H} and φ_{L} are known modulo π. Then, the complex mechanical admittance is defined as:

$$Y = Y' + jY'' = \frac{1}{Z} \tag{3.51}$$

3.3 Consequences of the modifications made during the thesis

Now that I have explained how the dSFA works in its final state, I will go back to the changes I made to the set-up during my thesis: the motivations that drove these changes, the improvements generated, the difficulties encountered and how I overcame them.

3.3.1 Mechanical Aspects

As previously mentioned, a passive anti-vibration table with a 0.5 Hz horizontal and vertical low-pass frequency is used to isolate the dSFA from the mechanical vibrations transmitted through the ground. Since a vacuum chamber was added for atmospheric and thermal control, and the interferometer was rebuilt to adapt to the new environment, one of the consequences was that the load and the gravity center of the set-up were modified. To correct this, new weight loads were replaced on the anti-vibration table allowing it to work in its optimal range. Additionally, some measurements were performed to characterize the mechanics of the set-up in the new surrounding conditions.

Noise Spectrum

The amplitudes of the signals on both interferometers were measured while scanning the frequency from 10 Hz to 1 kHz with no voltage applied to the piezo, using lock-in amplifiers with an integration time of 300 ms like in a normal experiment. This provided the dynamic noise levels for the distance and force dynamic measurements, $h_{\text{dyn, noise}}$ and $l_{\text{dyn, noise}}$ respectively. Figure 3.28 allows us to compare the noise levels of the current state of the dSFA with the noise level from the previous version of the machine.

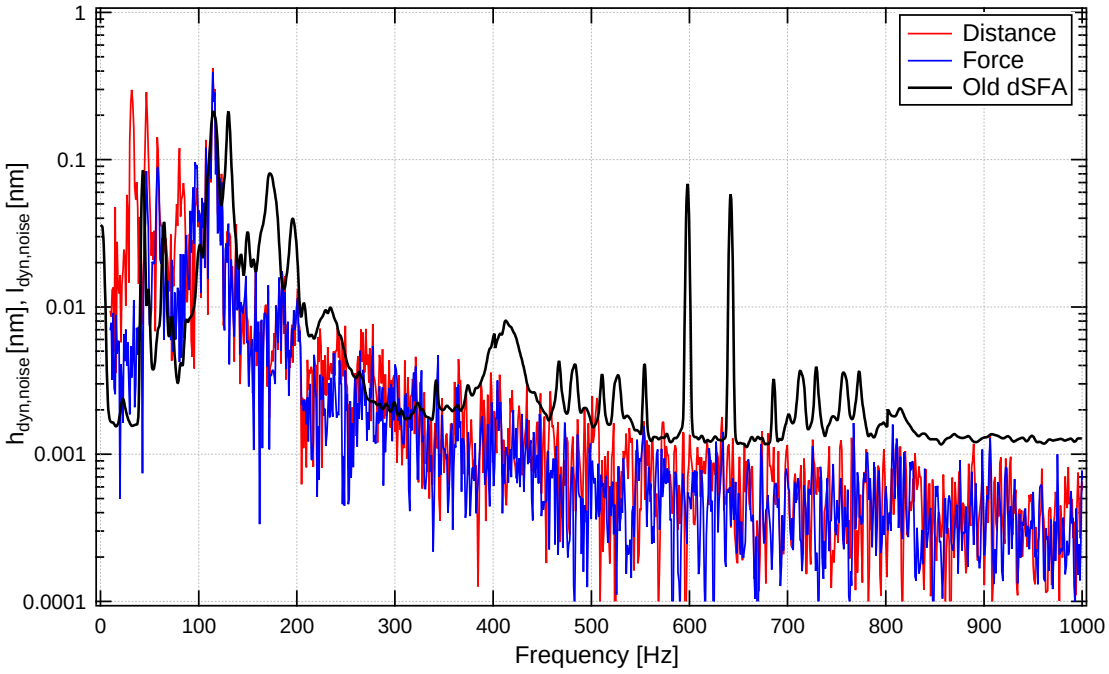

Figure 3.28 Amplitude of the noise spectrum for the distance and force interferometers in the current state of the dSFA, compared to the noise level of the previous version of the machine.

We observe an improvement for frequencies above the flexure hinge's resonance frequency ($f > f_0$) and on the contrary, higher noise levels below the resonance ($f < f_0$). We will describe later how we dealt with this noise in experiments.

Mechanical Cross-talk

Other measurements were performed with lock-in amplifiers by imposing a sinusoidal oscillation with defined amplitude onto the piezo-actuator, and measuring the magnitude of the response of each interferometer for a broad frequency spectrum, with a integration time of 300 ms (same as the acquisition time in our experiments).

Figure 3.29 shows the amplitude of the distance interferometer's response for excitation amplitudes of 20 mV and 100 mV, as well as the case for no excitation applied to the

piezo (dynamic noise level already shown previously). We observe that the interferometric measurement response is proportional to the excitation applied and typically 100 times above the noise level for the chosen amplitudes. The frequency dependence corresponds to the spectral response of the piezo-electric actuator.

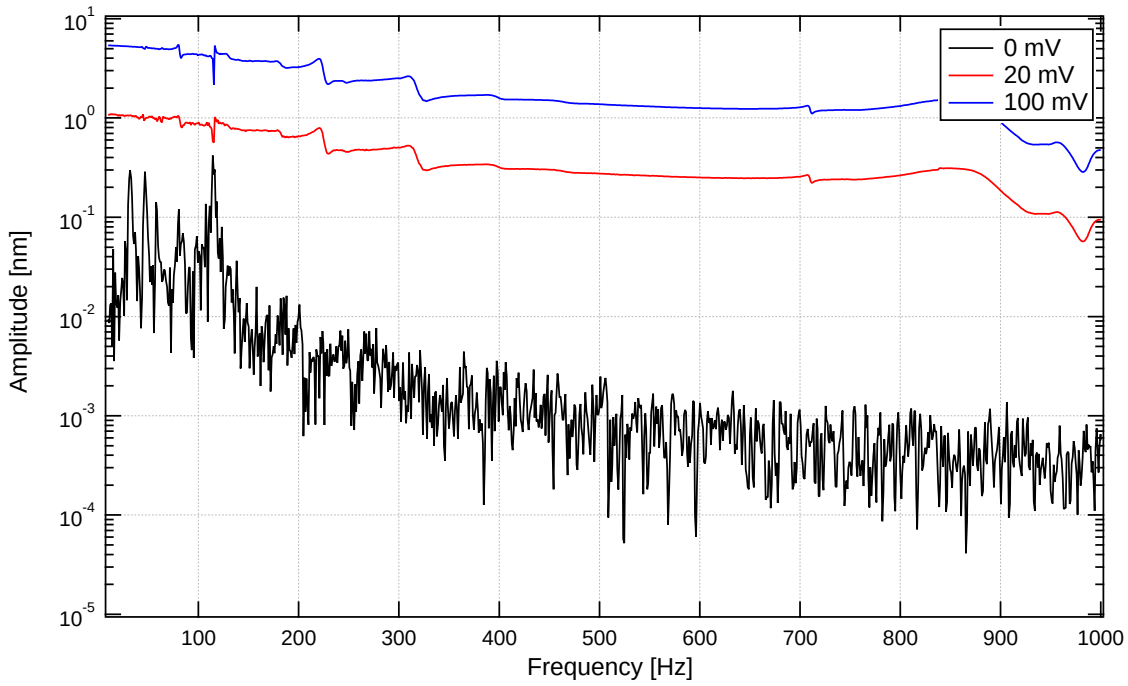

Figure 3.29 Magnitude of the distance interferometer response for oscillation amplitudes of 0 mV (no excitation), 20 mV and 100 mV applied to the piezo-electric actuator.

Figure 3.30 shows the amplitude of the force interferometer's response for excitation amplitudes of 0 mV, 20 mV and 100 mV imposed to the piezo actuator. During the measurements, we expected to measure only a response from the distance interferometer, related to the difference of distance between the mirror on the static flexure hinge and the one on the oscillating piezo. The surfaces are far from each other with no liquid in between, so ideally the dynamic force should have been zero. However, we observe in practice that this is not the case, for reasons that depend on the range of frequencies considered. As Figure 3.30 shows, below the resonance frequency, the response obtained is independent of the amplitude of the oscillation applied on the surfaces, and is equal to the noise level. Above the resonance frequency on the contrary, the force response is proportional to the amplitude of the oscillation applied on the piezo, with a magnitude significantly larger than the noise level. This implies the existence of an unwanted mechanical cross-talk between the distance and force measurements, suggesting that a part of the oscillation applied to one surface by the piezo-actuator is transmitted to the other surface by the dSFA frame or its surroundings. It is important to clarify that we made sure there was no optical cross-talk

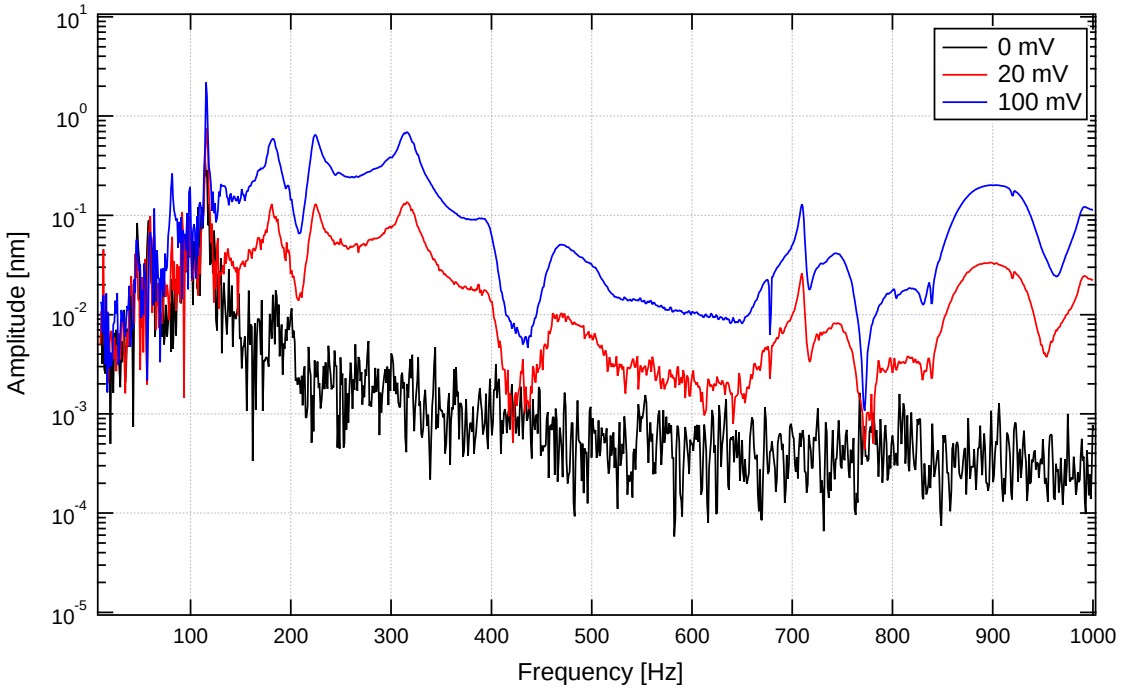

Figure 3.30 Magnitude of the force interferometer response for oscillation amplitudes of 0 mV (no excitation), 20 mV and 100 mV applied to the piezo-electric actuator.

between interferometric channels prior to performing the measurements (optical cross-talk is explained later in section 3.3.2). The mechanical cross-talk is confirmed in Figure 3.31, where the ratio $l_{\text{dyn, cross-talk}}/h_{\text{dyn}}$ between the force and distance interferometers is plotted for each excitation amplitude applied. A superposition of curves is observed above the resonance frequency, proving the proportionality between the magnitude responses in both interferometers.

We built a simple model for this mechanical cross-talk, supposing that the oscillation of the piezo actuator is partially transmitted to the (not perfectly) fixed mirror by an amplitude $x_{\text{fixed}} = \epsilon h_{\text{dyn}} \cos(\omega t)$. Similarly than for the calibration of the flexure hinge (section 3.2.4), we model the flexure hinge's free extremity and the mirror attached on it (at coordinate x_{hinge}) as an harmonic oscillator of effective mass M, stiffness K and damping coefficient C. Its equation of motion reads $M\ddot{x_{\text{hinge}}} = -C\dot{x_{\text{hinge}}} - K(x_{\text{hinge}} - x_{\text{fixed}})$. Using complex formalism $x_{\text{fixed}} = \epsilon h_{\text{dyn}} \exp(j\omega t)$, $x_{\text{hinge}} = x \exp(j(\omega t + \varphi))$, one can show that:

$$[K - M\omega^2 + j\omega C]x_{\text{hinge}} = x_{\text{fixed}} \tag{3.52}$$

We simply deduce:

$$x_{\text{hinge}} = \left[\frac{1}{1 - (\omega/\omega_0)^2 + j(\omega/\omega_0)/Q}\right] x_{\text{fixed}} \tag{3.53}$$

with $\omega_0/2\pi = \sqrt{K/M}/2\pi$ the resonance frequency and $Q = \sqrt{KM}/C$ the quality factor.

The force interferometer is sensitive to the difference of positions between the mirrors attached to the flexure hinge and to the (non perfectly) fixed frame, respectively:

$$x_{\text{hinge}} - x_{\text{fixed}} = \left[\frac{(\omega/\omega_0)^2 - j(\omega/\omega_0)/Q}{1 - (\omega/\omega_0)^2 + j(\omega/\omega_0)/Q}\right] x_{\text{fixed}} \tag{3.54}$$

The mechanical cross-talk finally reads:

$$l_{\text{dyn, cross-talk}}/h_{\text{dyn}} \equiv \frac{|x_{\text{hinge}} - x_{\text{fixed}}|}{h_{\text{dyn}}} = \epsilon\sqrt{\frac{(\omega/\omega_0)^4 + ((\omega/\omega_0)/Q)^2}{((1 - (\omega/\omega_0)^2)^2 + (\omega/\omega_0)/Q)^2}} \tag{3.55}$$

As shown as a dashed line in Figure 3.31, this simple model captures well the fact the mechanical cross-talk shows up above the resonance frequency. Qualitatively, this is because the flexure hinge acts a low-pass mechanical filter:

- At low frequencies, the mirror on the flexure hinge's extremity moves like the fixed mirror at $\epsilon h_{\text{dyn}} \cos(\omega t)$, leading to a constant distance between the mirrors and to no mechanical cross-talk observed.
- At high frequencies, the mirror on the flexure hinge's extremity does not move while the fixed mirror moves at $\epsilon h_{\text{dyn}} \cos(\omega t)$, leading to a oscillating distance between the mirrors and to a finite mechanical cross-talk.

Above the resonance, the model predicts a plateau of amplitude $\epsilon = 0.01$, whereas the data exhibit maxima and minima. This is probably because the partial transmission of the piezo oscillation by the dSFA frame or its surroundings depend on the resonance modes of the set-up, and so depends on the frequency.

We suspected the origin of the mechanical cross-talk to be the vacuum chamber, caused by the deformation of its bottom plate. Since the vacuum chamber has a hydraulic circuit passing through its walls, we believe the bottom plate might be composed by two thin metal layers, one above (internal face) and one below (external face) the hydraulic circuit, in a sandwich-like manner. Several solutions were tested, such as tightening up the bottom plate with a support rod below, or a thick plate attached above, or adding a layer of sand between the bottom plate and the dSFA's heart to damp the mechanical transmission, but no major improvement was observed.

Practical aspects to perform experiments

In order to choose the work frequencies, I systematically performed such noise and cross-talk measurements before every campaign of experiments when a new system (solid surfaces and liquid solution) was installed. To understand how the mechanical noise and cross-talk influence

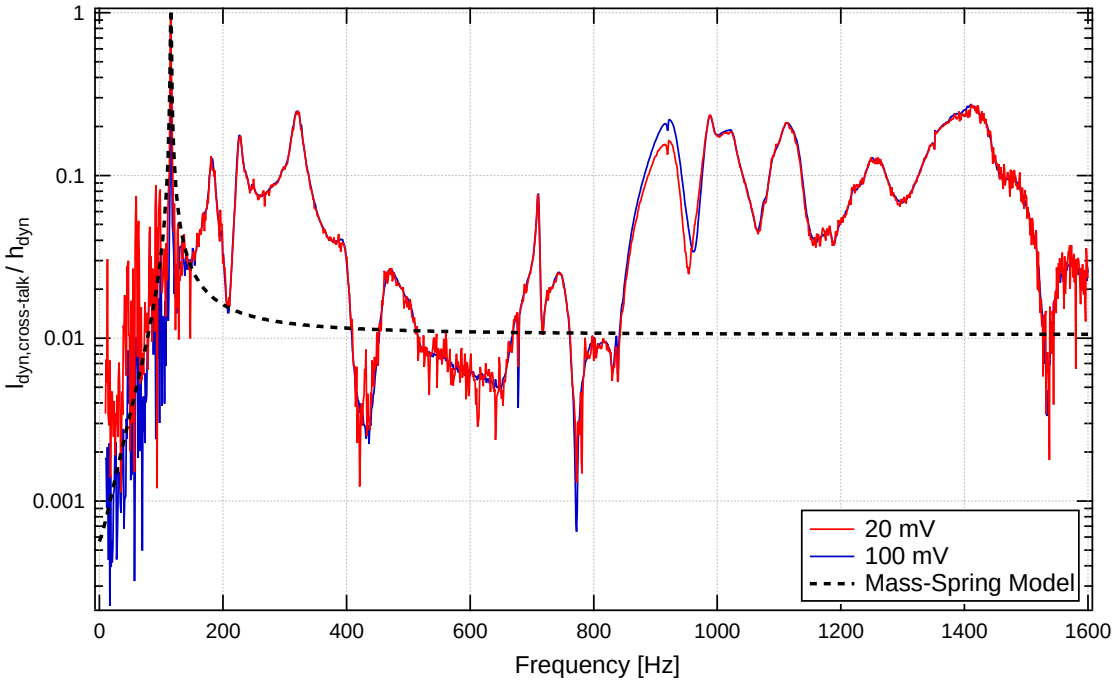

Figure 3.31 Ratio of Force and Distance interferometric responses, for different oscillations amplitudes applied onto the piezo-electric actuator. Theoretical curve given by the simple model describing the mechanical cross-talk, with $\epsilon = 0.01$.

our experiments, we must compare them with typical measurements. These imperfections show up when the physical force to measure is small. This is typically the case at large separation distances, where the main force originates from viscous damping in the liquid gap (for a Newtonian fluid, no slip and rigid surfaces):

$$l_{\text{dyn, physical}} = \left|G^{-1}(\omega)\right| \times \frac{12\pi^2\eta R^2 f}{D} \times h_{\text{dyn}} \tag{3.56}$$

where $G^{-1}(\omega)$ is the flexure hinge's complex transfer function, η the liquid viscosity (taken as 1 mPa.s in the following), R the sphere radius (taken as 3 mm in the following), f the excitation frequency and D the separation distance.

Below the resonance, the physical signal $l_{\text{dyn, physical}}$ has to be compared with the noise level $l_{\text{dyn, noise}}$. As observed in the red curve in Figure 3.32, the physical signal would be *drowned* by noise if we oscillated at $h_{\text{dyn}} = 1$ nm at large distance $D \sim 10$ µm. It is essential then to oscillate at large amplitudes, hence the interest of extending the operation of the distance interferometer in the non-linear regime. As shown as the blue curve, oscillating at $h_{\text{dyn}} = 30$ nm results in a physical signal about 15 times higher than the noise level. Because the physical force increases when approaching the surfaces, the linear regime of excitation $h_{\text{dyn}} = 1$ nm becomes enough for distances smaller than $D \sim 1$ µm (see the green curve). In

addition, work frequencies are chosen where the noise level is at the lowest, typically 30 Hz and 75 Hz.

Above the resonance, the physical signal has to be compared with the mechanical cross-talk. Because these two quantities increase proportionally with the excitation amplitude h_{dyn}, one has to compare the ratios $l_{\mathrm{dyn,\ physical}}/h_{\mathrm{dyn}}$ and $l_{\mathrm{dyn,\ cross-talk}}/h_{\mathrm{dyn}}$. In Figure 3.33, the physical signal is always lower than the mechanical cross-talk at large distance $D \sim 10$ µm (see the red curve). They start to be of the same order of magnitude at distance $D \sim 1$ µm (see the green curve). Work frequencies are chosen where the mechanical cross-talk is the smallest, around 210 Hz, 430 Hz and 770 Hz. During an experiement, i.e., when doing an approach at a fixed frequency, the finite mechanical cross-talk will manifest in the dynamic force as an constant contribution added to the physical signal. It will be deleted with the residual during the data analysis (as explained in the next chapter).

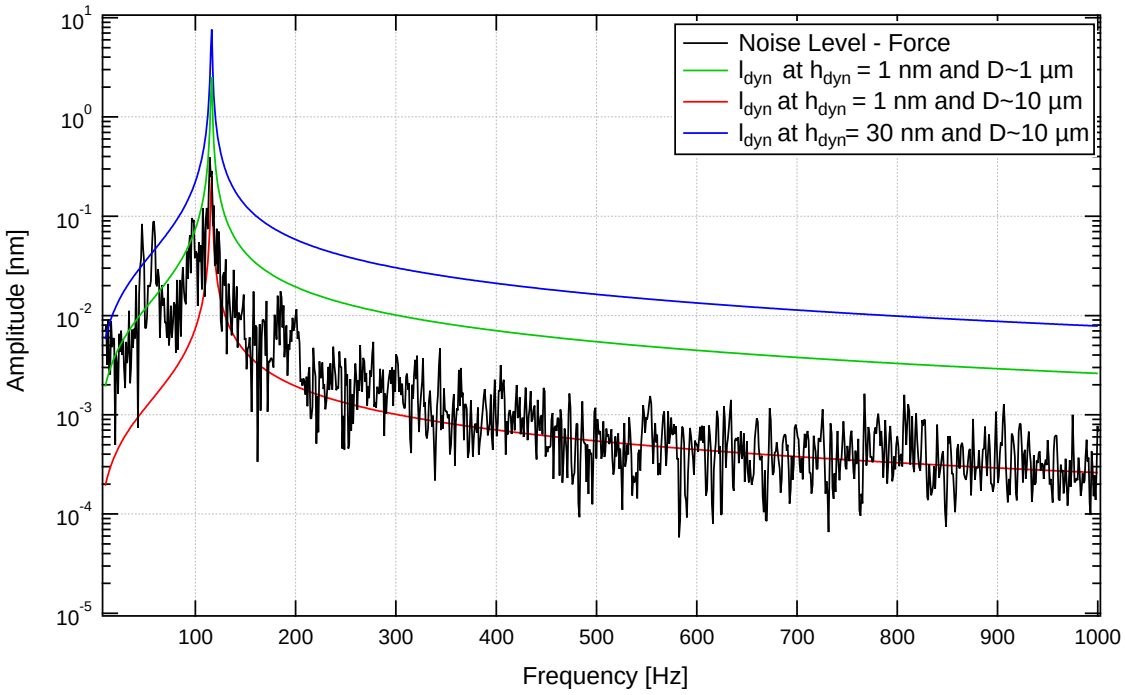

Figure 3.32 Comparison of the noise level with the dynamic force originating for viscous damping in the liquid gap, for different oscillation amplitudes h_{dyn} and separation distances D.

3.3.2 Optical Aspects

Due to the changes made in the dSFA's environment (see section 3.1.5), a redesigned interferometer was built in order to adapt to the new conditions. Although assembled in a more compacted manner, it possesses several degrees of freedom for optical and mechanical adjusting. For instance, the previous possibility of small adjustments to create large angular

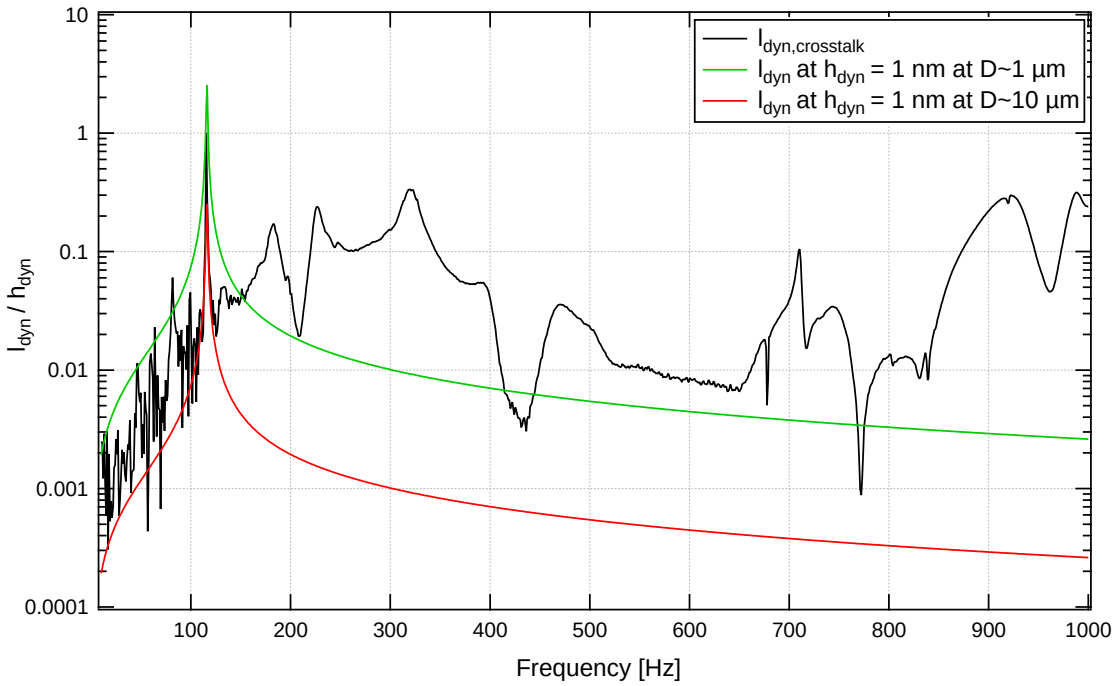

Figure 3.33 Comparison of the mechanical cross-talk with the dynamic impedance originating for viscous damping in the gap, for different separation distances D.

displacements (as in a lever arm) for optical tuning had become impractical, since the addition of the vacuum chamber decreased the available height inside the isolating box. In Figure 3.34, the old version of the SFA is presented, showing the heart of the machine next to the optical elements forming the old interferometer and surrounded by the isolating box.

Therefore, the new interferometer was built on one single level, reducing the occupied surface area by more than 70% compared to the old interferometer, and utilizing only 1/3 of the available volume inside the isolating box.

Previously, the force interferometer did not have a double optical path, meaning no quadrature-phase measurement, which was present only in the distance interferometer. The addition of the second optical path allowed to measure large amplitudes forces, such as those found when the surfaces are in contact.

Optical Crosstalk

We noticed that part of the information contained in one optical channel was being transferred to the other one (from the distance interferometer to the force one, or vice versa). This cross-talk was observed in the static and dynamic signals, and its amplitude was found to be independent of the oscillation frequency, in particular it was present even below the resonance frequency where the mechanical cross-talk is negligibly small (see section 3.3.1).

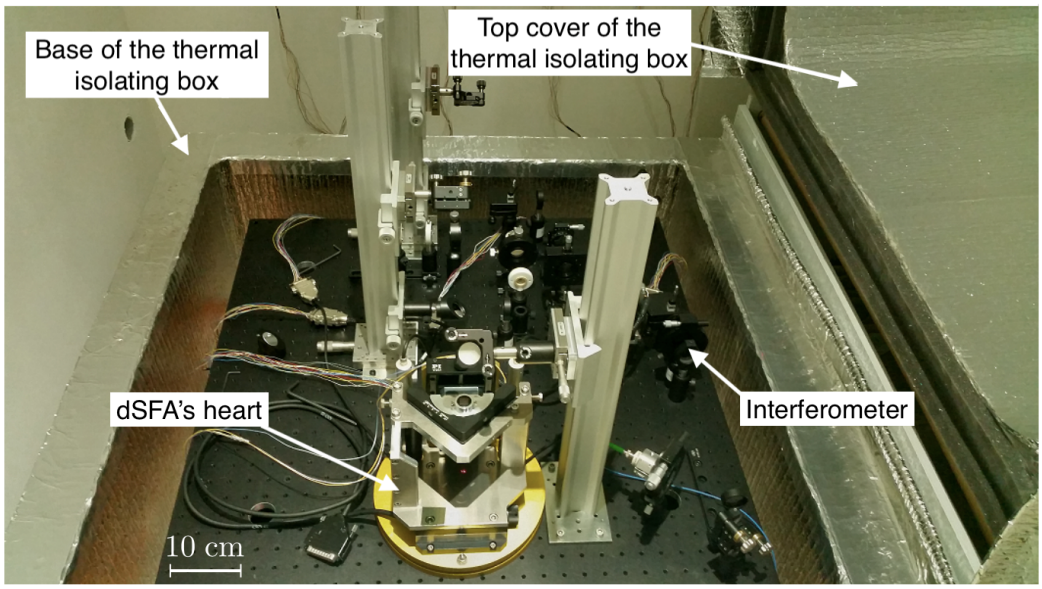

Figure 3.34 Photograph of the previous version of the dSFA. We can observe the dSFA's heart, the interferometer and the thermal isolating box. Image taken from [12], while text has been translated.

We characterized this artefact when no liquid is present between the surfaces and the surfaces are far from contact. The cross-talk from the distance interferometer to the force one was measured by imposing on the piezo-actuactor a quasi-static plus a sinusoidal motion (at a frequency below the resonance, typically 30 Hz and of large amplitude, typically 30 nm), and by looking at the force measurement (which should only exhibit random noise). On the left graph of Figure 3.35, we notice that the force dynamic modulus represents 0.1% of the displacement dynamic modulus. In the same way, on the right graph of Figure 3.35, we observe the phase in force signals changing with the phase of distance. The fact that this cross-talk exhibits oscillations in phase with the distance interferometer points towards an optical origin. Similarly, the cross-talk from the force interferometer to the distance one was measured by imposing on the coil-magnet system a quasi-static plus a sinusoidal motion (at a frequency below the resonance, typically 30 Hz and of large amplitude, typically 30 nm) while blocking the laser beam associated to the distance measurement before going to the dSFA's heart, and by looking at the distance signal (which should only exhibit random noise).

The source of this problem was difficult to identify, since such a pollution of the signals could be due to light beams of very small intensities compared to the main beam, and which are invisible to the eye. Finally, two causes for optical cross-talk were identified.

- *Parasite* light beams returned from the dSFA mirrors following the inverse optical path, arriving to the beam-splitter cube and polluting the opposite optical channel with

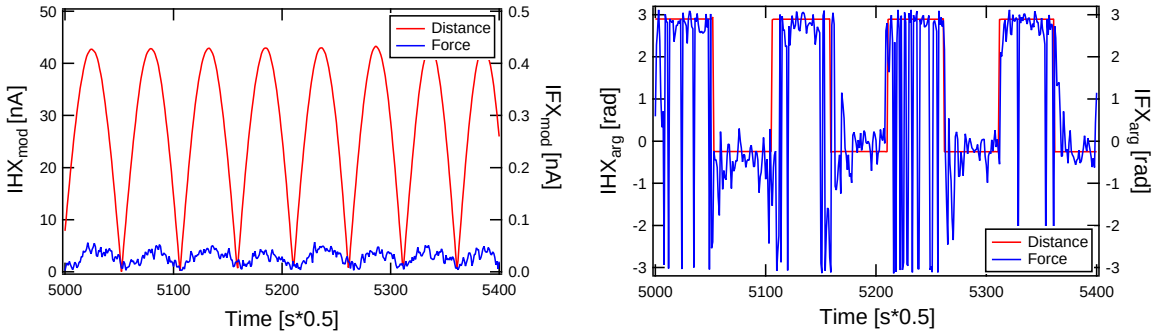

Figure 3.35 Optical cross-talk between channels in the interferometer, from distance onto force measurements on the X-analysis unit (also obtained from Y optical paths). On the left, the modulus of the raw dynamic signals, and on the right, the phase.

information that does not correspond to that interferometer (Figure 3.36). Hence, some modifications were set up to intercept this parasite light:

  - The optical path of the beam between the force and distance interferometers was increased.
  - The beam of the distance interferometer was tilted by a small angle.
  - A slit was added to block the parasite beams while keeping the beams of interest.

- The compact interferometer design, adapted to the new controlled environment, forced the light beams from the two channels to be parallel to each other and separated by 4 mm at almost all times. Supposing a Gaussian beam, the intensity of the tail of the beam (which is not perceived by human eye) decreases exponentially with the radial distance r as $I = I_0 \exp(-r^2/\sigma^2)$, where $\sigma \sim 1$ mm is the radius of the beam defined as the lateral distance over which the intensity is divided by e, the Euler number. A fraction $\epsilon = 0.1\%$ of the central intensity is reached at a distance $r = \sigma * \sqrt{-\ln(\epsilon)} \sim 2.6$ mm, meaning that 0.1% of the light is transferred between two beams separated by ~ 2.6 mm, which we found to be enough to induce the observed cross-talk. Since the critical spots for optical cross-talk were identified as the two right-angle prisms that deviate one beam and let the other one to pass straight forward before hitting the Wollaston prisms (see schematics on Figure 3.36), some changes were made into the interferometer:

  - The optical path of the beam on the distance interferometer has been maximized, allowing to impose the smallest possible angle on the path going down to the dSFA, but originating a larger tilt on the backward path, assuring a maximal separation of beams when reaching the prims.
  - Convergent lenses were added in order to reduce the size of beams when they reach the prisms.

– Prisms were mounted on manual translation plates, in order to catch the beam near its edge.

– Dark blocking elements were installed between the two interferometer beams, to absorb any light from the beam tails in between the two beams. They were mounted on manual translation plates, so as to let the beam pass close to its edge, while all the intermediate zone being absorbed by the blocking element.

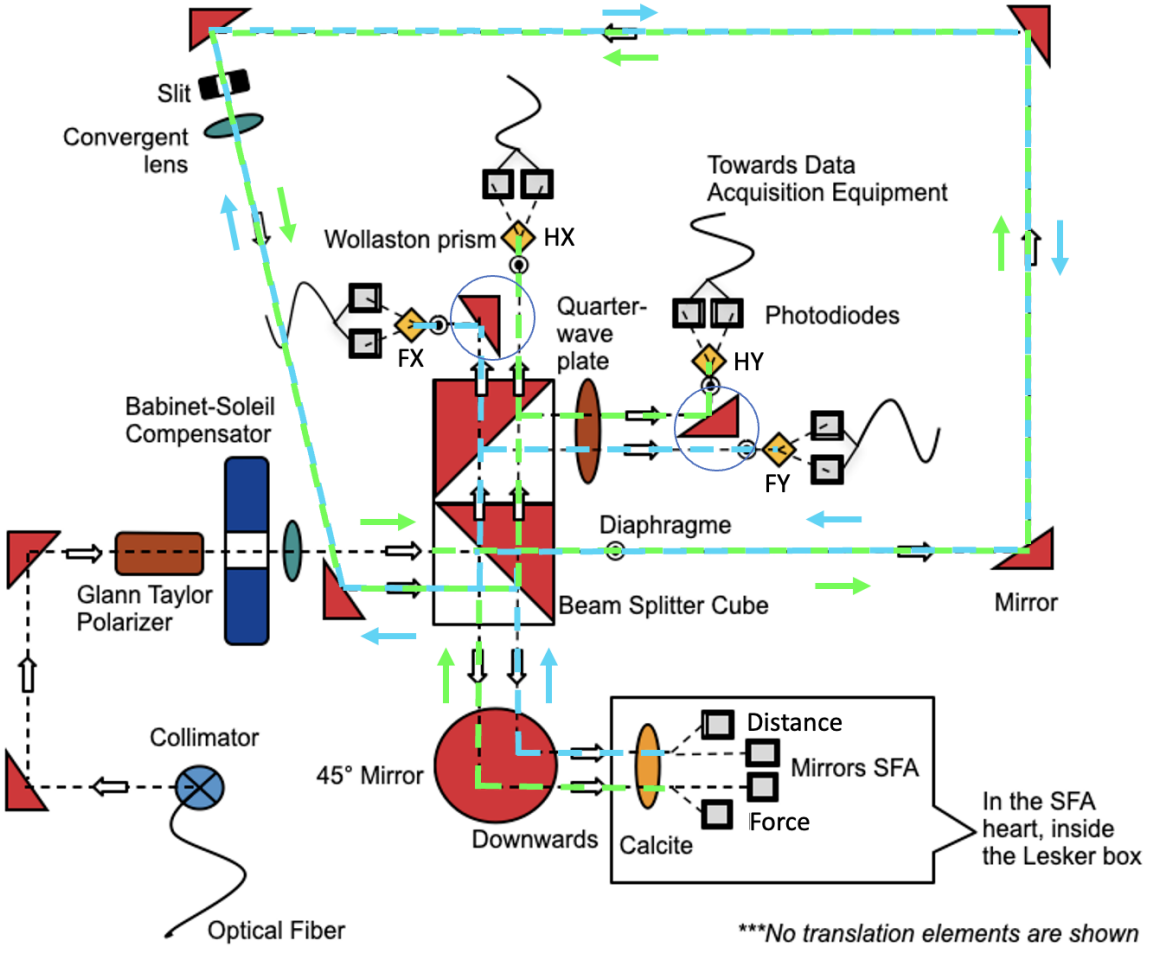

Figure 3.36 Schematic of the interferometer with the parasite beams that come backwards from the dSFA's heart and pollute the opposite optical path, creating optical cross-talk between sensors. The optical path in blue explains the cross-talk from distance to force interferometer, while the one in green explains the cross-talk from force to distance interferometer. The circles point to the sensible areas for optical cross-talk on the interferometer.

We observe in Figure 3.37 the modulus and phase of the dynamic signals after the modifications in the interferometer and the suppression of the optical cross-talk.

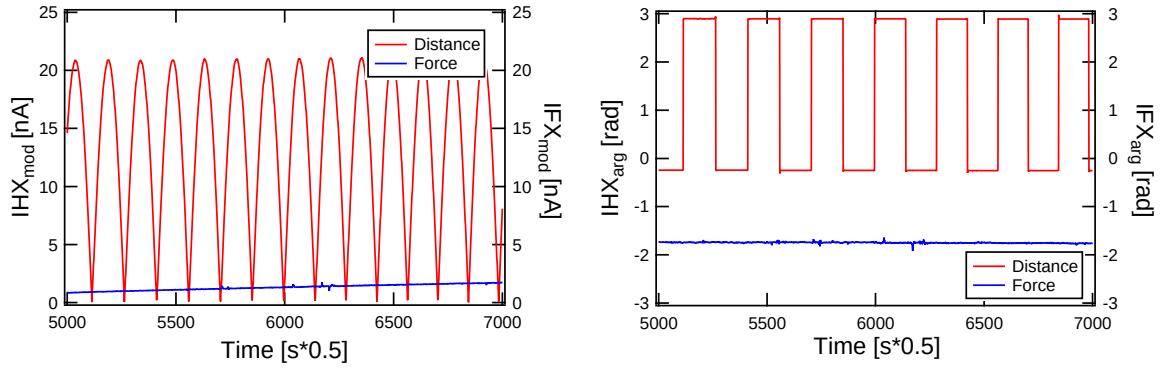

Figure 3.37 On the left the modulus, and on the right the phase signals after correction of the optical cross-talk. Red curves for the distance and blue curves for the force.

3.3.3 Electronic Aspects

In the previous version of the dSFA, electronic circuits made of several operational amplifiers were used to convert the photo-currents into normalized contrast quantities for each analysis unit. For example for HX:

$$V_{\mathrm{HX}} = K\frac{I_{\mathrm{HX1}} - V_{\mathrm{HX1}}}{I_{\mathrm{HX1}} + V_{\mathrm{HX1}}} \tag{3.57}$$

with $K = 10$ V a gain factor. These signals were simultaneously used in two different ways. First, the instantaneous contrasts were measured with precision multimeters to obtain quasi-static contrasts analogous to equation 3.14, to finally get the quasi-static displacements h_{stat}, l_{stat} (see details in [11], [12]). Secondly, the instantaneous and averaged contrasts were combined in another electronic circuit to compute a voltage equal to (for example for the distance interferometer):

$$\overline{V_{\mathrm{HX}}} \times V_{\mathrm{HY}} - V_{\mathrm{HX}} \times \overline{V_{\mathrm{HY}}} \tag{3.58}$$

with the bars stand for average values, providing a voltage whose dynamic component is in principle proportional to h_{dyn}. These signals were measured with lock-in amplifiers, to finally get the dynamic displacements h_{dyn}, l_{dyn} [11, 12].

Effects on the Quasi-Static Measurements

A first effect of this previous configuration comes from the fact that electronic calculations of normalized contrasts did not allow to correct for the imperfections present in the optical signals. In the previous version of the dSFA, the analysis of the quasi-static contrast supposed that the two signals of a given analysis unit are cosine functions of exact same amplitudes and in perfect phase opposition. We have shown in section 3.2.2 that it is not the case in

practice. This lead to a denominator of equation 3.57 which was not a constant (as in Figure 3.15) but presented a small sinusoidal oscillation (Figure 3.38).

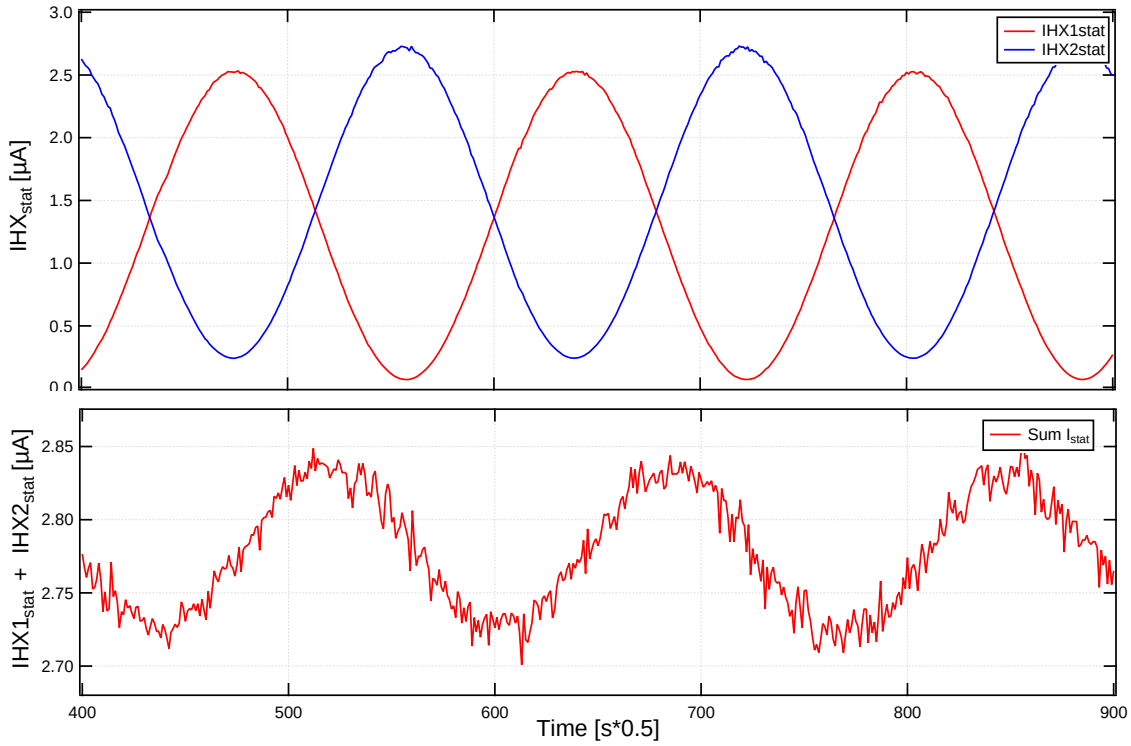

Figure 3.38 Current signals from photodiodes 1 and 2 of channel HX, and small sinusoidal oscillations observed when simply summing them, without correcting for their time lag and amplitude difference.

A direct consequence was that the variation of $V_{\mathrm{HY}}^{\mathrm{stat}}$ with $V_{\mathrm{HX}}^{\mathrm{stat}}$ did not follow a perfect ellipse. This could be seen by looking at the residuals associated to an elliptic fit during the quasi-static calibration, showing a trifolium of amplitude ~ 60 mV for ellipse amplitudes of ~ 9 V (Figure 3.39, to compare with Figure 3.17). The analysis of the quasi-static data in these conditions lead to artificial oscillations (at the frequency of the interference fringes) of the quasi-static displacements h_{stat}, l_{stat} around their true values, corresponding to periodic errors of relative amplitudes $\Delta h_{\mathrm{stat}}/h_{\mathrm{stat}} \sim \Delta l_{\mathrm{stat}}/l_{\mathrm{stat}} \sim 60 \cdot 10^{-3}/9 \sim 0.7$ %. Measurements obtained with the new set-up are free of such periodic errors.

A second effect is due to an unwanted offset added by the electronics in the denominator of equation 3.57, which was not proportional to the light intensity arriving on the analysis unit. This implied that the long-term variations of the laser intensity were not perfectly corrected by the normalization. As shown in Figure 3.40, the contrast calculated electronically (with the offset) exhibited artificial jumps, whereas the one calculated numerically (with no offset) exhibits no jump. It lead to errors on the determination of the true quasi-static

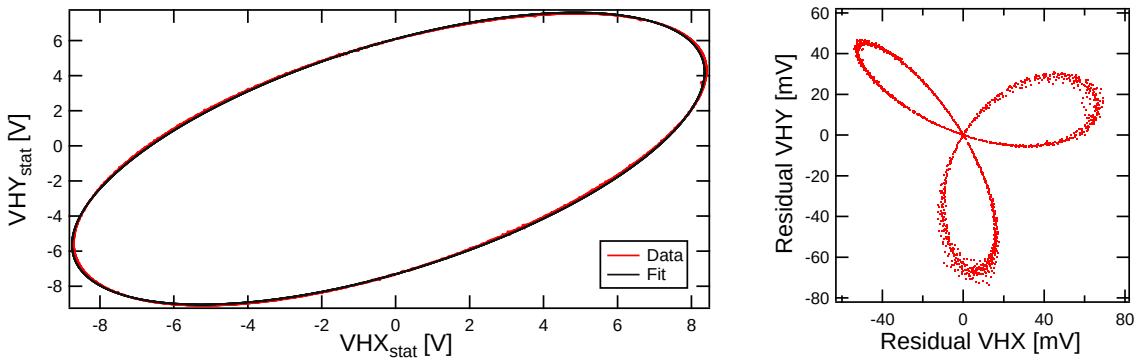

Figure 3.39 On the left, fitting of $V_{\mathrm{HY}}^{\mathrm{stat}}$ as a function of $V_{\mathrm{HX}}^{\mathrm{stat}}$ with an ellipse, for contrasts deduced from previous approach. On the right, residuals associated to the fit, showing a so-called trifolium.

displacements h_{stat}, l_{stat}, of relative amplitudes $\Delta h_{\mathrm{stat}}/h_{\mathrm{stat}} \sim \Delta l_{\mathrm{stat}}/l_{\mathrm{stat}} \sim 0.1$ %, which do not exist anymore in the new version of the set-up.

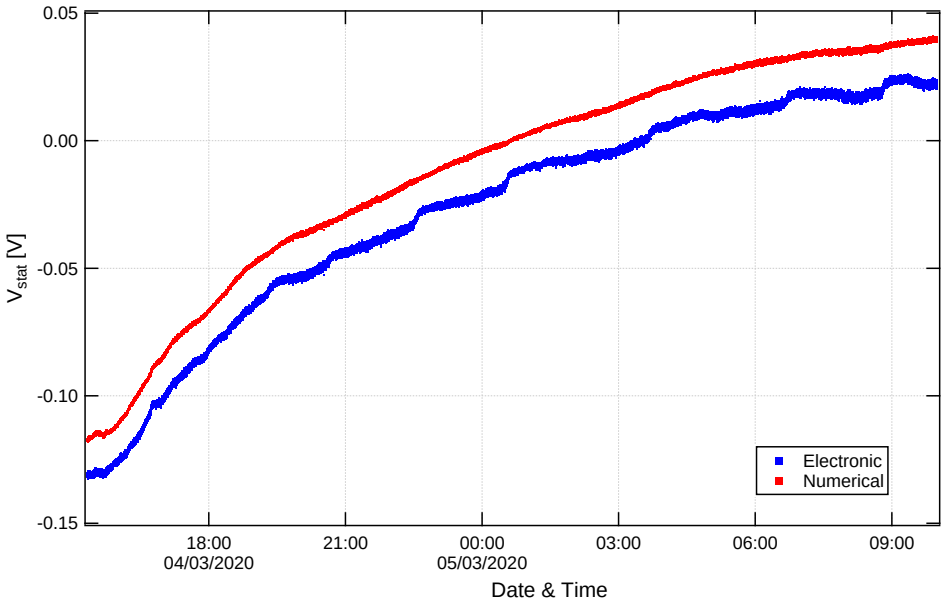

Figure 3.40 Long-term variations of the contrast calculated electronically (in blue) and numerically (in red), when no motion is applied with the actuators.

Effects on the Dynamic Measurements

A first effect comes again from the fact that electronic calculations of normalized contrasts did not allow to correct for the imperfections present in the optical signals. Similarly to the quasi-static measurements, the analysis of the dynamic data in these conditions lead to artificial oscillations (at the frequency, the double frequency and the triple frequency of

the interference fringes) around their true values of the dynamic displacements h_{dyn}, l_{dyn}, corresponding to periodic errors of relative amplitudes $\Delta h_{\mathrm{dyn}}/h_{\mathrm{dyn}} \sim \Delta l_{\mathrm{dyn}}/l_{\mathrm{dyn}} \sim 10$ %. An empirical calibration of this artefact was necessary in order to correct the signals and to obtain relative errors of the order of 1 % (Figure 3.41). In the new version of the dSFA, this calibration is not required anymore to get relative errors of ~ 1 % (see Figure 3.19).

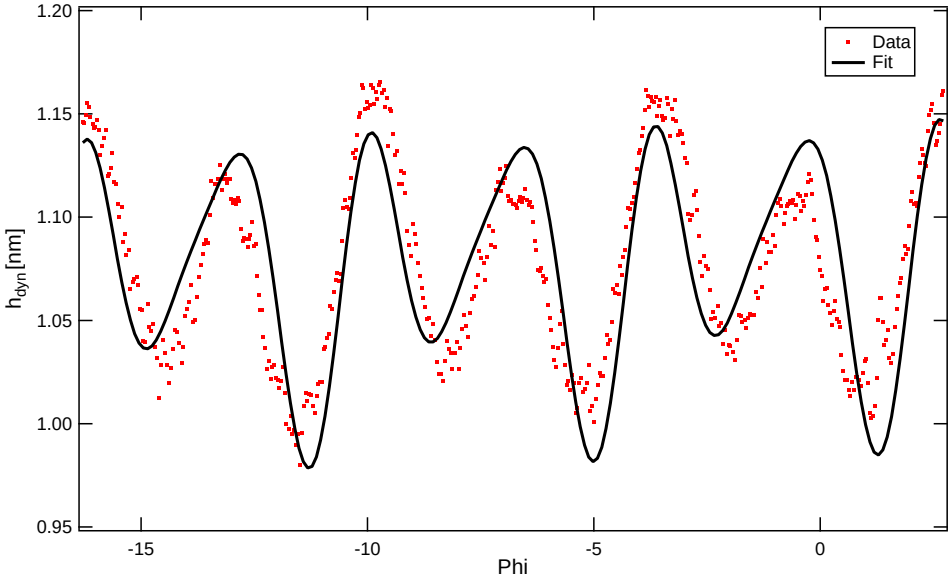

Figure 3.41 Empirical calibration of the artificial oscillations observed on the dynamic displacements h_{dyn}, due to the imperfections present in the optical signals which were not corrected by the electronic calculations.

A second effect is due to the low-pass behavior of the electronic circuit, and can be seen when measuring the mechanical transfer function of the flexure hinge. In Figures 3.42 and 3.43 are respectively shown the modulus and the phase of the flexure hinge's transfer function, measured with the previous (in red) and new (in black) set-ups. One can see that the data deviate significantly from each other, in particular for the phase signal, all the more than the frequency is high. As explained in section 3.2.4, the data obtained with the new set-up can be reasonably fitted with a harmonic oscillator model (green dashed line), i.e., a second order band-pass-filter. On the contrary, the data obtained with the previous set-up resulted from the mechanical transfer function of the flexure hinge multiplied by the electronical transfer function of the electronic circuit. We find a good agreement when supposing that the electronics acts as a first order low-pass filter (blue dashed line), of the form:

$$G_{\mathrm{el}}^{-1}(\omega) = \frac{1}{1 + j\omega/\omega_{\mathrm{c}}} \tag{3.59}$$

$$\left|G_{\mathrm{el}}^{-1}(\omega)\right| = \frac{1}{\sqrt{1 + (\omega/\omega_{\mathrm{c}})^2}} \tag{3.60}$$

$$\arg\left(G_{\mathrm{el}}^{-1}(\omega)\right) = -\arctan(\omega/\omega_{\mathrm{c}}) \tag{3.61}$$

with $\omega_{\mathrm{c}}/2\pi = 900 \pm 20$ Hz the cut-off frequency. The low-pass behavior of the electronics was not only deleterious to the calibration of the flexure hinge's mechanical response, but it also induced a systematic error in the determination of the dynamic phases φ_{H} and φ_{L}, associated respectively to the distance and force interferometers. This problem is solved in the new version of the set-up.

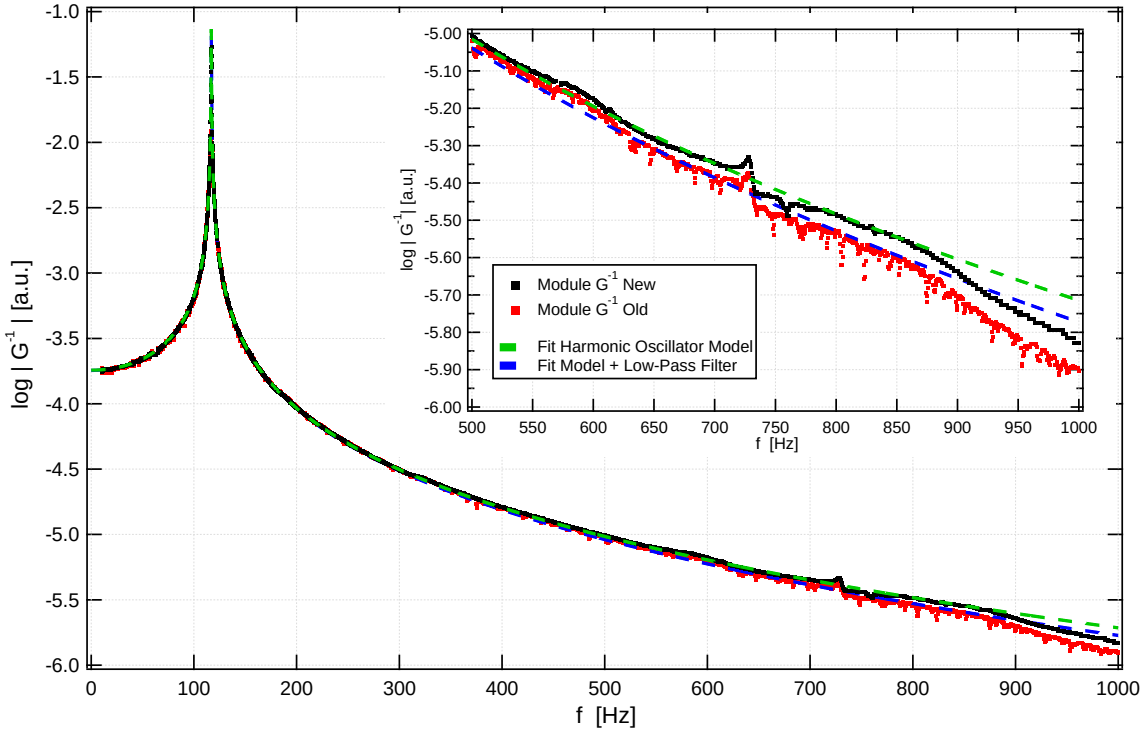

Figure 3.42 Modulus of the flexure hinge's transfer function obtained with the new and previous set-ups, and corresponding fits. Inset allows a clearer view of the gap between the measurements.

A third effect of the previous set-up is that it did not allow for a quantitative measurement of dynamic displacements in the non-linear regime. This is because it was not possible to take into account the reduction of the amplitudes of the quasi-static contrasts when calculating electronically the quantity given by equation 3.58. Such a quantitative analysis is now possible with the new set-up, as described in section 3.2.3.

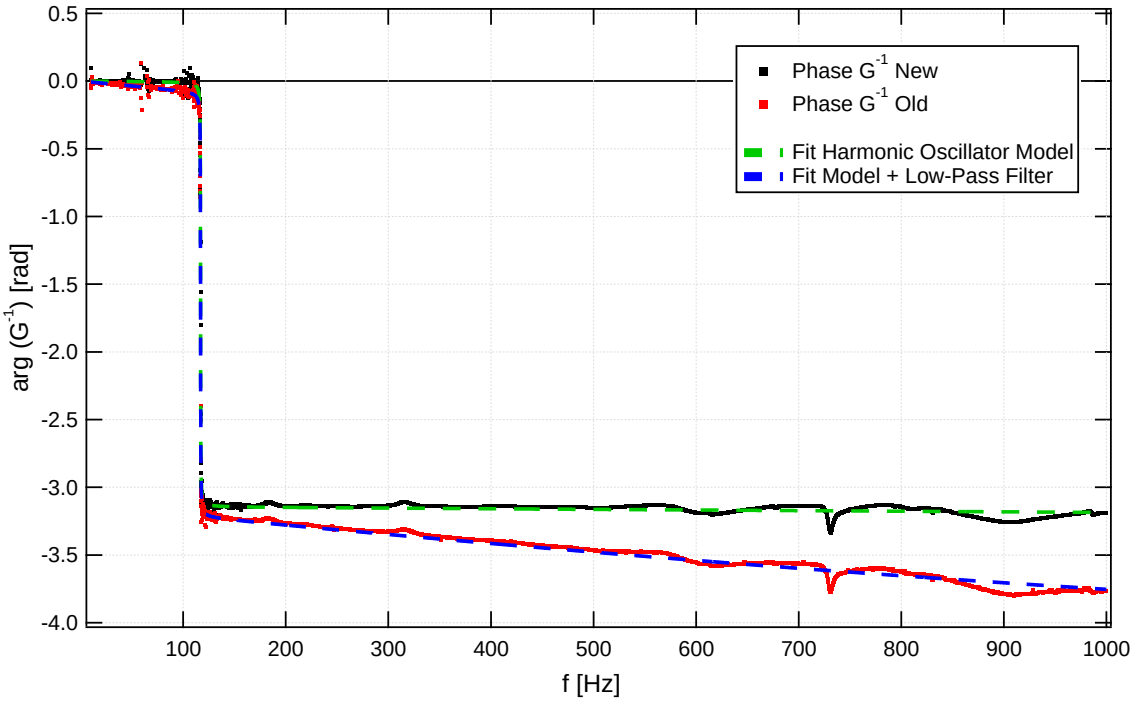

Figure 3.43 Phase of the flexure hinge's transfer function obtained with the new and previous set-ups, and corresponding fits.

3.3.4 Environmental Aspects

The atmospheric stability was the main problem faced in the previous version of the dSFA. The addition of the vacuum chamber allowed to work under vacuum, inert atmosphere (Ar, N_2, etc.), or controlled vapor pressure and humidity. This is crucial when using volatile or hygroscopic liquids, in order to avoid changes of the chemical composition of the liquid (for example salt concentration in aqueous electrolytes, or humidity level in ionic liquids) , or pollution of the surfaces (due to drainage of dust particles to the contact point by the contact line during evaporation).

The thermal stability was another difficulty in the previous version of the dSFA. Although the box significantly improved the thermal isolation of the set-up, stabilization during many hours was necessary before the measurements and long-term drifts were not eliminated. As explained in section 3.1.5, the encapsulation of the set-up with four thermalized levels allowed to obtain thermal drifts in the vacuum chamber as low as 0.04°C in 4 hours (the typical time needed for recording one approach-retraction curve). As a result, typical drifts of the quasi-static displacement on the force interferometer has been found to be as low as 0.2 pm/s, to compare with 5 pm/s in the previous version of the dSFA.

3.3.5 Stability of the Quasi-Static Signals

Pseudo-periodic fluctuations on the quasi-static signals were observed, with a peak-to-peak amplitude typically ranging from 1 to 2 nm and a period of about 20 to 30 s (Figure 3.44). The fluctuations are present on both interferometers and are in phase, albeit not perfectly identical. This artefact is particularly detrimental for the quasi-static force measurement, as it translates into a force sensitivity of 10 µN, i.e., the same order of magnitude than the typical electrostatic force to measure (see chapter 5).

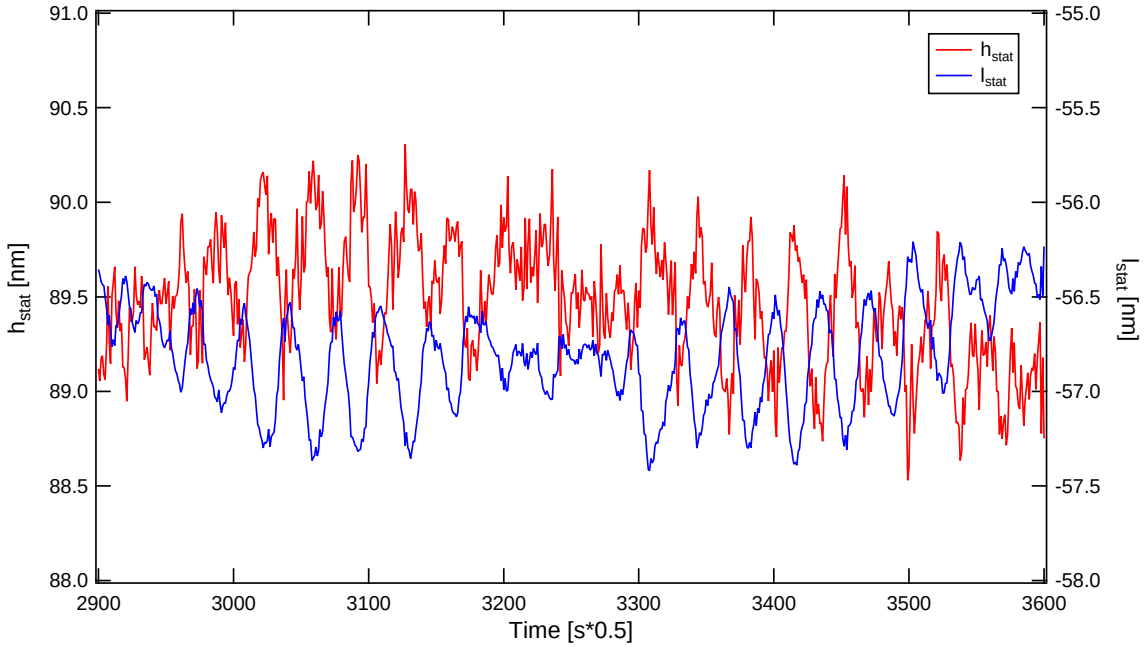

Figure 3.44 Quasi-static fluctuations of 1 nm of amplitude observed every 20 s approximately, on distance and force interferometric measurements.

Many tests were performed to find their origin, and will be discussed in the following.

Stability of laser intensity

First, we observed that these fluctuations were contained in the phase of the interfering beams, and not in their intensities (Figure 3.45). We confirmed this by monitoring directly the intensity of the light coming out of the optical fiber with a power-meter, which showed that the laser power fluctuates by less than 0.1% at the timescale of ~ 30 s.

In addition, our method to analyze the interferometric measurements involves the calculation of normalized contrasts, thus the quasi-static displacements obtained are insensitive to fluctuations of the laser intensity.

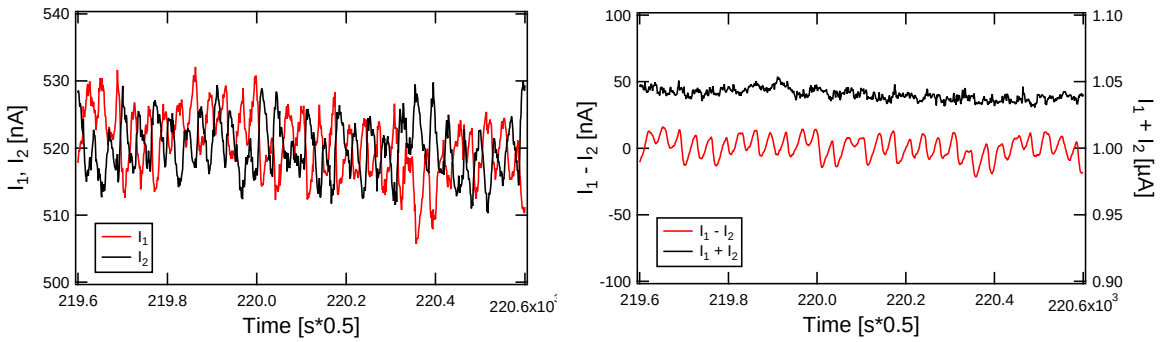

Figure 3.45 On the left, the raw signals from a pair of photodiodes, showing the fluctuations every ∼20 s. On the right, the addition and subtraction of these signals.

Stability of laser polarization

Our measurements are based on polarization interferometry, and are therefore very sensitive to the beam polarization. We included a Glann Taylor polarizer in the optical path, ensuring that any polarization fluctuation caused by the laser or the optical fiber would be converted into intensity fluctuations. But this had no effect on the artefact, and measurements of a stable intensity after the polarizer disproved the existence of fluctuations of such origin.

We tested the removal of the Babinet-Soleil compensator, with the idea that its mechanical fluctuations could translate into polarization fluctuations, but no improvement was obtained.

Stability of laser frequency

In a period of six months, two stabilized laser sources stopped functioning, thus at some point we used a non-stabilized laser. We then noticed synchronized oscillations in the distance and force signals, of amplitude ∼2 nm and period ∼30 s (Figure 3.46a). As these fluctuations with a non-stabilized laser were of similar amplitude and timescale than with the stabilized lasers, we hypothesized that these were due to stabilized lasers that were not functioning properly.

One can show that frequency fluctuations Δf would reflect as distance fluctuations Δh_{stat} by:

$$\Delta h_{\text{stat}} = \frac{\Delta f \lambda h_{\text{stat}}}{c} \tag{3.62}$$

with $\lambda = 632.8$ nm the average laser wavelength, $c = 3 \cdot 10^8$ m/s the speed of light in vacuum, and $h_{\text{stat}} \sim 1$ cm the distance between the two mirrors (considered here from optical contact). Distance fluctuations of 2 nm would be explained by this scenario if laser frequency fluctuations of $\Delta f \sim 100$ MHz were observed over 30 seconds.

We performed measurements with stabilized lasers working in the two types of stabilization modes (frequency or intensity stabilization), but no difference was observed. We also measured

directly the temporal variations of the laser frequency, thanks to a wave-meter provided by colleagues of "LAsers, Molecules and Environment" (LAME) team at LIPhy. We obtained typical fluctuations of about 10 MHz in a 30 s window (see cursors in Figure 3.46b), which are one order of magnitude larger than the specifications given by the manufacturer (2 MHz/hr), but one order of magnitude too small to explain the fluctuations observed in our signals.

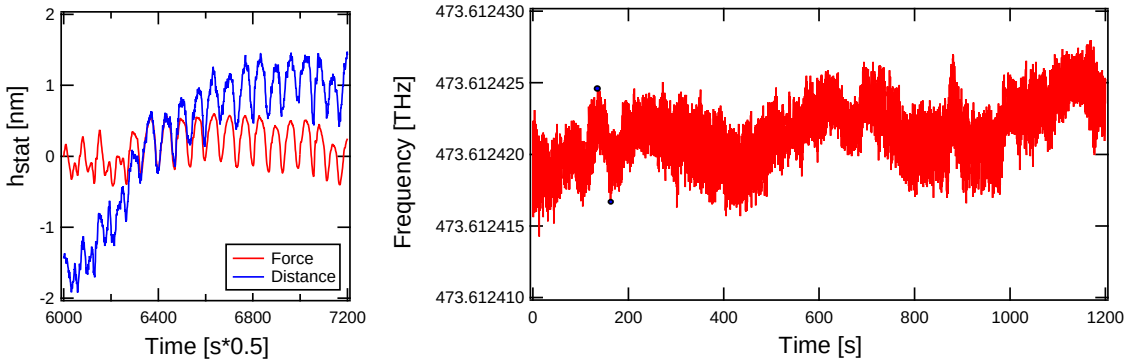

(a) Non-stabilized laser

(b) Measurement of the laser's wavelength

Figure 3.46 Tests to assess the influence of laser frequency.

Stability of laser beam direction

The interferometric measurement relies on the spatial superposition of the two interfering beams. Any fluctuation of the beam direction would therefore reflect into fluctuating signals. It is known for monomode fibers that any angular fluctuation of the beam at the fiber input translates into intensity fluctuation at the fiber output. Thus our artefact can not be explained by the pointing stability of the laser itself, but could be due to orientation fluctuations of optical elements after the fiber output.

Thanks to the collaboration with the LAME team at LIPhy, we performed measurements of the pointing (angular tracking) of the beam after the fiber output with a with four-quadrants diode, simultaneously with the interferometric measurement. In Figure 3.47, we present the results of the test that showed a clear correlation between the beam position and the distance measurements. A series of pointing measurements were performed at different distances from the fiber's output and we observed that the lateral displacement measured by the sensor increased with the optical path length. This told us that the angular fluctuations of the beam were at least partly responsible for our fluctuations on the quasi-static signals.

The pointing stability of a beam just after the output of the optical fiber is mainly determined by the mechanical and thermal stability of the mount supporting this output. We replaced the X-Y translating mount by a more rigid (fixed and thick) one, which resulted in a reduction of the fluctuations on the quasi-static signals down to approximately 0.5 nm. This reduction of the amplitude by a factor 4 was a major improvement, corresponding to an

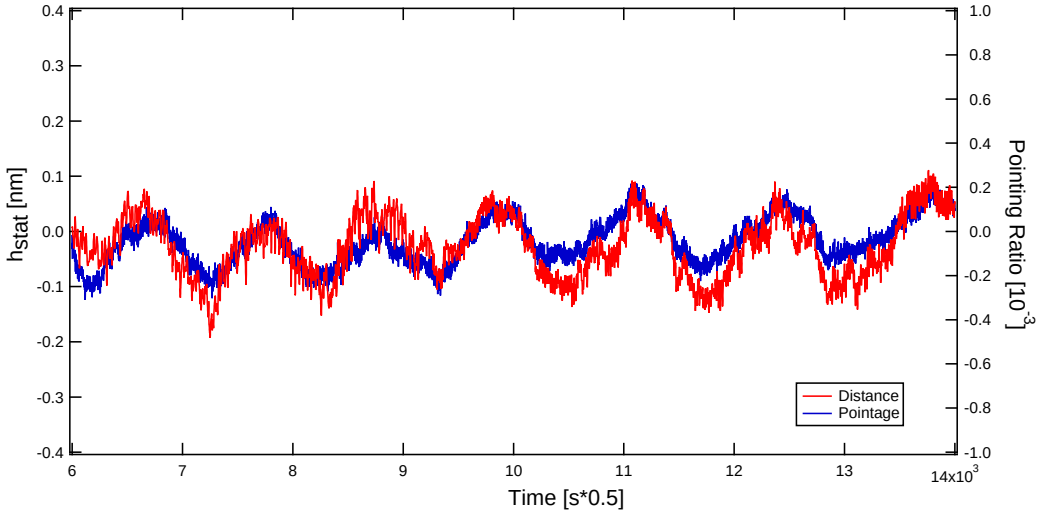

Figure 3.47 Correlation between distance measurement and angular tracking.

enhanced force sensitivity of ~ 2.5 µN, but it was still too high for optimal measurement of electrostatic forces. We checked that all the other optical elements were attached on stable mounts, but we did not further improve the stability of the signals by this method.

Given the little time I had left to perform the experiments for my thesis, we decided to move forward with this partial improvement. For all the presented experimental results in this manuscript, the quasi-static resolution was 0.5 nm (or equivalently ~ 2.5 µN). A trick we found to bypass this issue was to decrease the speed of approach or retraction of the piezo at small distances (typically 50 pm/s from ~ 100 nm to contact). This allowed to get approximately one pseudo-period of fluctuation while moving by one nanometer, which were smoothed with a sliding average filter of 400 points, equivalent to 200 seconds or about 10 pseudo-periods.

Thermal convection rollers

Additional observations at the end of my thesis allowed to identify another origin of the pseudo-periodic fluctuations present on the quasi-static signals.

First, we inserted a thick plate made of Al 7075-T6 Aluminum alloy in between the dSFA's heart and the bottom plate of the vacuum chamber, and removed the three screws at the base of the dSFA's heart (added in the past because of the non-planarity of the bottom plate). The initial motivation was to reduce the mechanical cross-talk on the dynamic signals (see section 3.3.1), but no significant improvement was made on this aspect. However, we observed that this lead to fluctuations on the quasi-static signals that were transiently not present, while they were always present in the past. An important change was the enhancement of the thermal coupling of the dSFA's heart with the vacuum chamber, and from this point we

strongly suspected that the fluctuations originated from thermal convection rollers in the vacuum chamber.

To examine this scenario, we made a first test consisting in setting the air in the vacuum chamber into motion with a fan, during about one minute before closing the chamber. As shown in Figure 3.48, we observed no fluctuations on top of a large drift, and the reappearance of the fluctuations after about 15 minutes.

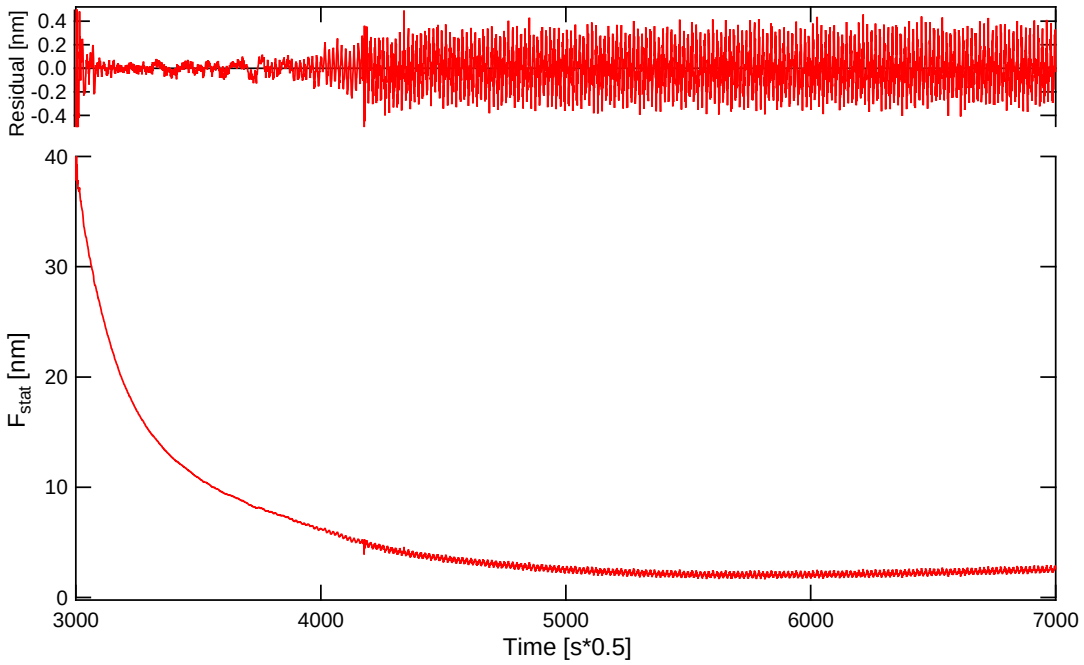

Figure 3.48 Quasi-static fluctuations reappearing after air motion test with fan inside the vacuum chamber.

As a second test, we added in the vacuum chamber a ~ 50 g piece of metal previously cooled down in a freezer. In a similar way, we obtained a disappearance of the fluctuations during about 15 minutes.

As a third test, we filled as much as possible the vacuum chamber with crumpled Aluminum foil, and noticed that it made the fluctuations change (peak-amplitude of 0.1 nm, pseudo-period of about 60 s), or even disappear (Figure 3.49).

The heat sources in the vacuum chamber are the piezo actuator (consuming ~ 5 W), the two PT-100 Platinum resistance sensors placed on top and bottom of the vacuum chamber (dissipating ~ 10 mW each by Joule effect), and the laser beams (a small fraction of laser power ~ 1.5 mW being adsorbed). The main heat source is the piezo actuator, transferring heat to the bottom plate by the M-126 translation stage and its support, and producing a small vertical gradient of temperature in the vacuum chamber. Such gradient may generate

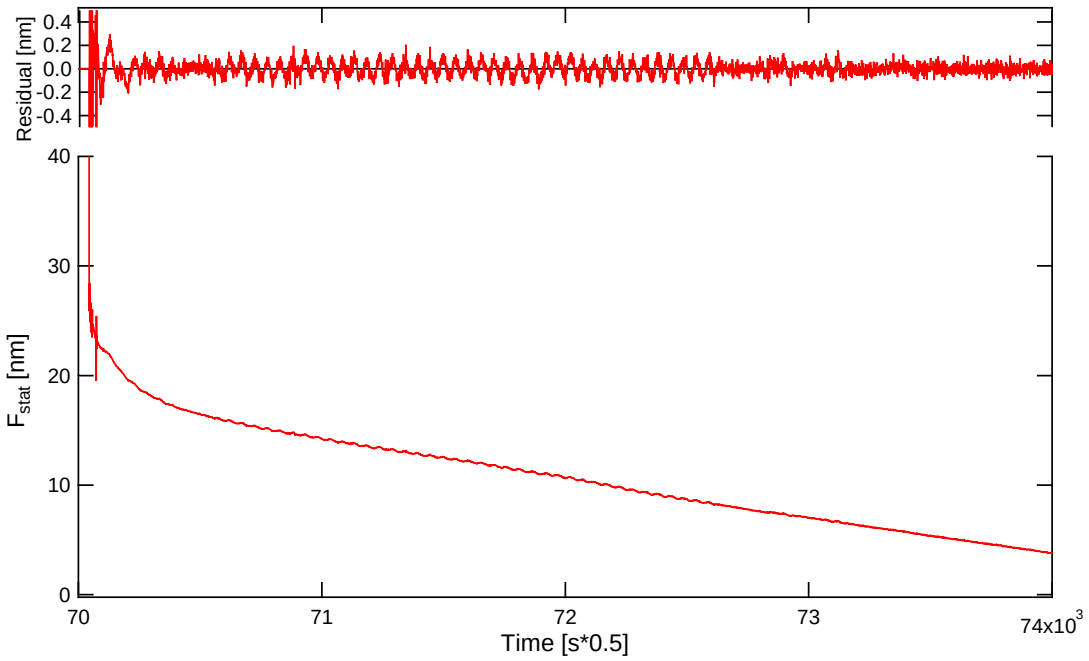

Figure 3.49 Quasi-static fluctuations changing features and eventually disappearing after test filling up the vacuum chamber with Aluminum foil.

thermal convection rollers in the vacuum chamber, depending on the value of the Rayleigh number:

$$\mathrm{Ra} = \frac{\beta g h^3 \Delta T}{\nu \kappa} \tag{3.63}$$

with $\beta \sim 1/297$ K^{-1}, $\nu \sim 1.5 \cdot 10^{-5}$ m^2·s^{-1}, $\kappa \sim 2 \cdot 10^{-5}$ m^2·s^{-1} respectively the thermal expansion coefficient, kinematic viscosity and thermal diffusivity of air, $h \sim 0.4$ m the vacuum chamber's internal height and $g = 9.81$ m $\cdot$ s^{-2} the gravitational acceleration. Convection instability starts when the Rayleigh number is larger than a critical value, of the order of 1700. In our case, we find that this threshold is reached for a very small temperature gradient: $\sim 2 \cdot 10^{-4}$ K between the bottom and top plates of the vacuum chamber. Thermal convection rollers are therefore very likely to be present, and to disturb the interferometric measurement by producing variations of the air refractive index. Indeed, a temperature fluctuation $\Delta T/T \sim (2 \cdot 10^{-4}/40)/299 \sim 2 \cdot 10^{-8}$ over the ~ 1 cm optical path where the interferometric beams are separated would induce an equivalent refractive index fluctuation $\Delta n/n$, which would be interpreted as a displacement fluctuation $\Delta h_{\mathrm{stat}} = h_{\mathrm{stat}} \times \Delta n/n$. With $h_{\mathrm{stat}} \sim 1$ cm the distance between the two mirrors (considered here from optical contact), we find $\Delta h_{\mathrm{stat}} \sim 0.2$ nm, i.e., the same order of magnitude than the fluctuations observed on the quasi-static signals.

To summarize, the different experimental observations and order of magnitude calculations strongly advocate for such a convection scenario. Note that the prominence of this phenomenon has been possible only because of the remarkable stability of the set-up, in particular the absence of air flow coming from the environment. In the next version of the dSFA, this phenomenon will be suppressed by adding a strong thermal coupling between the piezo actuator and the top of the vacuum chamber.

3.4 Conclusion on the new dSFA

The dynamic Surface Force Apparatus is a privileged tool for the study of the nanorheology of confined fluids within a sphere-plane geometry. Yet, the previous version of the dSFA at LIPhy presented limitations that were identified and overcame during my thesis. Namely, the atmospheric control and the thermal regulation system are major enhancements to the machine, in terms of accuracy, reliability and versatility.

The performances of the set-up, for both static and dynamic measurements, are presented in Table 3.1.

Table 3.1 Performances the new version of the dSFA.

	Quasi-Static measurement		Dynamic measurement
	Drift	Noise[1]	Noise[2]
Distance	2 pm/s	20 pm	1-10 pm
Force	0.2 pm/s	120 nN	6-60 nN

[1] After removal of the pseudo-periodic fluctuations on the quasi-static signals.
[2] Depending on the chosen work frequency.

Chapter 4

Experimental Procedure

Contents

Introduction

A campaign of experiments performed with the dynamic Surfaces Forces Apparatus at LIPhy requires a strict systematic procedure for the preparation and installation of samples, the characterization of the noise and mechanical cross-talk, the actual realization of the measurements and the data treatment. The steps of such procedure will be described in this chapter.

4.1 Experiment Preparation and Execution

The most critical aspect of the preparation of an experiment is the cleanness of a sample, since the presence of dust particles or any other pollution source on the surfaces, even of nanometric size, can ruin the experiment. Indeed, the sphere might *feel* parasite forces that do not actually belong to the interaction with the fluid and the plane, but with the dust particle, as schematized in Figure 4.1. In the sphere-plane geometry, since the separation between the surfaces is much smaller than the sphere's radius $D \ll R \approx 3$ mm, a parabolic approximation can be made locally for the thickness of the liquid film:

$$e(r) = D + \frac{r^2}{2R}$$

Assuming the height of the particle to be $e(r) = 10$ nm, we find that real contact between the sphere's apex and the plane cannot be achieved if the particle is situated at a radial distance of $r = \sqrt{2e(r)R} = 7.3$ µm or less from the sphere's apex. In other words, the lateral radius of influence of a dust particle is much larger than its size, because of the quasi-planar geometry. This is why the cleaning of surfaces is such an important step in the experiment's preparation.

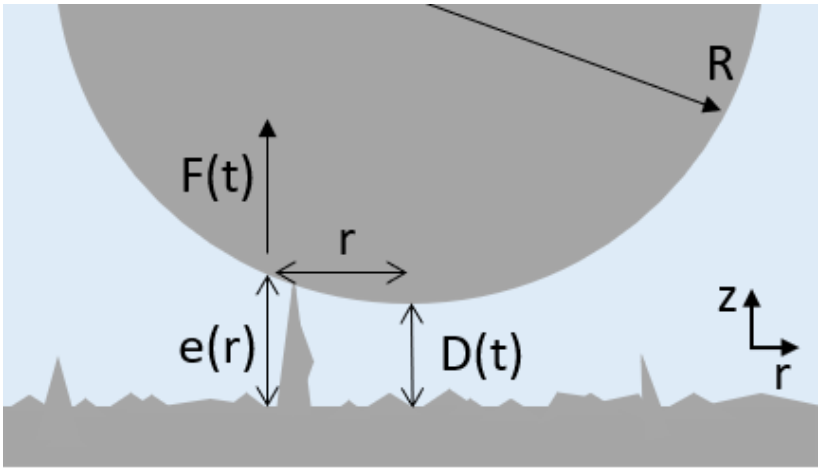

Figure 4.1 Schematic of the surface roughness effect in dSFA measurements. In the presence of a nanometric dust particle near the sphere's apex, the contact (molecular-size separation) between the sphere and the plane is not possible. Forces across the dust particle are dominant when the surfaces are still far from each other and that can fault our results.

4.1.1 Surfaces Preparation and Installation

The spheres and the planes are made out of Borosilicate glass (also known as Pyrex)[1]. The planes are fabricated by the supplier using the float glass process, resulting in squared glass

[1] Manufacturer: Pignat

sheets of 15 mm on each side and 3.8 mm thickness, having eased edges to avoid any pollution of glass fragments during their manipulation. The spheres are formed in the lab by cutting and melting a glass rod. The cutting process is performed with a diamond tip, on glass rods that are initially 50 cm in length and 5 mm of diameter, obtaining multiple 2-3 cm long pieces. Then, the tip of each glass rod is melted using oxyacetylene welding, until achieving a 3 mm radius of curvature approximately. Particular care is needed to have symmetrical and bubble-free spheres.

The measurement of the radius of the spheres were performed after each campaign of experiments, using a camera[2]. Images were taken in orthogonal sides of the sphere, in order to obtain the two full curvature profiles (Figure 4.2). The image processing was performed on ImageJ and the data was fitted on Igor with the equation of a circle

$$y(x) = \sqrt{R_i^2 - (x - x_0)^2} + y_0$$

where x_0 and y_0 are the two coordinates at the center of the circle and $R_i = R_1, R_2$ are the two sphere radii obtained from profiles taken at 90° of each other. The difference between R_1 and R_2 is typically of the few percents. The average curvature radius R is calculated from the Gaussian radius, i.e., by calculating a geometric mean $R = \sqrt{R_1 R_2}$ [13].

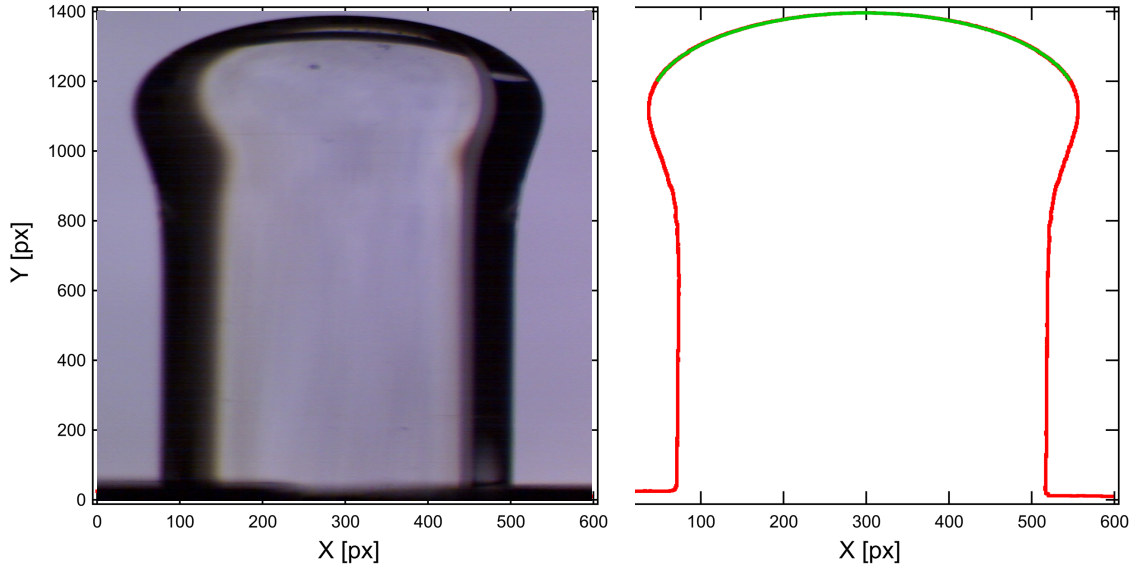

Figure 4.2 Measurement of the sphere's curvature radius. On the left, a picture taken with a optical camera of one of the two orthogonal sides of the sphere. On the right, the profile obtained from image processing and the fit of the sphere's curvature from a circle approximation.

[2]Manufacturer: Digital Microscope

The cleaning protocol consists in putting the surfaces in their respective glass containers (pre-washed with the same protocol as the surfaces), filled with a cleaning solution (Microson from Fisher Scientific) diluted in deionized water[3]. They are washed in an ultrasonic bath at 50°C for 15 minutes, rinsed by overflow with deionized water. The procedure is repeated twice. They are left to dry under a laminar flow hood.

In order to quantify the roughness of our cleaned surfaces, AFM tapping-mode measurements were performed at LIPhy by C. Cramail, PhD student. As shown in Figure 4.3, the area of study of a plane is set to 10 µm^2 and certain corrections are applied to eliminate artefacts in the measurement that could change the sample's measured flatness and false the measured roughness, such as a non-straight displacement of the tip of the AFM or an eventual angle between the AFM's tip and the sample. The image is cropped to obtain a 0.01 µm^2 surface and the measured surface heights distribution is presented in the histogram of Figure 4.3. For a Borosilicate glass plane, a RMS roughness of 1 Å RMS is found, which agrees with Garcia's results [11].

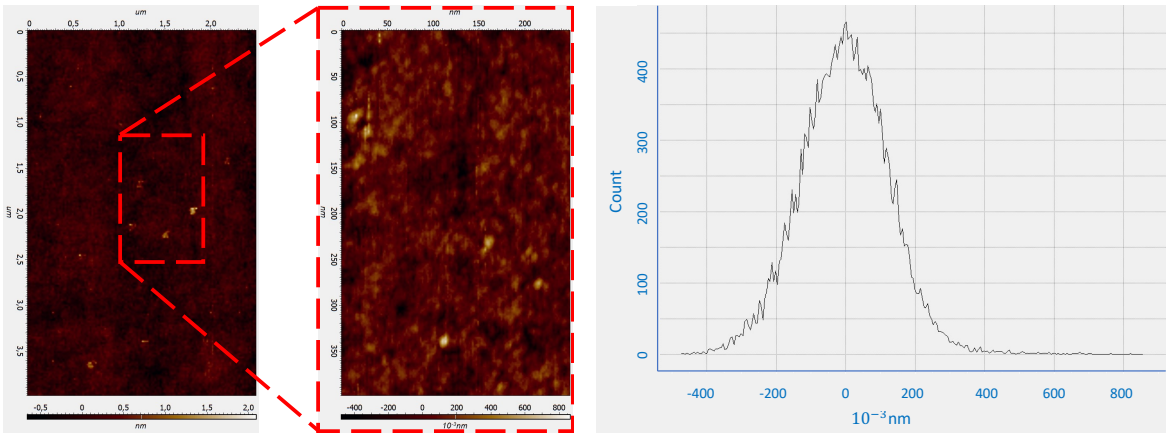

Figure 4.3 Surface roughness measurements by AFM for a Borosilicate glass surface. On the left, at 10 µm^2 initial area of study, and the 0.01 µm^2 cropped surface. On the right, the histogram distribution for the 0.01 µm^2 area.

C. Cramail also carried out a material deposition using the sputtering machine present at LIPhy to obtain a dielectric surface of different nature. A 30 nm layer of Boron Nitride was coated onto Borosilicate glass surfaces, performed on AC mode. Following the same measurement protocol on the AFM, the measured surface heights distribution is presented in Figure 4.4, providing a a RMS roughness of 3.6 Å RMS. This is slightly larger than the supporting glass, but in both cases the roughness values fulfill the requirements for our experiments.

The cleaned spheres are mounted on the flexure hinge under a laminar flow hood. All elements needed for the installation (surfaces, surface holders and tools) that have been

[3]DI water (18.2 MΩ · cm, Millipore water purification system)

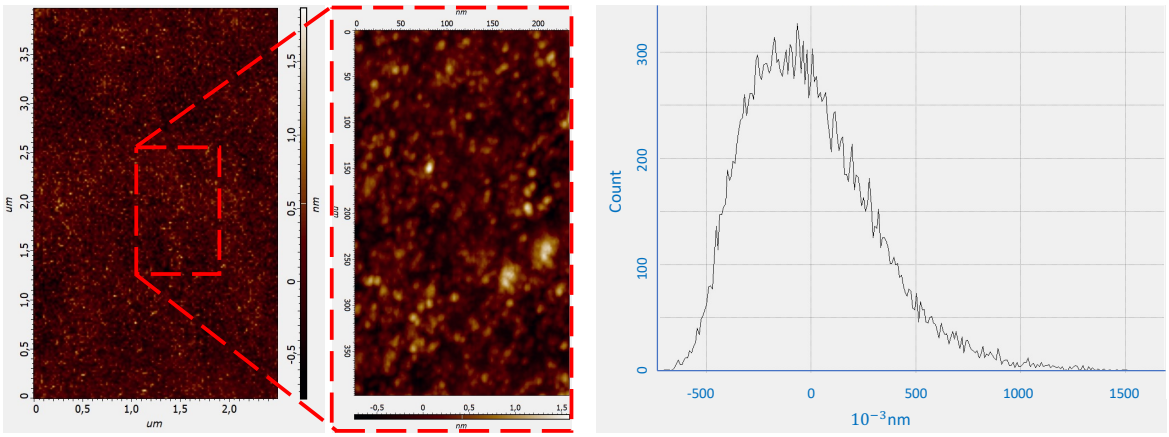

Figure 4.4 Surface roughness measurements by AFM for a Boron Nitride coated surface. On the left, at 10 µm^2 initial area of study, and the 0.01 µm^2 cropped surface. On the right, the histogram distribution for the 0.01 µm^2 area.

cleaned, are put into air-tight boxes and transported to the dSA experimental room. The flexure hinge holding the sphere is installed, in a way to achieve the closest parallelism possible with the interferometers. The plane is mounted on its holder, fixed to the piezo actuator. The fluid is filtered for particles larger than 100 nm before injection with a particle filter mounted on a syringe. When the liquid is not volatile, one or two droplets are enough to form a capillary bridge between the surfaces (Figure 4.5a). Otherwise, a 120 mL reservoir is installed for the surfaces to be fully immersed in the liquid of study so they would not be affected by evaporation (Figure 4.5b). In this case, another reservoir with the same solution (same pH and concentration) is added inside the vacuum box in order to saturate the air with humidity.

The interferometer and the dSFA's four mirrors are finely adjusted for parallelism. The vacuum chamber as well as the polyurethane isolating box are closed, the air extraction system is turned off, the anti-vibration table is adjusted and the system is left to stabilize thermally and mechanically until the next morning, when we can observe the drift in signals on the order of $\sim 1-5$ pm/s. Normally, a whole campaign of experiments can be performed with the same set of surfaces and liquid (if not evaporated or contaminated).

4.1.2 Measurement protocol

Once the surfaces are well installed in the dSFA, the liquid of study has been injected and the system is relaxed, the first step is to run a calibration, following the procedure explained in section 3.2.2. A new calibration is needed each time the interferometer has been adjusted, more liquid has been injected or the frequency of excitation has been changed. Even if no modifications have been made, a new calibration is needed for each experiment to take into account the time lag between electronic equipment, which can change from run to run.

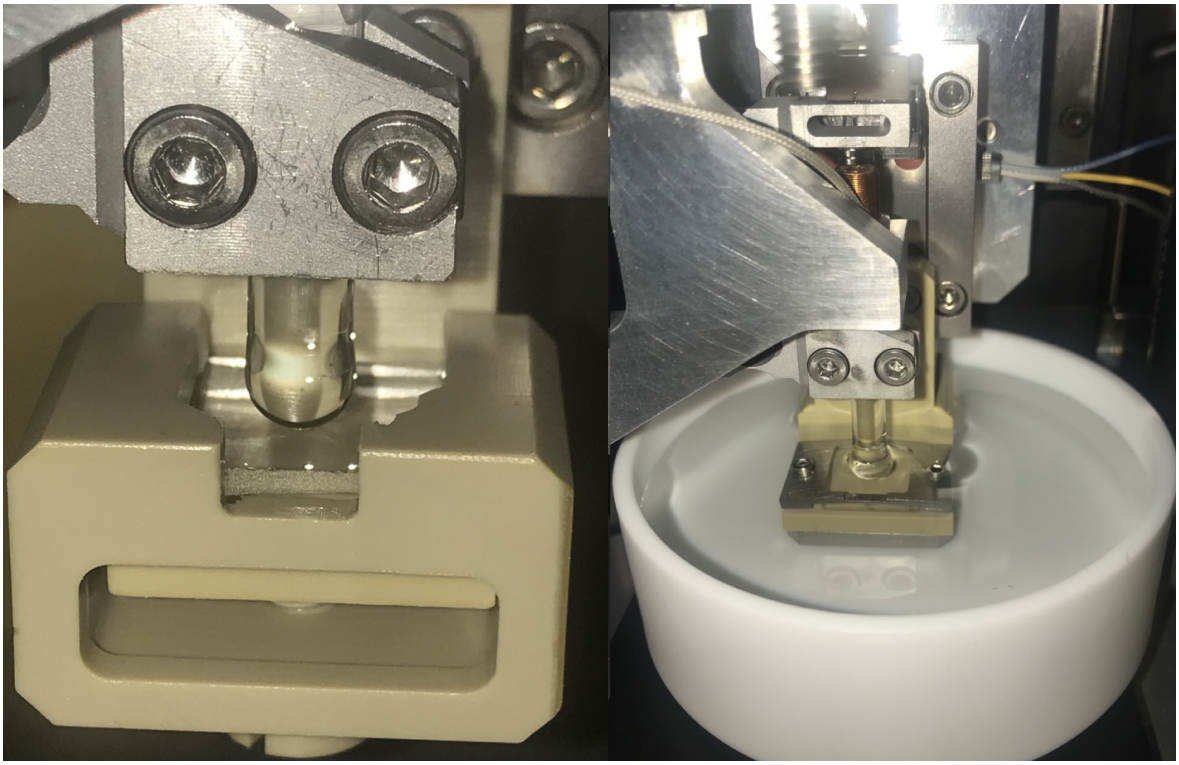

(a) Capillary bridge in "droplet" mode. (b) Fully immersed surfaces in "dipped" mode.

Figure 4.5 Arrangement of surfaces and liquid during an experiment.

Following the calibration, a noise and a mechanical cross-talk measurement are performed while the surfaces are far away, so no interaction force can be sensed. The first one is useful to determine the work frequencies below the resonance threshold, where the physical signal is mainly affected by noise. The second measurement tells us which frequencies above the resonance threshold show the lowest level of mechanical cross-talk.

Once we obtain this information, it is necessary to know the separation distance between sphere and plane. This step is also performed only once for a whole set of experiments where the surfaces have not been changed. The surfaces are approached coarsely by the M-126 motor, with steps ranging from 10 to 100 µm, while finely displacing the piezo-electric actuator at speed $U \sim 2$ nm/s. While the surfaces are carefully being approached, we observe the evolution of the admittance. The extrapolation of the admittance with the distance gives us an estimate of the contact position. The surfaces are then separated again by approximately 10 µm from each other with the M-126 motor while the piezo actuator is fully expanded, and then we are ready to start the experiments.

The quasi-static approach of the surfaces during an experiment is performed finely by the piezo actuator, starting with a velocity of 2 nm/s and decreasing down to 0.05 nm/s for separations below 100 nm (Figure 4.6). Simultaneously, the amplitude of dynamic excitation of the piezo is set to a high value when surfaces are far from each other, typically ~ 25 nm (non-linear regime) for frequencies below the resonance, or ~ 10 nm (linear regime) for frequencies above the resonance. The amplitude is then lessened progressively as the surfaces approach, to be of the order ~ 5 nm when the separation of surfaces is below 1 µm, and as small as 0.3 nm when the distance is smaller than 10 nm. The sensitivities of the four lock-in amplifiers are adjusted accordingly. The inverse progressive augmentation of the velocity and excitation amplitude is applied for the separation of the surfaces (Figure 4.6). A typical approach-retraction cycle lasts around 6 hours.

4.2 Data Treatment

In order to duly extract the correct information from an experiment, a step of corrections must be applied to the data, since it can contain artefacts and other systematic errors. For instance, no matter how small a drift in temperature is, it can influence the displacement measurement due to an induced thermal expansion of some elements in the interferometer.

A systematic correction protocol has been implemented in the same order as it is detailed below. All the data in this section was obtained from an experimental campaign performed with pure Propylene Carbonate confined between Borosilicate glass at different frequencies. The radius of the sphere was measured to be 2.885 ± 0.007 mm, and the temperature of the experiments was $24 \pm 1°$C.

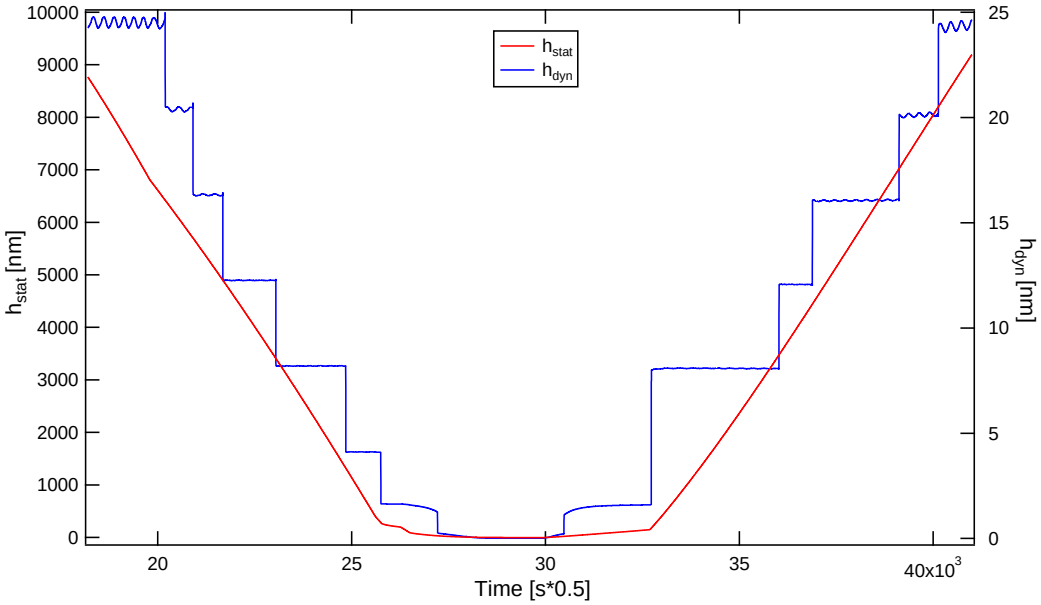

Figure 4.6 On the left axis, the displacement measured h_{stat} for the quasi-static approach and retraction of the piezo. On the right axis, the dynamic amplitude h_{dyn} simultaneously applied to the piezo during an experiment performed at a frequency below the resonance.

4.2.1 Variation of calibration parameters

Deviations were identified between the parameters obtained from the calibration of the distance interferometer with the coil-magnet system and the piezo-electric system. Other deviations were also noticed when a calibration was performed during the approach of surfaces or their retraction. Clearly, the ellipse followed by the distance interferometer was not exactly the same depending on the actuator and the direction of motion. This could be due to slightly different translation directions between the actuator, and a tiny rotation of the traveling part of the piezo actuator when changing direction.

Consequently, three calibrations are needed in one experiment: the one performed with the coil-magnet system before the experiment for the force interferometer, another with the piezo for the distance interferometer when approaching the surfaces, and the third, also with the piezo for the distance interferometer when retracting the surfaces. The variables of interest are then recalculated by segments depending of each calibration.

4.2.2 Non-Linear Parameters

It is at this moment that we adjust the parameters α and β according to the method explained in section 3.2.3 to consider the non-linearities in the distance interferometer.

4.2.3 Thermal Drifts and Mechanical Contact

After the stabilization of the system, we can still observe a slow thermal drift in the quasi-static force curves, which we can fit with a straight line far from contact in order to be subtracted from the data. Figure 4.7 presents the measured force curve as a function of time, which shows the mentioned drift before and after the contact of surfaces. The corrected force curve is presented as well, with the drift which has been subtracted according to the linear expression with the coefficients α_F, β_F as in:

$$F = f_{stat} - (\alpha_F + \beta_F t)$$

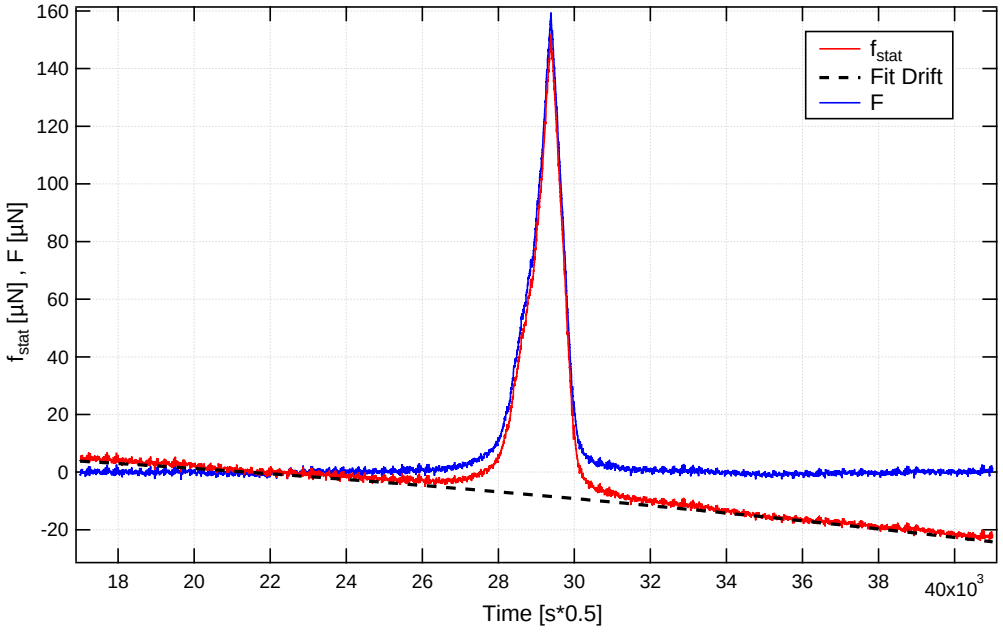

Figure 4.7 Correction of the thermal drift from the force measured signal. In red, the measured force and in blue the corrected curve after the subtraction of a straight line. The peak corresponds to the contact of the surfaces, with a maximum due to the change in direction of movement.

The β_F parameter compensates for the thermal drift on the force interferometer, while the α_F parameter allows to position the zero for the quasi-static force far from contact. We have observed typically a constant thermal drift of 1.1 nN/s or 0.2 pm/s from the force interferometer.

In the same way, the drift on the distance interferometer has to be subtracted from the measured distance h_{stat}. However, by definition h_{stat} was varied continuously, so the drift is observed by plotting the imaginary part of the mechanical admittance as a function of the distance between surfaces. We expect a curve where approach and retraction are superimposed, supposing the conditions of the liquid and the surfaces did not change during

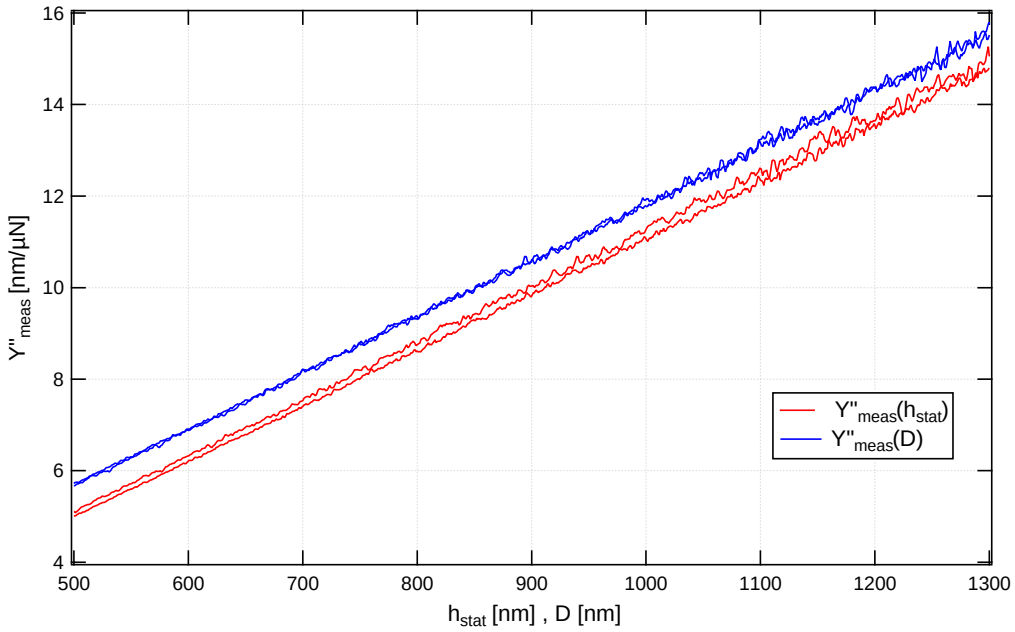

Figure 4.8 Correction of the thermal drift from the displacement measured signal. The red curve shows a separation between the approach and retraction pieces of the admittance curve as a function of distance. For illustration purposes, this separation was slightly increased. In blue, the two pieces of the curve overlap after correction.

an approach-retraction cycle. In reality, the small drift on the distance interferometer slightly adds a gap between the approach and retraction parts of the measurement, observed in Figure 4.8. The correction of the drift brings them both back together, overlapping the approach and retraction pieces of the curve.

The correction in the displacement measurement is approximated to a linear drift velocity, with the coefficients $\alpha_{\mathrm{H}}, \beta_{\mathrm{H}}$ following the expression:

$$D = h_{\mathrm{stat}} - (\alpha_{\mathrm{H}} + \beta_{\mathrm{H}} t)$$

The β_{H} parameter compensates for the thermal drift on the distance interferometer, while the α_H parameter is adjusted to position the origin for the quasi-static distance, defining the mechanical contact between the surfaces. The model used to estimate this mechanical origin changes according to the system of study. More details of the different models are given in section 4.3.1.

4.2.4 Residuals on the Mechanical Impedance

Both the measured real and imaginary components of the mechanical impedance contain parasite residuals. As seen on the left-side graph of Figure 4.9, an elastic residual and a viscous residual of similar magnitude are identified when observing Z' and Z'' near 10 µm of

separation of the surfaces. One origin of this artefact is the mechanical cross-talk (section 3.3.1). Other origins are capillary and viscous forces at the contact lines, non-stationary effects [11, 12], etc.

The residual on Z' is easy to correct since it reaches a quasi-constant regime at large distances. On the right-side graph in Figure 4.9, the corrected Z'_{co} is presented, after subtracting a constant residual:

$$Z'_{\text{co}} = Z'_{\text{meas}} - Z'_{\text{res}}$$

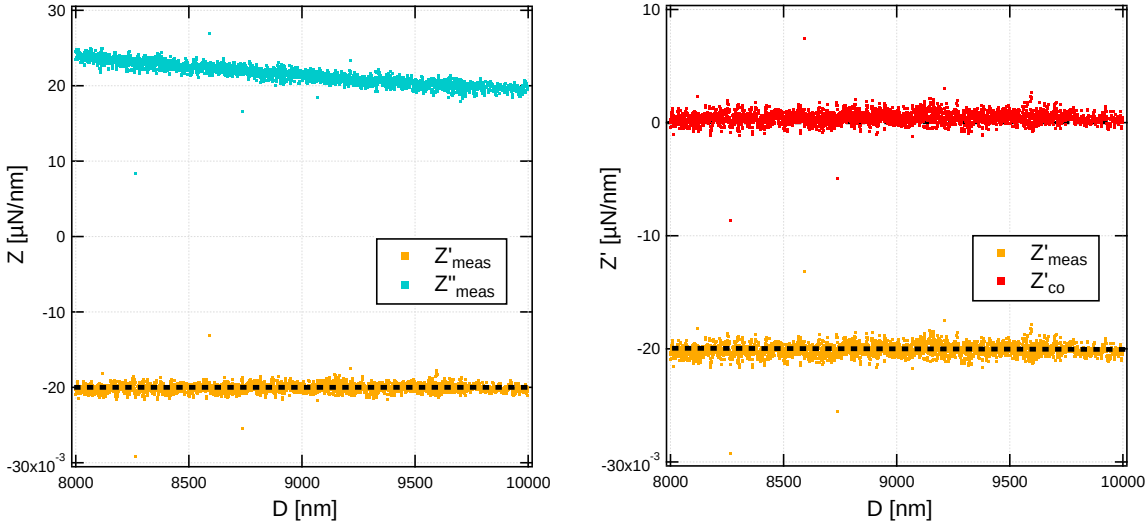

Figure 4.9 On the left, the measured residuals on the real and imaginary components of the mechanical impedance. On the right, for the same experiment at 74 Hz, correction of the residual on the real part of the mechanical impedance.

The residual on Z'' is more difficult to subtract, as Z'' still contains physical signal even at such distance, namely the viscous dissipation in the liquid. To correct it, it is better to observe the inverse of the imaginary part of the mechanical impedance as a function of the distance. Figure 4.10 shows the measured and the corrected curve of $1/Z''(D)$, with the respective fit corresponding to a Reynolds impedance $Z''_{\text{Rey}} = \frac{6\pi\eta\omega R^2}{D}$. A linear fit is performed in a distance interval approximately around 200 nm and 1300 nm, since no additional dissipative effects should be measured in this region. To obtain the corrected Z''_{co}, we subtract a constant residual, which is adjusted to obtain $1/Z''$ proportional to distance D up to largest distances:

$$Z''_{\text{co}} = Z''_{\text{meas}} - Z''_{\text{res}}$$

4.2.5 Machine Stiffness

When all effects previously mentioned have been corrected, there is an additional cause of error in the dSFA measurements. This is the machine stiffness, a systematic error in the

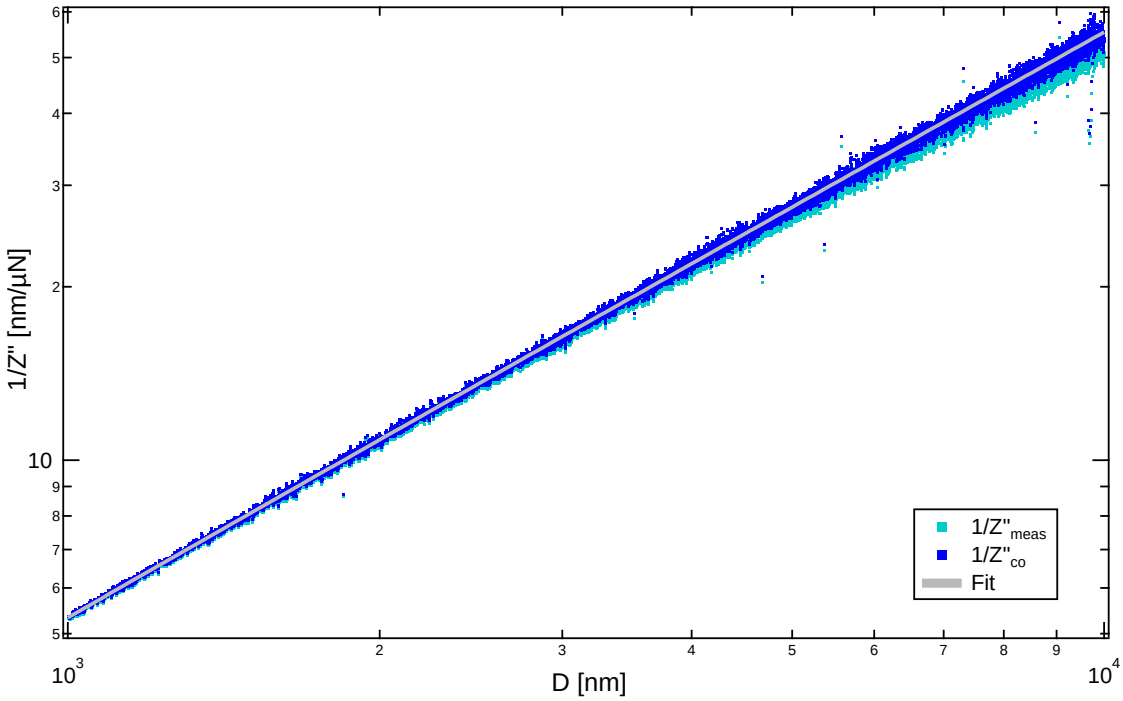

Figure 4.10 Correction of the residual on the imaginary part of the mechanical impedance, for an experiment at 74 Hz.

distance measurement due to the finite stiffness of the machine, and in particular of the chain of transmission of the efforts between the confining surfaces and the mirrors being used to measure their relative displacement. Figure 4.11 shows how this transmission chain can be modeled as an unique spring in series with the system of study. The measured distance $D_{\text{tot,meas}}$ and the true distance $D_{\text{tot,true}}$ are related by the expression:

$$D_{\text{tot,meas}} = D_{\text{tot,true}} + \frac{F_{\text{tot}}}{K_{\text{M}}}$$

where K_{M} the machine stiffness and F_{tot} the total force transmitted by the flexure hinge.

The machine stiffness has an influence on the quasi-static measurement, which we can write simply as $D_{\text{meas}} = D_{\text{true}} + \frac{F}{K_{\text{M}}}$. This effect is significant only when the quasi-static force is large, i.e., when the surfaces are in contact. The machine stiffness also affects the dynamic measurement, as $h_{\text{dyn,meas}}\ e^{j\varphi_{\text{H}}} = h_{\text{dyn,true}}\ e^{j\varphi_{\text{H}}} + \frac{f_{\text{dyn}}\ e^{j\varphi_{\text{F}}}}{K_{\text{M}}}$. This effect translates into the measured mechanical impedance Z_{meas} as:

$$Z_{\text{meas}} = \frac{f_{\text{dyn}}\ e^{j\varphi_{\text{F}}}}{h_{\text{dyn,meas}}\ e^{j\varphi_{\text{H}}}} = \frac{f_{\text{dyn}}\ e^{j\varphi_{\text{F}}}}{h_{\text{dyn,true}}\ e^{j\varphi_{\text{H}}} + \frac{f_{\text{dyn}}\ e^{j\varphi_{\text{F}}}}{K_{\text{M}}}} = \frac{Z_{\text{true}}}{1 + \frac{Z_{\text{true}}}{K_{\text{M}}}} \tag{4.1}$$

At large distances ($D \gg D_{\text{c}}$) the elasto-hydrodynamic response is mostly viscous and given by the Reynolds formula with $Z_{\text{Rey}} \ll K_{\text{M}}$:

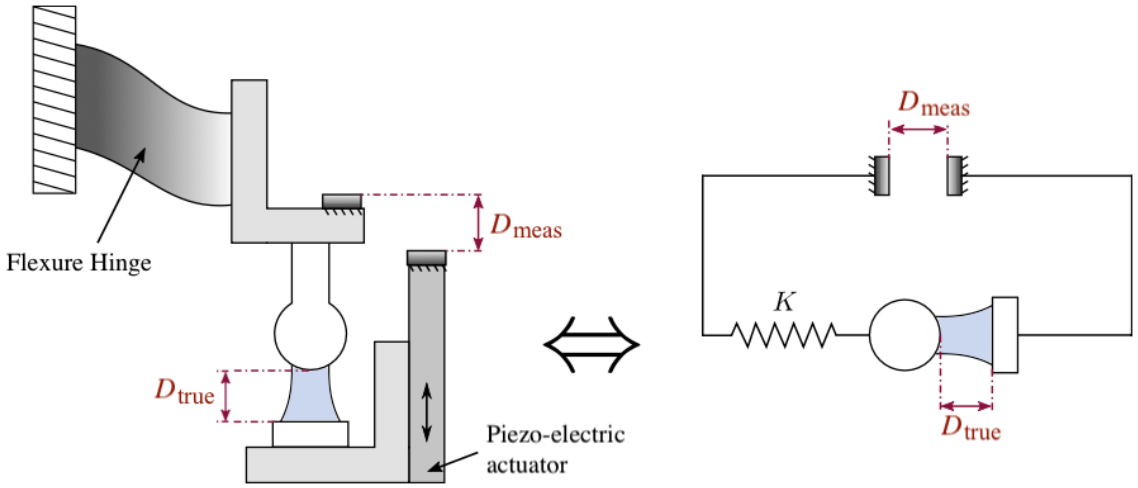

Figure 4.11 Schematic of the machine stiffness, modeled by a spring in series with the system of surfaces and liquid. Image adapted from [12].

$$Z_{meas} \simeq \frac{Z_{Rey}}{1 + \frac{Z_{Rey}}{K_M}} \simeq \frac{(6\pi\eta\omega R^2)^2}{K_M D^2} + j\frac{6\pi\eta\omega R^2}{D} \tag{4.2}$$

The machine stiffness produces a parasitic elastic response at large distances. By plotting the squared root of the inverse of real component of the mechanical impedance as a function of distance (Figure 4.12), we observe its influence as a linear trend whose slope allows us to retrieve the value of the machine stiffness. Before correction of the experimental data, the elastic response of the system scales as D^{-2} (Figure 4.12). The $D^{-5/2}$ scaling expected from elasto-hydrodynamics is recovered after machine stiffness correction. The measured values of K_M are dependent on the work frequency, and here is equal to 303000 N/m at 435 Hz.

4.3 Characterization of a Simple Fluid

The results presented in this section have been obtained with a system composed of Hexadecane as liquid and Borosilicate glass as surfaces. The radius of the sphere was measured to be 2.882 ± 0.001 mm, and the temperature of the experiments was 23 ± 1°C. The displayed curves show data already corrected from the previously described effects. These data are in agreement with well-known results in the field, such as those reported by Chan and Horn [34] for alkanes confined between mica surfaces, and they are used to bring to light quantitative information about the performances of the machine.

4.3.1 Quasi-Static Force

Figure 4.13 presents the interaction force between sphere and plane, transmitted by the liquid, as a function of separation of the surfaces. At large distances, no quasi-static force is

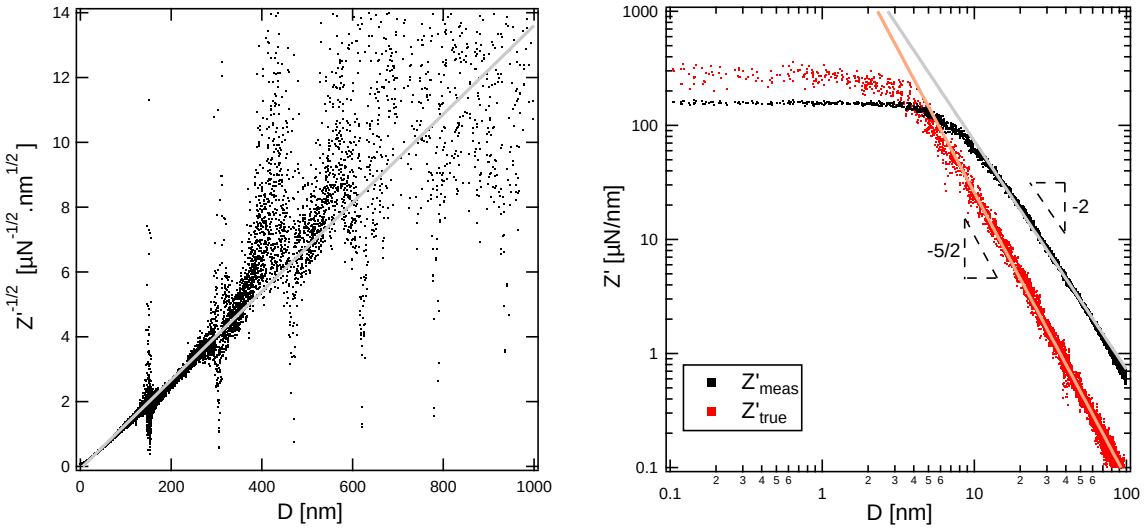

Figure 4.12 On the left, the squared root of the inverse of Z' as a function of separation of surfaces. The slope from the linear fit gives the value of the machine stiffness. On the right, the measured Z' curve for 435 Hz without the correction of the machine stiffness is presented in black, and the corrected curve in red. The value found for this experiment is 303000 N/m.

measured, until separation distance is decreased to some molecular sizes, in this case below ~ 1 nm. The effect of adhesion present in the retraction movement (separation of surfaces) is evident, as negative forces down to $F_{\text{adh}} = -76 \pm 6$ µN are reached, and prove the cleanliness of surfaces. The distance at which the force is minimum has been chosen as the mechanical origin. It is at this minimum that the surfaces jump apart with a slope equal to the flexure hinge's stiffness. This jump is due to the spring instability, i.e., the fact that the flexure hinge's stiffness is smaller than the gradient of the attractive van der Waals force interaction force.

It has been shown that the adhesion force is equal to:

$$F_{\text{adh}} = -\frac{AR}{6D_0^2}$$

where A is the amplitude of the van der Waals attraction integrating the different continuous bodies, and $D_0 = 0.165$ nm is a microscopic cut-off due to the (at least atomic) roughness of the solid surfaces [13]. With this formula we find an Hamaker constant $A_{\text{exp}} = (4.3 \pm 0.4) \cdot 10^{-21}$ J, in reasonable agreement with the theoretical value $A_{\text{theo}} = 3.0 \cdot 10^{-21}$ J expected for the Borosilicate/Hexadecane/Borosilicate system [11]. The $\sim 43\%$ overestimation on the Hamaker constant A may come from a $\sim 22\%$ overestimation on the microscopic cut-off D_0, which would indicate the very low roughness of the Borosilicate glass surfaces.

In some cases, the measured force profile does not exhibit a minimum of adhesion. An example is shown in Figures 4.14a and 4.14b. In this case, the repulsion of large amplitude is

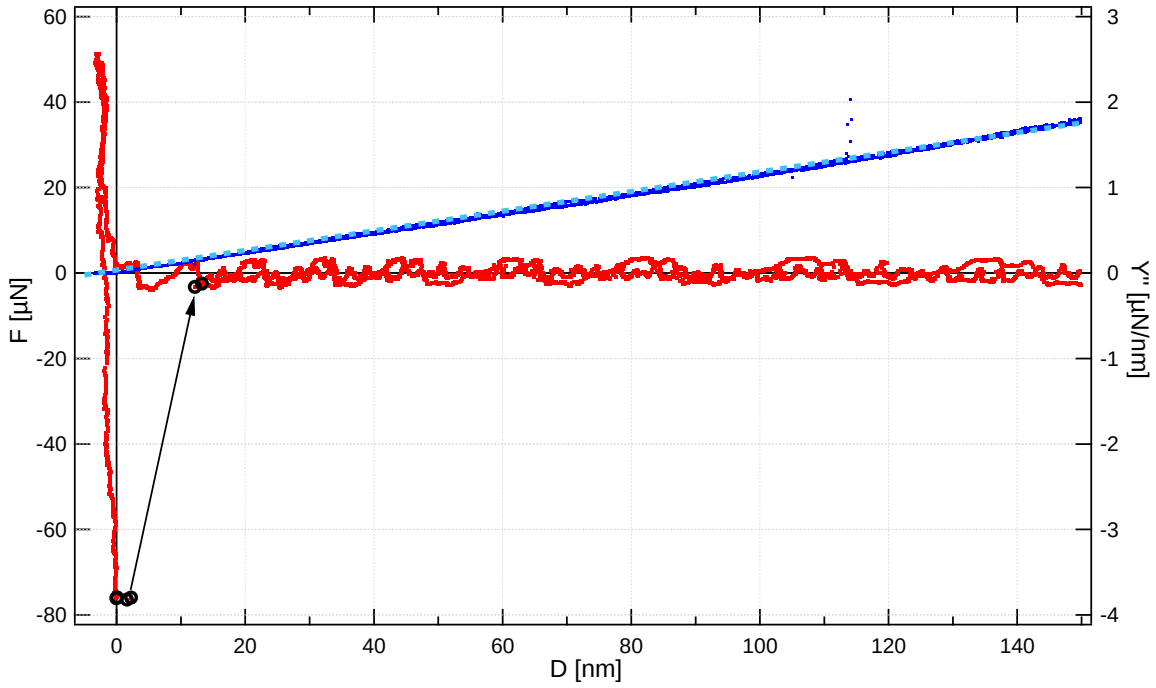

Figure 4.13 On the left axis in red, quasi-static force as a function of distance for Hexadecane and Borosilicate surfaces at 30 Hz. Strong adhesion is observed at the retraction of the surfaces. The black arrow and markers are a visual help to follow the data points at the jump of separation of surfaces. On the right axis in dark blue, the imaginary part of the mechanical admittance as a function of distance. The dashed light blue line corresponds to the linear fit of data at large distances, in agreement with the Reynolds admittance. Note that the hydrodynamic origin (intersect of the dynamic dissipation) coincides with the mechanical origin (position of force minimum).

adjusted with an elastic deformation law for the surfaces in order to determine the mechanical origin. In our geometry with $R \gg D$, the elastic deformation of the surfaces is given by the Hertz theory [49]:

$$F_{\text{Hertz}} = a(D_0 - D)^{3/2}$$

with $D \leq D_0$ and $a = \frac{4E^*\sqrt{R}}{3(1-\nu^2)}$ with $E^* = E/2(1-\nu^2)$, where E^* is the effective Young modulus, E the Young modulus and ν the Poisson ratio of the surface material and R is the radius of the sphere. Fitting the quasi-static force as a function of the distance with Hertz law allows in principle to find the mechanical contact (Figure 4.14a). However, the curve is very steep and to get a better fit, we inverse the equation:

$$D_{\text{Hertz}} = -(F/a)^{2/3} + D_0$$

and the correct mechanical contact D_0 is found. Then the distance D can be shifted by D_0, in such a way that the mechanical contact corresponds to $D = 0$ (as in Figure 4.14b). Furthermore, knowing the sphere radius $R = 2.882 \pm 0.001$ mm and taking a Poisson ratio $\nu = 0.2$ from the literature [50], we can deduce the Young modulus from the parameter a, providing $E = 64 \pm 2$ GPa, in agreement with manufacturer specifications for Borosilicate glass[4].

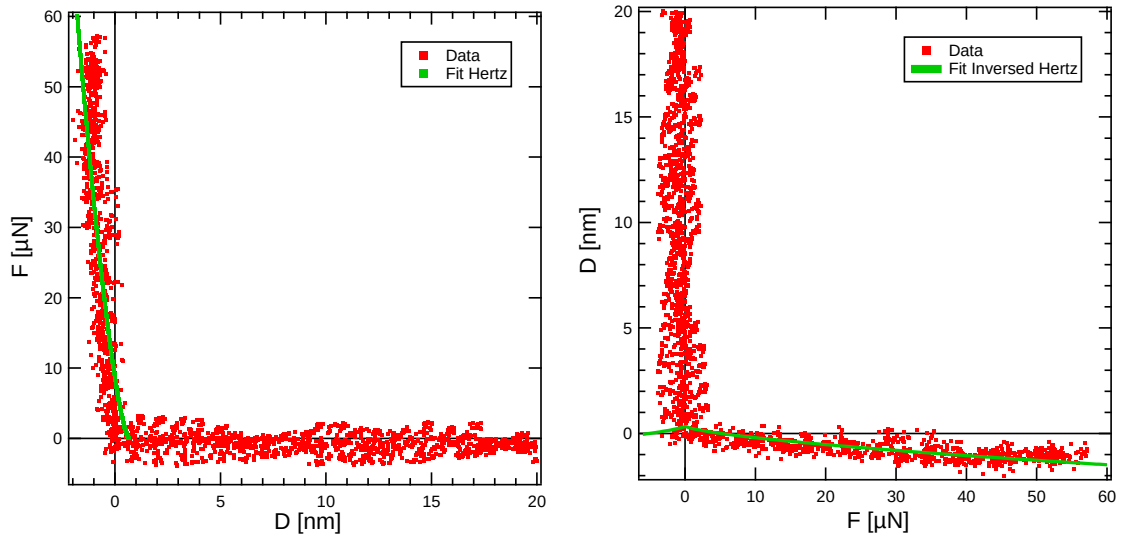

(a) Data fitted with Hertz equation.

(b) Data fitted with Hertz inversed equation.

Figure 4.14 Quasi-static force as a function of distance for Hexadecane and Borosilicate surfaces at 435 Hz. No adhesion is observed in this run. The mechanical origin is deduced from the Hertz law fit, as well as the Young modulus $E = 64 \pm 2$ GPa.

[4] Borosilicate glass - Information sheet available at https://www.continentaltrade.com.pl/en/downloads/technical-glass

4.3.2 Hydrodynamic Behavior

As shown in Figure 4.15, Y'' is proportional to the distance between the surfaces, for distances up to ~ 10 µm. Experiments with three different oscillation frequencies show that the slope of this linear relation depends on the frequency. After normalizing the admittance by frequency, all three curves are superimposed (Figure 4.16), following the Reynolds admittance (derived in section 2.2).

The slope of the master curve provides a viscosity $\eta = 2.91 \pm 0.04$ mPa s[5] at 298 ± 1 K, which agrees with tabulated values for Hexadecane $\eta = 3.03$ mPa s at 298 K and $\eta = 2.67 \pm 0.04$ mPa s at 300 K [51].

The intersection of the master curve with the X axis allows to determine the hydrodynamic origin, which is found to coincide with the mechanical origin with the experimental uncertainty of the order of ± 1 nm. In other words, we find that the hydrodynamics of this system is well accounted for with a no-slip boundary condition, in agreement with [52].

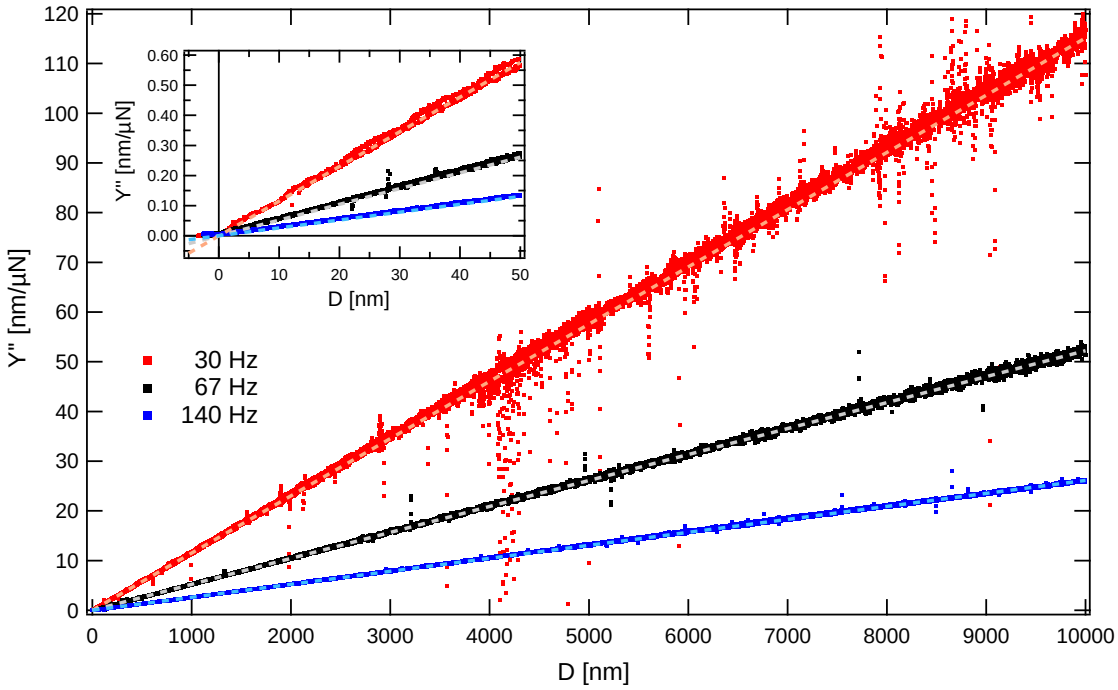

Figure 4.15 Imaginary component of the mechanical admittance as a function of separation of surfaces, for different frequencies. In all cases, the Reynolds admittance holds up to a distance of 10 µm, shown in the dashed fit lines.

[5]The limiting factor in determining the viscosity from impedance/admittance curves comes from the incertitude on the sphere radius measurement.

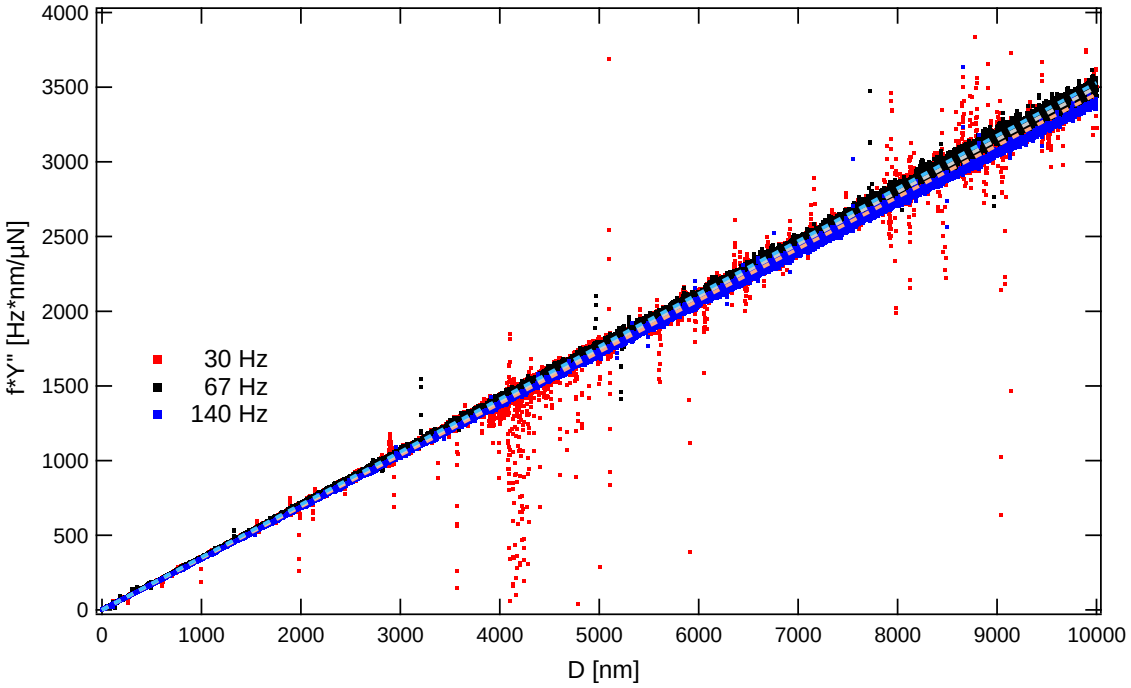

Figure 4.16 Imaginary component of the admittance normalized by frequency for three sets of experiments at 30, 67 and 140 Hz. The slightly imperfect superposition of the curves comes from the error on the sphere radius measurement. As shown by the dashed fit lines, the Reynolds admittance holds up to a distance of 10 µm.

4.3.3 Elasto-hydrodynamics

Figure 4.17 shows that at large distances the main response to the harmonic oscillation is viscous, i.e., $Z'' \gg Z'$, with a dissipative response Z'' varying as D^{-1} and an elastic response Z' varying as $D^{-5/2}$. However, as confinement increases, draining the liquid is more and more difficult, and below a critical distance $D_c \sim 3$ nm it becomes easier to deform elastically the surfaces, i.e., $Z' \gg Z''$.

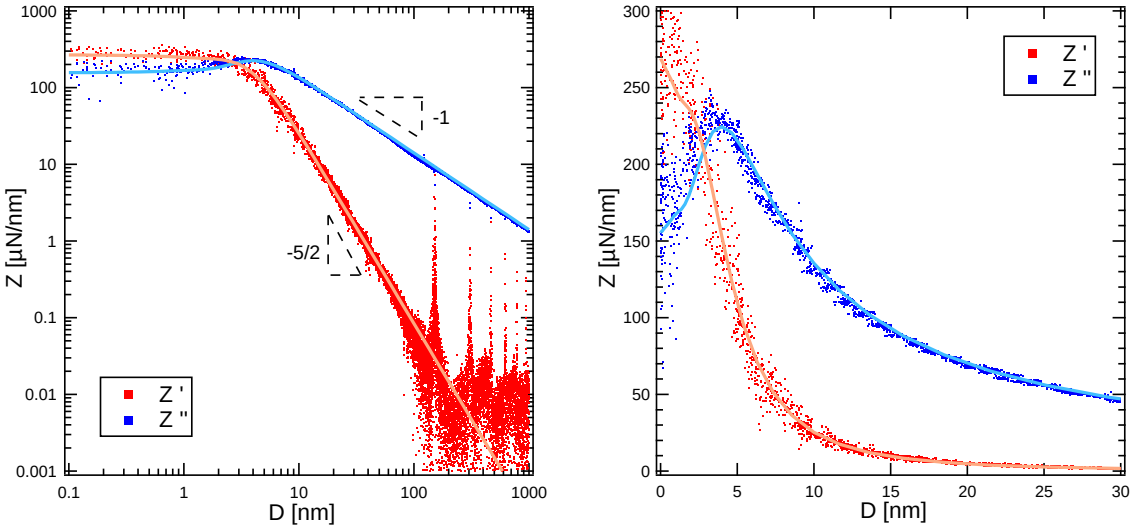

Figure 4.17 Real and imaginary components of the mechanical impedance measured for Hexadecane between Borosilicate surfaces at 435 Hz (dots), and predicted by the elasto-hydrodynamic model (lines), on log-log scale on the left and lin-lin scale on the right.

Analogous observations can be made when looking at the mechanical admittance (Figure 4.18), with at large distances a dissipative response Y'' varying as D^1 and an elastic response Y' varying as $D^{-1/2}$.

This elasto-hydrodynamic behavior is quantitatively captured by the complete theory developed by Leroy *et al.* [39] (see section 2.4). The parameters used in the calculation are the sphere radius, the frequency, the viscosity $\eta = 2.91 \pm 0.04$ mPa s obtained from the fit of the dissipation at large distances (previous section), the Young modulus $E = 64 \pm 2$ GPa obtained from the fit of the quasi-static force at large amplitudes by the Hertz model (section 4.3.1) and the Poisson ratio $\nu = 0.2$ [50].

We can see from Figures 4.17 and 4.18 that the calculation of the mechanical response, done without adjustable parameters, perfectly describes the measurements at all length scales, from macroscopic down to molecular levels.

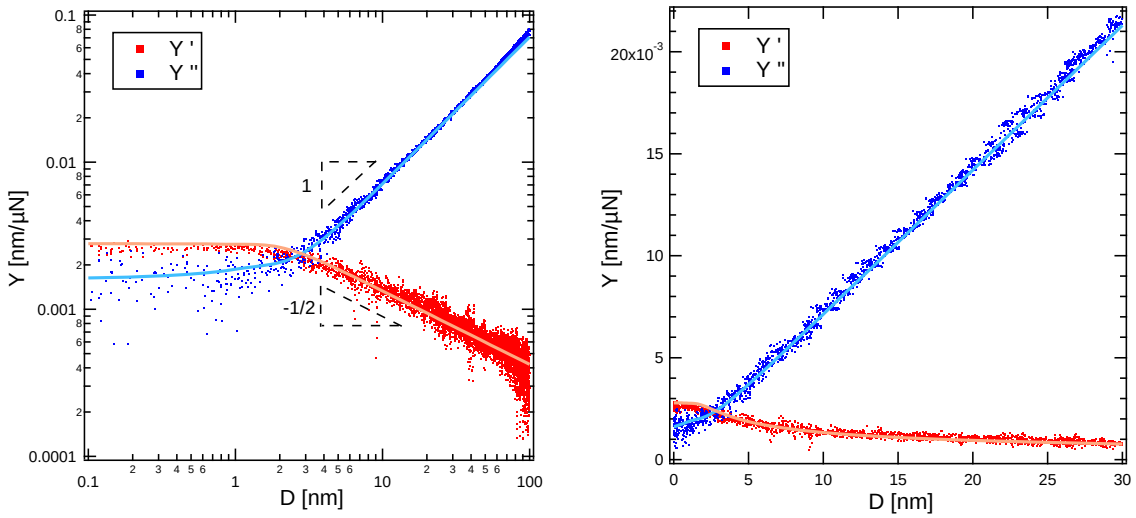

Figure 4.18 Real and imaginary components of the mechanical admittance measured for Hexadecane between Borosilicate surfaces at 435 Hz (dots), and predicted by the elasto-hydrodynamic model (lines), on log-log scale on the left and lin-lin scale on the right.

4.4 Conclusion

The dSFA at LIPhy allows the simultaneous, independent and accurate measurement of the quasi-static interaction force and of the dynamic mechanical impedance of a system composed of a fluid confined between two solid surfaces, over five orders of magnitude of confinement from 10 µm to 1 Å.

Part III

Results and Discussion

Chapter 5

Phenomenology of electrolytes in confinement

Contents

Introduction

The objective of this chapter is to present the results of measurements performed using the dSFA on NaCl aqueous solution of concentration $C = 10^{-3}$ mol/L and pH 6 confined between Borosilicate glass surfaces. We show how the electrostatic and electrokinetic phenomena that were introduced in the state-of-the-art chapters are involved in surface force measurements, in terms of quasi-static and dynamic responses.

5.1 Quasi-static response

In this section I will discuss the measured quasi-static force and how to determine the surface charge, related to the electrostatic interaction between the two charged surfaces across the electrolyte. I will show how the Poisson-Boltzmann theory describes the physics observed through the experimental data and how an error in the positioning the mechanical origin can alter the value obtained for the surface charge.

5.1.1 Electrostatic force

The quasi-static interaction force as a function of separation of surfaces is showed in Figure 5.1, for measurements performed at 32 Hz and 158 Hz. A first observation is that we have a repulsion, which is consistent with the use of symmetrical surfaces of same surface charges. We cannot deduce the sign of the surface charge from this curve, but we know from the literature that the surface charge of glass is negative at neutral pH [26].

Secondly, we observe the same exponential behavior for both curves at distances larger than a few nanometers. This is characteristic of electrostatic interactions in the limits of a weak potential $|V| \ll \frac{k_B T}{e}$, where the Poisson-Boltzmann (PB) equation can be linearized. At shorter distances, the potential increases and the exponential trend is lost. At "negative" distances, the force increases steeply because of the elastic deformation of the surfaces.

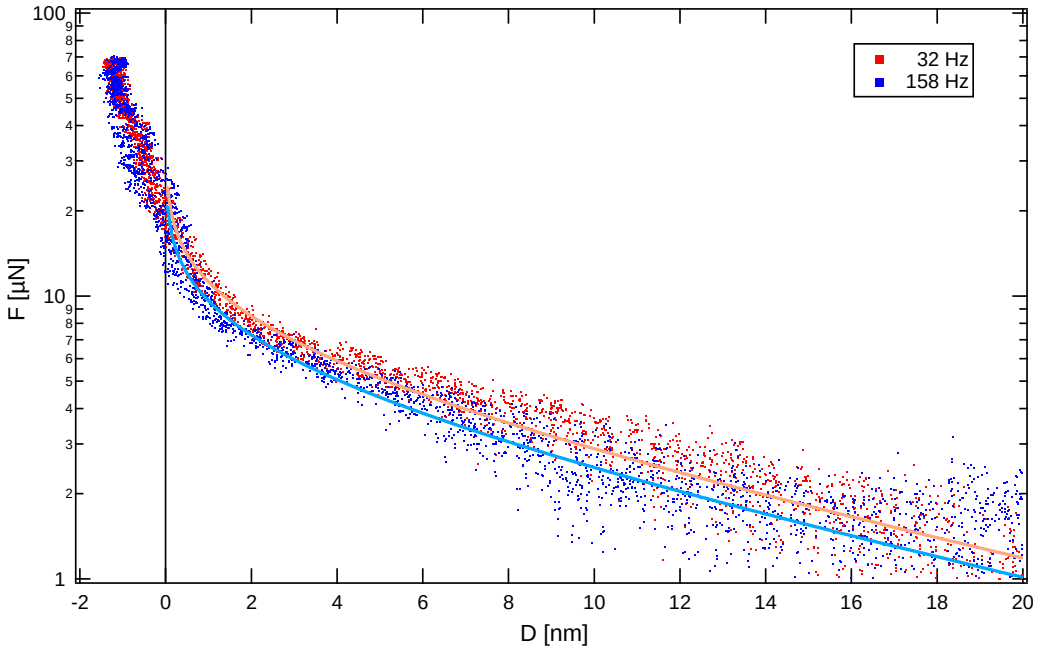

Figure 5.1 Quasi-static force as a function of distance between surfaces, for measurement done at 32 Hz and 158 Hz. The lines correspond to the adjustment with the Poisson-Boltzmann theory supposing a constant surface charge boundary condition.

To fit our data with the PB theory, two possible boundary conditions are tested: the constant surface charge and the constant surface potential. In Figure 5.2, we observe the quasi-static force-distance curve at 32 Hz with the respective PB theory adjustment at constant surface charge (in green) and constant surface potential (in black). The adjustment procedure is presented in detail, including the constant surface charge force calculation developed in Garcia's thesis, Appendix D [11]. The boundary condition that best describes our results is the constant surface charge, in agreement with experiments performed on similar systems [13]. The screening length is given by the length-scale of the exponential decay, corresponding to 12 ± 0.5 nm, close to the Debye length of 10 nm expected for the chosen salt concentration ($C = 10^{-3}$ mol/L). The surface charge is determined by the height of the exponential curve and the shape of the force profile at short distances. The adjustment with a constant surface charge boundary condition results in an absolute value of the surface charge equal to $|\sigma| = 4.9 \pm 0.3$ mC/m^2. Using the Grahame equation, this value of surface charge corresponds to an absolute value of surface potential equal to $|V_s| = 65 \pm 0.5$ mV. Both values are in agreement to the ones which can be found in the literature [11, 53].

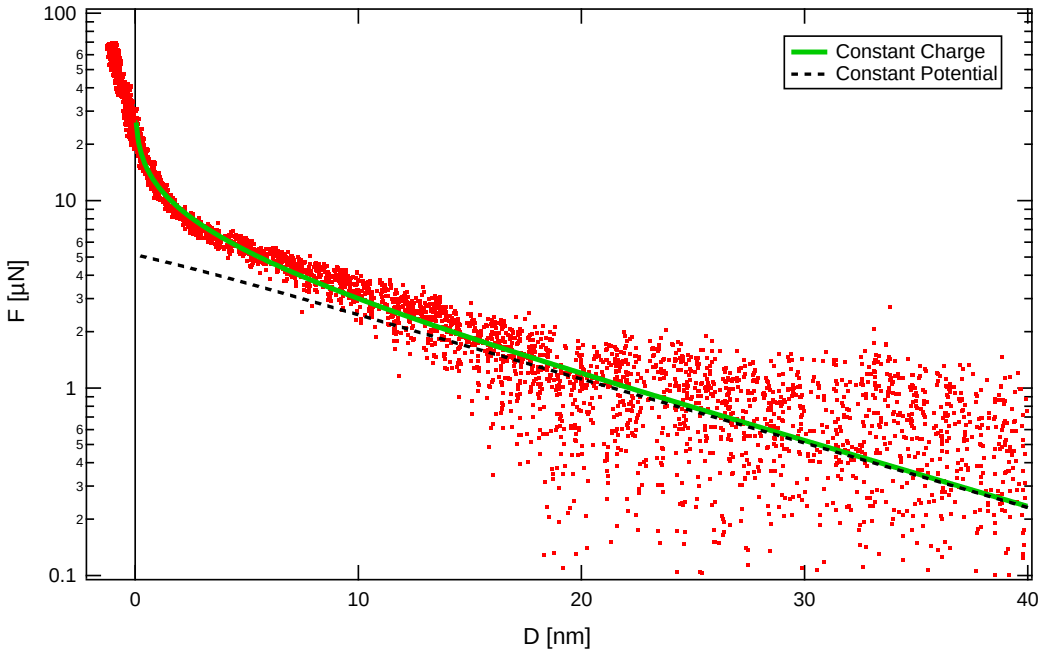

Figure 5.2 Quasi-static force as a function of distance between surfaces, at 32 Hz. The green full line is a fit with the PB theory supposing a constant surface charge boundary condition, while the dashed black line corresponds to the PB theory with a constant surface potential boundary condition.

5.1.2 Influence of the mechanical origin

The position of the origin of distances is defined as the mechanical contact between the surfaces. It has no effect on the fitted screening length. However, the determination of the surface charge is based on an important hypothesis, which is that the contact position of surfaces has been perfectly determined. An error in the origin of distances directly translates into an error in the surface charge.

One can estimate that the mechanical origin is determined with an error of ±1 nm with the method described in section 4.3.1. Figure 5.3 presents the quasi-static force at 32 Hz, for three different mechanical origins, shifted by -1 nm, 0 nm and +1 nm. The PB theory is used to fit the data. As expected, the Debye length is the same in all cases, but the absolute value of the surface charge results in 4.4 mC/m^2, 4.9 mC/m^2 and 5.4 mC/m^2 for the green, red and blue curves respectively. Therefore, the error of ±1 nm on the mechanical contact of surfaces induces an error of ±0.5 mC/m^2, i.e., 11% on the surface charge.

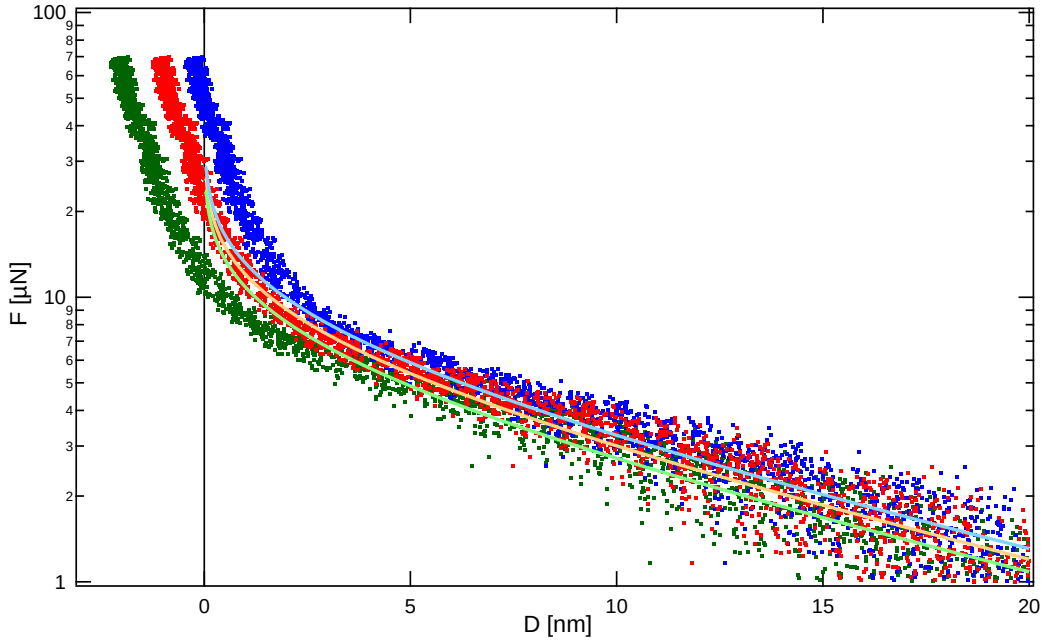

Figure 5.3 Effect of the position of the origin of distances on the surface charge, for the quasi-static forces at 32 Hz. A difference on the position of surfaces of ± 1 nm results in a change of surface charge values of ±0.5 mC/m^2.

5.2 Conservative contribution to the dynamic response

At the same time as the equilibrium response is measured, the dynamic response is characterized by the mechanical impedance. In this section, the real part Z' is presented, corresponding to the conservative dynamic response of the confined electrolyte.

5.2.1 Dependence with the frequency?

Figure 5.4 presents the real part of the mechanical impedance for 32 Hz and 158 Hz as a function of the separation of distances. All the necessary corrections (for drifts, residuals, etc.) have been applied to the data, except the machine stiffness which deserves to be discussed here since we have a priori a non-zero elastic response of the liquid film.

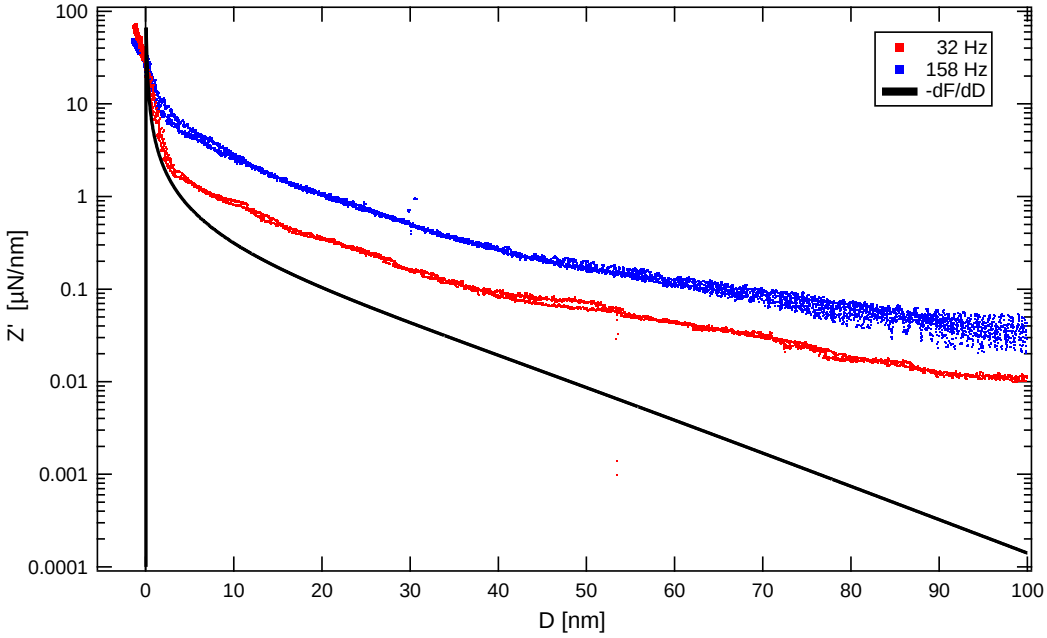

Figure 5.4 Elastic part of the mechanical impedance for measurements performed at 32 Hz and 158 Hz. All corrections on the data are done, except the machine stiffness which is left as infinite.

At zero frequency, the elastic part of the dynamic response should coincide with the quasi-static response, i.e., we expect to get:

$$Z'_{\text{eq}} = -\frac{\mathrm{d}F}{\mathrm{d}D} \tag{5.1}$$

We plotted on Figure 5.4 the opposite derivative of the quasi-static force-distance curve, which we calculated by taking the derivative of the fit with the PB theory. Although with a shape compatible with exponential behaviors, we observe that the elastic response exhibits an amplitude which is significantly larger than the quasi-static limit and which increases with the frequency. Such behavior was already observed during the thesis of Léo Garcia, and has been qualitatively attributed to the relaxation dynamics of the electric double layers [11].

In the following sections, I will show that this effect is an experimental artefact due to the machine stiffness.

5.2.2 Influence of the machine stiffness

The determination of the right value of the machine stiffness K_M is not straightforward. After correction of the residuals (see 4.2.4), the slope of $1/\sqrt{Z'}$ as a function of distance should provide the value of the machine stiffness (as shown in section 4.2.5). However, in Figure 5.5 we observe that the slope of $1/\sqrt{Z'}$ depends on the distance interval chosen for the fit, giving different values for the machine stiffness K_M, respectively:

- $K_M = 240$ µN/nm between ~ 140 nm and ~ 170 nm,
- $K_M = 15$ µN/nm between ~ 70 nm and ~ 140 nm,
- $K_M = 4$ µN/nm between ~ 0 nm and ~ 70 nm.

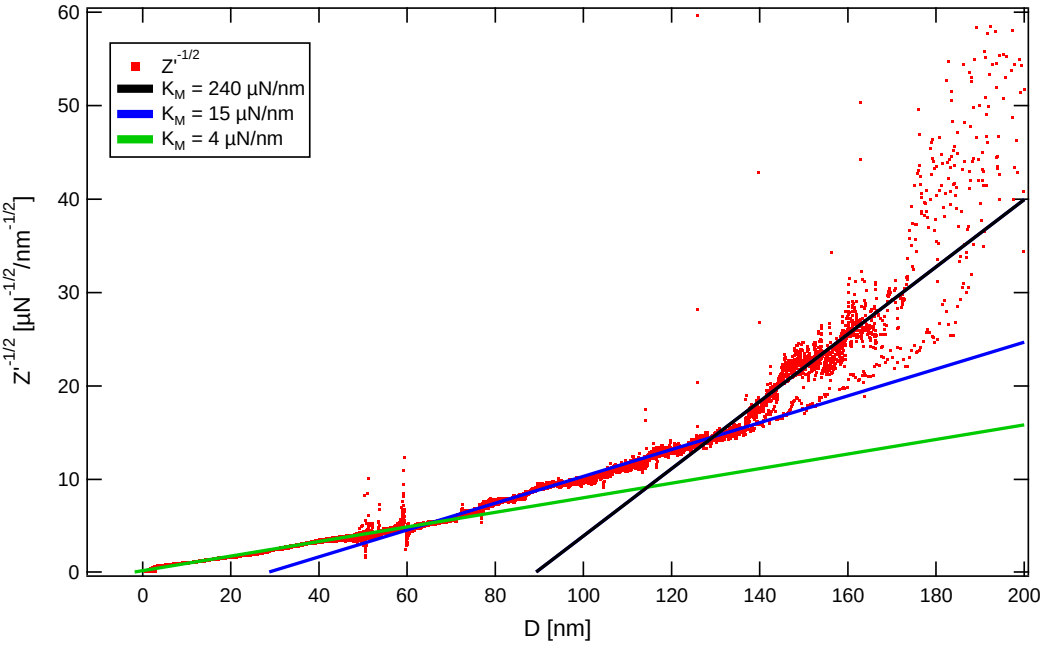

Figure 5.5 Fitting of $1/\sqrt{Z'}$ as a function of distance for a experiment at 32 Hz. The distance interval chosen to fit the slope results in different values of the machine stiffness.

Figure 5.6 shows the resulting Z' curves obtained with these machine stiffness values:

- $K_M = 240$ µN/nm has no effect on the data,
- $K_M = 15$ µN/nm reduces the amplitude of the elastic response,
- $K_M = 4$ µN/nm results in nonphysical negative values for the elastic response.

The difficulty comes from the fact that a long-range electrostatic interaction is involved, contrary to the case of Hexadecane which was described in section 4.2.5, for which the

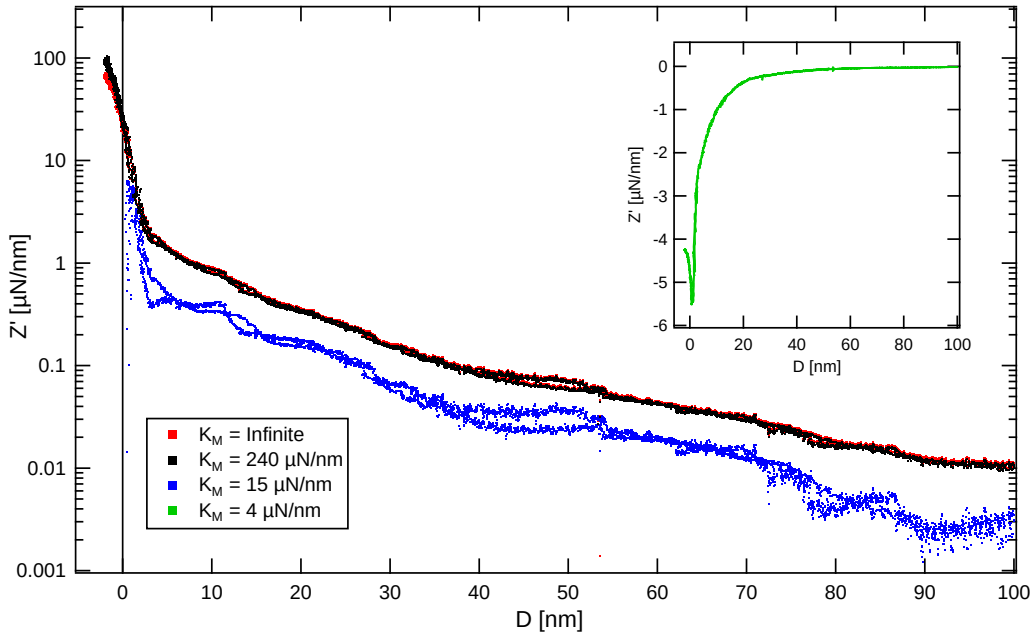

Figure 5.6 Conservative part of the mechanical impedance at 32 Hz after correction of different machine stiffness values, taken from the fits in Figure 5.5 obtained at different distance intervals.

dynamic response was piloted by elasto-hydrodynamics only. Therefore, we have to adapt the method of determination of the machine stiffness in the case where an electrostatic contribution is present in Z'. By inverting equation 4.1 we get:

$$Z_{\text{true}} = \frac{Z_{\text{meas}}}{1 - \frac{Z_{\text{meas}}}{K_{\text{M}}}} \simeq Z_{\text{meas}} + \frac{{Z_{\text{meas}}}^2}{K_{\text{M}}} \tag{5.2}$$

at first order in $\frac{|Z_{\text{meas}}|}{K_{\text{M}}} \ll 1$ (condition 1). The real and imaginary parts of this equation read:

$$Z'_{\text{true}} \simeq Z'_{\text{meas}} + \frac{{Z'_{\text{meas}}}^2 - {Z''_{\text{meas}}}^2}{K_{\text{M}}} \simeq Z'_{\text{meas}} - \frac{{Z''_{\text{meas}}}^2}{K_{\text{M}}} \tag{5.3}$$

$$Z''_{\text{true}} \simeq Z''_{\text{meas}} \left(1 + \frac{2Z'_{\text{meas}}}{K_{\text{M}}}\right) \tag{5.4}$$

if $|Z'_{\text{meas}}| \ll |Z''_{\text{meas}}|$ (condition 2). At large distances ($D \gg D_{\text{c}} \sim 3$ nm - condition 3) the elasto-hydrodynamic response is mostly viscous and given by the Reynolds formula, i.e., $Z''_{\text{true}} = \frac{6\pi\eta\omega R^2}{D}$. We combine the last two equations to obtain, at first order in $\frac{|Z_{\text{meas}}|}{K_{\text{M}}}$:

$$Z'_{\text{true}} \simeq Z'_{\text{meas}} - \frac{(6\pi\eta\omega R^2)^2}{K_{\text{M}} D^2} \tag{5.5}$$

To determine the machine stiffness, we should obtain a linear relationship between $1/\sqrt{Z'_{\text{meas}}}$ and D. This happens only in a distance range where the physically relevant contributions to Z'_{true} (electrostatics and elasto-hydrodynamics) are negligible compared to the machine stiffness term, i.e., $|Z'_{\text{el}}|, |Z'_{\text{eh}}| \ll \frac{{Z''_{\text{meas}}}^2}{K_{\text{M}}}$ (condition 4).

In Figure 5.7 are shown the real and imaginary parts of the measured impedance as a function of the distance in semi-log scales. On one hand, we observe that the imaginary part is a least one order of magnitude larger than the real one, i.e., condition 2 is fulfilled, for distances $D \gtrsim 70$ nm. On the other hand, we see that real part changes abruptly and becomes extremely small for distances $D \gtrsim 140$ nm. This is due to the lock-in amplifiers, which are not able to resolve phase differences smaller than 0.01°, corresponding to a ratio $\left|\frac{Z'_{\text{meas}}}{Z''_{\text{meas}}}\right|$ smaller than $\sim 10^{-4}$. Therefore, it appears clearly that only distances ranging from ~ 70 nm to ~ 140 nm are appropriate for the determination of the machine stiffness, giving $K_{\text{M}} = 15$ µN/nm.

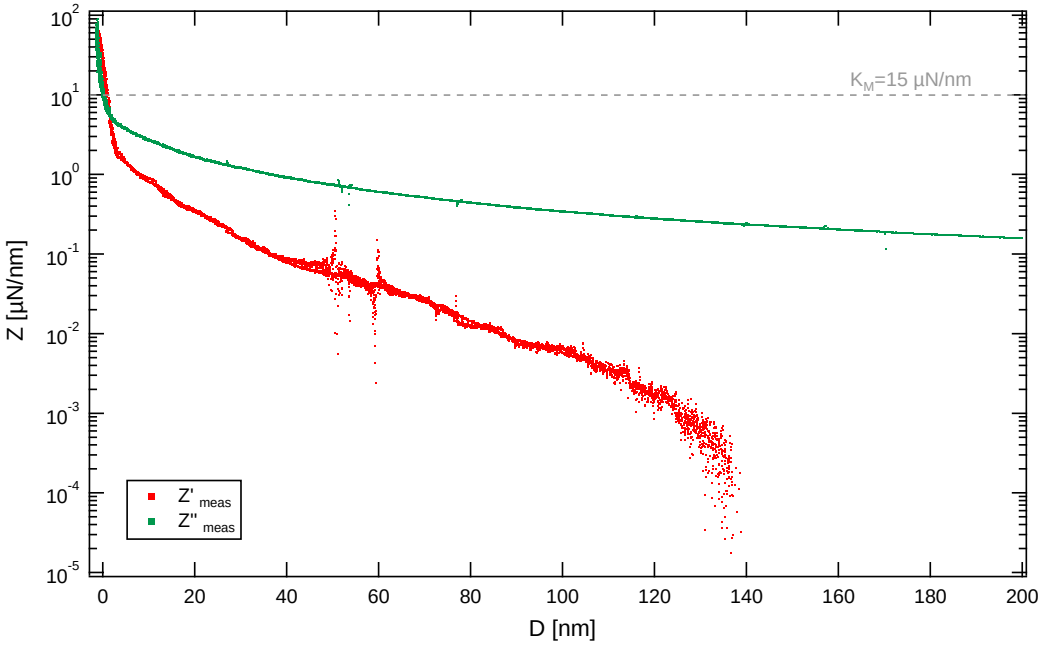

Figure 5.7 Comparison between the conservative Z' and dissipative Z'' components of the mechanical impedance measured at 32 Hz (before correction of the machine stiffness), and the machine stiffness $K_{\text{M}} = 15$ µN/nm.

Then, one has to check that this distance interval and this value of machine stiffness allow to verify the conditions listed previously. In Figure 5.7 we observe that this value of machine stiffness is much larger than the impedance in the considered distance range, i.e., condition 1 is fulfilled. Condition 3, i.e., $D \gg D_{\text{c}} \sim 3$ nm, is also trivially true. To assess whether condition 4 is verified, we plotted in Figure 5.8 the correction factor ${Z''_{\text{meas}}}^2/K_{\text{M}}$, the measured real impedance Z'_{meas}, the contribution Z'_{eh} from the elasto-hydrodynamics theory,

and the electrostatic contribution Z'_{el}, supposed equal to the equilibrium one $Z'_{\mathrm{eq}} = -\frac{\mathrm{d}F}{\mathrm{d}D}$. This graph confirms the fact that, between ~ 70 nm and ~ 140 nm, the correction factor is much larger than the physically relevant contributions to Z'_{true}, and it accounts for most of the measured real impedance Z'_{meas}.

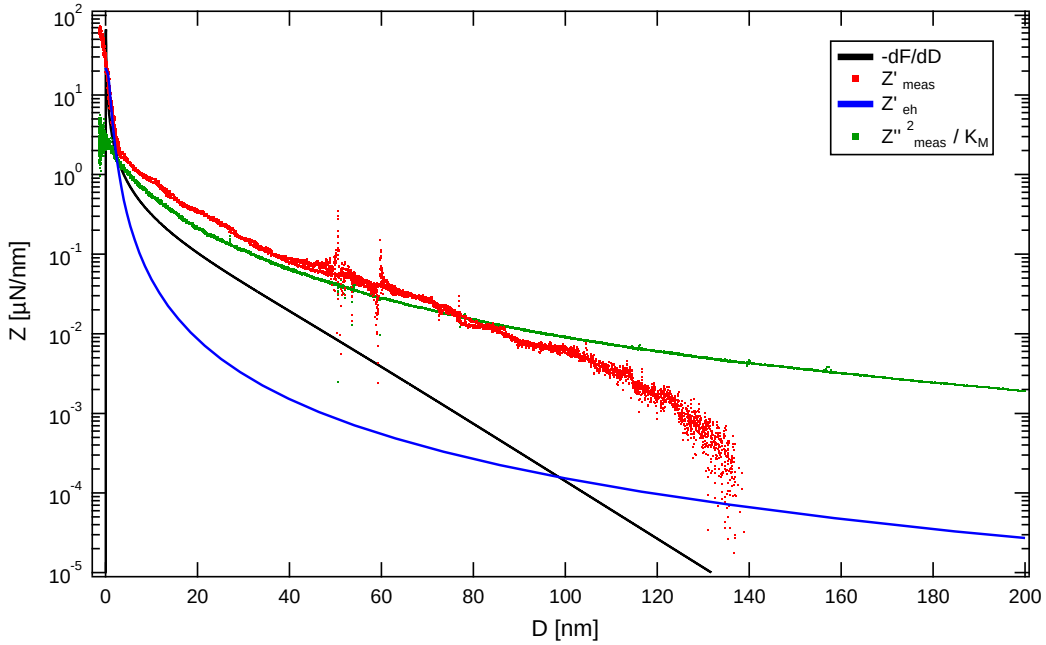

Figure 5.8 Comparison between the conservative component expected at zero frequency, Z' measured at 32 Hz (before correction of the machine stiffness), and the correction factor ${Z''_{\mathrm{meas}}}^2/K_{\mathrm{M}}$.

The Z'_{true} curves at 32 Hz and 158 Hz, after correction of the machine stiffness, are shown in Figure 5.9. Their amplitudes have been lowered by the correction, making the frequency effect disappear and the curves superpose each other. The curves are also well superimposed with the equilibrium prediction Z'_{eq}, given the noise on the dynamic and quasi-static measurements. Note that the latter is not visible in this representation, as we have shown the negative derivative of the PB fit to the quasi-static force profile.

More precisely, we observe:

- at 32 Hz (Figure 5.10a), that the main origin of Z' is the electrostatic equilibrium contribution, while elasto-hydrodynamics plays a negligible role,
- at 158 Hz (Figure 5.10a), that the origins of Z' are elasto-hydrodynamics and electrostatics, with the former acting almost twice as much the latter.

We used our method of machine stiffness correction to reanalyze the data from Garcia [11], which were obtained with Propylene Carbonate at 30 Hz and 220 Hz (Figures 5.11a and 5.11b). This allowed us to confirm our interpretation with another set of data, i.e., the

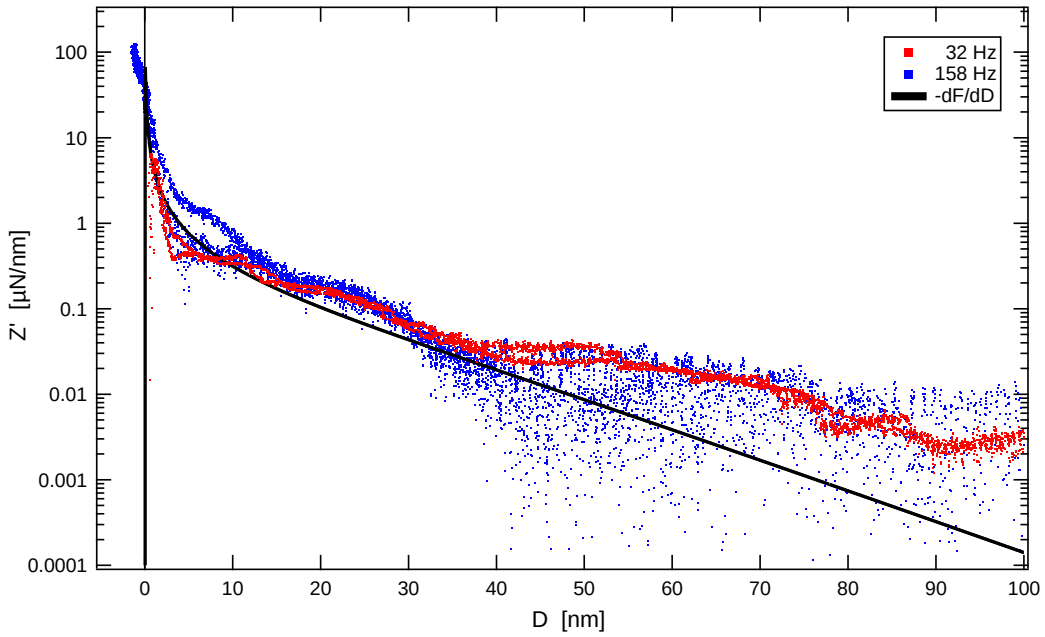

Figure 5.9 Z' curves at 32 Hz and 158 Hz after correction of the right value of the machine stiffness, i.e., $K_{\mathrm{M}} = 15$ µN/nm. Both sets of data agree with the equilibrium response predicted by Eq. 5.1, given the noise on the dynamic and quasi-static measurements (the latter being not visible in this representation).

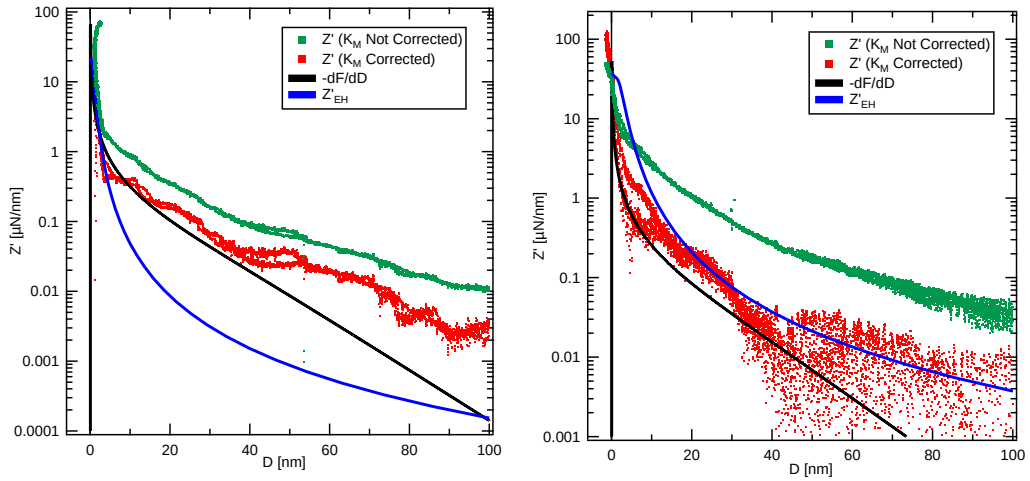

(a) Experiment at 32 Hz

(b) Experiment at 158 Hz

Figure 5.10 Correction of the machine stiffness on the real part of the measured mechanical impedance. Comparison with the negative derivative of the quasi-static force and the conservative contribution predicted by the elasto-hydrodynamic theory.

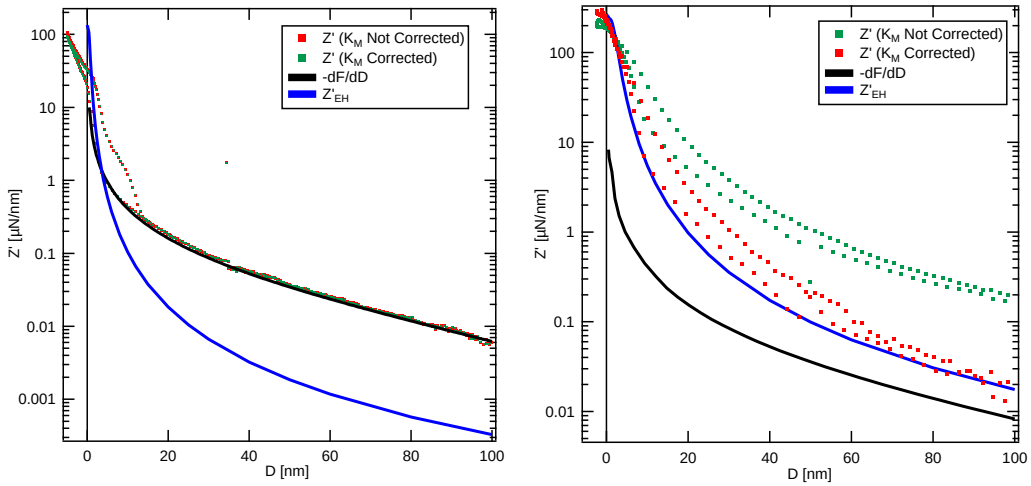

(a) Experiment at 30 Hz

(b) Experiment at 220 Hz

Figure 5.11 Correction of the machine stiffness on the real part of the measured mechanical impedance, from Garcia's results [11]. Comparison to the negative derivative of the quasi-static force and the conservative contribution predicted by the elasto-hydrodynamic theory.

fact that the conservative dynamic response of the confined electrolyte is not affected by a relaxation process of the electric double layers, but is due to the electrostatic repulsion between the surfaces and the elasto-hydrodynamic deformation of the surfaces. To summarize, with our current resolutions and in the frequency range explored, we have no evidence of a frequency dependence of the conservative response associated to the electrical double layer.

Finally, note that here we have considered two limit models:

- electrostatics with rigid surfaces,
- elasto-hydrodynamics with charge-less surfaces and liquid.

In order to quantitatively fit the conservative dynamic response when these two effects are of the same order (around 80 Hz for our system), we would need a combined model describing both the electrostatics and the elasto-hydrodynamics.

5.3 Dissipative contribution to the dynamic response

In this section we discuss the measured imaginary part of the mechanical impedance Z'', corresponding to the dissipative dynamic response of the confined electrolyte. In particular, we demonstrate the presence of an electrolytic over-dissipation at short distances, compared to a Newtonian fluid of same viscosity.

5.3.1 Newtonian behavior at large distances

In Figure 5.12 we observe that the imaginary part of the admittance Y'' varies linearly with the distance between the surfaces, for two different frequencies and for distances ranging from ~ 500 nm up to 10 µm. In the inset, we show that the two curves at 32 Hz and 158 Hz are well superimposed at large distances after normalized by the frequency and the squared sphere's radius. These observations show that the dissipative response of the system follows the Reynolds behavior of confined fluids (see section 2.2).

The slope of the normalized curve provides a dynamic viscosity $\eta = 0.95 \pm 0.01$ mPa.s, in reasonable agreement with the viscosity of pure water of 0.89 mPa.s at 25°C [54]. Note that the error in the determination of the viscosity with this method mostly comes from the error in the measurement of the sphere's radius, which participates as R^2 in the expression of the admittance Y''.

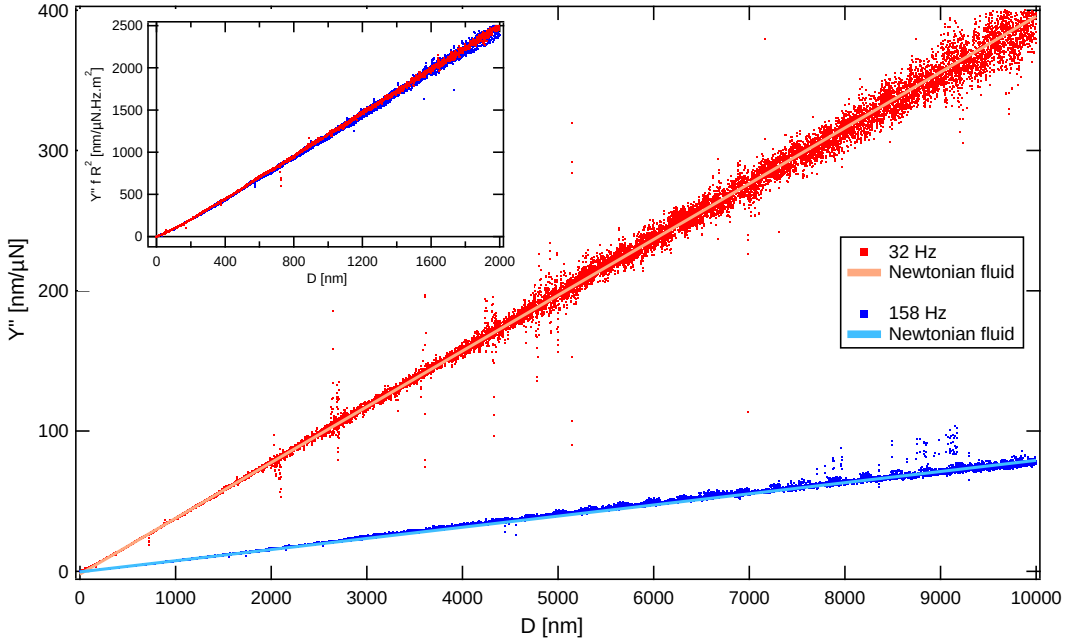

Figure 5.12 Admittance Y'' as a function of separation distance for 32 Hz in red and 158 Hz in blue, and respective linear fits at large distances. In the inset, both curves are normalized by the frequency and the squared sphere's radius.

5.3.2 Slip boundary condition

In Figure 5.13 are plotted the same data at shorter distances. We observe that the linear fits performed between ~ 500 nm and 10 µm cross the X axis at a positive distance. Such behavior is typical of a negative slip boundary condition, with a negative slip length $b = 49 \pm 1$

nm (see section 2.3). This corresponds to a situation where the no-slip plane is located within the liquid phase.

Generally, such slip boundary condition is qualitatively interpreted as two films of thickness $b/2 = 24.5 \pm 0.5$ nm at the vicinity of the solid surfaces that do not flow [34]. However, characterizing the slip boundary condition from large scale extrapolation tells us nothing about the microscopic origin of such slip. To this end, one has to look at the data at shorter distances. This is the purpose of the next section.

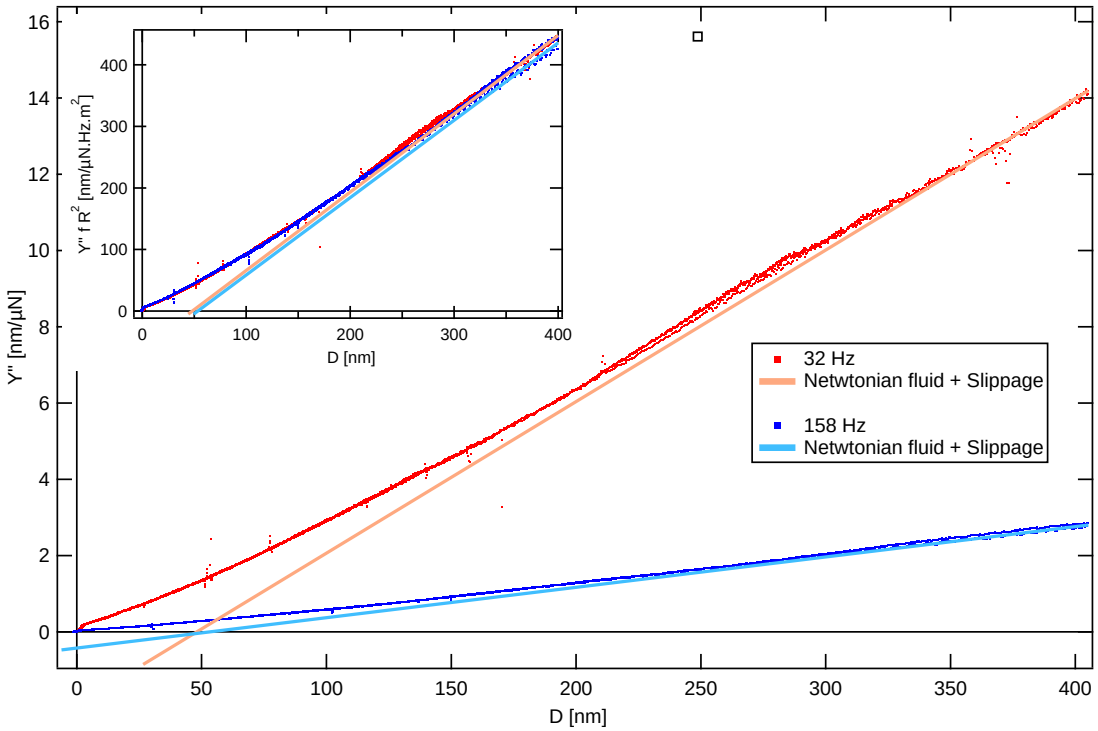

Figure 5.13 Admittance Y'' as a function of separation distance for 32 Hz in red and 158 Hz in blue, the two curves being normalized by the frequency and the squared sphere's radius. The linear fits stand for the Reynolds behavior at large distances, crossing the X axis at a negative slip length $b = 49 \pm 1$ nm.

5.3.3 Over-dissipation

In Figure 5.14 is represented the proportional law expected for a Newtonian fluid of same viscosity but with no slippage. To do so, the linear fit at large scales has been shifted to pass through the origin. We clearly see that the data are located below this reference line, showing that the measured imaginary part of the admittance is smaller than the Reynolds admittance. In other words, the system exhibits an over-dissipation in comparison with a Newtonian fluid of same viscosity without slippage.

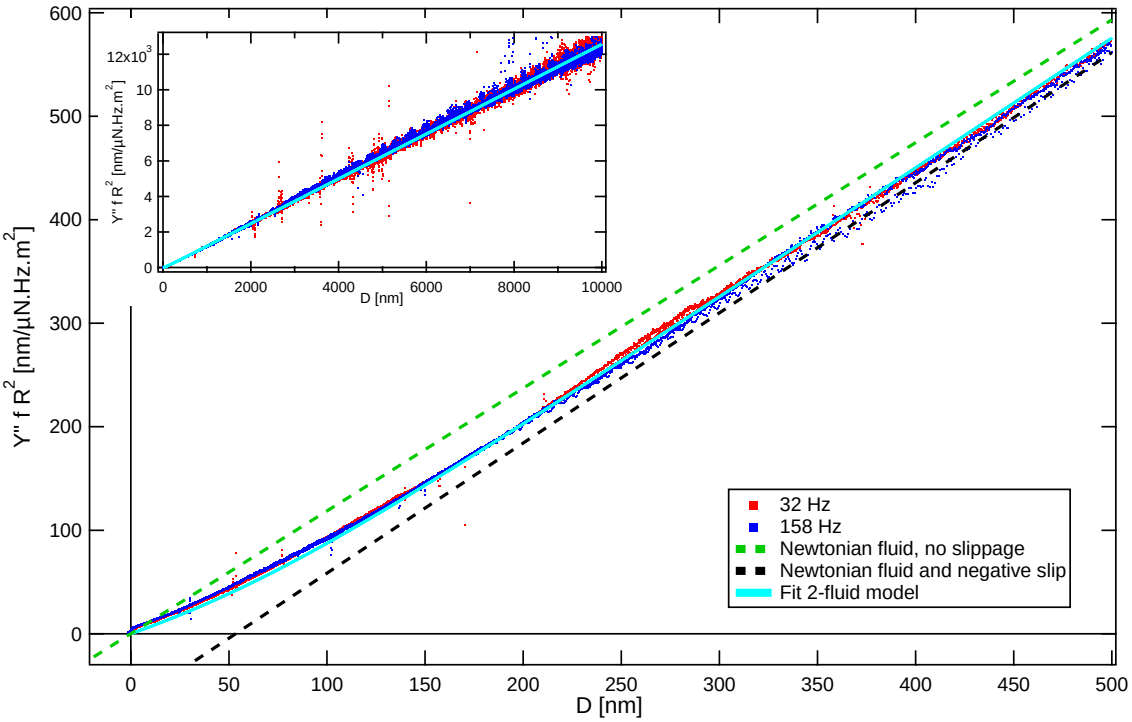

Figure 5.14 Admittance Y'' as a function of separation distance for 32 Hz in red and 158 Hz in blue, the two curves being normalized by the frequency and the squared sphere's radius. The black dashed line is the linear fit at large distances, while the green dashed line represents what would have been the result of a Newtonian fluid of same viscosity but with no slippage. The two-fluid model fit in bright blue describes our data accurately.

More precisely, the two curves at 32 Hz and 158 Hz are remarkably well superimposed at small distances after normalizing by the frequency, showing that the over-dissipation is simply proportional to the excitation frequency. In addition, we observe at large distances that the imaginary admittance as a function of the distance exhibits a slope that is consistent with the bulk viscosity. But below $\sim$ 500 nm, the curve starts to bend with a slope that decreases even more as the mechanical contact is approached. This progressive inflection corresponds to an "effective" viscosity (linked to the inverse of the slope) which grows with confinement.

The concept of effective viscosity has been used by Chauveteau *et al.* in 1984 [55] to describe the rheology of polymer solutions flowing in micrometric pores. In the case of repulsive walls, they observed a decrease of the effective viscosity when the pore size was reduced, which they attributed to a depletion layer near the walls. On the contrary, in the case of attractive walls, they observed an increase of the effective viscosity when the pore size was reduced, which they attributed to the adsorption of polymers onto the walls.

A similar reduction with confinement of the effective viscosity of polymer solutions has been measured with the dSFA during the thesis of Chloé Barraud at LIPhy [12]. A two-fluid model, illustrated in Figure 5.15, has been developed to account for such effective viscosity reduction [56]. It consists in splitting the confined fluids into two regions : a fluid of bulk viscosity η_{bulk} in the middle of the gap, and a fluid of viscosity $\eta_{\text{layer}} \neq \eta_{\text{bulk}}$ forming a liquid layer of thickness e covering the solid surfaces. The underlying idea was that the depleted region near the walls presents a smaller viscosity than the bulk polymer solution, equal to the solvent viscosity. The two-fluid model formally expresses the imaginary admittance as:

$$Y'' = -\frac{D}{6\pi\eta_{\text{bulk}}\omega R^2 f^*(\frac{D}{e}, \frac{\eta_{\text{layer}}}{\eta_{\text{bulk}}})} \tag{5.6}$$

where f^* is a master function which depends on the ratio between the surface separation and the layer thickness and the ratio between the layer viscosity and the bulk viscosity. At large distances $D \gg e$, f^* tends towards 1 and the dissipation is dominated by the fluid in the bulk. At small distances $D \ll e$, f^* tends towards $\eta_{\text{layer}}/\eta_{\text{bulk}}$ and the dissipation is dominated by the fluid in the layers. More details on the model can be found in [56].

We tested whether such two-fluid model is able to describe our data quantitatively. In Figure 5.14 we can observe that a remarkably good fit of the normalized admittance at 32 Hz and 158 Hz can be achieved at all scales, with a bulk viscosity $\eta_{\text{bulk}} = 0.95 \pm 0.01$ mPa.s determined at large scales and layers of thicknesses $e = 50 \pm 1$ nm and viscosity $\eta_{\text{layer}} = 1.75 \pm 0.05$ mPa.s determined at small scales. Note that in the present case the model accounts for an increase of the effective viscosity, with a fluid which is more viscous at the solid-liquid interfaces than in the bulk, with $\eta_{\text{layer}}/\eta_{\text{bulk}} = 1.8 \pm 0.08$.

The two-fluid model seems effective to describe our data, and it allows to characterize quantitatively the over-dissipation. However, the observed increase in effective viscosity

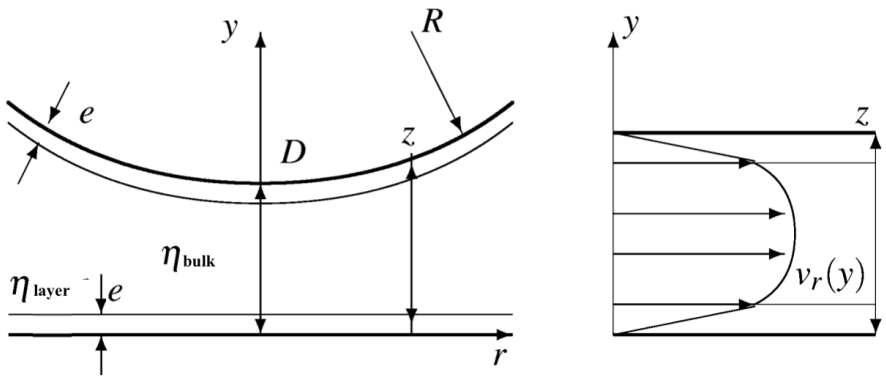

Figure 5.15 Schematic of the variables present in the two-fluid model, where a liquid layer of thickness e and viscosity η_{layer} is covering both the sphere and the plane, and the surrounding fluid has a viscosity η_{bulk}. Figure adapted from [56].

cannot not be explained by an increase in ionic concentration in the EDL. Considering $C_{\pm}(z) = Ce^{\mp\frac{eV}{k_{\text{B}}T}}$ and that the glass surface is negatively charged at neutral pH, the cations are in excess in the EDL in comparison with the bulk, and their concentration is bounded by $Ce^{+\frac{e|V_{\text{s}}|}{k_{\text{B}}T}}$, with $|V_{\text{s}}| = 65 \pm 0.5$ mV the absolute value of the surface potential. For a concentration in solution of $C = 1.10^{-3}$ mol/L, we obtain 2.10^{-2} mol/L as the upper limit of ionic concentration in the diffuse layer. A paper by Kestin *et al.* [57] reports viscosities of NaCl aqueous solutions, for concentrations larger than the one discussed here. At 20°C, the viscosity varies from 1.002 mPa.s for pure water to 1.043 mPa.s for a 0.5 mol/L solution, therefore the increase in viscosity due to ion excess in the EDL is much smaller than the one given by the two-fluid model.

Similarly, the observed increase in effective viscosity cannot be reasonably related to the electroviscous effects reported by Klein [58]. In the vicinity of the surface, we have an electric field E that could have an influence on the viscosity of the diffuse ionic layer. Indeed, viscous friction can increase under the effect of an electric field according to the relation $\eta(E) = \eta_{\text{bulk}}(1 + fE^2)$. Taking the measured value of $f = 1.10^{-15}$ m^2/V^2 for water [58] and assuming an electric field in the electric double layer given by the surface potential divided by the Debye length $E \approx 65$ mV/12 nm, we find a viscosity increase of $\sim 3\%$ for $\eta(E)$ well below the values found here for η_{layer}.

As it is an effective model, it does not tell us much about the underlying physics. If the over-dissipation is not due to the increase in viscosity under an electric field, it can only originate from electrokinetic transport phenomena in the electrolyte, which is confined between charged surfaces. A possible general mechanism is illustrated in Figure 5.16. Qualitatively, when the surfaces are approached, a viscous flow leads to the ejection of the electrolyte from the apex towards the sides. As the surfaces are charged and the electric double layers are electrically non-neutral, counter-ions are virtually in deficit at the apex and in excess far

away. Such unbalance virtually creates radial gradients of concentration and electric potential, leading to diffusio-osmotic and electro-osmotic flows. These counter-flows would ultimately result in an over-dissipation and apparent slippage, in comparison with a charge-less fluid of same viscosity.

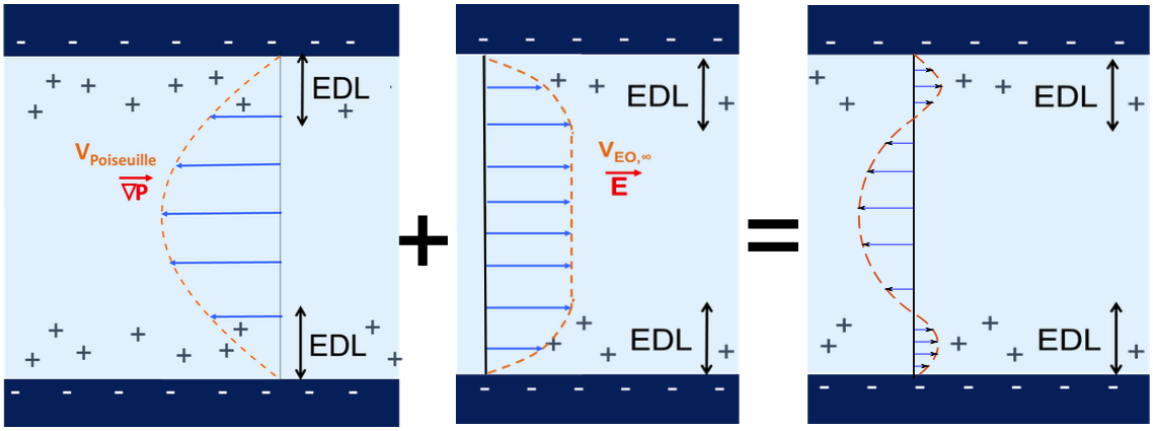

Figure 5.16 Schematic of the formation of simultaneous electrokinetic flows: a Poiseuille flow is induced by a pressure gradient and drags charged electric double layers, which in its turn induces concentration and electric potential gradients, creating diffusio-osmotic and electro-osmotic flows. Credits: [11].

Preliminary measurements of Garcia's thesis [11] had allowed to glimpse this over-dissipation. During my thesis, I have first confirmed the presence of such over-dissipation. My second goal was to collect new experimental information in order to achieve a more precise understanding of the mechanisms at play. In particular, a central question was the confinement scale at which such over-dissipation emerges. In this perspective, it is worth noting that the range of the over-dissipation obtained in this reference measurement, characterized empirically by the negative slip length or the layer thickness in the two-fluid model, seems to correspond to the scale given by the Dukhin length ($\ell_{Du} = 51$ nm), and not by the Gouy-Chapman length ($\ell_{GC} = 7.3$ nm) or the Debye length ($\lambda_D = 12$ nm). These aspects will be discussed in chapter 6.

5.4 Conclusion

In this chapter, I have chosen to present the phenomena observed experimentally with the dSFA, for a representative system composed of an aqueous solution of NaCl at 10^{-3} mol/L and pH 6 confined between Borosilicate glass surfaces. We have shown that :

- The quasi-static response presents a repulsive electrostatic force, which can be fitted with the Poisson-Boltzmann theory to obtain a true, equilibrium surface charge (unlike most of the literature which relies on transport measurements),

- The measured electrostatic force is best described with a constant surface charge boundary condition, and the value of the surface charge critically depends on the determination of the mechanical contact between the surfaces,
- The conservative dynamic response can be explained by the combination of electrostatics and elasto-hydrodynamics (model to be developed), after accurate correction of the machine stiffness,
- The dissipative dynamic response exhibits an over-dissipation at small distances, which is the signature of electrokinetic phenomena at play, leading to an apparent negative slip length,
- The over-dissipation is proportional to the excitation frequency, opening the way to the concept of effective viscosity that increases with confinement, and which can be characterized quantitatively thanks to a two-fluid model.

Chapter 6

Influence of Screening Length, Surface Charge and of Nature of the Surfaces

Contents

Introduction

After having presented in Chapter 5 a reference measurement obtained with a NaCl aqueous solution at a concentration of $C = 10^{-3}$ mol/L and pH 6 confined between Borosilicate glass surfaces, this chapter aims to investigate the influence of key parameters on the electrolytic over-dissipation.

In order to determine the role of the screening length λ_D, the ion concentration C of the solution was varied. In the same way, solutions with different pH allowed us to analyze the influence of the surface charge σ of Borosilicate glass. Finally, the Borosilicate glass surface was coated with a Boron Nitride (BN) layer, which has been reported as a promising material for energy conversion in nanofluidic applications [6].

In each section, the results are compared to the reference measurement presented in Chapter 5 (here in red in all graphs). Because all these dSFA experiments have been performed with different sphere radii R and excitation frequencies f, a proper normalization of the

measurements by these parameters was required in order to compare them. Therefore, I present the results for the quasi-static measurement as a normalized quasi-static force-distance curve $F/R(D)$ (following the Derjaguin approximation presented in Chapter 1), and the results for the dynamic measurement as a normalized imaginary admittance - distance curve $Y''fR^2(D)$ (according to the observations made in Chapter 5).

6.1 Varying the screening length λ_D with the ion concentration C

I performed two experiments at different concentrations of NaCl in water at pH 6, confined between Borosilicate surfaces : $C_1 = 10^{-3}$ mol/L (reference) and $C_2 = 10^0$ mol/L.

Figure 6.1 shows the measured quasi-static force-distance curves, and the corresponding adjustments with the Poisson-Boltzmann theory for a constant surface charge boundary condition. For the reference at $C_1 = 10^{-3}$ mol/L, we recall that we got $\lambda_{D,1} = 12 \pm 0.5$ nm (in reasonable agreement with the Debye length of 10 nm expected) and $|\sigma_1| = 4.9 \pm 0.3$ mC/m^2. For $C_2 = 10^0$ mol/L, the interaction force is below the sensitivity limit, until a short-range repulsion is measured at distances $D \lesssim 2$ nm. We obtained a screening length $\lambda_{D,2} = 1.5 \pm 0.5$ nm and a surface charge $|\sigma_2| = 2.5 \pm 0.1$ mC/m^2. At such a high concentration, the Debye length is equal to 0.3 nm, i.e., close to the ion size and we are clearly beyond the limit of validity of the PB theory. The fit of the data with the PB theory has therefore no theoretical support in this case, but it allows to characterize qualitatively the electrostatic repulsion. In particular, we can say that the screening length has been shorten by about one order of magnitude with the highest concentration compared to the reference.

Figure 6.2 shows the measured imaginary admittance as a function of distance. The linear fits at large distances shown in the inset provide viscosities $\eta_1 = 0.95 \pm 0.01$ mPa.s and $\eta_2 = 0.95 \pm 0.03$ mPa.s, in agreement with the expected values of 0.89 mPa.s for pure water at 25° and 1.02 mPa.s at 20°C for a 10^0 mol/L NaCl aqueous solution respectively [54]. In the main graph, we can observe the presence of an over-dissipation for both experiments. Very surprisingly, we found that the curves overlap remarkably well, providing the same value of negative slip length and same parameters when fitting with a two-fluid model. In other words, varying the concentration of the solution by three orders of magnitude or the screening length by about one order of magnitude has no measurable effect on the over-dissipation. Simultaneously, significant changes have been made on the Dukhin length ($\ell_{Du,1} = 51$ nm, $\ell_{Du,2} = 0.026$ nm) and the Gouy-Chapman length ($\ell_{GC,1} = 7.3$ nm, $\ell_{GC,2} = 15$ nm), but no clear correlation can be found with the range of the over-dissipation, when characterized it empirically by the values of negative slip length or layer thickness in the two-fluid model. Therefore, from these experiments it seems that the range of the electrolytic over-dissipation is not piloted by the screening length, the Dukhin length or the Gouy-Chapman length.

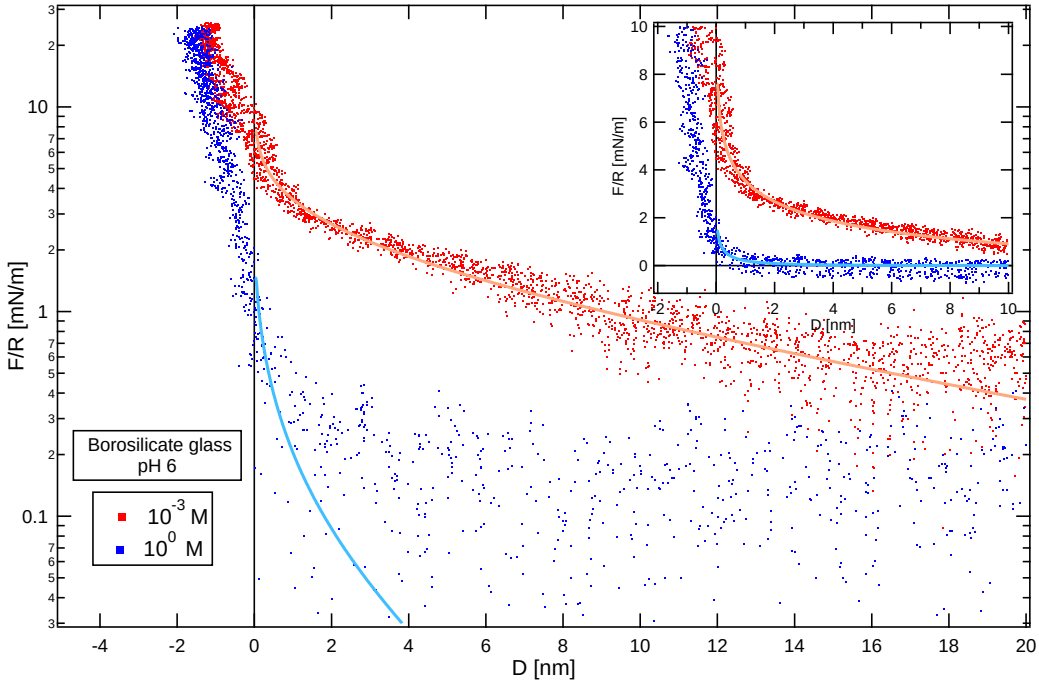

Figure 6.1 Quasi-static force as a function of distance in semi-log scales, for NaCl aqueous solutions of pH 6 between Borosilicate glass surfaces, at different concentrations: $C_1 = 10^{-3}$ mol/L (reference) and $C_2 = 10^0$ mol/L. The lines correspond to the adjustment with the Poisson-Boltzmann theory for a constant surface charge boundary condition. In the inset, a zoom near contact is presented in linear scales.

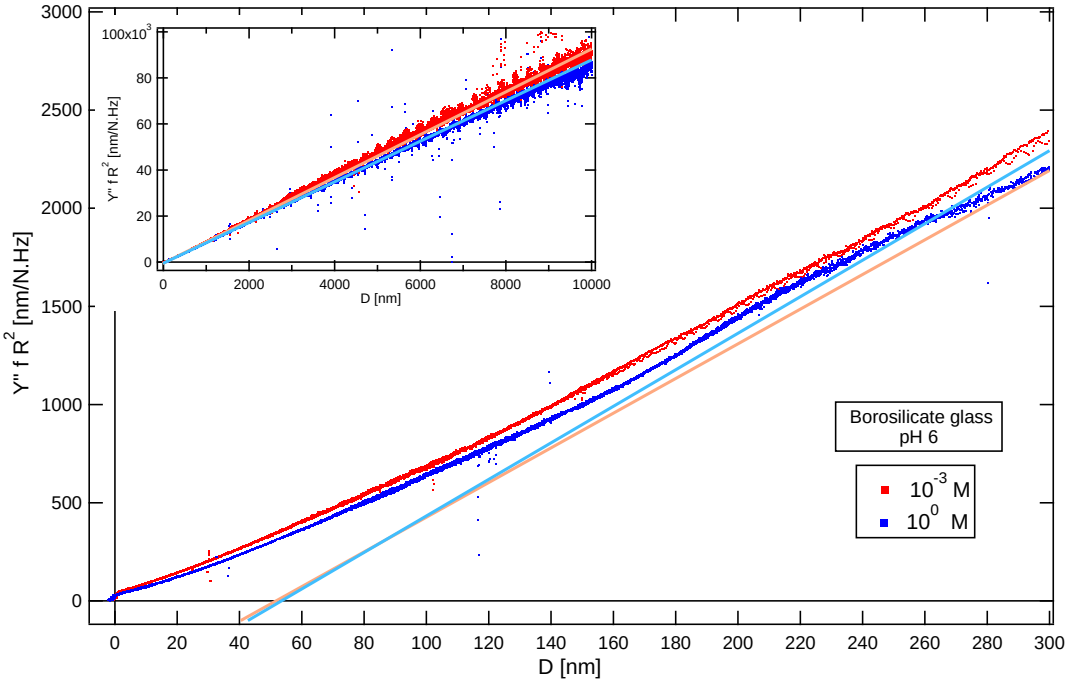

Figure 6.2 Imaginary admittance as a function of distance, for NaCl aqueous solutions of pH 6 between Borosilicate glass surfaces, at different concentrations: $C_1 = 10^{-3}$ mol/L (reference) and $C_2 = 10^0$ mol/L. The inset shows the linear fits at large distances, while the main graph shows the behavior at small distances.

6.2 Varying the surface charge σ with the pH of the solution

The surface charge supported by dielectric surfaces in contact with an aqueous solution is known to depend on the pH of the solution. Such dependency is well documented in the case of glass [26], for which the surface charge is negative at neutral pH, and even more negative at basic pH (see Figure 1.7 from Chapter 1). The solution used for the reference measurement presented in Chapter 5 has been obtained by simply dissolving NaCl salt into fresh DI water. Its pH was measured before and after the experiment and found to be equal to 6, a slightly acidic pH attributed to spontaneous dissolution of atmospheric carbon dioxide. To investigate the effect of the surface charge, I performed another dSFA experiment with a NaCl aqueous solution of concentration $C = 10^{-3}$ mol/L between Borosilicate glass surfaces, but at pH 10. The solution was prepared by adding droplets of NaOH solution to fresh DI water to reach the desired pH, and then by dissolving NaCl salt into this basic solution. Again, pH was measured before and after the experiment and found to be equal to 10.

Figure 6.3 shows the measured quasi-static force-distance curves at pH 10 and pH 6 (reference), and the corresponding adjustments with the Poisson-Boltzmann theory for a constant surface charge boundary condition. Note that for pH 10, the mechanical origin was positioned on the minimum of adhesion on the retraction curve, and is known at a precision better than ± 1 nm. The electrostatic repulsion shows a slightly smaller screening length $\lambda_{D,2} = 8 \pm 1$ nm at pH 10 than $\lambda_{D,1} = 12 \pm 1$ nm obtained at pH 6. These two values are reasonably close to the expected Debye length of 10 nm, with discrepancies attributed to the quasi-static sensitivity of the dSFA at that time (as explained in section 3.3.5). The fitted absolute value of the surface charge is found to be $|\sigma_2| = 12 \pm 0.5$ mC/m^2 at pH 10, instead of $|\sigma_1| = 4.9 \pm 0.3$ mC/m^2 at pH 6. Increasing the pH thus allowed to increase the absolute surface charge by a factor of ~ 2.7 in comparison with the reference measurement.

Figure 6.4 shows the measured imaginary admittance as a function of distance. The linear fits at large distances shown in the inset provide a slightly smaller viscosity $\eta_2 = 0.84 \pm 0.05$ mPa.s at pH 10 compared to $\eta_1 = 0.95 \pm 0.01$ mPa.s obtained at pH 6. These two values are reasonably close to the viscosity of pure water (0.89 mPa.s at 25° [54]), with discrepancies that can be due to experimental errors on the determination of the sphere radius, or on small temperature differences. In the main graph however, we observe a major difference between both curves: the over-dissipation that is observed for the solution at pH 6 is not present for the solution at pH 10. Indeed, for the basic solution we find that the linear fit at large scales intersects the X axis at a position compatible with the mechanical origin ($D = 0$), given the ± 5 nm uncertainty on the extrapolation of the dissipation. The system is correctly described by a simple Reynolds admittance, like Hexadecane presented in Chapter 4. Note that this difference cannot be explained by a possible difference in concentration, as we have seen in the previous section that the screening length has no influence on the over-dissipation. This behavior is extremely surprising from the perspective of the scenario we proposed in

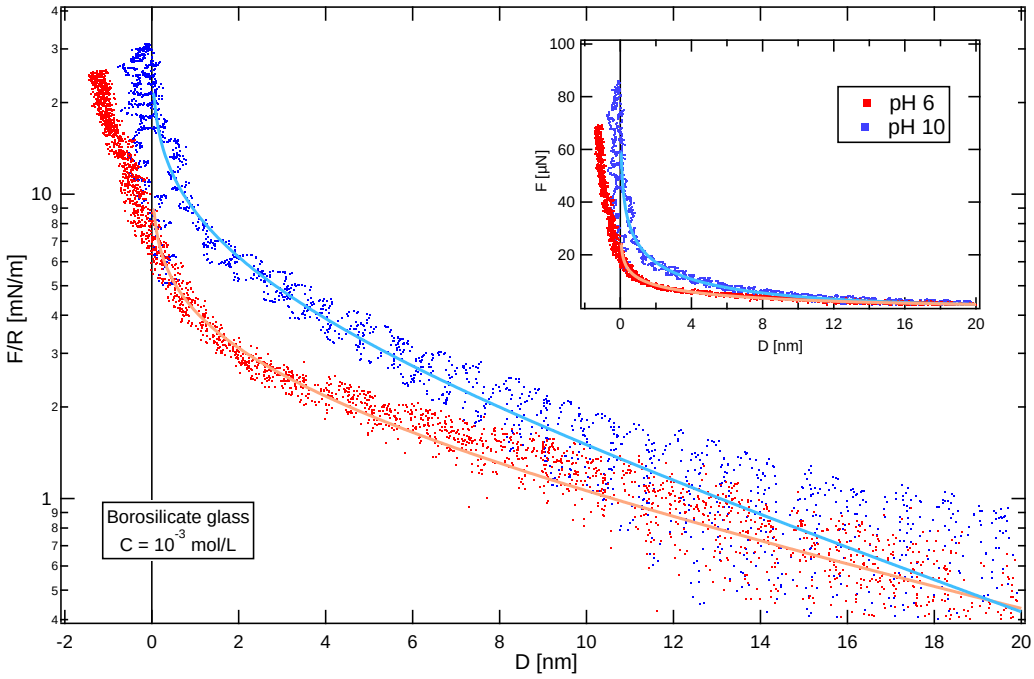

Figure 6.3 Quasi-static force as a function of distance, for NaCl aqueous solutions of concentration $C = 10^{-3}$ mol/L between Borosilicate glass surfaces, at pH 6 (reference) and pH 10. The lines correspond to the adjustment with the Poisson-Boltzmann theory for a constant surface charge boundary condition.

Chapter 4, where surface charge is the driving force behind the electrolytic over-dissipation. Indeed, an increase rather than a suppression of the over-dissipation with the absolute of the surface charge was expected in this qualitative picture.

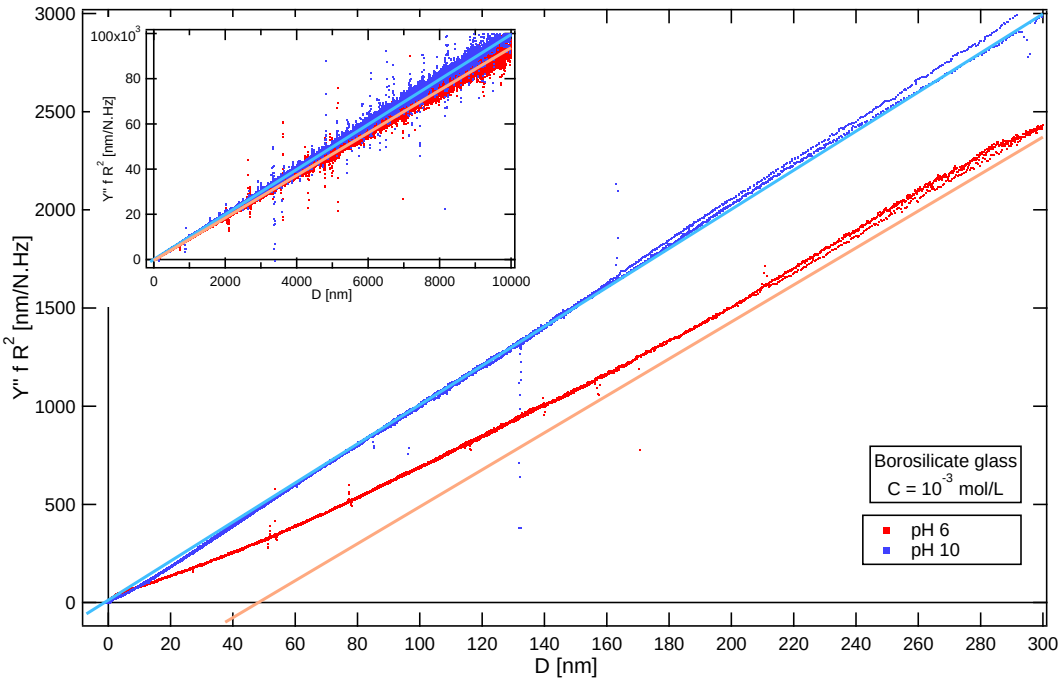

Figure 6.4 Imaginary admittance as a function of distance, for NaCl aqueous solutions of concentration $C = 10^{-3}$ mol/L between Borosilicate glass surfaces, at pH 6 (reference) and pH 10. The inset shows the linear fits at large distances, while the main graph shows the behavior at small distances.

6.3 First dSFA measurements performed on Boron Nitride surfaces

As presented in Chapter 4, 30 nm thick Boron Nitride layers were coated on Borosilicate glass substrates. Measurements were performed at difference frequencies with an aqueous solution of NaCl with a concentration $C = 10^{-3}$ M and different pH.

6.3.1 BN-coated glass surfaces at pH 6

Origin of distance and surface charge

Figure 6.5c shows the measured quasi-static force-distance curves measured at pH 6 for BN-coated glass surfaces and Borosilicate glass surfaces (reference). We observe an hysteresis between the approach and the retraction curves with the BN-coated glass surfaces, on the last

~ 4 nm before contact. This could a priori signify the presence of a dust particle, however we do not observe any hysteresis on the dynamic measurement.

Three mechanical origins for the sphere-plane distance were tested to adjust the data with the Poisson-Boltzmann theory. In Figure 6.5a, the mechanical origin has been determined by fitting with a Hertz law the portion of the retraction curve with large forces. The best fit of the portion of the approach curve with low forces with the Poisson-Boltzmann theory for a constant surface charge boundary condition gives $\lambda_{D,1} = 5$ nm and $|\sigma_1| = 13$ mC/m^2, but the fit is clearly not satisfying for distances smaller than ~ 4 nm. In Figure 6.5b, a minimum offset has been applied on the mechanical contact, in order to have a good PB adjustment with a constant charge boundary condition. The minimum shift was of +3.8 nm, and it provided $\lambda_{D,2} = 5$ nm and $|\sigma_2| = 65$ mC/m^2. A slightly larger shift can still result in a good PB fit, but the shift cannot be arbitrary large. A first reason is that the amplitude of the electrostatic force at large distances ($D \gtrsim \lambda_D$) saturates for large surface charges (see Appendix A). This is because at some point any increase of the surface charge is screened by the counter-ions in the very close proximity of the surfaces ($D \ll \lambda_D$), which is possible in the PB theory where the ions have no excluded volume. A second reason is that real surfaces cannot support arbitrary large surface charges. Figure 6.5c shows the PB prediction for $\lambda_{D,3} = 5$ nm and a maximum surface charge $|\sigma_3| = 1000$ mC/m^2, corresponding to an average distance $(|\sigma_3|/e)^{-1/2} = 4$ Å between each elementary charge on the surface. A good fit of the data is achieved in this case with a maximum offset on the mechanical contact equal to +4.8 nm.

In summary, the position of the mechanical contact is determined within an uncertainty of ± 2.4 nm, and the surface charge is > 13 mC/m^2, possibly equal to 65 mC/m^2, but in any case it is larger in comparison with the reference measurement (4.9 mC/m^2).

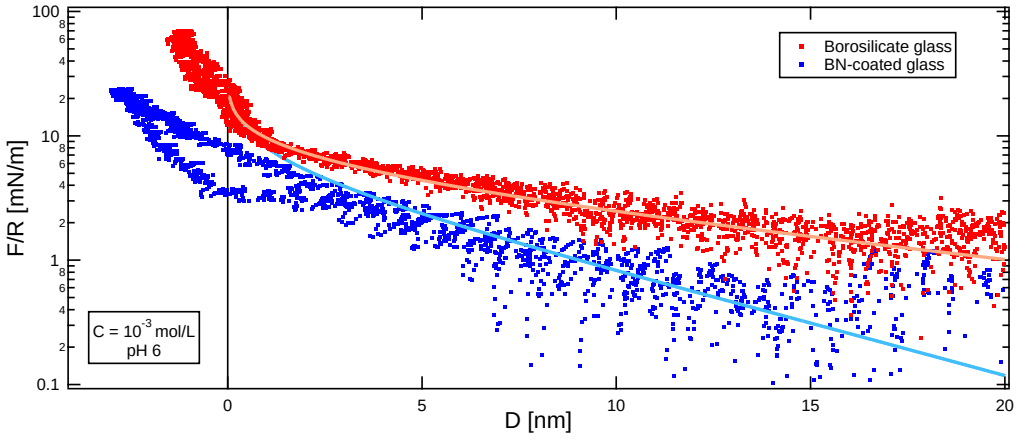

(a) Mechanical origin fixed by Hertz law on retraction curve.

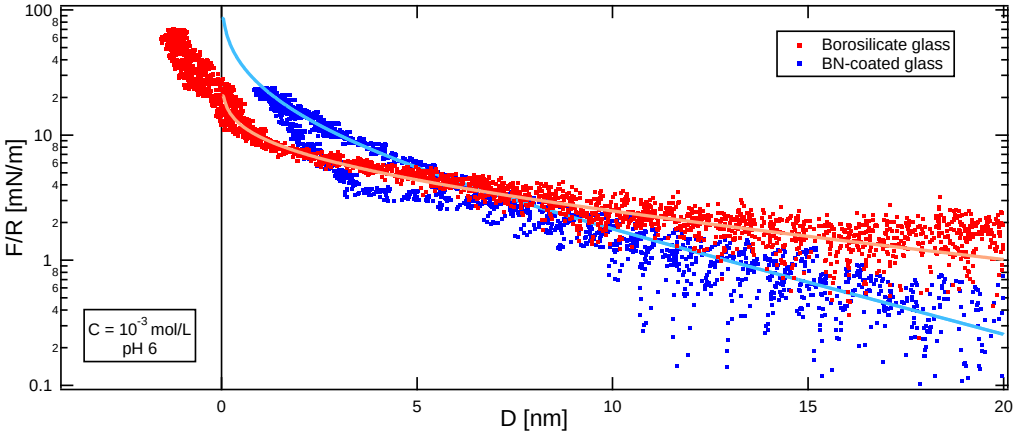

(b) Mechanical origin shifted by +3.8 nm.

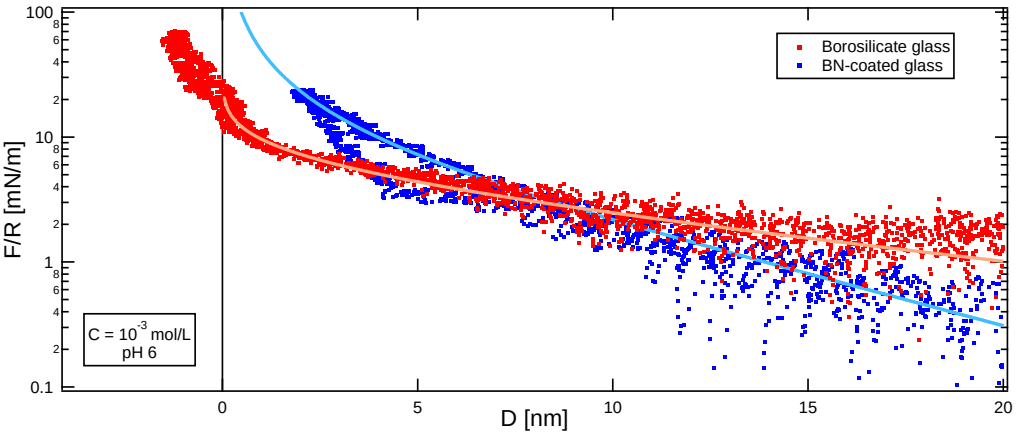

(c) Mechanical origin shifted by +4.8 nm (at PB saturation and maximum surface charge).

Figure 6.5 Quasi-static force as a function of distance, for NaCl aqueous solutions of concentration $C = 10^{-3}$ mol/L and pH 6, confined between Borosilicate glass surfaces (reference) and BN-coated glass surfaces. For the latter, three attempts are made to adjust the approach curve with the Poisson-Boltzmann theory for a constant surface charge boundary condition.

Dissipation

Figure 6.6 shows the measured imaginary admittance as a function of distance at pH 6 for BN-coated glass surfaces and Borosilicate glass surfaces (reference). As shown in inset, the linear fit at large distances of the data with BN-coated glass surfaces provides a viscosity of 0.86 ± 0.05 mPa.s, in reasonable agreement with the water viscosity's value of 0.89 mPa.s for pure water at 25° [54]. In the main graph, we observe that the system is characterized by a negative slip length of 55 ± 1 nm and exhibits an over-dissipation. More precisely, we see in Figure 6.7 that the over-dissipation is larger for BN-coated glass surfaces than for the reference. A fit with the two-fluid model results in two layers of thicknesses $e = 30 \pm 5$ nm and viscosity $\eta_{\text{layer}} = 5 \pm 0.2$ mPa.s, i.e., a ratio $\eta_{\text{layer}}/\eta_{\text{bulk}} = 5.8 \pm 0.6$.

Therefore, in the present case where the absolute value of the surface charge has been increased significantly by changing the nature of the surfaces while keeping the same solution, it seems that the amplitude of the electrolytic over-dissipation has indeed been increased. In line with the measurements at different concentrations, we find that the range of the over-dissipation, characterized by the value of the negative slip length or of the layer thickness in the two-fluid model, does not correlate with the Dukhin length ($\ell_{\text{Du}} \geq 135$ nm), or the Gouy-Chapman length ($\ell_{\text{GC}} \leq 2.8$ nm).

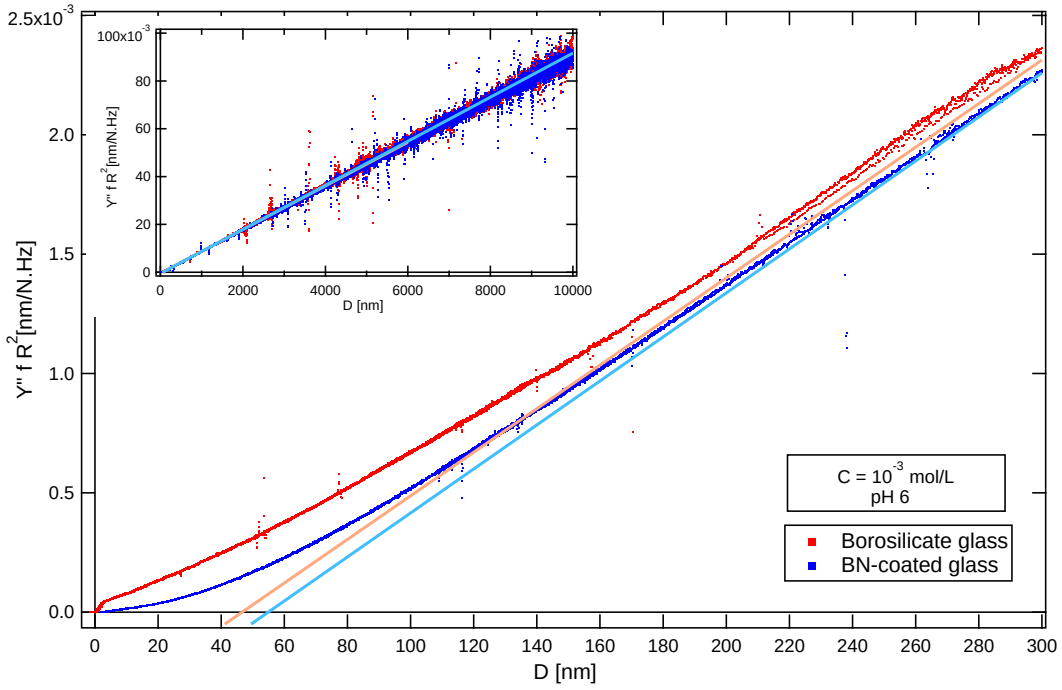

Figure 6.6 Left: Imaginary admittance as a function of distance, for NaCl aqueous solutions of concentration $C = 10^{-3}$ mol/L and pH 6, confined between Borosilicate glass surfaces (reference) and BN-coated glass surfaces. The lines are linear fits at large distances.

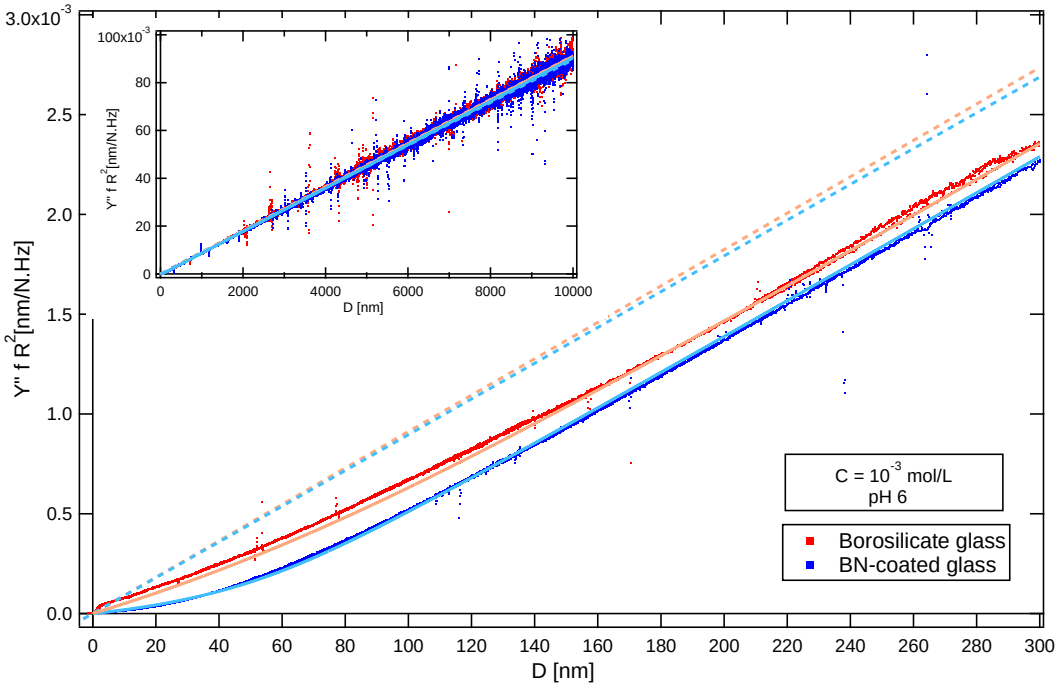

Figure 6.7 Imaginary admittance as a function of distance, for NaCl aqueous solutions of concentration $C = 10^{-3}$ mol/L and pH 6, confined between Borosilicate glass surfaces (reference) and BN-coated glass surfaces. The dashed lines represent the trends that would be obtained in the absence of over-dissipation, while the full lines are adjustments with the two-fluid model.

6.3.2 BN-coated glass at pH 10

Figure 6.8 shows the measured quasi-static force-distance curves measured at pH 10 for BN-coated glass surfaces, compared the data at pH 6 with Borosilicate glass surfaces (reference). Here there is no ambiguity on the positioning of the mechanical contact, which is fixed by fitting a Hertz law on the portion of the curve with large forces. The constant surface charge PB adjustment of the portion of the curve with low forces is satisfactory, and provides $\lambda_D = 8 \pm 0.2$ nm and $|\sigma| = 10.5 \pm 0.5$ mC/m^2, about twice as high as the reference one. We do not find the value reported at pH 11 in Boron Nitride nanotubes [6]. The particularly high value of 1 C/m^2, measured by conductivity measurements, is indeed two orders of magnitude above the value found here. The difference lies either in the pH value, the molecular structure of BN or in the method of measurement. This point remains to be investigated.

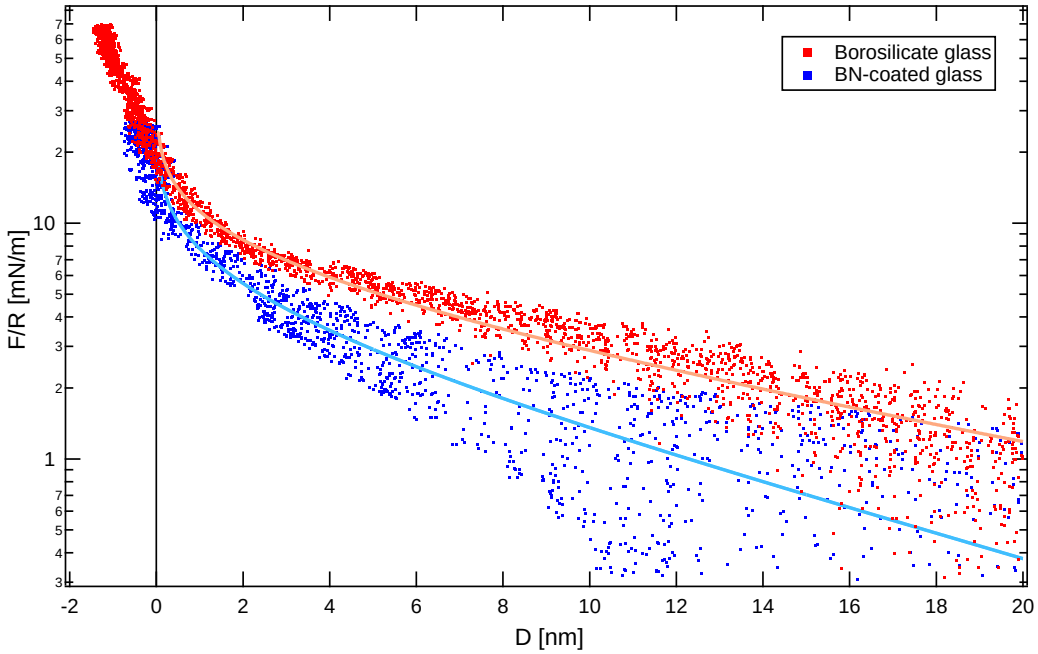

Figure 6.8 Quasi-static force as a function of distance, for NaCl aqueous solutions of concentration $C = 10^{-3}$ mol/L, with pH 6 between Borosilicate glass surfaces (reference), or with pH 10 between BN-coated glass surfaces. The lines correspond to the adjustment with the Poisson-Boltzmann theory for a constant surface charge boundary condition.

Figure 6.9 shows the measured imaginary admittance as a function of distance at pH 10 for BN-coated glass surfaces, compared the data at pH 6 with Borosilicate glass surfaces (reference). We observe that this system exhibits no measurable over-dissipation, similarly to the measurements performed at pH 10 with Borosilicate glass surfaces (section 6.2). Again, such behavior is extremely surprising, as we expected an increase rather than a suppression of the over-dissipation when increasing the surface charge.

A possible explanation could come from the fact that increasing the pH increases not only the surface charge, but also the concentration of HO^- ions in solution. At pH 10 the hydroxide concentration is $[HO^-] = 10^{-4}$ mol/L, i.e., about 10 times smaller than the chloride concentration $[Cl^-] = 10^{-3}$ mol/L and the sodium concentration $[Na^+] = 1.1 \cdot 10^{-3}$ mol/L. Hydroxide ions may have negligible effect on the equilibrium, i.e., electrostatic screening of the surface charge (in particular on the value of the Debye length), however they could affect significantly the transport, i.e., the electrolytic over-dissipation. Indeed, hydroxides ions have a high mobility in water, because the negative charge can be transferred by creation / breakage of bonds between Oxygen and Hydrogen of a chain of water molecules, more efficiently than by the transport of the hydroxide ion in the solution. Such enhanced mobility of hydroxide as a charge carrier is reflected in a diffusion coefficient equal to $D_{HO^-} = 5.27.10^{-5}$ cm^2/s, about 2.5 times larger than the chloride diffusion coefficient $D_{Cl^-} = 2.03.10^{-5}$ cm^2/s and 4 times larger than the sodium diffusion coefficient $D_{Na^+} = 1.33.10^{-5}$ cm^2/s [54]. Qualitatively, the rapid diffusion of HO^- ions in solution could prevent any dynamic deviation of charge distribution from equilibrium, thus annihilating any possibility of over-dissipation.

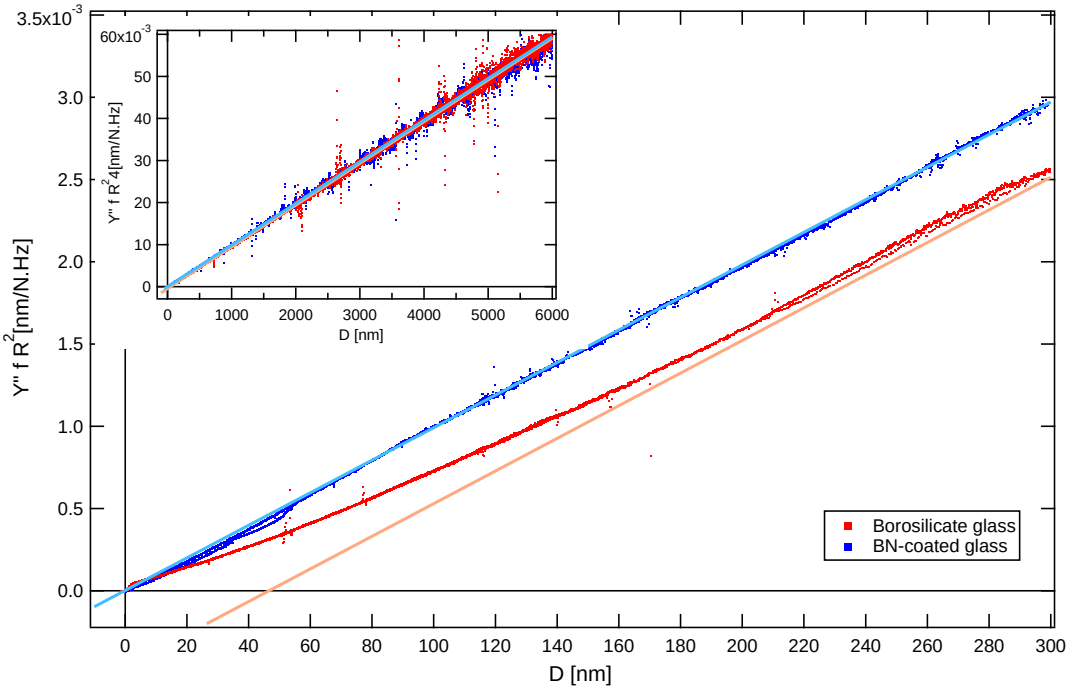

Figure 6.9 Imaginary admittance as a function of distance, for NaCl aqueous solutions of concentration $C = 10^{-3}$ mol/L, with pH 6 between Borosilicate glass surfaces (reference), or with pH 10 between BN-coated glass surfaces. The inset shows the linear fits at large distances, while the main graph shows the behavior at small distances.

6.4 Conclusion

In this chapter, we investigated the influence of three key parameters on the over-dissipation: the screening length, the surface charge and the nature of the surfaces. Table 6.1 aggregates the results obtained. We can summarize the main observations made on a few systems as:

- The range of the over-dissipation, quantified as a negative slip length or layer thickness in a two fluid model, does not seem to correlate with the Debye length, the Dukhin length or the Gouy-Chapman length,
- The amplitude of the over-dissipation increases with the surface charge, if the surface charge is varied significantly by changing the nature of the surfaces while keeping the exact same solution (in particular the same pH),
- Increasing the pH of the solution can simultaneously lead to an increase of the surface charge and a suppression of the over-dissipation, a behavior that could be due to the large mobility of hydroxide ions in water.

Table 6.1 Summary of the results obtained.

Surfaces	pH	C (mol/L)	λ_D (nm)	$\lvert\sigma\rvert$ (mC/m^2)	ℓ_{GC} (nm)	ℓ_{Du} (nm)	b (nm)	e (nm)	η_{layer}/η_{bulk}
Borosilicate	6	10^{-3}	12	4.9	7.3	51	49	50	1.8
Borosilicate	6	10^{0}	1.5	2.5	15	0.026	49	50	1.8
Borosilicate	10	10^{-3}	8	12	3	125	0	0	1
Boron Nitride	6	10^{-3}	5	≥ 13	≤ 2.8	≥ 135	55	30	5
Boron Nitride	10	10^{-3}	8	10.5	3.5	109	0	0	1

Conclusion and Perspectives

The equilibrium and transport properties of confined electrolytes were the object of study of my thesis. A dynamic Surface Force Apparatus (dSFA) has been employed to investigate them experimentally. This instrument can be used to confine a fluid between two surfaces (a sphere and a plane) and to measure the fluid-surface interactions. The dSFA allows to explore 5 decades of confinement from 10 µm to 1 Å during one experiment, and to simultaneously perform quasi-static and dynamic measurements, in order to access at-equilibrium and out-of-equilibrium properties of confined fluids.

The existing dSFA at LIPhy required important modifications in order to be able to obtain reproducible measurements with volatile fluids, such as aqueous solutions which are at the center of Blue Energy applications. Thus the first step taken during my thesis was to work on the atmospheric control. A vacuum chamber has been added, reducing evaporation and thermal drifts, and giving the possibility to control the temperature and pressure. Thermal drifts have decreased by ten times in comparison with the previous version of the machine, with current temperature changes smaller than 0.01°C/h. However, this addition of a vacuum chamber led to other changes in the set up, in order to adapt the mechanics and optics to the new version of the machine. This is why new, more compact, interferometers have been built. The electronics has also been modified, by directly measuring the photocurrents coming from the interferometers with precision multimeters and lock-in amplifiers in current mode, eliminating some non-desired effects in both static and dynamic measurements. Based on a number of different tests and calibrations, issues such as the optical cross-talk or the fluctuations on the quasi-static signals have been solved. Imperfections like the dynamic noise or the mechanical cross-talk have been identified, and protocols have been implemented to characterize them and to determine the optimum working conditions.

A benchmark experimental campaign consisting of Hexadecane confined between two Borosilicate glass surfaces has been performed in order to characterize the performances of the machine. The results have proved that the new version of the dSFA allows to obtain quasi-static interaction profiles with a resolution of 20 pm for distance and 120 nN for force (after fixing the problem of fluctuations on the quasi-static signals), and to perform dynamic measurements with resolutions of 1-10 pm and 6-60 nN for distance and force respectively.

Then, an experimental campaign has been conducted with an aqueous NaCl solution of low concentration and neutral pH between Borosolicate glass surfaces, demonstrating the rich phenomenology which can be access with the dSFA. First, adjustment of the electrostatic repulsion with the Poisson-Boltzmann theory has allowed to characterize the screening length and the surface charge. Then, careful correction of the machine stiffness, by fitting the data in the right distance interval (essentially such that the electrostatic contribution is negligible), has shown that the conservative dynamic response results from contribution of electrostatics and elasto-hydrodynamics. There, analysis of the dissipative dynamic response has revealed the presence of an over-dissipation, proportional to the excitation frequency. This over-dissipation has been characterized empirically with a negative slip length or with a two-fluid model, even if its physical origin remained to be determined.

Several experimental campaigns have been performed to investigate the influence of the screening length, the surface charge and the nature of the surfaces on the over-dissipation. This has been done by changing the ion concentration, the pH of the solution and by performing the first dSFA measurements on Boron Nitride (BN)-coated glass surfaces. Varying the screening length turned out to have no measurable influence on the over-dissipation. The over-dissipation has been found to present a larger amplitude and shorter range for BN-coated glass than for Borosilicate glass at neutral pH, which could result from the larger surface charge measured quasi-statically. Very surprisingly, for the two natures of surfaces, increasing the pH to 10 resulted simultaneously in the increase of the surface charge and the suppression of the over-dissipation. The very large mobility of hydroxide ions has been hypothesized to be responsible for such behavior.

Several perspectives to this thesis work can be formulated. First, a few improvements could be made on the instrumental point of view:

- Reduction of the dynamic noise and of the mechanical cross-talk could be achieved by working on the design of the bottom of the vacuum chamber, namely by making it solid, stiff and in direct contact with the damping table, to reduce resonances and unwanted transmission of motions to the surfaces by the surroundings,
- Setting-up a syringe pump system would allow to change the solution during one experimental campaign, i.e., without changing the surfaces, and so to multiply the number of feasible experiments, in order to investigate more systematically the influence of key parameters like concentration or pH.

Second, new directions emerge from this thesis work for dSFA experiments with confined electrolytes:

- Varying the ions mobility while keeping the surface charge constant, by using large ions without changing the solvent, the concentration, the pH or the nature of the surfaces,

- Varying the surface charge while keeping the ions mobility constant, by using various dielectric substrates at same neutral pH, or by polarizing conductive substrates.

Third, important theoretical work is needed to reach a fundamental understanding of the physics of confined electrolytes probed with the dSFA:

- A model that would be able to reproduce quantitatively the observed over-dissipation, in order to decipher whether this dynamic dissipative response can be accounted for in a consistent way with the electrostatic response,
- A model combining electrostatics, elasticity and hydrodynamics to describe in the same framework the quasi-static force profile and the dynamic conservative response.

Appendix A

Force curves for two boundary cases

We present here the curves calculated for the electrostatic force profile in two limiting electric boundary conditions: constant surface charge or constant surface potential.

A.1 Constant Surface Charge Boundary Condition

Figure A.1 shows the interaction forces for different values of the surface charge, in the case of a symmetric system and a 1:1 electrolyte with a Debye length $\lambda_D = 10$ nm.

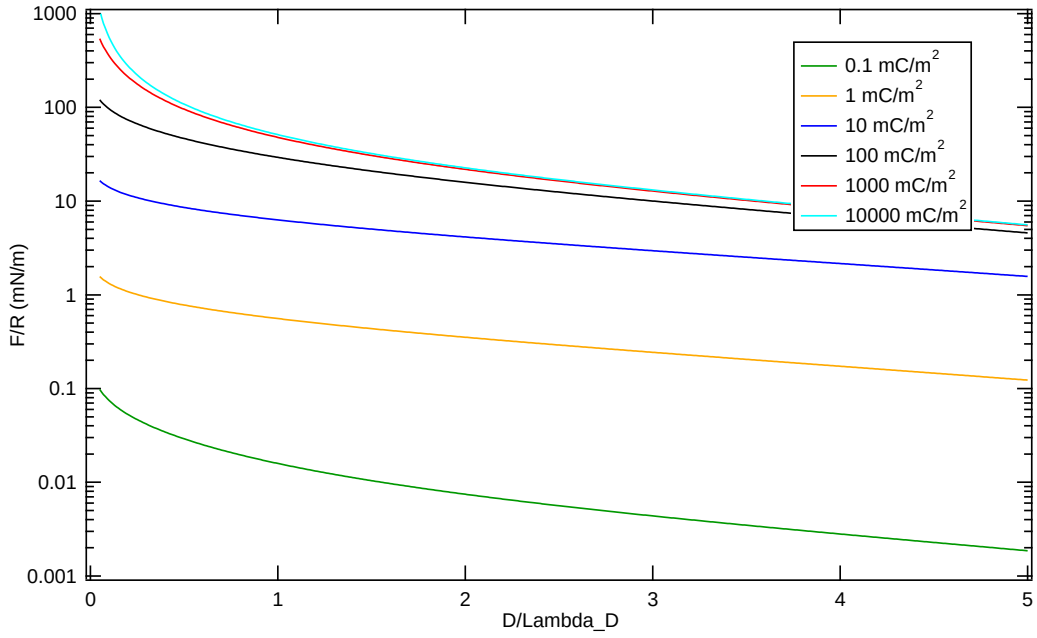

Figure A.1 Electrostatic force predicted by the Poisson-Boltzmann theory for $\lambda_D = 10$ nm and a constant surface charge boundary condition, in the case of symmetric surfaces with absolute surface charges $|\sigma|$ of 0.1, 1, 10, 100 and 1000 mC/m^2.

We observe that the magnitude of the electrostatic force does not simply increase linearly with the surface charge, especially at large distances. At very high surface charge ~ 1000 mC/m^2, the curves saturate.

A.2 Constant Surface Potential Boundary Condition

Figure A.2 shows the interaction forces for different values of the surface potential, in the case of a symmetric system and a 1:1 electrolyte with a Debye length $\lambda_D = 10$ nm.

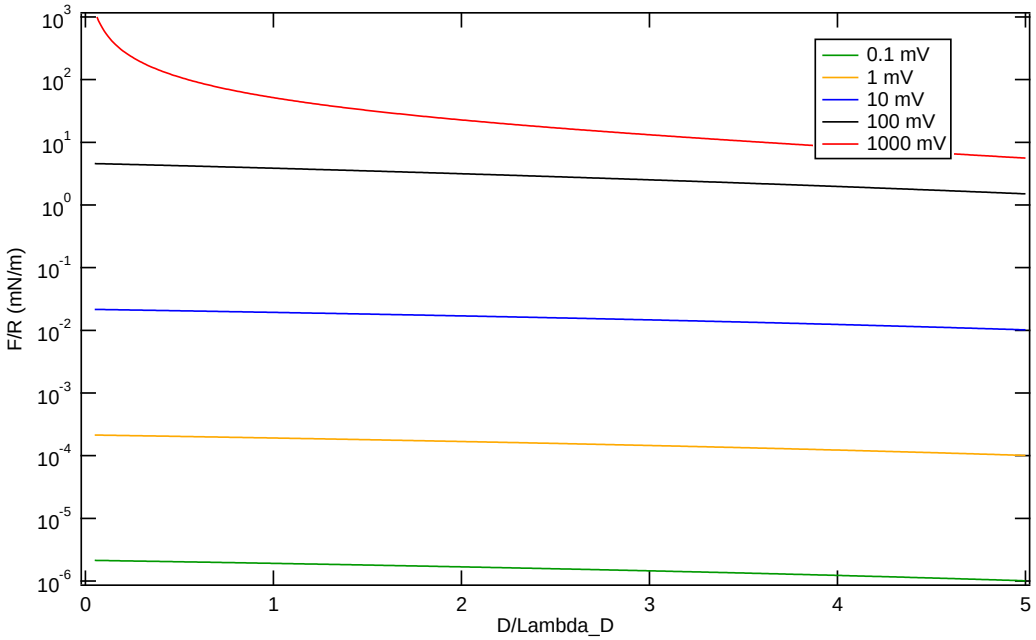

Figure A.2 Electrostatic force predicted by the Poisson-Boltzmann model for $\lambda_D = 10$ nm and a constant surface potential boundary condition, in the case of symmetric surfaces with absolute potentials $|V_s|$ of 1, 10, 100 and 1000 mV.

At low surface potential (~ 100 mV), the force varies exponentially with the distance, and its magnitude scales like the surface potential at the power 2. At larger surface potential and $D \lesssim \lambda_D$, a deviation from the exponential behavior is clearly visible.

Bibliography

[1] Lucas Knobloch, Rafael Hincapie, Hendrik Födisch, and Leonhard Ganzer. Qualitative and quantitative evaluation of permeability changes during eor polymer flooding using micromodels. *World Journal of Engineering and Technology*, 06:332–349, 01 2018.

[2] Brian Kihun Kim, Serubbable Sy, Aiping Yu, and Jinjun Zhang. *Electrochemical Supercapacitors for Energy Storage and Conversion*. John Wiley & Sons, Ltd, 7 2015.

[3] Yu Chang Kim and Menachem Elimelech. Potential of osmotic power generation by pressure retarded osmosis using seawater as feed solution: Analysis and experiments. *Journal of Membrane Science*, 429:330–337, 2013.

[4] Alessandro Siria, Marie Laure Bocquet, and Lydéric Bocquet. New avenues for the large-scale harvesting of blue energy. *Nature Reviews Chemistry*, 1, 10 2017.

[5] Youcef Brahmi and Annie Colin. New membrane and electrode assembly concept to improve salinity energy harvesting. *Energy Conversion and Management*, 254:115297, 2022.

[6] Alessandro Siria, Philippe Poncharal, Anne Laure Biance, Rémy Fulcrand, Xavier Blase, Stephen T. Purcell, and Lydéric Bocquet. Giant osmotic energy conversion measured in a single transmembrane boron nitride nanotube. *Nature*, 494:455–458, 2 2013.

[7] Lydéric Bocquet and Elisabeth Charlaix. Nanofluidics, from bulk to interfaces. *Chemical Society Reviews*, 39:1073–1095, 2010.

[8] Jacob N. Israelachvili. Measurement of forces between surfaces immersed in electrolyte solutions. *Faraday Discussions*, 65:20–24, 1978.

[9] Remco Hartkamp, Anne Laure Biance, Li Fu, Jean François Dufrêche, Oriane Bonhomme, and Laurent Joly. Measuring surface charge: Why experimental characterization and molecular modeling should be coupled. *Current Opinion in Colloid and Interface Science*, 37:101–114, 9 2018.

[10] Léo Garcia, Chloé Barraud, Cyril Picard, Jérôme Giraud, Elisabeth Charlaix, and Benjamin Cross. A micro-nano-rheometer for the mechanics of soft matter at interfaces. *Review of Scientific Instruments*, 87, 11 2016.

[11] Léo Garcia. *Étude rhéologique des électrolytes confinés en appareil à forces de surfaces dynamique*. PhD thesis, Université Grenoble Alpes, 2017.

[12] Chloé Barraud. *Nanorhéologie de fluides complexes aux interfaces*. PhD thesis, Université Grenoble Alpes, 2017.

[13] Jacob N. Israelachvili. *Intermolecular and Surface Forces*. Academic Press, Boston, third edition, 2011.

[14] Reto B. Schoch, Jongyoon Han, and Philippe Renaud. Transport phenomena in nanofluidics. *Reviews of Modern Physics*, 80:839–883, 7 2008.

[15] Reto B. Schoch, Arnaud Bertsch, and Philippe Renaud. ph-controlled diffusion of proteins with different pi values across a nanochannel on a chip. *Nano Letters*, 6(3):543–547, 2006.

[16] Boris Derjaguin. Untersuchungen über die reibung und adhäsion, iv. *Kolloid-Zeitschrift*, 69(2):155–164, 1934.

[17] Jacobus H. van't Hoff. Die rolle des osmotischen druckes in der analogie zwischen lösungen und gasen (the function of osmotic pressure in the analogy between solutions and gases). *Zeitschrift für Physikalische Chemie*, 1U:481 – 508, 1887.

[18] *LoSal™ Enhanced Oil Recovery: Evidence of Enhanced Oil Recovery at the Reservoir Scale*, volume All Days of *SPE Improved Oil Recovery Conference*, 04 2008. SPE-113976-MS.

[19] Kåre Jensen, Emmanuelle Rio, Rasmus Hansen, Christophe Clanet, and Tomas Bohr. Osmotically driven pipe flows and their relation to sugar transport in plants. *Journal of Fluid Mechanics*, 636:371 – 396, 10 2009.

[20] Sophie Marbach and Lydéric Bocquet. Osmosis, from molecular insights to large-scale applications. *Chemical Society Reviews*, 48:3102–3144, 6 2019.

[21] Peter Mazur and Johannes Th. G. Overbeek. On electro-osmosis and streaming-potentials in diaphragms: Ii. general quantitative relationship between electro-kinetic effects. *Recueil des Travaux Chimiques des Pays-Bas*, 70(1):83–91, 1951.

[22] Edouard Brunet and Armand Ajdari. Generalized onsager relations for electrokinetic effects in anisotropic and heterogeneous geometries. *Physical Review E - Statistical Physics, Plasmas, Fluids, and Related Interdisciplinary Topics*, 69:9, 2004.

[23] Marian von Smoluchowski. Contribution à la théorie de l'endosmose électrique et de quelques phénomènes corrélatifs = przyczynek do teoryi endosmozy elektryczneji niektorych zjawisk pokrewnych. *Bulletin international de l'Académie des Sciences de Cracovie, Classe des Sciences Mathématiques et Naturelles = Anzeiger der Akademie der Wissenschaften in Krakau, Mathematisch-Naturwissenschaftliche Klasse*, pages 182 – 200, 1903.

[24] Derek Stein, Maarten Kruithof, and Cees Dekker. Surface-charge-governed ion transport in nanofluidic channels. *Physical Review Letters*, 93, 7 2004.

[25] Johannes Lützenkirchen, Tajana Preocanin, Davor Kovačević, Vladislav Tomišić, Lars Lövgren, and Nikola Kallay. Potentiometric titrations as a tool for surface charge determination. *Croatica Chemica Acta*, 85:391–417, 12 2012.

[26] Tharwat F Tadros and Johannes Lyklema. Adsorption of potential-determining ions at the silica-aqueous electrolyte interface and the role of some cations. *Electroknalytical Chemistry And Interfacial Electrochemistry*, 17:267–275, 1968.

[27] J Lyklema and J G Th Overbeek. On the interpretation of electrokinetic potentials. *Journal Of Colloid Science*, 16:501–512, 1961.

[28] Brian J. Kirby and Ernest F. Hasselbrink. Zeta potential of microfluidic substrates: 1. theory, experimental techniques, and effects on separations. *Electrophoresis*, 25:187–202, 2004.

[29] Cédric Bouzigues, Paul Tabeling, and Lydéric Bocquet. Nanofluidics in the debye layer at hydrophilic and hydrophobic surfaces. *Physical review letters*, 101:114503, 10 2008.

[30] Matthew A. Brown, Alok Goel, and Zareen Abbas. Effect of electrolyte concentration on the stern layer thickness at a charged interface. *Angewandte Chemie*, 128:3854–3858, 3 2016.

[31] Alice Sze, David Erickson, Liqing Ren, and Dongqing Li. Zeta-potential measurement using the smoluchowski equation and the slope of the current-time relationship in electroosmotic flow. *Journal of Colloid and Interface Science*, 261:402–410, 2003.

[32] Cédric Bouzigues, Lydéric Bocquet, Elisabeth Charlaix, Cécile Cottin-Bizonne, Benjamin Cross, Laurent Joly, Audrey Steinberger, Christophe Ybert, Patrick Tabeling, C I Bouzigues, L Bocquet, E Charlaix, C Cottin-Bizonne, B C Ross, L J Oly, A S Teinberger, C Ybert, and P Tabeling. Using surface force apparatus, diffusion and velocimetry to measure slip lengths. *Transactions of the Royal Society of London. Series A, Mathematical and Physical Sciences*, 366, 2008.

[33] Elena F. Silkina, Evgeny S. Asmolov, and Olga I. Vinogradova. Electro-osmotic flow in hydrophobic nanochannels. *Physical Chemistry Chemical Physics*, 21:23036–23043, 2019.

[34] Derek Y.C. Chan and Roger G. Horn. The drainage of thin liquid films between solid surfaces. *The Journal of Chemical Physics*, 83:5311–5324, 1985.

[35] Jacob N. Israelachvili. Measurement of the viscosity of liquids in very thin films. *Journal of Colloid and Interface Science*, 110:263–271, 1986.

[36] André Tonck, Jean-Marie Georges, and Jean-Luc Loubet. Measurements of intermolecular forces and the rheology of dodecane between alumina surfaces. *Journal of Colloid and Interface Science*, 126(1):150–163, 1988.

[37] Frédéric Restagno, Jérôme Crassous, Élisabeth Charlaix, Cécile Cottin-Bizonne, and Michel Monchanin. A new surface forces apparatus for nanorheology. *Review of Scientific Instruments*, 73:2292, 6 2002.

[38] Samuel Leroy. *Les forces de surface dynamiques pour l'investigation mécanique des surfaces molles.* PhD thesis, Université de Lyon, 2011.

[39] Samuel Leroy and Elisabeth Charlaix. Hydrodynamic interactions for the measurement of thin film elastic properties. *Journal of Fluid Mechanics*, 674:389–407, 5 2011.

[40] Jean-Marie Georges, S. Millot, Jean-Luc Loubet, and André Tonck. Drainage of thin liquid films between relatively smooth surfaces. *The Journal of Chemical Physics*, 98:7345–7360, 1993.

[41] Daniel Bernoulli. *Hydrodynamica: sive de viribus et motibus fluidorum commentarii.* 1738.

[42] Henri Navier. *Mémoire sur les lois du Mouvement des Fluides.* Académie Royale des Sciences de l'Institut de France, 1823.

[43] Olga I Vinogradova. Drainage of a thin liquid film confined between hydrophobic surfaces. *Langmuir*, 11:2213–2220, 1995.

[44] Élisabeth Charlaix, Cécile Cottin-Bizonne, Jérôme Crassous, Samuel Leroy, Frédéric Restagno, and Audrey Steinberger. Propriétés hydrodynamiques au voisinage d'une surface. *Reflets de la physique*, pages 14–18, 12 2011.

[45] Richard Villey. *Nanorhéologie des liquides confimés : application à la nanomécanique des couches minces.* PhD thesis, Université de Lyon, 2013.

[46] Chloé Barraud, Léo Garcia, Jérôme Giraud, Cyril Picard, Elisabeth Charlaix, and Benjamin Cross. Nanorhéomètre pour l'étude des liquides confinés. In *7ème Colloque Interdisciplinaire en Instrumentation*, 2016.

[47] Cholé Barraud, Léo Garcia, Benjamin Cross, and Elisabeth Charlaix. Real-time single analog output for quadrature phase interferometry. *Measurement Science and Technology*, 28, 4 2017.

[48] Stuart T. Smith, Derek G. Chetwynd, and D. Keith Bowen. Design and assessment of monolithic high precision translation mechanisms. *Journal of Physics E: Scientific Instruments*, 20:977–983, 1987.

[49] Heinrich Hertz. Ueber die berührung fester elastischer körper. *J. Reine Angew. Math.*, 1882(92):156–171, 1881.

[50] Narottam P. Bansal and Robert H. Doremus. *Handbook of glass properties.* Academic Press, 1986.

[51] Yolanda Sanchez-Vicente, Ian Emerson, Richard Glover, Oliver Herbage, Rodrigo Susial Martin, and JP Martin Trusler. Viscosities of liquid hexadecane at temperatures between 323 k and 673 k and pressures up to 4 mpa measured using a dual-capillary viscometer. *Journal of Chemical & Engineering Data*, 64(2):706–712, 2019.

[52] Cécile Cottin-Bizonne, Audrey Steinberger, Benjamin Cross, Olivier Raccurt, and Elisabeth Charlaix. Nanohydrodynamics: The intrinsic flow boundary condition on smooth surfaces. *Langmuir*, 24:1165–1172, 2 2008.

[53] Hugo K. Christenson and Roger G. Horn. Direct measurement of the force between solid surfaces in a polar liquid. *Chemical Physics Letters*, 98(1):45–48, 1983.

[54] William M. Haynes. *CRC Handbook of Chemistry and Physics, (93th Edition).* CRC press, 2012.

[55] Guy Chauveteau, Matthew Tirrell, and A. Omari. Concentration dependence of the effective viscosity of polymer solutions in small pores with repulsive or attractive walls. *Journal of Colloid and Interface Science*, 100(1):41–54, 1984.

[56] Chloé Barraud, Benjamin Cross, Cyril Picard, Fréderic Restagno, Lilianne Léger, and Elisabeth Charlaix. Large slippage and depletion layer at the polyelectrolyte/solid interface. *Soft Matter*, 15:6308–6317, 2019.

[57] Joseph Kestin, H. Ezzat Khalifa, and Robert J. Correia. Tables of the dynamic and kinematic viscosity of aqueous NaCl solutions in the temperature range 20–150°C and the pressure range 0.1–35 MPa. *Journal of Physical and Chemical Reference Data*, 10(1):71–88, 01 1981.

[58] Di Jin, Yongyun Hwang, Liraz Chai, Nir Kampf, and Jacob Klein. Direct measurement of the viscoelectric effect in water. *Proceedings Of The National Academy Of Sciences Of The United States Of America*, 119(1), JAN 4 2022.